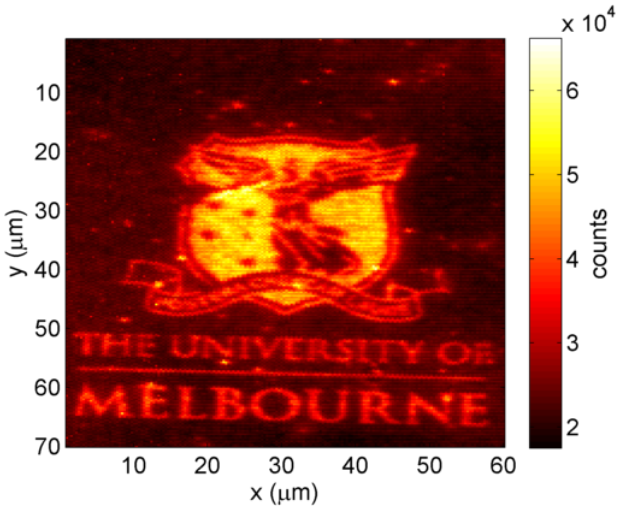
Novel Plasmonic Elements for the Generation, Manipulation and Detection of Polarised Light.

Jasper J. Cadusch

ORCID: 0000-0002-1353-7005



This thesis presented for the degree of
Doctor of Philosophy
Submitted in total fulfilment of the requirements
of the degree of Doctor of Philosophy

School of Physics
The University of Melbourne
Australia

October 25, 2017

Abstract

Plasmonics provides an opportunity to develop nanoscale optical devices, where the spectral, angular and polarisation response can be tailored. The aim of this research is to determine which designs prove suitable as polarisation sensitive features, how novel nanofabriction techniques can be employed to scale up the production and in what settings can we use these scalable plasmonic polarising devices to address current nanophotonics challenges.

Presented here is a study of potential plasmonics based methods of manipulating polarisation, including converting the polarisation state of a beam from linear to circular with carefully designed cross nanoapertures in a metallic film, strong filtering of left and right circular polarised light using 2D chiral geometries as well as creating a compact nanoantenna-enabled metal–semiconductor–metal photodetector to determine the polarisation state of a beam.

To ensure the economic feasibility of the devices, special attention is also paid to novel scalable nanofabrication techniques. The cost of a feature is of great concern, as it is of little use to have an expensive feature for applications in consumer photonics. To that end a direct imprinting technique for the low cost production of plasmonic metasurfaces is investigated, including a study of the optical phenomena achievable and some potential applications are discussed.

Finally, altering the quantum properties of emitters coupled to these scalable plasmonic features is investigated. Particular attention is paid to increasing the emission rate and polarising or focussing light from quantum sources using plasmonic nanocavities. These plasmon-exciton devices could see a reduction in the energy requirements of LED displays.

This is to certify that

(i) this thesis comprises only my original work towards the degree of Doctor of Philosophy except where indicated.

(ii) due acknowledgement has been made in reference to where the work of others has been used.

(iii) the thesis is less than 100,000 words in length, exclusive of tables, figures, bibliographies and appendicies.

Jasper J. Cadusch .....

Preface

Some of the figures used in this thesis have been taken from other works. In these instances the appropriate source has been cited at the end of the figure caption to acknowledge the source and permission obtained from the publisher for reproduction.

Dr Timothy James must be recognised for the early sample preparation before I was licensed to operate the electron beam evaporation system at the Melbourne Centre for Nanofabrication (MCN). The thin silver films prepared by Dr James were used in the chiral metasurface and plasmonic quarter waveplate experiments. Dr Daniel Gomez, Dr Timothy James, Dr Matteo Altissimo and Dr Fatima Eftekhari all gave expert advice regarding advanced fabrication techniques during my various process development stages. Evgeniy Panchenko assisted with the development, fabrication and measurement during the spiral photodiode experiment, including developing two custom balanced transimpedance amplifiers. Dr Nicholas Kirkwood synthesised the quantum dots used throughout this research project.

Experimental advice in regard to device development and characterisation was given by Dr Timothy James, Dr Daniel Gomez, Dr Timothy Davis, Prof Paul Mulvaney, A/Prof Jeff McCallum, Prof Kevin Webb and Prof Ann Roberts. Over the course of this work several publications and presentation were based on the work presented herein. They are listed below for reference.

0.1 List of Peer Reviewed Publications

J. J. Cadusch, T. D. James, and A. Roberts, "Experimental demonstration of a wave plate utilizing localized plasmonic resonances in nanoapertures," *Optics express*, vol. 21, no. 23, pp. 28 450–28 455, 2013.

J. J. Cadusch, T. D. James, A. Djalalian-Assl, T. J. Davis, and A. Roberts, "A chiral plasmonic metasurface circular polarization filter," *IEEE Photonics Technology Letters*, vol. 26, no. 23, pp. 2357–2360, 2014.

J. J. Cadusch, E. Panchenko, N. Kirkwood, T. D. James, B. C. Gibson, K. J. Webb, P. Mulvaney, and A. Roberts, "Emission enhancement and polarization of semiconductor quantum dots with nanoimprinted plasmonic cavities: towards scalable fabrication of plasmon-exciton displays," *Nanoscale*, vol. 7, no. 33, pp. 13 816–13 821, 2015.

E. Panchenko, **J. J. Cadusch**[1], T. D. James, and A. Roberts, "Plasmonic metasurface-enabled differential photodetectors for broadband optical polarization characterization," *ACS Photonics*, vol. 3, no. 10, pp. 1833–1839, 2016.

L. Du, S. S. Kou, E. Balaur, **J. J. Cadusch**, A. Roberts, B. Abbey, X.-C. Yuan, D. Tang, and J. Lin, "Broadband chirality-coded meta-aperture for photon-spin resolving," *Nature Communications*, vol. 6, 2015.

C. Ng, **J. J. Cadusch**, S. Dligatch, A. Roberts, T. J. Davis, P. Mulvaney, and D. E. Gomez, "Hot carrier extraction with plasmonic broadband absorbers," *ACS Nano*, vol. 10, pp. 4704–4711, 2016.

P. Zeng, **J. J. Cadusch**, D. Chakraborty, T. A. Smith, A. Roberts, J. E. Sader, T. J. Davis, and D. E. Gómez, "Photoinduced electron transfer in the strong coupling regime: Waveguide–plasmon polaritons," *Nano Letters*, vol. 16, pp. 2651–2656, 2016.

A. Djalalian-Assl, **J. J. Cadusch**, Z. Q. Teo, T. J. Davis, and A. Roberts, "Surface plasmon wave plates," *Applied Physics Letters*, vol. 106, no. 4, p. 041104, 2015.

A. Djalalian-Assl, **J. J. Cadusch**, E. Balaur, and M. Aramesh, "Tunable surface plasmon wave plates," *Optics Letters*, vol. 41, no. 13, pp. 3146–3148, 2016.

[1] equal-first author

Acknowledgements

First and foremost, this research project would not have been possible if it were not for the guidance, encouragement and pertinent instructions and advice of my Supervisor, the wonderful Professor Ann Roberts. Prof Roberts provided me with critical advice which provided me with much needed momentum when I was stagnating as well as working tirelessly to ensure I had the critical feedback necessary to finish this body of work. Dr. Timothy James also played a critical role throughout this research as he produced the metallic films used in Chapter 5, imparted important knowledge regarding research in general, how best to characterise my plasmonic arrays and present the results. He was the perfect Yin to Ann's Yang. The advice of Dr. James saved me many hours of toil and truly facilitated the bulk of this research.

Discussions with Dr. Daniel Gomez about fabrication and dark field and fluorescence microscopy techniques were extremely helpful to the author. Advice from Dr Timothy Davis concerning chirality and dichcroism was critical to the development of parts of this project. Without the many discussions, diversions, support, explanations (both to and from them) and ideas of my peers, this project would not have succeeded. Amir, Stuart and Eugene all contributed to this research in uncountable ways, both intangibly and directly. For, were it not for their willingness to be used as a collective sounding board and as an inexhaustible well of knowledge the ideas discussed herein would have struggled to have have made even a shadow of an impression on my prefrontal cortex. For this I am grateful. For all the coffees, beers, memes and laughs I am indebted.

I must acknowledge the unwavering support and encouragement of my family.

Needless to say, I would not have been in a position to undertake this project if it were not for them! Thank you mum, dad, Nan and Mia for all you have done for me.

Finally, the endless patience, support and encouragement throughout, from my loving wife Michelle has fundamentally underpinned my ability to carry out this research, as well as motivating me to work as hard as I have needed. For this, I can never fully repay you.



In Loving Memory of My Friend, Scrappy 1999-2016

"Remember kids, the difference between screwing around and science, is writing it down." –ADAM SAVAGE

The following report is potentially subject to 3rd party intellectual property rights. Therefore, the material herein is of a confidential nature. Please treat with sensitivity.

Contents

0.1 List of Peer Reviewed Publications iv

1 Introduction **1**

1.1 Metasurfaces and Nanophotonics 3

1.1.1 Polarising Plasmonic Features 4

1.1.2 Compact Detection of Polarisation States 5

1.1.3 Altered Emission and Absorption States in Plasmon Coupled Quantum Sources 6

1.1.4 Industrial Scale Production of Nanoscale Features 7

1.1.5 Thesis Goals Summary 9

1.1.6 Thesis Organisation 10

2 Theoretical Background Underpinning the Plasmonic Devices Studied Here **11**

2.1 Introduction 11

2.2 Plasmonics 12

2.2.1 The Surface Plasmon Resonance 12

2.3 Chirality in Nature 14

2.4 Chiral Nanoantennas 16

2.4.1 Far-field Scattering and Localised Surface Plasmon Resonances 17

2.4.2 Potential Applications of Differential Scattering 19

2.5 Nanocavities 20

2.5.1 Waveguide Modes and Standing Waves 22
2.6 Perfect Absorbers 25
2.6.1 Green's Function Approach 26
2.7 The Purcell Effect 28
2.8 Summary 29

3 Numerical Methods and Fabrication **30**
3.1 Electron Beam Lithography 30
3.2 Electron Beam Evaporation 35
3.3 Focused Ion Beam Milling 35
3.4 Nano Imprint Lithography 38
3.4.1 Thermal NIL 38
3.4.2 Resistless NIL 39
3.5 Deep Reactive Ion Etching 43
3.6 Numerical Methods 44
3.7 The Finite Element Method in COMSOL Multiphysics 45
3.8 RF module of COMSOL Multiphysics 47
3.9 Summary 48

4 Optical Characterisation Techniques **49**
4.1 Spectral Measurements 49
4.1.1 Inverted Microscope 50
4.1.2 Bench-Top Optical Setup 50
4.2 Polarimetry 50
4.2.1 Stokes' Vectors 51
4.2.2 Maximum Likelihood Measurement of Mueller Matrices . . 52
4.3 Fluorescence Scanning Confocal Microscopy, Time Correlated Single Photon Counting and Beaming Measurements 54
4.3.1 Fluorescence scanning confocal microscopy 54
4.3.2 Time correlated single photon counting 55

4.3.3 k-space Imaging of Emission Patterns 56
4.3.4 Electronic Characterisation of Photodiodes 58
4.4 Summary 59

5 Circular Polarisation States and Plasmonics 60
5.1 Introduction 60
5.2 A Plasmonic Quarter Wave Plate 61
5.2.1 Analytic model and numerical calculations 61
5.2.2 Fabrication 63
5.2.3 Device characterization 64
5.3 A Nanoaperture based Chiral Metasurface 68
5.3.1 Design Considerations 68
5.3.2 Device Fabrication and Characterization 71
5.3.3 Experimental Results 72
5.4 Plasmonic Nanoantenna Coupled Photodiodes for Polarisation State Detection 76
5.4.1 Photodiode Design 76
5.4.2 Nanoantenna Enabled Differential MSM Photodiode 77
5.4.3 Response of Chiral Nanoantennas to Linearly Polarised Light 78
5.4.4 Fabrication of the Spiral Photodiode 82
5.4.5 Electro-Optical Properties of the Spiral Photodiode 82
5.4.6 Polarisation Sensitive Photodiode Performance 84
5.5 Summary 88

6 Scalable Fabrication of Nanocavities 90
6.1 Introduction 90
6.2 Creating Nanocavtites with RNIL: Effects of Applied Pressure and Material Choice 91
6.2.1 Imprint Pressure Determines Cavity Depth 96
6.3 The Optical Properties of Scalable Plasmonic Nanocavities 102

6.3.1 Cavity Depth Determines Resonant Wavelength 103
6.4 Nanocavity Arrays as Optical Elements 107
6.4.1 Large Area Arrays 107
6.4.2 Scalable Polarising Frequency Selective Metasurfaces 108
6.4.3 Refractive Index Sensing Substrates 114
6.5 Summary 117

7 Plasmonic Cavities for Quantum Source Control 119
7.1 Introduction 119
7.2 Quantum Dot–Metasurfaces 121
7.2.1 Fabrication and Experimental Methods 123
7.2.2 Results and discussion 126
7.3 A Quantum Dot Doped Gires-Tournois Metalon 134
7.3.1 Fabrication of the Device and Integration of QDs 136
7.3.2 Device Characterisation and Results 139
7.4 Polarised Bullseye Slot Nanoantennas for QD emission shaping and Polarisation 145
7.4.1 FEM Beam Optimisation 145
7.4.2 Fabrication 148
7.4.3 Polarisation Resolved Scanning Confocal Imaging of the Bullseye 150
7.4.4 Polarisation Resolved Far-Field Intensity Patterns 152
7.5 Summary 155

8 Conclusions and Future Work 157
8.1 Thesis Goals 157
8.2 Outcomes of Work 157
8.3 Key Contributions to Knowledge Stemming from the Work 159
8.4 Future Work 160
8.4.1 Extended Spiral Photodiode for Full Stokes' Polarimetry . . 160

8.4.2 Nanoimprint Version of QD-Slot-Bullseye 162
8.5 Summary 163

Appendices **164**

A Far-field Scattering and Localised Surface Plasmon Resonances **165**

B Calibration of Polarisation Resolved Far-Field Emission Pattern Images **169**

C Random Plasmonic Metalon for Hot Carrier Generation **171**
C.1 Introduction 171
C.2 A Broadband Gires-Tournois Metalon Based Hot Electron Photodetector 172
C.2.1 Finite element method (FEM) calculations of Fields and Absorption in Random Metalons 174
C.2.2 Broadband Absorption 176
C.2.3 Sub-Bandgap Hot Electron Injection Photocurrent 178
C.2.4 Summary 181

List of Figures

1.1 An illustration of a single wavelength, polarisation multiplexed communication scheme [6]. 1

1.2 Birefringence images of a *Nephrotoma suturalis* cells. By measuring the birefringence of the cell it is possible to image the transparent internal components [4]. 2

1.3 SEM images of plasmonic metasurfaces for polarisation manipulation [9]. 3

1.4 (a) Photograph of Australian Prime Minster Edward Gough Whitlam and Vincent Lingiari. (b) A 1.5 cm array of nanoantennas viewed through a linear polariser vertical and (c) horizontal [12]. . 5

1.5 (a) Aluminium nanoantenna enabled polarisation sensitive photodetector, (b) a polarisation insensitive control, (c) a linear polarisation sensitive detector and (d) a circular polarisation state detector. Insets show the nanoantenna dimensions. Scale bars are 10 μm (a) and 1 μm (b-d). 6

1.6 Typical structure of a QD-LED with the QD layer between a metallic cathode/back-reflector and transparent conducting oxide anode (left). Electroluminescence spectra for different coloured QD-LEDs (right) [2]. 7

1.7 A comparison of throughput versus appropriate feature length scale of several top down fabrication techniques [16]. 8

1.8 A darkfield microscope image of a plasmonic array of nanocavities fabricated using RNIL. 9

2.1 Example of LSP modes of a chiral nanoparticle [32] 18

2.2 The calculated emission spectra (a) for an electric dipole source, oriented along the short axis of the cavity for closed- (b) and open-ended (c) geometries. (b) and (c) show the electric field magnitude at resonance for each geometry. 21

2.3 The calculated dispersion diagram for odd-TM modes for a 50 nm wide Au–SiO_2–Au MIM waveguide. Here the colorbar represents the logscale difference between the LHS and the RHS of equation 2.8. 23

2.4 The calcuated dispersion diagram from 2.3 recast in terms of excitation wavelength λ and cavity depth, d. Here the colorbar represents the logscale difference between the LHS and the RHS of equation 2.8. 24

2.5 The calculated dispersion diagram for odd-TM modes for a 50 nm wide Ag–SiO_2–Ag MIM waveguide. Here the colorbar represents the logscale difference between the LHS and the RHS of equation 2.8 24

2.6 The calcuated dispersion diagram from 2.5 recast in terms of excitation wavelength λ and cavity depth, d. Here the colorbar represents the logscale difference between the LHS and the RHS of equation 2.8. 25

2.7 The typical geometry of a perfect absorber structure. With spacer thickness, d and refractive index n, the field accululates e^{ink_0d} phase as it passes through. The metasurface array has a period p and a reflectivity r_m, whilst the optically thick mirror or ground plane has reflectivity r_g. 26

3.1 A schematic of the Vistech EBPG 5000+ [53]. 34

3.2 A schematic of a bilayer lift off EBL process [56]. 34
3.3 An example Ag polycrystalline film deposited with e-beam evaporation. 36
3.4 An example of a FIB milled cat's eye structure in a 100 nm Ag film (left) and the source bitmap image used to instruct the FIB (right). 37
3.5 15 kDa PMMA film imprinted with a HSQ master with 100 nm diameter circular posts. 38
3.6 (a) the etched Si master is pressed into a thin Au or Ag film and the pattern transfered, (b) the imprinted pattern in a Au film, (c)-(h) a variety of patterns can be transferred using cold forging (including a mere 8 nm gap) [17]. 40
3.7 (a) the remainig metal residue as a function of applied pressure, (b)-(d) the imprinted patterns in a Ag film (note the very smooth and angled sidewalls) [17]. 40
3.8 Various colour filtering patterns transferred to a Ag film using RNIL [17]. 41
3.9 An RNIL imprint of circular nanoholes in 100 nm of Ag. Note the double imprint pattern due to master slippage and the piece of Si mater in the centre of the image. 43
3.10 A DRIE etched Si wafer with vertical side walls. The etch depth in this case is 900 nm. 44
3.11 A comparison of different mesh densities generated by the COMSOL meshing algorithm [62]. 47

4.1 A schematic of the bench-top setup used for spectral and polarisation measurements. 51
4.2 A polar plot of the intensity of light transmitted through two LPs as a function of relative angle as measured using markers provided by the manufacturer. There is a 10° offset from the expected curve. 52

4.3 A schematic diagram of the scanning fluorescence confocal microscope used in this work. Short wavelength light is used to excite emitters in the focal plane. The emitted light is then focussed onto a pinhole aperture and then transmitted light intensity is measured by an avalanche photodiode (APD). Rays from beyond the focal plane are blocked by the aperture. The sample is scanned in the focal plane using a piezo-electric stage. 54

4.4 An example TCSPC result for a 2-level system (blue) and a system of multiple energy levels, either in one emitter or a collection of similar emitters (orange). Here the mean lifetime for both cases is 10 ns. 55

4.5 Schematic diagram of the Fourier microscope used for polarisation resolved k-space fluorescence imaging. 57

4.6 A schematic diagram of the experimental set-up used for the electrical and spectral characterisation of polarisation senstive MSM photodiodes. 58

5.1 Schematic diagram of the unit cell of a plasmonic quarter-wave plate, (a). The geometric parameters are film thickness, $T = 40$ nm, slot width, $W = 40$ nm, unit cell periodicity $P = 300$ nm and L_x, L_y, the slot lengths, are varied. A 2 nm Ge adhesion layer is also shown in green. (b) Transmission spectra for an array of 120 nm by 140 nm cross apertures, with a period of 300 nm in a 40 nm Ag film calculated using the FEM for three polarization angles; 0° (blue line) 45° (black) and 90° (red). At a wavelength of 700 nm the intensity transmission is independent of the angle of linear polarization; this is the operating wavelength of the QWP. 62

5.2 (a) Computed transmission, $T_\lambda(L)$, of 700 nm light through a rectangular aperture in a 40 nm Ag film on a SiO_2 substrate as a function of aperture length, L. The full-width-half-maximum, Δ_λ, is 28 nm and is indicated by the dashed lines. (b) An SEM image of the fabricated plasmonic QWP. The cross apertures were milled using a focused ion beam. Each element is 300 nm from its neighbour . . 64

5.3 (a) A schematic diagram of the bench top polarimetry set up. The incident beam passes through a collimator, a linear polariser (LP) and an achromatic quarter wave-plate (QWP) and is then focused onto the array with an objective lens (OL). The analyser consists of the same optical elements, in reverse order. (b) The principal axis of the array forms an angle, α, with the x-axis. The angle of polarization, θ is measured from the x-axis. (c) The measured intensity of linearly polarized light transmitted through the plasmonic QWP for 0° (blue line) 45° (black line) and 90° (red line) angle of polarization. At a wavelength of 702 nm the transmission is polarization independent. 65

5.4 A plasmonic 2D planar chiral unit cell consisting of two offset slot apertures in a metallic film. The red arrows represent the electric dipole directions of LSP modes k and j. The separation angle, $(\theta_k - \theta_j)$, is shown in blue. 69

5.5 SEM images of the FIB fabricated chiral aperture arrays in a 50 nm Ag film. The separation angles are (a) 30°, (b) 45°, (c) 60° and (d) 90°. 72

5.6 (a) The normalized difference in transmission for LCP and RCP through an array of apertures with separation angle 45° (blue line) and 90° (red line). The solid lines represent experimental results and the dashed lines are from simulation. The inset shows the calculated differential transmission through arrays of nanoholes (blue dashed) and nanorods (green dashed) of the same dimensions, with a 45° separation angle. (b) Circular polarization transmission contrast as a function of separation angle. The dotted line is $\sin 2\theta$, the red squares are the measured contrasts and the blue circles are the contrasts calculated using the FEM. 74

5.7 Normalized surface charge distributions (SCD) calculated using the finite element method to solve Maxwells equations. The blue regions indicate areas of a negative surface charge and the red regions indicate positive surface charge density. The top two rows are the SCD for a separation angle of 45° and the bottom two are for a 90° separation angle. The black arrows indicate the handedness of the incident field, with clockwise rotation corresponding to a RCP field. Each column is the SCD at different points of a half cycle, where ω is the frequency of the field and t is time. 75

5.8 Difference, ΔR, between the scattering of linear polarised light from enantiomers of chiral nanoantennas with a 45° opening angle at normal incidence as a function of polarisation angle and LSP phase difference. 80

5.9 Scanning electron microscope image of the spiral photodetector (a). Nanoantennas are absent between two signal leads. The active regions with square (b), rectangular (c) and chiral (d) nanoantennas respectively. The scale bar for image (a) is 10 μm and 1 μm for images (b),(c),(d). 83

5.10 The current-voltage characteristics and power dependence (inset) of our MSM photodiode. The black I-V curve shows the dark current characteristics of the device, while the red curve shows the device performance with the room lights on, an order of magnitude increase in photocurrent.The inset shows the measured photocurrent for increasing 635 nm laser power. 84

5.11 The incident polarisation state for a rotating waveplate (the blue line is for a QWP and the orange line is for a HWP) mapped onto the Poincaré Sphere. The curves depict the change in Stokes' vector for a 180° rotation of the waveplate. 86

5.12 Normalised detected photocurrent for each channel of photodetectors with rectangular (a), square (b) and chiral (c) sets of nanoantennas (inset). As can be seen, the differential photocurrent of each photodetector (d),(e),(f) is not affected by power fluctuations in the raw signals. (g),(i) and (j) show the amplitude of the differential signal at each orthogonal state of polarisation, from which the degree of polarisation of the incident beam can be determined. . . 87

5.13 The amplitude of the difference in responsivity between each channel of the linear polarisation photodetector for x-polarised light as a function of wavelength. A -3V bias voltage was used and the optical power was kept fixed at 5 μW for each 10 nm linewidth range of wavelengths. 89

6.1 The RNIL process used here consists of lithogrpahic patterning of a Si master, then pressing the nanofeatures of the master into a metal film using a hydraulic press. 92

6.2 A depiction of the resistless nanoimprinting process. A 40 nm layer of HSQ is spun onto a silicon wafer (a), which is patterned using EBL (b) and etched using RIE (c), an anti-stick layer is applied to the master(d), then pressure is applied to force the master into into a silver film (e). The inverse pattern is now imprinted into the silver film (f). 93

6.3 RNIL can be used to create complex shaped cavities: imprinted symmetric cross cavities in a 200 nm Au film. The scale bar is 1 μm and each cross arm is 120 nm by 40 nm. Excess metal from each cavity can be seen at the bottom left of each cross. 94

6.4 An example of slippage during the imprint process into a silver film. The master consisted of 50 nm x 50 nm (cross-section) squares, yet the resulting imprint is as shown. The scale bar is 300 nm. 94

6.5 A failed attempt at imprinting nanocavities into Al. It appears the presence of the native oxide layer diffuses the applied force across a large area. The measured feature depth is only 12 nm. Large scale bar is 5 μm and 100 nm inset. 95

6.6 (a) The layout of the master used to create single nanocavities, each nanofeature is 5 μm apart and has cross-sectional dimensions of 150 nm by 50 nm. The features cover an entire 4" wafer. (b) and (C) The master is stamped into a thin metal film, either gold or silver and nanocavities created. The nanofeatures are 150 nm high and the cavity depth depends on the applied pressure. (d) A SEM image of one of the nanofeatures, taken at a tilt angle of 45°, the scale bar is 200 nm and the measured height is 157 nm. 97

6.7 A nanoimprinted 200 nm gold film, here the cavities are 120 nm deep. The scale bar is 1 μm. A close up of a single nanocavity, scale bar 200 nm (inset). 98

6.8 Imprint depth for 5 different applied pressures (triangles) for a 200 nm Ag film on a Si substrate. The silver dashed line is the maximum possible depth (157 nm, the height of the master). The blue dashed line is $d(P, 200; Ag)$, a logarithmic line of best fit. 100

6.9 Imprint depth for 5 different applied pressures (triangles) for a 200 nm (a) and a 90 nm (b) Au film on a Si substrate. The gold dashed lines are the maximum possible depth ((a) 157 nm, the height of the master and (b) 90 nm, the thickness of the film). The blue dashed lines are (a) $d(P, 200; Au)$ and (b) $d(P, 90; Au)$, logarithmic lines of best fit. 101

6.10 Single nanocavity absorption spectra for varied applied imprint pressure in a 200 nm thin Ag film on a Si substrate. 103

6.11 Single nanocavity absorption spectra for varied applied imprint pressure in a 90 nm Au film (a)and a 180 nm thin Au film (b) on Si substrates. 104

6.12 Peak absorption wavelengths of nanocavities as a function of the applied imprint pressure (a)(c)(e). Maximum absorption of nanocavities as a function of the applied imprint pressure (b)(d)(f). The dashed lines are logarithmic lines of best fit to guide the eye. 106

6.13 A large area array of nanocavities (see inset) imprinted into a silver film. The scale bar is 200 μm and 100 nm in the inset. The total area imprinted was 4900 mm^2. 108

6.14 An SEM image of a HSQ/Si master template, consisting of a structured array of 200 nm by 50 nm nanorods. The white scale bar is 5 μm. The image has been reversed. 110

6.15 An SEM image of the imprint in a silver film produced using the master shown in Fig. 6.14. Note the fine details are made up of only a few nanocavities. The white scale bar is 5 μm 111

6.16 AFM trace of the nanoimprinted cavity array in a 200 nm Ag film. The imprint depth is 45 nm, including the pile up of excess metal at the cavity opening. 112
6.17 Polarisation extinction ratio (PER) of the nanoimprinted metasurface shown in Fig. 6.18(a) at normal incidence. 113
6.18 Darkfield microscope images of the University Crest metasurface imprinted into a thin silver film (a) and the MCN logo metasurface imprinted into a thin silver film (b). The nanocavities comprising the metasurfaces are the same dimensions. 113
6.19 Imprinted refractive index sensor array in a gold film. The red region indicates the presence of water in the nanocavities. The bright white regions are silicon debris left over from the master failing during imprint. 115
6.20 (a) FEM calculated reflection spectra for nanocavity arrays for superstrates with n=1 to n=2 (from bottom to top, in steps of $\Delta n = 0.1$). (b) Resonant wavelength, λ_0 as a function of refractive index. 116
6.21 (a) Reflection from a nanocavity array as a function of superstrate refractive index. (b) An example refractive index tomograph of a CA9-22 cell taken from [108]. 117

7.1 (a) An array of nanocavities in a thin silver film, covered with CdSe/CdS/ZnS QDs. (b) The QDs can be excitied with green light then emit red light, which drives a cavity plasmon mode. 122
7.2 A scanning electron micrograph of the resistless nanoimprinted cavity array in a silver film. The cavities are highly asymmetric, measuring 200 nm long by 40 nm wide. 123
7.3 A HRTEM image of the monodisperse graded alloy shell QDs. . . . 124

7.4 The measured reflectance of the SU8 encapsulated silver nanocavity array (blue) and the normalized emission from the $Cd_xZn_{1-x}S$ quantum dots in SU8, measured on a glass microscope slide (red). 126

7.5 A fluorescence microscope scan of the quantum dots interacting with the nanoimprinted cavities. The emission from QDs near the cavities have around 3.5 times the intensity than for QDs near the bare Ag film. This is evidence of coupling between the plasmonic cavity modes and the quantum dot excitons. 127

7.6 A comparison of the collected fluorescence from the QDs above the cavity array (blue) and above the unpatterend film (red). 129

7.7 Confocal scans of the QD/SU8 mixture on the unpatterned silver film, (a) at the silver surface and (b) 12 μm from the silver surface. 129

7.8 Spectra from QDs on the cavities (blue) and on the unpatterned silver (yellow). The presence of the cavities increases the EQE by 95%. 130

7.9 Normalised emission spectra (a) for the cavity coupled quantum dots with an analyser at 0° (blue), 45° (black) and 90° (red) to the long axis of the nanocavities. (b) the spatial distribution of the degree of linear polarisation, or S1, of the QD emission. The value of S1 for light collected above the cavities is up to 0.73, whilst over the Ag film it is 0. 131

7.10 (a) Normalised TCSPC histograms for quantum dots in SU8 from the same batch on glass (red) with $\tau = 17.4$ ns, on the bare silver film (blue) $\tau = 14.4$ ns and on the nanoimprinted cavity array (green) $\tau = 3.9$ ns. It is clear that plasmon-exciton interactions lead to a greatly reduced radiative lifetime. (b) The calculated total decay rate distributions $\sigma(\Gamma)$, normalized to their peak values, σ_{max}, for quantum dots in SU8 on glass (red), on an unpatterned silver film (blue) and on nanoimprinted cavities (green). The mean decay rate increases from $\Gamma_m = 0.07$ per ns for QDs on glass to $\Gamma_m = 0.237$ per ns for the cavity coupled QDs, an increase of three and a half times. The spread of the decay rate distribution also increases from $\Delta\Gamma = 0.14$ per ns for QDs on glass to $\Delta\Gamma = 0.56$ per ns for cavity coupled QDs. 133

7.11 An array of silver nanoantennas on a glass substrate is covered with QD doped PMMA of varying thickness, t, then a 200 nm silver mirror is evaporated on top to form a QD doped metalon. The device can be pumped with blue light and emits red light. 136

7.12 CFM images of QD-PMMA with (a) anisole and (b) chlorobenzene as the solvent. 138

7.13 Measured film thickness of the spin coated QD-PMMA polymer as a function of dilution ratio. 3% PMMA in chlorobenzene (PMMA-3C) was diluted with chlorobenzene. 138

7.14 Absorption spectra for 5 different QD-PMMA film thicknesses, the emission spectrum of the QD-PMMA is superimposed under the absoprtion spectra. 140

7.15 A CFM scan of the 150 nm thick metalon (a) and the emission spectrum on (blue) and off (orange) the metasurface array (b). The location of the measurements is indicated in (a) by the coloured circles. 142

7.16 Fluoresence lifetime measurements for QD-PMMA on glass, silver mirror and in the metalon. The y-axis is logarithmic. 143
7.17 A comparison of each cavities Q-factor $\times$ the spectral overlap between QD emission and cavity absorption (red line) and the Purcell factor increase in radiative decay rate determined from fluoresence lifetime measurements of the QDs as a function of QD-PMMA layer thickness, t. 144
7.18 FEM calculation results for the optimised sBE structure: (a) electric field amplitude at the silver/QD-PMMA interface, (b) the total far-field radiation pattern and x- and y-polarised components, (c) and (d) respectively, all with the same scale. 147
7.19 A schematic cross section of the slot bullseye structure covered in a layer of QD-PMMA. p is the radial spacing of the nanocavities. The first ring of nanocavities is offset from the centre of the bullseye by a, so occurs at $p + a$. 148
7.20 SEM images of the linear (a) and azimuthal (b) sBE structures. The scale bar is 1.2 μm. 149
7.21 SEM cross sectional image of the azimuthal sBE structures, taken through the centre of the device. The scale bar is 1 μm. 149
7.22 CFM scans of the emission from linear (top row) and azimuthal (bottom row) sBE structures. The x- and y-polarised scans are the first two columns respectively and the final columnn shows the spatial distribution S_1 parameter for both devices. 151
7.23 TCSPC data from QDs near the linear sBE structure (blue) and on the unpatterned silver film (orange). 151
7.24 Polarisation resolved k-space emission intensites for QD-PMMA on unpaterned silver (control sample). 152

7.25 Polarisation resolved k-space intensites for the linearly polarised sBE structure, the arrows indicate analyzer direction and Δ denotes the difference between the k-space distributions. 152
7.26 Polarisation resolved k-space intensites for the azimuthally polarised sBE structure,the arrows indicate analyzer direction and Δ denotes the difference between the k-space distributions. 153
7.27 FEM calculations of the radiated electric field for the linear sBE with superstrate index $n = 1.49$ (left) and $n = 1.53$ (right). A small discrepency in material properties leads to a large change in the radiation pattern. 155

8.1 GDSII layout file of 6 intertwined MSM photodiodes capable of full Stoke's Vector readout. Each pair of channels is designed to detect one of the polarisation eigenstates. 162
8.2 Artist's impression of a RNIL master for imprinting a linear slot bullseye. 163

A.1 Example of LSP modes of a chiral nanoparticle [32] 166

B.1 Diffraction pattern from a 2000 nm period grating as measured by the far-field imaging set-up. 170

C.1 (a) SEM of the random gold metasurface (scale bar is 1 μm) and (b) Measured size distribution of the Au nanoparticles. 174
C.2 (a)Metalon geometry used in FEM calculations, overlaid with calculated electric field at $\lambda = 650$ nm and (b) photograph of the large area metalons (from left to right) AlNPs on 50 nm TiO_2 on Au mirror, AuNPs on 50 nm TiO_2 on Au mirror and AuNPs on 50 nm TiO_2 on Al mirror. 174

C.3 A scheme for calculating absorption from SEM image. Convert the SEM (a) into a monochrome bitmap (b), then use this to define a material with $\epsilon(x, y)$, a spatially dependant relative permittivity, (c). This material can then be used in FEM calculations to determine the electric field (d) and thus the electromagnetic absorption, α, in the layer (e). 176

C.4 Architecture and working principle of plasmonic broadband absorber structure. (A) Schematic of the broadband absorber structure with TiO_2 positioned in between the Au mirror and Au nanoparticles. Inset: multiple internal reflection and interference interpretation of unit absorption [125]. Also shown is an SEM of the Au nanoparticle monolayer. (B) Absorbance spectra of the metalon, metalon without Au NPs, metalon without mirror and bare TiO_2 on glass. (C) Spatial distribution of the Electric field of the metal–semiconductor–nanoparticle structures at 650 nm. The values are shown on a logarithmic scale of the absolute magnitude square of the electric field relative to the incident field. (D) Plot of the absorption of incident light *vs.* wavelength for the top and bottom metal layers. 178

C.5 Photoelectrochemical and absorption performance of the plasmonic broadband absorber structure. (A) Illustration of the working principle: Upon visible light illumination and plasmon non–radiative relaxation, hot electrons in the Au nanoparticles can be injected into TiO_2 and be transported subsequently to the Pt counter electrode and measured as photocurrents. E_{CB}, E_{VB} and E_g refer to conduction band, valence band and band gap energy of TiO_2 respectively. (B) Photocurrent generation under both visible light illumination ($\lambda \geq 495$ nm) and in the dark in a 2 electrode system vs Pt wire; applied voltage of 0.5 V and 0.5 M Na_2SO_4 + 20 v/v% methanol electrolyte solution. (C) IPCE values for the metalon (black), TiO_2 on a gold mirror (orange) and on glass (pink). Also shown is the absorption spectrum of the metal–semiconductor–nanoparticle structure (solid black). 180

Chapter 1

Introduction

The polarisation of an optical beam describes the behaviour of the direction of the electric field vector over one oscillation [1]. It is an important property of light that can be exploited for many applications including imaging transparent biological samples, radio communications, controlling the spin state of excited atoms in an optical trap, sending quantum encrypted messages or to rapidly turn on and off light from a pixel in a display [1–4]. There are even claims that ancient Vikings used polarised skylight for navigating the North Atlantic [5].

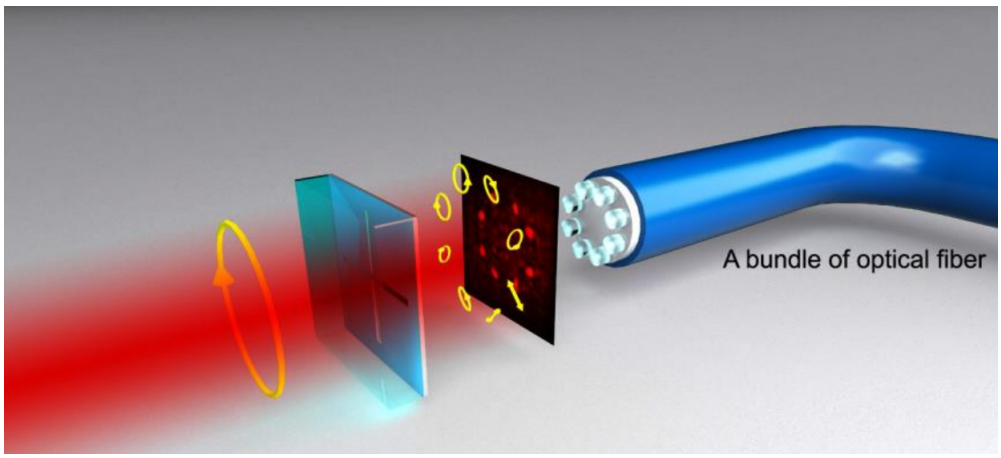


Figure 1.1: An illustration of a single wavelength, polarisation multiplexed communication scheme [6].

Two of the more prominent applications of polarised light are (i) developing methods for increased bandwidth in for telecommunication systems and (ii) sub-cellular imaging of biological samples. Polarisation multiplexing either via fibre,

as illustrated in figure 1.1 or via free-space provides a path to increased bandwidths by using orthogonal polarisation states to increase the number of channels for a given carrier frequency. In particular, circular polarisation and orbital angular momentum (vortex) beams have been shown to provide very high bit-rates up to several terabits [7]. There is however, still much room for further developments and improvements.

Polarisation based biological imaging has been directly responsible for imaging the architectural dynamics of cellular components during cell growth [8], a critical process for life. Figure 1.2 shows a comparison of two birefringence images of *Nephrotoma suturalis* cells [4]. Here the importance of polarisation based imaging to researchers can be clearly seen, where the dynamics of internal components of a live cell can be monitored and measured without staining, which may disrupt certain processes.

With the importance of the generation, manipulation and detection of polarised optical states to a diverse range of applications in mind, the research presented here seeks to investigate and develop novel nanometric polarising devices.

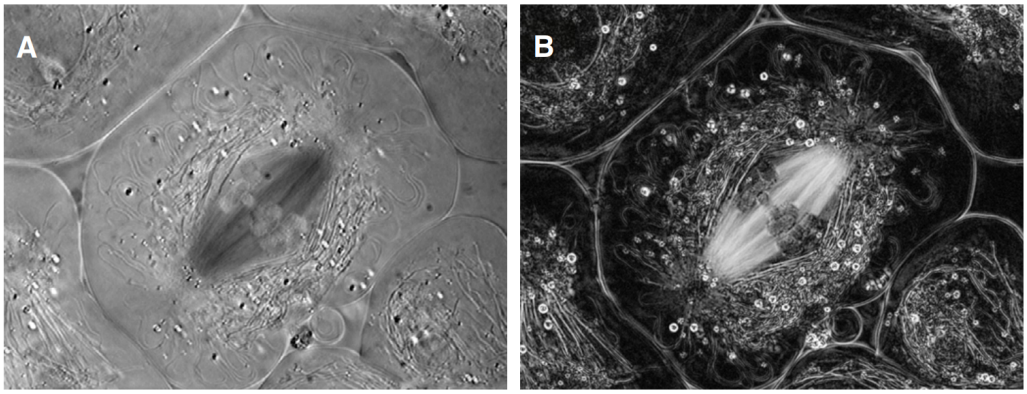


Figure 1.2: Birefringence images of a *Nephrotoma suturalis* cells. By measuring the birefringence of the cell it is possible to image the transparent internal components [4].

1.1 Metasurfaces and Nanophotonics

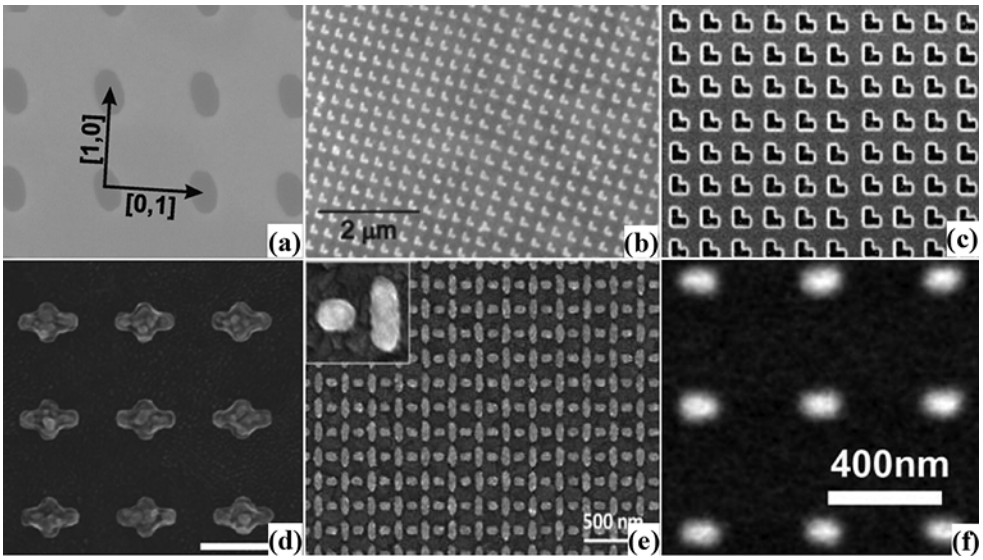


Figure 1.3: SEM images of plasmonic metasurfaces for polarisation manipulation [9].

Advances in nanotechnology fabrication techniques have allowed for the miniaturisation of optical and photonic elements. The same scaling law that has driven the semiconductor industry for decades –Moore's Law– can also be applied to the photonics sector. Miniature, on-chip devices such as lasers, LEDs, waveguides, beam splitters, lenses, modulators and detectors have been developed with future communication and computing needs in mind. By scaling these devices down it is possible to increase switching speeds, decrease signal latency as well as include more and more elements in a photonic device. The improvement of photovoltaics and quantum light sources is another highly active research area in nanophotonics, with great effort focussing on improving energy efficiency. To help address the growing demand for higher bandwidth and greater energy efficiency photonics research has, in part, turned to plasmonics. The ability to tailor the optical response of a plasmonic metasurface (a planar device made up of sub-wavelength optical resonators) is an attractive solution to address these problems [10, 11]. Figure 1.3 shows a collection of polarisation sensitive metasurfaces designed to operate at optical frequencies. In this body of work novel metasurface based

devices are developed to provide some of the building blocks required for a plasmon based nanophotonic systems, which could help address these challenges. The work herein is broadly divided into three research areas: Developing metasurfaces that allow for the generation, manipulation and detection of different polarisation states are explored; exploring novel nanofabrication techniques to allow for low cost, high throughput fabrication of metasurfaces; and developing metasurfaces to alter the emission of light from quantum sources, with a view to reduce energy consumption of non-solid-state LED based displays.

1.1.1 Polarising Plasmonic Features

The tailoring of the polarisation response of a metasurface is crucial for the operation and application of many plasmonic devices. It can be beneficial to design plasmonic metasurfaces to add a polarisation response to established polarisation insensitive technologies. For example, James *et al.* have produced a centimetre-scale polarised colour image [12], shown in figure 1.4. The image is formed when viewed through a polariser. The colour pixels of this metasurface could be used to print 3D images (by printing two offset, orthogonally polarised copies), which will not degrade with exposure to ultraviolet light like regular ink. On the other hand, plasmon resonances and metasurfaces can also be used to create highly compact versions of existing optical elements such as lenses, bandpass filters and polarisers [13–15]. Metasurfaces that either transform polarisation states between linear and circular (a plasmonic quarter-wave plate) or preferentially transmit a particular circular polarisation state (a chiral metasurface) are presented here. The first two devices discussed in this work are aperture based plasmonic metasurfaces, like the one shown in figure 1.3(c). Aperture based metasurfaces provide better heat dissipation than nanoantenna based design, and as such can be operated at higher optical powers. Both metasurfaces could find applications in telecommunication or photonic computing settings. To fabricate these devices precise control over the phase difference of the transmitted field components is required,

therefore precise control of the nanostructure dimensions are required.

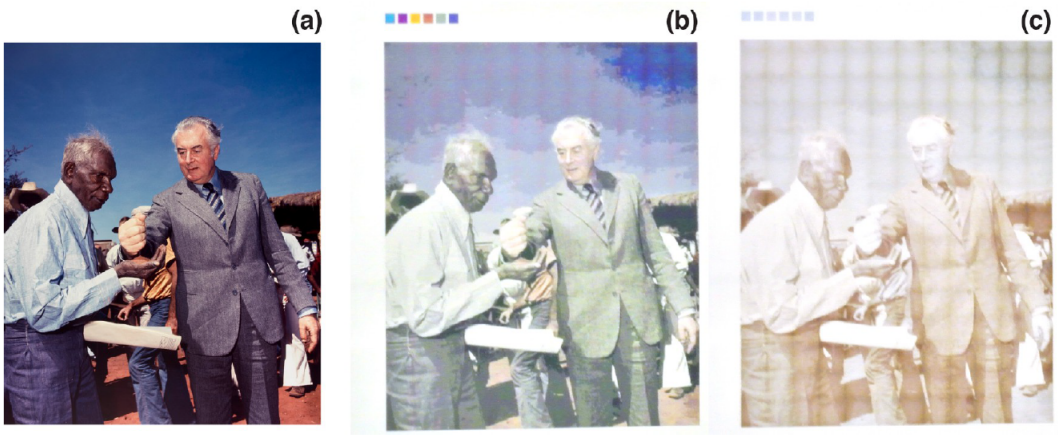


Figure 1.4: (a) Photograph of Australian Prime Minster Edward Gough Whitlam and Vincent Lingiari. (b) A 1.5 cm array of nanoantennas viewed through a linear polariser vertical and (c) horizontal [12].

1.1.2 Compact Detection of Polarisation States

The polarisation state of an optical field is important for applications in optical communications, imaging, and data storage as well as furthering our understanding of biological and physical systems. Here two doped silicon based photodetectors are integrated with aluminium nanoantennas capable of distinguishing orthogonal states of either linearly or circularly polarized light with no additional filters. The localised plasmon resonances of the antennas lead to selective screening of the underlying silicon from light with a particular polarisation state. The planar device, fully compatible with conventional CMOS fabrication methods, incorporates antennas sensitive to orthogonal states of polarisation into two back-to-back Schottky photodetectors to produce a differential electrical signal that changes sign as the polarization of an incident optical beam changes from one basis state to the orthogonal state. Each device is wrapped into a spiral footprint to provide compatibility with the circular profile of conventional optical beams and has an overall diameter of 50 μm. The sensitivity of these devices are investigated experimentally over a wavelength range from 500 to 800 nm, establishing their potential for integration into a wide range of optical systems. The major advantages over conventional polarimetry methods of this device is that bulky,

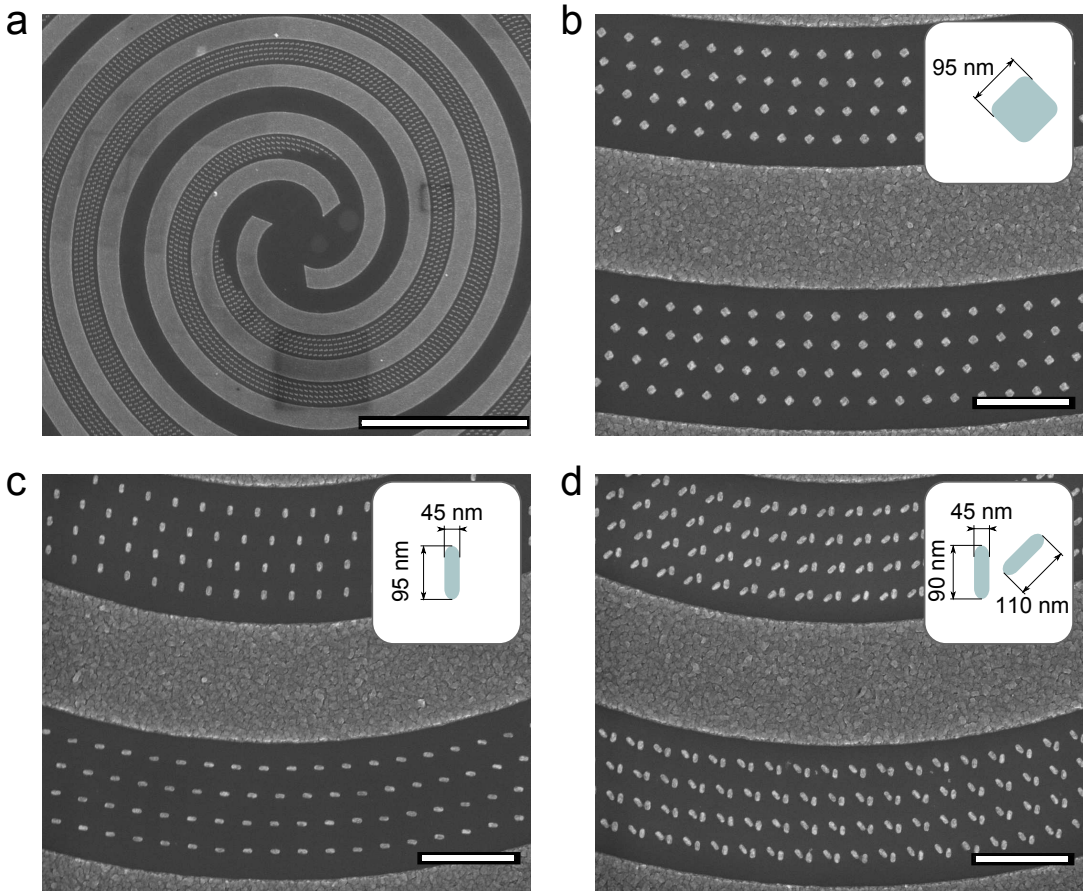


Figure 1.5: (a) Aluminium nanoantenna enabled polarisation sensitive photodetector, (b) a polarisation insensitive control, (c) a linear polarisation sensitive detector and (d) a circular polarisation state detector. Insets show the nanoantenna dimensions. Scale bars are 10 μm (a) and 1 μm (b-d).

expensive optics are no longer required, there are no moving parts and the system does not need regular alignment. This reduces both the initial and running costs of the device. Figure 1.5 shows the fabricated photodiodes.

1.1.3 Altered Emission and Absorption States in Plasmon Coupled Quantum Sources

When quantum sources such as fluorescent organic dyes and quantum dots (QDs) are placed in close proximity to optical resonators, such as plasmonic nanocavities or nanoantenna the emission and absorption characteristics of the emitter changes. This is typically due to weak coupling between the emitter and the plasmonic mode where the resonator is lossy and the emitter has a broad spectral linewidth. The result of this coupling can be reduced excited state lifetimes, en-

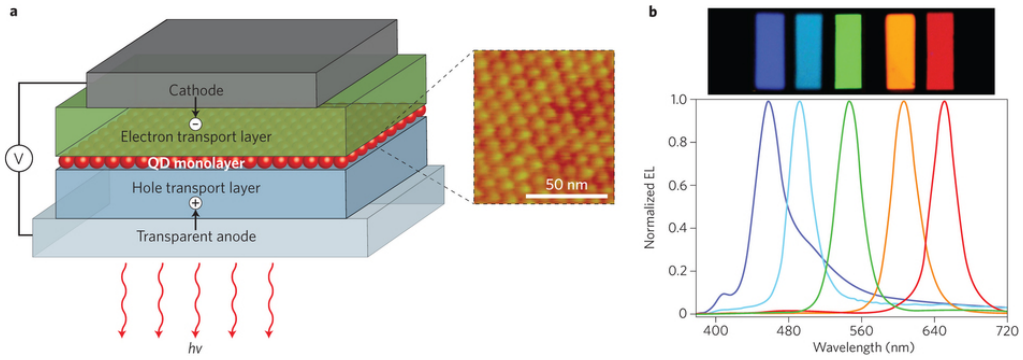


Figure 1.6: Typical structure of a QD-LED with the QD layer between a metallic cathode/back-reflector and transparent conducting oxide anode (left). Electroluminescence spectra for different coloured QD-LEDs (right) [2].

hanced brightness and polarised emission or in some situations a large increase in non-radiative energy transfer and quenching of emission. Here the coupling of random quantum dots in a thin polymer film to plasmonic nanostructures including nanorod arrays, rectangular nanocavity arrays as well as nanocavities arranged so as to focus the emitted light are investigated. Particular attention is paid to employing a rigorous statistical determination of the quantum properties such as radiative decay rate and mean lifetime of these coupled QD-plasmon systems, as well as the polarisation state of the emission. Such devices could find broad application in modern low energy displays such as those found in mobile telephones. A typical QD-LED geometry is shown in figure 1.6, including metallic cathode which could support a metasurface.

1.1.4 Industrial Scale Production of Nanoscale Features

The research presented in this thesis is focussed on the manipulation, through plasmonics, of light both from distant sources such as the Sun, LED lamps and laser diodes as well as near field sources such as quantum dots, with a view to develop novel optical features. The designs described herein require advanced nanofabrication techniques. This is to allow for sub-micron features, with reduced diffractive effects. However, it is of little commercial use to develop a

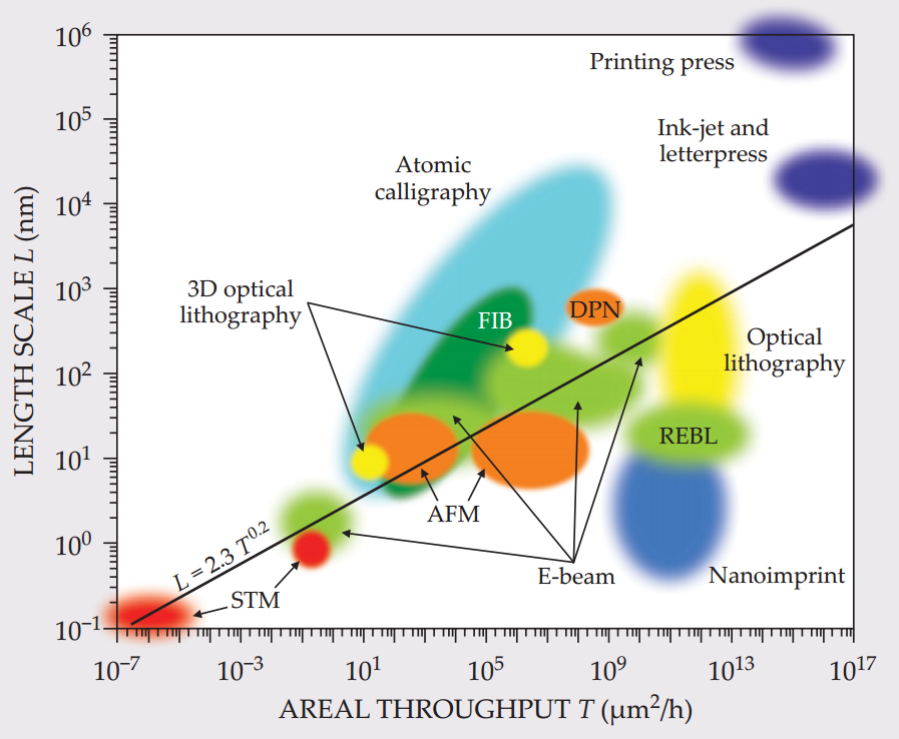


Figure 1.7: A comparison of throughput versus appropriate feature length scale of several top down fabrication techniques [16].

feature which has significant production throughput limitations and thus a large cost [16]. With that in mind, the secondary aim of this research project is to investigate nanofabrication techniques that can be cost-effectively scaled up to suit an industrial setting. Figure 1.7 shows a comparison of the feature sizes versus throughput achievable of several fabrication methods. Recently a technique known as resistless nanoimprint lithography (RNIL) was pioneered by Varghese *et al* [17]. Whilst the initial fabricaton steps require nanolithography, to create a master template or shim, plasmonic features can be created quickly by stamping the master into a metal film or foil. A study of the parameter space of the RNIL process is carried out here, in particular to determine the relationship between the applied imprint pressure, the resulting cavity depth and the subsequent spectral response of the cavities for gold, silver and aluminium films. Arrays of nanocavities are created using this technique and show a broad range of colours. Figure 1.8 shows a dark field microscope image of imprinted array of nanocavities in a thin gold film. The entire 50 μm array was imprinted in less that 30



Figure 1.8: A darkfield microscope image of a plasmonic array of nanocavities fabricated using RNIL.

seconds. The polarisation response of these nanocavity arrays depend entirely on the shape of the unit cell in the array, with rectangular cavities producing a strong polarisation dependant response. The ability to tune the spectral response of the plasmonic cavities produced with RNIL by altering the imprint pressure is an attractive proposition to reduce the cost of scaling up metasurface designs.

1.1.5 Thesis Goals Summary

In summary the following specific goals guide the research herein:

- Development of compact metasurfaces that alter the polarisation state of an incident beam.
- Design and prototyping of a novel metasurface enabled photodetector to determine the polarisation state of a beam.
- Investigate scalable nanofabrication techniques and device designs, in particular those amenable to a high-throughput environment.

- Produce plasmonic metasurfaces which alter the absorption and emission of photons.

1.1.6 Thesis Organisation

Chapter 1 provides a summary of the motivation, context and aims of the research presented in this work. Chapter 2 covers in some detail the theoretical framework and methods that were exploited during the course of this research. In Chapter 3, the details of all the nanofabrication techniques for prototyping active and passive plasmonic security devices as well as a scalable fabrication technique are discussed. Chapter 4 provides details on the optical and electrical characterisation methods used for assessing the performance of devices developed in this work. Chapter 5 covers original research concerning the generation, manipulation and detection of circularly polarised light with compact planar arrays of plasmonic nanoantennas. An investigation of the industrial scale production of plasmonic nanocavity metasurfaces, related optical phenomena and their application as spectral filters is discussed in chapter 6. Chapter 7 covers the integration of plasmonic nanocavities with quantum dot doped polymer films to improve the brightness and to polarise and direct the emission of quantum sources. Finally, a summary of the findings in this work as well as potential future avenues for research are presented in the chapter 8.

Appendix A provides a detailed derivation of the scattering of circularly polrised light from two in-plane dipoles. Appendix B details a method for calibrating a $k-$space measurement using a metallic diffraction grating. The Appendix found in C contains the results of an experiment jointly conducted with Dr Daniel Gomez's team at CSIRO, where a plasmonic hot electron device was fabricated for the purpose of water splitting.

Chapter 2

Theoretical Background Underpinning the Plasmonic Devices Studied Here

2.1 Introduction

This chapter outlines some of the established theoretical background that will be needed for the research presented in the coming chapters. This includes a brief introduction to surface plasmons, both localised and propagating. The second section provides an in-depth discussion of circularly polarised light scattering from a chiral pair of nanoantennas, which will be used in the design of the devices presented in chapter 5. The third section discusses the behaviour of plasmonic nanocavities and a closed-ended metal–insulator–metal (MIM) waveguide model is presented, which can give insights into the metasurfaces created with RNIL in chapter 6. Following on from nanocavities is a discussion pertaining to the quantum source coupled plasmonic devices presented in chapter 7 of the metamaterial-etalon structure, and a method for calculating the reflectance of such a device. Finally an introduction to the Purcell Effect, which leads to a reduction in excited state lifetimes of quantum emitters coupled to nanoantennas, is presented.

2.2 Plasmonics

A *plasma* is a phase of matter where charges have dissociated from each other and form a charged gas. Typically, plasmas are associated with nuclear reactions in stars, certain televisions and fusion reaction experiments. A *plasmon* is a quantized collective charge oscillation in a plasma.

2.2.1 The Surface Plasmon Resonance

Shortly after R.W. Wood noticed anomalies at specific frequencies in the reflection spectra of metal backed gratings *surface plasmon resonances* (SPR) became of interest to the optics community [18]. An SPR is an oscillation of the electron charge density at the surface of particular metals. Typically gold, silver and aluminium are used in plasmonic experiments. *Plasmonics* is the study or application of plasmon resonances.

Surface plasmon resonances fall into two categories, each with their own characteristics. There are Surface Plasmon Polaritons (SPPs) and Localised Surface Plasmons (LSPs). Both types of SPRs occur at the interface between a metal and a dielectric medium and depend strongly on the dielectric function of the metal supporting the resonance.

Surface Plasmon Polaritons

SPPs are a manifestation of the evanescent solutions to Maxwell's equations at the boundary between a metal and dielectric. SPPs can be excited only when the transverse component of momentum of the incident electric field matches that of the excited SPP. This can be expressed as [19];

$$|\vec{k}_{SPP}| = \frac{2\pi}{\lambda cos\theta} \sqrt{\frac{\epsilon'_{metal}\epsilon_{dielectric}}{\epsilon'_{metal} + \epsilon_{dielectric}}} \tag{2.1}$$

where λ is the freespace wavelength of incident light, θ is the angle of incidence measured form the surface normal, $\vec{k}_{SPP}$ is the SPP momentum, ϵ'_{metal} and $\epsilon_{dielectric}$ are the real parts of permittivities, at λ, of the metal and dielectric respectively. Momentum matching between photons and SPPs can be achieved using a prism in the Otto or Kretschmann configurations [19]. The most commonly used techniques to momentum match, however, is through grating coupling, corrugation excitation or the introduction of periodic features on the surface. In the latter case the evanescent surface waves are excited at each of the array elements and combine constructively to form a propagating surface mode [19]. This is analogous to Bragg scattering of electron waves in crystal lattices. Because the surface charge density waves will constructively interfere only for specific, geometry dependent wavelengths, SPP excitations are quantized (that is, occur only at discrete energies). The condition for excitation of SPPs in a 2D array with period a is given in [20] by

$$\vec{k}_{SPP} = \vec{k}_{\parallel} + i\vec{G}_x + j\vec{G}_y \tag{2.2}$$

where i and j are integers SPP mode indices, $\vec{k}_{\parallel}$ is the in-plane component of the incident field's wavevector and $\vec{G}_x$ and $\vec{G}_y$ are the reciprocal lattice vectors associated with the array structure ($|\vec{G}| = \frac{2\pi}{a}$). When tailoring optical effects using SPPs, equations (2.1) and (2.2) are combined and the reciprocal lattice vectors are determined.

Localised Surface Plasmons

Localised surface plasmons (LSPs), as the name suggests, are confined to the vicinity of a particle or aperture at a metal-dielectric interface. Hence LSP resonances are strongly dependent on the geometry of the host particle or aperture. The dielectric environment also strongly influences the wavelength of resonance, but the ability to tailor the resonant wavelength is usually done via selecting the

geometry of the nano-structure [20]. The period of the arrays of nanoparticles or nanoholes can also be used to tune resonances as well as controlling resonances associated with the excitation of SPPs [21]. Besides their multi-parametric tunability, LSP based plasmonic devices are also attractive because they tend to be more robust to the angle of incidence of the exciting field than their SPP based counterparts [21, 22]. Stefan Maier gives an excellent account of LSPs, Mie scattering, hybridisation of plasmon modes and the polarisability of nanoparticles in Chapter 5 of "Plasmonics: Fundamentals and Applications" [23, 24].

2.3 Chirality in Nature

Chiral objects have the property that the mirror image of the object cannot be superposed on top of the original object via any translation or rotation. The mirror image of a chiral object is known as its *enantiomer*. Typically, one enantiomer will be denoted right handed and the other left handed. For example circularly polarised light, where the electric field component of the wave traces out a circular path in space over one period, is chiral, one enantiomer is left hand circularly polarised (LHCP), the other right (RHCP).

Chiral structures are abundant in nature, at all scales. Spiral galaxies, snail shells and sucrose molecules all exhibit chirality. Chirality is vitally important in the Standard Model of particle physics, particularly when studying how potential Dark Matter candidates, such as neutrinos interact with electrons. As it turns out, left handed antineutrinos interact only with right handed electrons via the Weak nuclear force, which is important in processes such as beta decay and fusion reactions [25]. Besides these exotic cases chirality is also critical to human biology. Human DNA, the genetic code that determines everything from the colour of your eyes to your predisposition to breast cancer is a chiral molecule, with only the one enantiomer (the left handed one) found in human DNA. The same

molecule, twisted in the opposite direction, (that is, the enantiomer) cannot be used by the body the same way our DNA can [26]. Besides chirality being critical to biology, it is also vital to understand its importance in medicine.

In the late 1950's and early 1960's pregnant women in Australia were prescribed thalidomide to alleviate morning sickness [27]. Thalidomide is a chiral molecule,with a stereogenic carbon centre. In 1961 is was found that whilst one particular handedness of thalidomide, when consumed, has the desired effect on the mother's nausea. Tragically however, the opposite enantiomer is teratogenic (leads to malformation of embryos, from the Greek word for monster), this lead to many thousands of children born with stunted limbs as the thalidomide prescribed was not chirally pure. Complicating matters, subsequent research has shown that thalidomide racemizes in the body, so even if chirally pure thalidomide is taken, some of it will be converted to the other enantiomer [27–29].

The interaction between light and chiral molecules gives a great deal of information about the structure of a molecule, which can be used to determine how a particular molecule will interact with others. Typically a chiral molecule will exhibit optical activity. That is, when plane polarised light is passed through a solution of right handed chiral molecules, the plane of polarisation will rotate through an angle, β, for left handed molecules it rotates by $-\beta$. By knowing the optical activity of a solution, we can calculate the ratio of left handed molecules to right handed ones in the solution. In addition to optical activity, solutions of chiral molecules typically exhibit circular dichroism, where one circular polarisation state is preferentially transmitted over the other [30]. By measuring the degree of circular dichroism, the secondary chemical structure of the molecule can be determined [26].

There is no doubt that determining and understanding the chirality of chemi-

cal structures is of the utmost importance for future developments in many fields such as molecular biology, pharmacology and chemical engineering. It is therefore not surprising that plasmonic devices with a degree of chirality are of current interest in nanophotonics.

2.4 Chiral Nanoantennas

In order to develop a metasurface based circular polarisation filter for use as a passive device and then later incorporated in a polarisation sensitive photodiode, scattering of circularly polarised light from chiral nanoantennas needs to be understood. Plasmonic structures can often be thought of as collections of "meta-atoms", where each element of the structure is considered to be an artificial atom. This mode of thought is appealing as the similarities between real atoms and these artificial ones are abundant, especially considering we can model both as harmonic oscillators. Both have discretised excitation levels, where the frequency of incident light will determine if an electron or plasmon is excited. We can even extend this to collections of particles, we see that excitation modes can hybridise into pairs, just like energy levels in simple molecules, which form bonding and anti-bonding pairs [31]. Of course the root of this analogy lies in the fact that the energy levels of an atom are given by the solution to the time independent Schrodinger equation subject to boundary values just like the excitation of surface plasmons can be predicted by solving the Helmholtz Equation 2.4. In both of these equations the second order spatial derivative depends linearly on the function itself:

$$-\frac{\hbar^2}{2m}\nabla^2\psi - (E-V)\psi = 0 \tag{2.3}$$

and

$$\nabla^2\psi + 4\pi k^2\psi = 0. \tag{2.4}$$

Hence, in light of the previous section, we should expect that arrangements of these meta-atoms that exhibit some degree of chirality should also interact with polarised light in a similar manner as chiral molecules. That is we expect to see some degree of "optical activity", and especially circular dichroism. Circular dichroism is the difference in absorption of circularly polarised light, independent of the orientation of the sample (such as a sucrose solution). Whereas if a quasi-two-dimensional (that is, very thin) chiral array is reversed, the far-field response will be different (in fact it will be the same as the radiation pattern due to its enantiomer). Clearly some more fundamental work needs to be conducted to help clarify the response of chiral metamaterials to polarised light. Once this is understood, chiral metamaterials can be utilised to help determine the chirality of molecules on a sub-micron scale.

2.4.1 Far-field Scattering and Localised Surface Plasmon Resonances

To determine the far-field response of a 2D planar plasmonic structure, we need to understand the interaction between the incident EM waves and the electrons at the surface of the structure. Here we follow the work of Davis *et al.* [32], by making the electrostatic approximation, and so decoupling the magnetic flux density from the electric field in Maxwell's Equations, we can model the field scattered from a collection of nano-antennas as a sum over excitation modes. An example geometry is shown in figure 2.1.

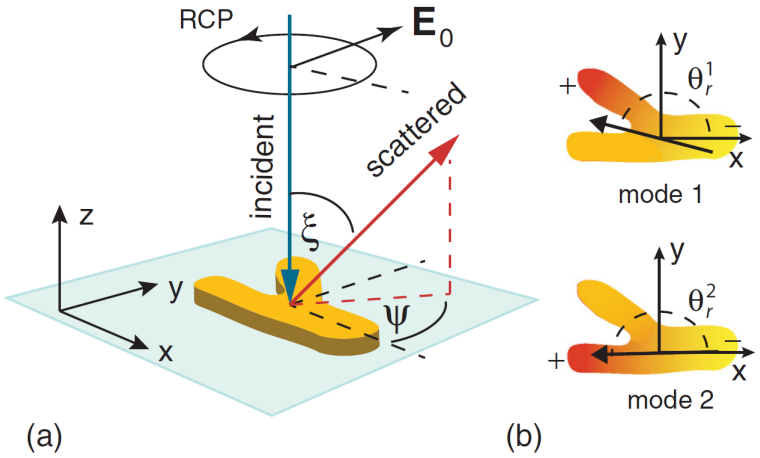


Figure 2.1: Example of LSP modes of a chiral nanoparticle [32]

The excited modes are the localised surface plasmons (LSPs) on the surface of metallic nano-features, excited by the incident light field. The electrostatic approximation applies to this case because the particle size is much smaller than wavelength of the incident field. To mathematically describe the far-field scattering we start with the power radiated per solid angle for a dipole emitter:

$$\frac{dP}{d\Omega} = \frac{ck^4}{32\pi^2\epsilon_0}(\hat{n} \times \mathbf{p}) \cdot (\hat{n} \times \mathbf{p}^*), \tag{2.5}$$

where c is the speed of light *in vacuo*, k is the wavenumber, ϵ_0 is the permittivity of free space, $\mathbf{p}$ is the complex dipole moment, $\mathbf{p}^*$ is its conjugate and $\hat{n}$ is a unit vector in the scattered direction. Algebraic manipulation (see Appendix A for full details) yields the result reported in [32]:

$$\frac{dP}{d\Omega} = \frac{ck^4E_0^2}{32\pi^2\epsilon_0}\sum_k\sum_{j\leq k}|f_k||f_j|(p_k^{xy}p_j^{xy})^2[\cos(\theta_k-\theta_j)+N_{kj}][\cos(\phi_k-\phi_j)\cos(\theta_k-\theta_j) \mp \sin(\phi_k-\phi_j)\sin(\theta_k-\theta_j)]. \tag{2.6}$$

Here k,j labels each LSP mode of polarisability $f_{j,k}$, $\theta_{j,k}$ and $\phi_{j,k}$ are the geometric and phase angles respectively, $p_{j,k}^{xy}$ is the magnitude of the in-plane dipole moment and N_{kj} contains all the off-normal incidence terms. The term that depends on

the handedness of the incident field is the one associated with the $\pm$ sign:

$$\begin{aligned}[\cos(\theta_k - \theta_j) + N_{kj}][\pm \sin(\phi_k - \phi_j)\sin(\theta_k - \theta_j)] = \\ \pm\frac{1}{2}\sin(\phi_k - \phi_j)[\sin(2(\theta_k - \theta_j)) + 2N_{kj}\sin(\theta_k - \theta_j)].\end{aligned} \tag{2.7}$$

We see for normally incident light the difference in transmitted power in the far-field depends on the angle θ between the LSP modes on the nanoparticle. In fact we see that this difference is maximised when $\theta_k - \theta_j = \frac{\pi}{4}$ not $\frac{\pi}{2}$. This is the key finding of Davis and Eftekhari's paper, which they tested for arrays of pairs of gold nanorods at various angles to each other. It shows that 2D planar chiral nanostructures need to have resonant LSP modes with a different phase ($\phi_k \neq \phi_j$, achieved by having each particle of a different length) as well as having an angular separation not equal to 0 or $\frac{\pi}{2}$, and the maximum differential scattering occurs for an angular separation of $\pi/4$ and a phase difference of $\pi/2$.

2.4.2 Potential Applications of Differential Scattering

The study and subsequent improved understanding of chiral metamaterials has led to many advances in nanophotonics. Metamaterials-based second harmonic generation (SHG) [33], cloaking [34], negative refractive index metamaterials [35, 36] and circular polarisation sensitivity, [37, 38] have all been demonstrated with geometrically chiral designs. Of particular importance are chiral metamaterials that can distinguish between circular polarisation states of light on the nanoscale. These metamaterials could find use probing the stereochemistry of molecules [39], determining the chiral structure of amino acids, proteins and viruses or as part of a secure quantum information system. The small effective mode volumes associated with localised surface plasmon resonances [40], and the scalability of fabrication through advances in assisted self-assembly [41] or nano imprint lithography [42] make plasmonic metasurfaces a strong candidate for these applications. Recent work has shown that planar metasurfaces can exhibit a difference in transmission of light depending on the state of circular polar-

isation of a normally incident electromagnetic wave. Here we extend this concept to the demonstration of a chiral metasurface consisting of an array of nanoscale slots in a thin film of metal exhibiting an asymmetry in its response to left and right circularly polarised light. This result is not circular dichroism, but a far field interference effect, which is purely electrical in nature [32]. This interference effect can be used as the basis for a nanoscale circular polarisation filter. Such a filter could be fabricated on the tip of an optical fibre or incorporated into a photodiode, to give information on the circular polarisation state of incident light.

2.5 Nanocavities

The nanostructures created by direct nanoimprinting of metal films using RNIL results in nanocavities, where incident light is absorbed in the cavity. This scalable nanofabrication technique produces metasurfaces with many desirable properties. Plasmonic nanocavity resonators offer strong field confinement, are robust to angle-of-incidence and have a strong dependence on polarisation angle [43]. When comparing the spectral response of nanocavities to their nanorod and nanoaperture cousins the fundamental mode, for the same dimensions, occurs at a much shorter wavelength, a useful property when trying to create a large colour gamut. Figure 2.2 shows a finite element method (FEM) comparison of the fundamental mode of arrays of nanocavities (b) and nanoapertures (c) of equal dimensions (200 nm long, 30 nm wide, 100 nm deep and a period of 300 nm, see §3.7 for more information on the FEM). In this calculation both cavities are driven by an electric point dipole oriented across the short axis of the cavity or aperture, the dipole's frequency is swept across the visible and NIR spectrum and the total far-field radiated power collected. The calculation shows for the closed ended nanocavity, the fundamental mode is at a wavelength of 500 nm, whereas for the open ended apertures the mode occurs at 750 nm. This is the same ratio one would expect when comparing the fundamental resonances of an open

ended flute and a closed ended clarinet. To better capture the physics of light scattering from nanocavities one can model the nanocavities optical response as similar to closed ended metal–insulator–metal (MIM) waveguides. It is possible to calculate the dispersion curves for the MIM waveguide modes and restrict the allowed wavevector, $\vec{k}$, such that the reflected and driving fields destructively interfere, that is, when the cavity depth is deep enough for the reflected wave to have accumulated a $m\pi$ phase difference with m an odd integer. Because of the metal at the bottom of the nanocavity, the electric field must go to 0 there (with some frequency dependent skin effect) and so only odd standing wave modes are permitted inside the cavity.

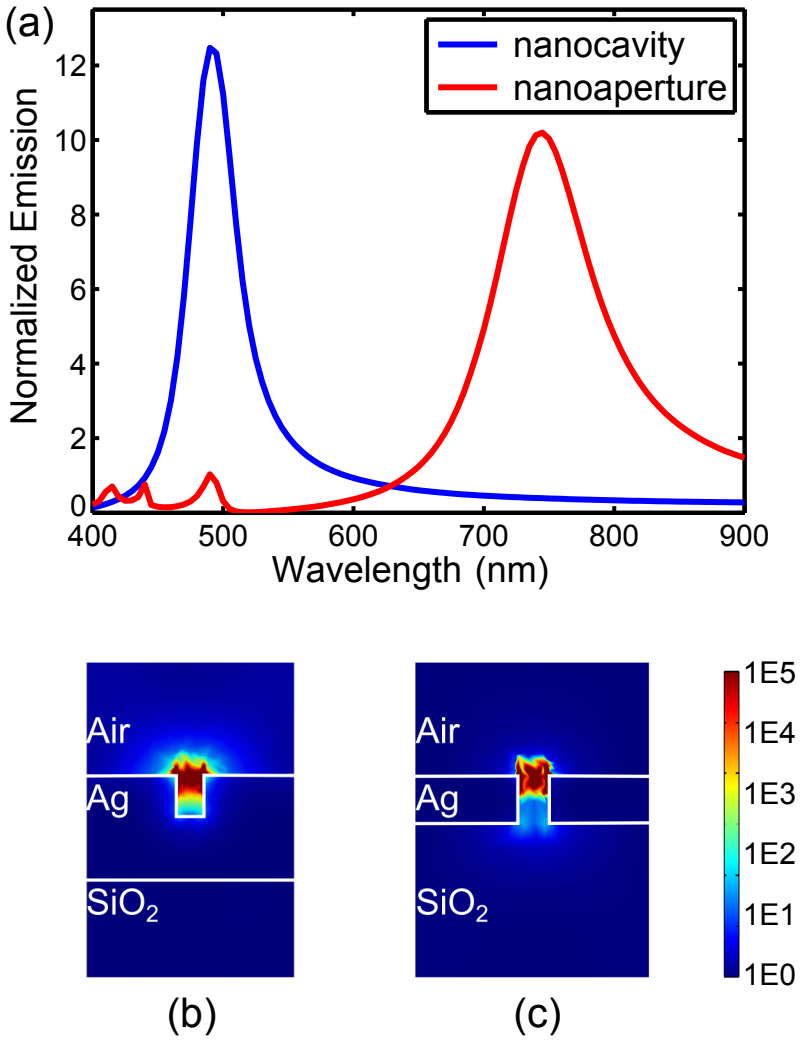


Figure 2.2: The calculated emission spectra (a) for an electric dipole source, oriented along the short axis of the cavity for closed- (b) and open-ended (c) geometries. (b) and (c) show the electric field magnitude at resonance for each geometry.

2.5.1 Waveguide Modes and Standing Waves

An important property of MIM waveguides is that transverse magnetic (TM) modes are always supported, even in the very small ($\leq$ 50 nm) insulator gaps found in the nanocavities studied here. In fact waveguides only 3 nm wide have been shown to support propagating plasmon modes [44]. The dispersion relation for odd modes in such waveguides is as follows,

$$\tanh \frac{k_i L}{2} = \frac{-k_i \epsilon_m}{k_m \epsilon_i} \tag{2.8}$$

and

$$\tanh \frac{k_i L}{2} = \frac{-k_m \epsilon_i}{k_i \epsilon_m} \tag{2.9}$$

for even modes, where $k_{i,m}$ is the in-plane wavenumber in the waveguide, i, m indicate the insulator or metal parts and L is the length of the long axis of the nanocavity. The in-plane wavenumber can be rewritten as

$$k_{i,m} = \sqrt{k_z^2 - k_0^2 \epsilon_{i,m}} \tag{2.10}$$

where k_z is the wave-vector component directed along the nanocavity (that is, normal to the surface) and $k_0 = \frac{2\pi}{\lambda}$ is the free space wave-number. When k_i is real, we have a plasmonic waveguide mode and when it is imaginary we have a photonic waveguide mode [44].

Taking the difference between the left and right sides of 2.8 and plotting the logarithm (to highlight the differences) of the result for a range of energy and momentum values gives the odd-TM mode dispersion curve, shown in figure 2.3. The fundamental TM mode, as opposed to the TE mode, is considered here as the primary contributor to the device absorption, as shown by Webb *et al.* [43]. Here a 50 nm wide Au–SiO_2–Au MIM waveguide geometry is assumed, using materials data from Ref. [45]. For low energies the dispersion follows the light line. Above 2.2 eV however, there is significant divergence from the light line.

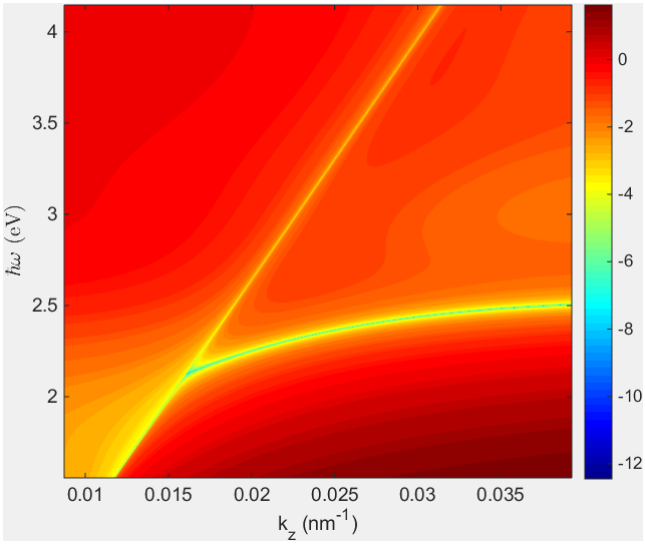


Figure 2.3: The calculated dispersion diagram for odd-TM modes for a 50 nm wide Au–SiO_2–Au MIM waveguide. Here the colorbar represents the logscale difference between the LHS and the RHS of equation 2.8.

In order to understand the absorption peaks exhibited by nanocavities one must consider the effect of cavity depth as well as MIM waveguiding. For a cavity with depth d, for maximum absorption there should be destructive interference between the incident field and the field reflected from the bottom of the cavity. The cavity will have a Fabry-Perot-like resonance when the accumulated phase difference is $m\pi$, m being an odd integer. The round-trip condition is thus

$$2d_{eff}k_z = m\pi. \tag{2.11}$$

Where d_{eff} is the effective length of the cavity, taking into account the skin effect at these frequencies. By substituting $k_z = \frac{m\pi}{2d}$ into 2.10 and then into 2.8 it is possible to calculate the dispersion diagram for the peak absorption mode of the Au MIM waveguide, as a function of wavelength and cavity depth. This is shown in figure 2.4. It appears that increasing the depth of the nanocavity will red-shift the resonant wavelength, starting from a wavelength around 500 nm.

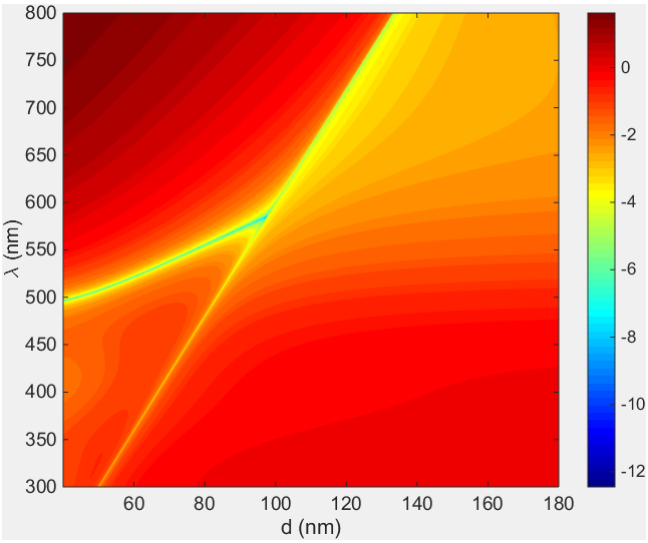


Figure 2.4: The calcuated dispersion diagram from 2.3 recast in terms of excitation wavelength λ and cavity depth, d. Here the colorbar represents the logscale difference between the LHS and the RHS of equation 2.8.

To produce absorption peaks at shorter wavelengths the metal could be changed from gold to silver. Figure 2.5 shows the dispersion calculation with the metal changed from Au to Ag [45]. The mode diverges from the light line for energies around 2.5 eV in this case, due to the lower ohmic losses in silver at optical frequencies.

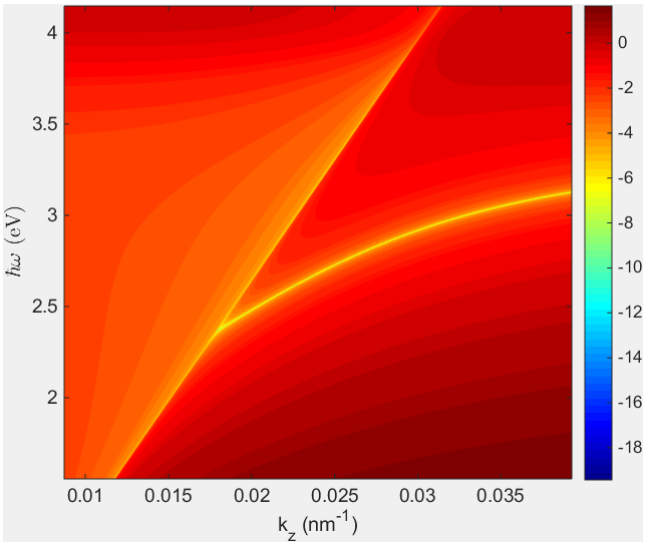


Figure 2.5: The calculated dispersion diagram for odd-TM modes for a 50 nm wide Ag–SiO_2–Ag MIM waveguide. Here the colorbar represents the logscale difference between the LHS and the RHS of equation 2.8

Applying the Fabry-Perot resonance condition 2.11 yields figure 2.6, where it

can be seen that altering the cavity depth allows for resonant wavelength tuning from 400 nm, allowing for a wider colour gamut than gold nanocavities.

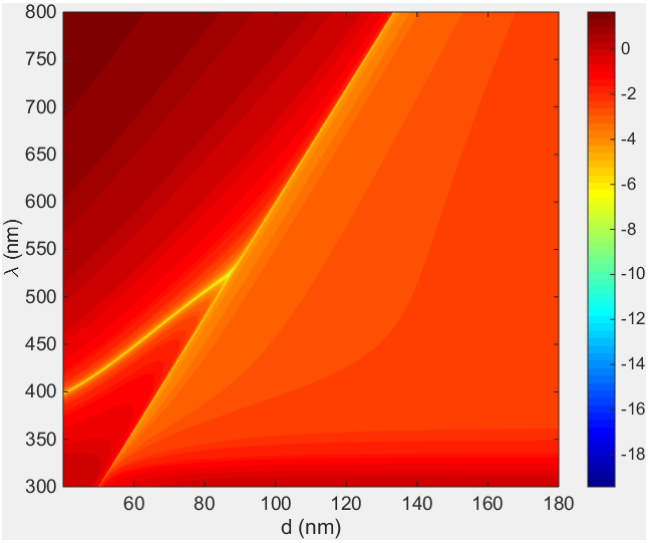


Figure 2.6: The calcuated dispersion diagram from 2.5 recast in terms of excitation wavelength λ and cavity depth, d. Here the colorbar represents the logscale difference between the LHS and the RHS of equation 2.8.

2.6 Perfect Absorbers

The optical properties of plasmonic metasurfaces to adjacent thin films of quantum emitters depends not only upon the emitter and antenna details but also the effect of the emitter-incorporated film thickness and optical properties. Therefore it is important to understand the role these thin dielectric layers can play, especially for the incorporation of metasurfaces into current OLED, QDLED or polymer solar cell technologies. The use of Fabry-Perot (FP) etalons in conjunction with plasmonic metasurfaces has led to the development of the 'perfect absorber', of which examples in the literature abound [46–49]. In fact, the visible and NIR spectrum perfect absorber is just a re-imagining of the microwave regime Salisbury screen. In this thesis a quantum dot doped metasurface etalon is studied as a simple analogue for the structure of a quantum dot light emitting diode. Much like the nanocavities of the previous section the key geometric parameter is the thickness, d, of the dielectric layer in the etalon, as it will determine if the reflected wave destructively or constructively interferes with the incident light to

produce subradiant or superradiant modes, respectively. These modes are a hybridisation of plasmon modes and the FP cavity modes. In order to predict the spectral properties of a particular design it is possible to assign the metasurface layer a complex reflectivity, r_m and treat the device as a 3 layered Fresnel reflection system. Reference [46] notes that (with some algebra) in such a three layer system, the total reflectance, R, at normal incidence, can be written as

$$R = |r|^2 = \left| r_m - \frac{r_g t_m^2 e^{2ink_0 d}}{1 + r_m r_g e^{2ink_0 d}} \right|^2 \tag{2.12}$$

where r_g is the ground plane or back mirror reflectivity, t_m is the complex transmission coefficient of the metasurface and as usual $t_m = 1 + r_m$, n is the refractive index of the dielectric layer and k_0 is the free space wavenumber. All that is left to do is calculate, r_m the reflectivity of the metasurface. The typical geometry of a perfect absorber is shown in figure 2.7.

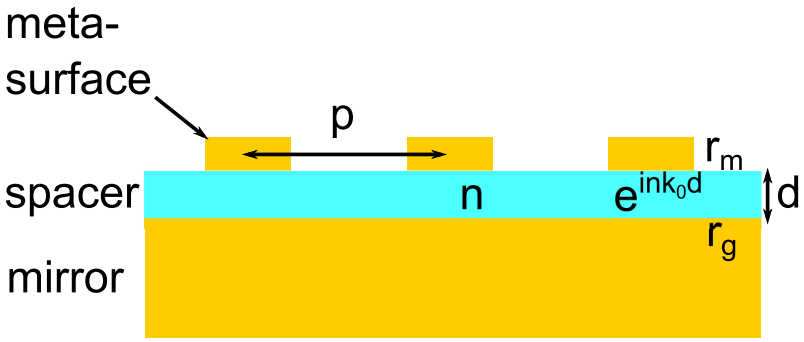


Figure 2.7: The typical geometry of a perfect absorber structure. With spacer thickness, d and refractive index n, the field accululates $e^{ink_0 d}$ phase as it passes through. The metasurface array has a period p and a reflectivity r_m, whilst the optically thick mirror or ground plane has reflectivity r_g.

2.6.1 Green's Function Approach

A method to analytically determine the reflectivity of a metasurface of dipole nanoantennas in a periodic array coupled to a reflective ground plane has been presented by Kwadrin *et al.*. The method also accounts for the back action effect the mirror has on the plasmon resonance of the nanoantennas [46]. The result is quite computationally intensive even considering the conversion of an integral

over all k-vectors to a sum over reciprocal lattice vectors afforded by the periodic nature of the array. In fact, in the supplementary material the authors mention that this approach has poor convergence properties. It also seems that effect of the back action on LSP resonances is not significant. Considering all of this, the approach taken here is to ignore the back action and use 2.12 along with a known Green's function result for the reflectivity of a periodic metasurface [50]. The metasurface reflectivity is given by

$$r_m = \frac{2\pi i k_0}{p^2(\frac{1}{\alpha} - G)} \tag{2.13}$$

where G is the sum of the Green's function for an array of nanorods evaluated at all the lattice sites of the array [50]. The array has period p and each dipole has dynamic polarisability,

$$\alpha = \frac{V\omega_0^2}{\omega_0^2 - \omega^2 - i(\gamma\omega + \frac{2}{3}n^3k_0^3)} \tag{2.14}$$

where we have assumed a Lorentzian resonance centred on ω_0 with γ ohmic damping, depending on the metal used and a scatter volume, V, which can be tuned so that the resonance is of a realistic strength. According to Ref. [50], for non-diffractive lattices ($p \leq \lambda$), G is well approximated by

$$G \approx \left(\frac{4\pi^2\sqrt{2}}{p^3\sqrt{\frac{2\pi}{k_0 p} - 1}} - \frac{118}{p^3} \right) - i\left(\frac{2\pi k_0}{p^2} - \frac{2k_0^3}{3} \right). \tag{2.15}$$

By combining equations 2.12, 2.13, 2.14 and 2.15 it is possible to calculate the reflection spectrum of a metasurface etalon, where the metasurface consists of a periodic array of nanorods and is excited at normal incidence.

2.7 The Purcell Effect

The coupling of emitters to resonators is a complicated and important matter, where a number of remarkable phenomena can occur. Most relevant to the work presented here is the Purcell effect. The Purcell effect, named after its discoverer, Edward Purcell, occurs when a quantum emitter, such as a QD, couples to a resonator, such as a nanocavity or nanoantenna [51]. Due to the increase in radiative decay pathways provided by the resonator it is possible to greatly reduce the excited state lifetime and a brighter source. This is a direct result of Fermi's Golden Rule, where the decay rate depends on the local density of optical states (LDOS) [52]. The Purcell factor, F, is the ratio of the decay rate of the emitter's excited state, Γ when (weakly, such that the radiation damping is greater than the coupling strength) coupled to the resonator to the decay rate in free space, Γ_0. That is,

$$F = \frac{\Gamma}{\Gamma_0}. \tag{2.16}$$

Purcell was able to show that the Purcell factor depends on the emitter's wavelength in the cavity, $\frac{\lambda_0}{n}$, the mode volume V_0 and the quality factor, Q of the particular resonator. He found that

$$F = \frac{3\lambda_0^3 Q}{4\pi^2 n^3 V_0}. \tag{2.17}$$

From 2.17 it is clear that in order to optimise the enhancement of a quantum source with a nanoresonator the Q-factor needs to be maximised and the mode volume reduced. 2.17 obscures the fact that if there is no spectral overlap between emitter and resonator then the Purcell effect is muted. This is revealed in the definition of F, equation 2.16, when the radiative decay rate, Γ, is written in full according to Fermi's Golden Rule

$$\Gamma = \frac{2\pi}{\hbar} \langle f | H | i \rangle \rho_{LDOS} \tag{2.18}$$

where H is the interaction Hamiltonian, $\langle f|$ is the final energy eigenstate and $|i\rangle$ the initial excited state, and ρ_{LDOS} is the local density of states into which the exciton decays. The importance of spectral overlap is now plain to see. Such considerations will be important in the coming chapters where decay rates are measured.

2.8 Summary

This chapter covered the significant theoretical background on which the research discussed in the following chapters relies. This included an in-depth discussing of circularly polarised light scattering from chiral nanoapertures and how the effect can be exploited and optimised. Strong absorption in nanocavities and how to calculate the modal properties of these structures was presented. A method for determining the reflectivity of perfect absorber structures, which relies on an approximation for the sake of computational efficiency was discussed. Finally an outline and some comments on the Purcell effect were covered in the final section.

Chapter 3

Numerical Methods and Fabrication

This chapter outlines in detail the nanofabrication techniques used throughout this research project to develop polarisation sensitive plasmonic elements. It will also outline the numerical methods used to design and optimize the structures in question.

3.1 Electron Beam Lithography

Electron beam lithography (EBL) offers the finest resolution and repeatability of all the common nanofabrication techniques [53]. The Melbourne Centre for Nanofabrication (MCN) houses a Vistech EBPG 5000+ which was used to undertake all the EBL in this project. Electrons from a field emission tip are accelerated through a potential of 100 kV, and focused with electromagnetic lenses.The benefit of this tool, compared to the converted SEM type of EBL systems is that the writing fields are divided into a main field, controlled by on set of electromagnets and a subfield, controlled by a smaller set of electromagnets. This allows for rapid exposure of large arrays of nanoscale patterns, with very fine beam control. The Vistech EBPG 5000+ automatically corrects for astigmatism. It also utilizes a laser interferometer system to detect for substrate height variance, adjust the focal plane as required and automatically realign samples for multi-exposure processes. The tool itself has a minimum beam spot size of 2 nm when the minimum beam

current of 200 pA is used with the 200 μm aperture. The majority of exposures in this work used a larger aperture (300 μm) with a 500 pA beam current. These settings result in a 2.5 nm beam spot size and a considerable reduction in write time. However, with the electron sensitive resists used in this research project, the resolution is not limited by the EBL, but by the resolution of the resists themselves.

The EBL process relies upon the use of electron sensitive polymer resists, that either cross link (negative tone) or unlink (positive tone) when exposed to an electron flux. Methyl methacrylate (MMA) and polymethyl methacrylate (PMMA) are both negative resists, with PMMA having a higher resolution than MMA. This fact can be exploited with a bilayer stack of PMMA/MMA to create an undercut, which results in smoother particle side walls. A schematic of a bilayer lift off process is shown in Fig. 3.2. The substrate is first cleaned via a solvent clean, where the solvents are stepped up in polarity. The substrate is placed in an acetone bath and sonicated for 5 minutes, then placed in an isopropanol (IPA) bath for 5 minutes. The remaining IPA is thoroughly rinsed from the substrate with deionised water and blown dry with nitrogen. The cleaned substrate is loaded onto a Laurel spinner and the surface covered with MMA and spun at 4000 rpm for 90 seconds. The coated substrate is then baked at 170°C for 5 minutes, force cooled and returned to the Laurel spinner. PMMA is then applied and spun at 4000 rpm for 90 seconds and baked at 170°C for 5 minutes. Depending on the conductivity and reflectivity of the substrate the resists made need the addition of a 20 nm thin conductive layer of chromium, so that there is no charge build up during e-beam exposure and the laser interferometer has a reflective surface to sense. For the positive tone resist hydrogen silsesquioxane (HSQ, $H_8Si_8O_{12}$), the resist is spin coated at 3000 rpm for one minute and post baked at 150°C for 3 minutes.

Pattern Preparation and Exposure

The open source 2D CAD software, Klayout [54], is used to designate the patterns to be exposed with the Vistech EBPG 5000+. The output file type is GDSII. Once a design is finalized, Layout Beamer is used to fracture the GDSII file into beam steps which can be implemented with the digital analogue converter (DAC) in the EBPG5000+. At this stage it is possible to set the beam step size, address any pattern overlap errors or perform proximity error correction (PEC). To optimize writing times and minimize stitching artefacts, the subfield size should be set to the largest multiple of the array periodicity less than 4096, as this is the maximum number of steps the subfield DAC can make. For example, if the array period is 300 nm, the subfield size should be set to 3900 nm, so that each subfield consists of a subarray of 13x13 unit cells, as opposed to 13.653x13.653 unit cells for a subfield of 4096 nm. When the subfields are stitched together, any alignment errors occur away from the exposed areas. The fractured output file from Layout Beamer, known as a .gpf, can then be used in a 'jobfile' created using CJob. Here the desired beam current, write frequency, labels, dose and location of the exposures can be set. The pattern generator is capable of a frequency of 50 MHz, limited only by the decay times of the magnetic fields in the beam steering electromagnets. As long as the beam current settings and dose settings result in a frequency less than 50 MHz, the EBPG5000+ will carry out the exposure defined in the jobfile. The typical doses used range from 1000 μC/cm^2 to 5000 μC/cm^2.

Development and Lift-off

Once exposed the resists are then developed for one minute. For a PMMA/MMA bilayer the developer, a 1:3 mixture of methyl isobutyl ketone (MIBK) to IPA and glassware is chilled to 4°C prior to development of the exposed resists. The sample is placed in the chilled beaker and agitated for one minute, then rinsed with fresh IPA and blown dry with nitrogen. This cold development technique has been

shown to make a marked difference to the resolution of corners and side walls in the exposed features [55]. Metal is then deposited by e-beam evaporation and lift-off performed.

Lift-off of a PMMA/MMA bilayer resist is carried out as follows; a beaker of fresh acetone (or anisole in the case of Chromium) is heated to 70°C and the sample submerged. After 5 minutes the PMMA/MMA begins to dissolve in the solvent beneath the metal film, at this point it is agitated with a pipette to encourage lift-off. After the film has completely lifted-off, the sample is rinsed in IPA then DI water and blown dry with nitrogen. Areas that were exposed to the electron beam remain, while the rest is lifted-off when the resists dissolve.

For HSQ development, an alkaline metal ion free (MIF) solution is required. The sample is bathed in AZ 726 (2.38% TetraMethylAmmoniumHydroxide (TMAH) in H_2O, with some added surfactants) for one minute, then rinsed in DI water for 2 minutes and blow dried with nitrogen. For nano imprint master fabrication, the HSQ is baked after development at 350°C for two hours.

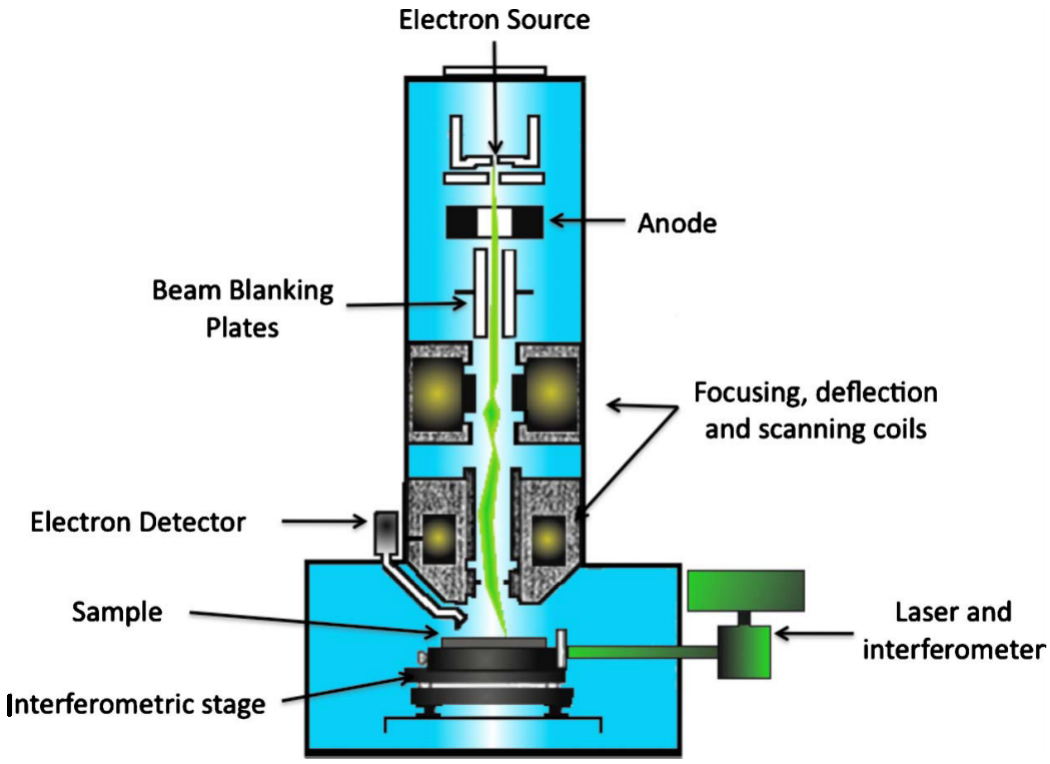


Figure 3.1: A schematic of the Vistech EBPG 5000+ [53].

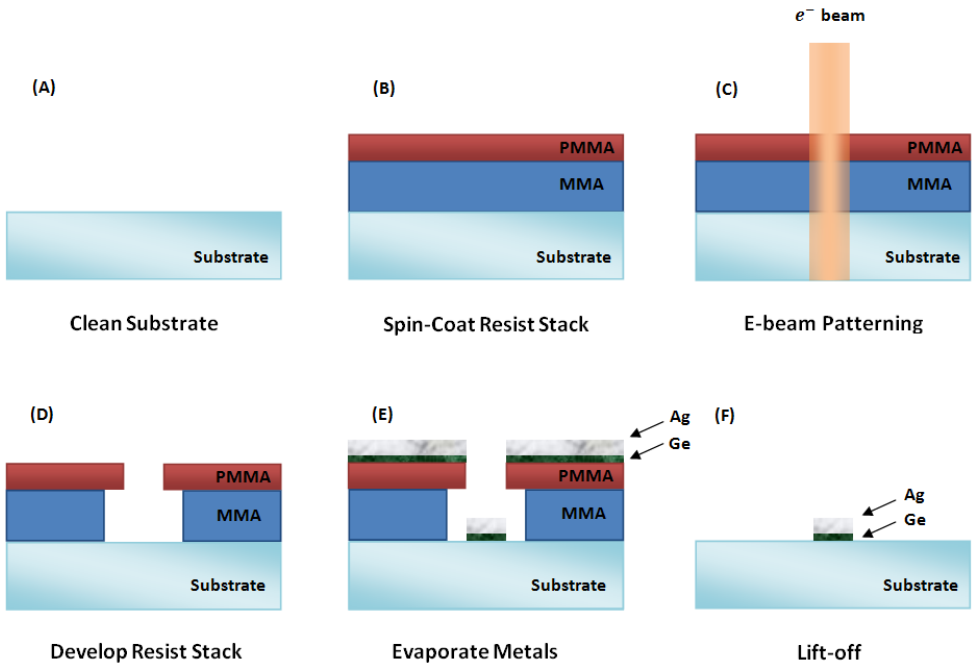


Figure 3.2: A schematic of a bilayer lift off EBL process [56].

3.2 Electron Beam Evaporation

Throughout the research presented here an 10 kV Intlvac NanoChrome II Electron beam evaporation system is used to deposit thin films both metallic and dielectric. Flat samples are mounted in the dome whilst patterned samples are mounted in a central ring to avoid shadowing effects on the sample. The chamber is pumped down to a pressure less than 7×10^{-6} Torr while the sample is rotated at 100 rpm. An electron beam is incident on a graphite crucible containing the target material. The beam traces a spiral pattern over the entire crucible so that there is an even spread of thermal energy across the target. After one minute soaking time at a beam current of 10 mA the current is increased so that the deposition rate, as measured by an in situ quartz microbalance, is between 0.8 and 1 Å/s.

Typically, for deposition of gold or silver, a 2 nm Ge seed layer is used to aid adhesion to the substrate and promote the growth of smaller crystal grains [57]. This layer is not needed for Al or Cr deposition as they both easily adhere to silicon and silica. Unless otherwise stated a 5 nm silica layer is evaporated on top of the films to slow the rate of oxidization. Simulations show that for localized surface plasmon based devices, the adhesion and capping layers have a negligible effect. For propagating surface plasmons the effect of the 5 nm silica layer needs to be considered as it will affect propagation lengths as well as the resonance condition. Films of Au, Ag and Al made in this manner are polycrystalline, with a grain size around 20 nm and a RMS surface roughness around 10 nm.

3.3 Focused Ion Beam Milling

Focused ion beam (FIB) milling provides a highly accurate method for the fabrication of nanoapertures in metallic films. Unlike EBL, there is no need for any post-processing steps. In this project FIB milling was carried out on a FEI Helios Nanolab 600 DualBeam FIB-SEM at the MCN. This tool has a 30 keV Ga ion column and a SEM column at 52° to the ion column. For the milling of nanos-

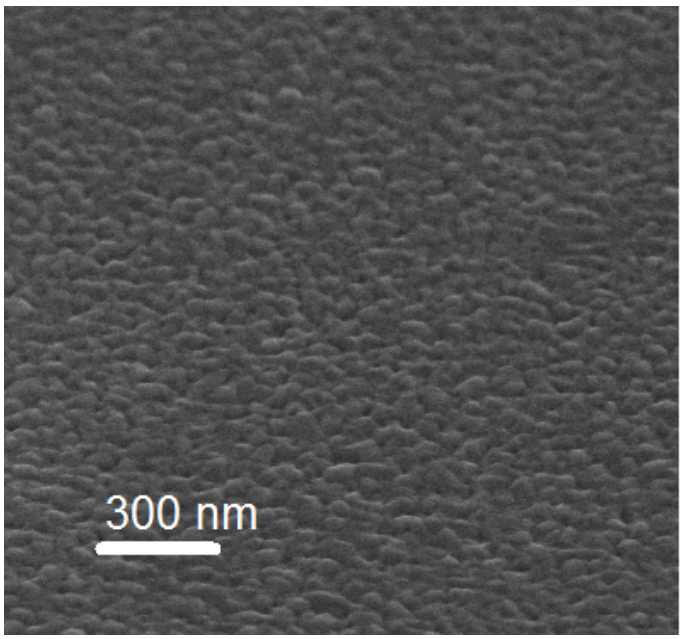


Figure 3.3: An example Ag polycrystalline film deposited with e-beam evaporation.

tructures in a thin metallic film on a non-conductive substrate charging effects are considered. By securing the sample to a 4" aluminium chuck with copper tape, ensuring good contact with the metal surface, the sample is earthed and excess charge is conducted away. The underside of the sample is also secured to the chuck with carbon tape, which helps address the issue of drifting during FIB milling. Once mounted the FIB chamber is pumped down to a vacuum better than 1.09×10^{-3} atm. The FIB current is set to 1.5 pA, producing a nominal spot size of 7 nm, is focused and the beam astigmatism adjusted. Depending on the structures to be milled the beam current is kept either on the minimum 1.5 pA or increased to 9.7 pA for large array fabrication. This compromise increases the beam spot size but reduces the milling time by a factor of 6. The dwell time of the beam dictates the depth and to a lesser extent the lateral dimensions of the sputtered hole. The beam is scanned in a serpentine fashion across the target area and makes 6 to 10 passes in total. Depending on the geometry, a higher or lower number of passes may be preferable, for example for large arrays having fewer passes reduces the effect of stage and beam drift, whereas for single apertures multiple passes produce sharper corners. Each fabrication run requires recalibra-

tion of the required dwell time and number of passes as it depends strongly on the state of the ion source and the average grain size of the film. For a 50 nm Ag film a dwell time around 2.5 ms is required with six serpentine passes. A 24-bit true colour bitmap image defines the area to be milled. The black pixels blank the beam and the white pixels unblank it. A resolution of 3.5 nm per pixel is used when creating the source bitmap images. The dwell time per pixel then needs to reduced to a third of the calibrated value. This has been found to produce more regular structures.

The focused ion beam is also used to measure the cross sections of imprinted structures. To define and protect the top surface clearly a platinum layer is deposited using ion assisted chemical vapour deposition (CVD) of Pt which is part of the FIB-SEM's functionality. After deposition a large rectangle is milled through the sample and the cross section can be measured with the electron column, as it is at 52° to the surface normal of the sample.

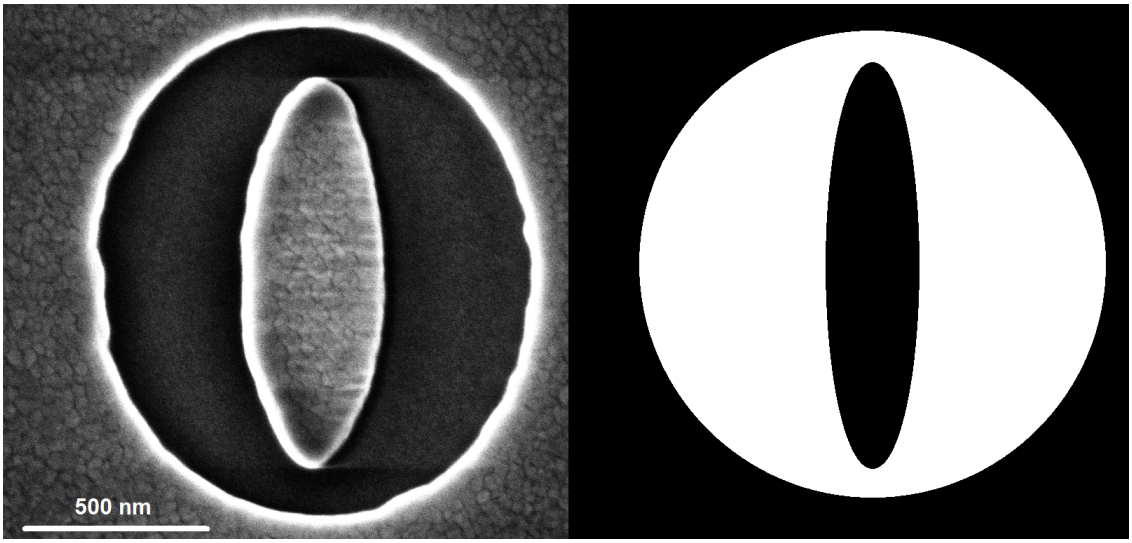


Figure 3.4: An example of a FIB milled cat's eye structure in a 100 nm Ag film (left) and the source bitmap image used to instruct the FIB (right).

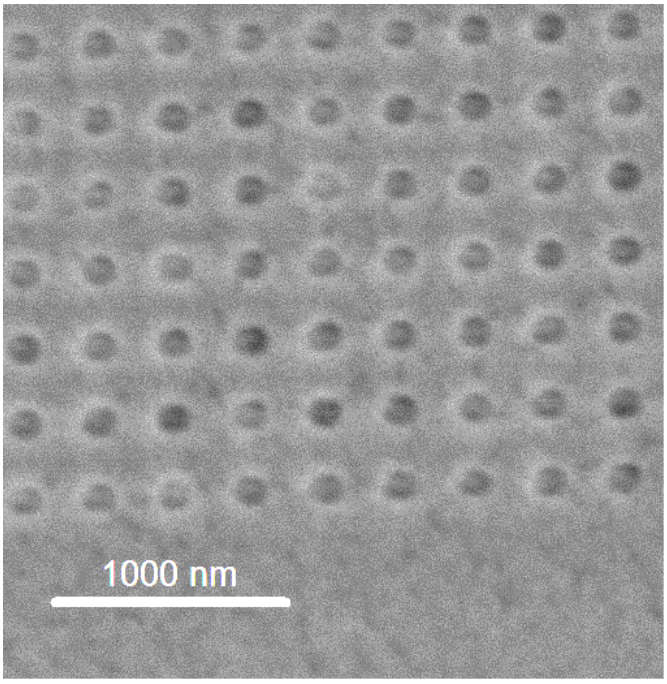


Figure 3.5: 15 kDa PMMA film imprinted with a HSQ master with 100 nm diameter circular posts.

3.4 Nano Imprint Lithography

The nano imprint lithography (NIL) conducted in this research project is implemented using an EVG 520 IS Hot Embosser. All master templates were coated with a proprietary anti-sticking layer (ASL) known as 3M Novec 7100. This is a low viscosity solvent used to clean and lubricate medical replacement joints and is applied via spin coating at 3000 rpm for one minute.

3.4.1 Thermal NIL

To transfer a pattern from a HSQ master to 15 kDa molecular weight PMMA films, the imprint temperature is set to 150°C, with a 20°C per minute heating ramp. Once both top and bottom plates reach 150°C the piston force is increased to 21 kN at a slew rate of 600 N/s. The embossing chamber is evacuated to 1 mTorr. Once the set force is reached the mold and target are held under pressure for 5 minutes, then cooled to 70°C and the pressure released. The mold and target are then separated and the mold can be reused.

3.4.2 Resistless NIL

Researchers from Purdue University have demonstrated cold forging as a NIL technique that does not require a large thermal budget or very high pressures [17]. Using thin Ag and Au films on silicon wafers and an etched silicon molds, a variety of patterns were transfered including a bow tie array with a 8 nm gap. The process is outlined in Fig. 3.6 This comprehensive study also demonstrated that there is no benefit in heating during the imprint in terms of fidelity of the imprinted structures. This is extremely promising for industrialization of this procedure as the longest part of a NIL duty cycle is the heating and cooling of the substrate. This is also the biggest energy cost of the process, so eliminating the need for heating is highly desirable. The pressure required to cold forge a thin Au or Ag film is between 1 MPa and 4 MPa, which is 10% to 30% of the pressure Chou used in his seminal NIL experiment [42]. Fig. 3.7 shows the exponentially decaying dependence on metal residue left behind (which is a measure of how well the pattern imprinted) on pressure applied. Fig. 3.7 also shows the smooth side walls that can be achieved with this technique, which isn't achievable with lift-off. RNIL also allows for sloped sidewalls, which could potentially lead to some interesting plasmonic applications.

RNIL always results in a metal residue at the bottom of the imprint cavity. In the supplementary material of Ref. [17], the authors show through COMSOL simulation that the residue left at the bottom of an imprint tends to slightly red shift the localized surface plasmon mode [58]. Fig. 3.8 shows a variety of LSP based colour filters arranged to form micron scale images that were created with cold forging. This figure also illustrates the fact that the red shift associated with the metallic residue is not an insurmountable issue for full spectrum colour reproduction. Clever design of the plasmonic structures incorporating this artifact can be used to achieve the desired spectral response.

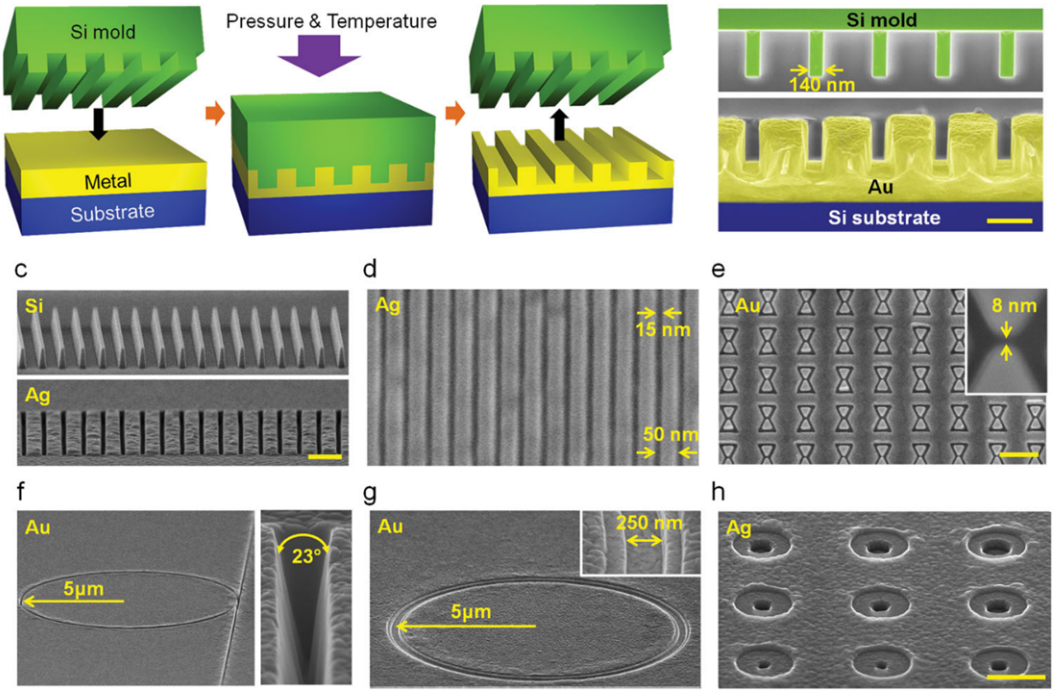


Figure 3.6: (a) the etched Si master is pressed into a thin Au or Ag film and the pattern transfered, (b) the imprinted pattern in a Au film, (c)-(h) a variety of patterns can be transferred using cold forging (including a mere 8 nm gap) [17].

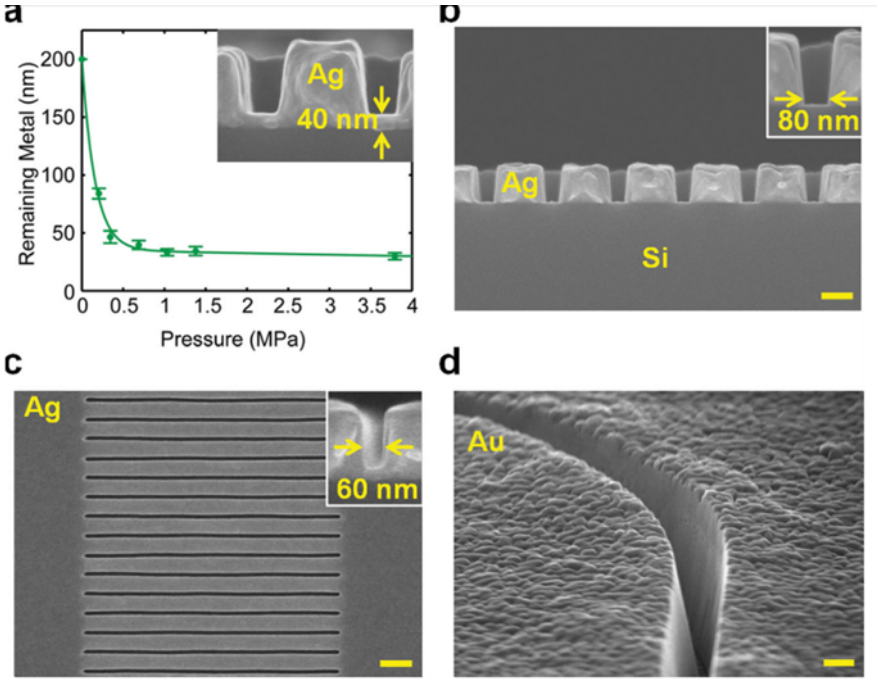


Figure 3.7: (a) the remainig metal residue as a function of applied pressure, (b)-(d) the imprinted patterns in a Ag film (note the very smooth and angled sidewalls) [17].

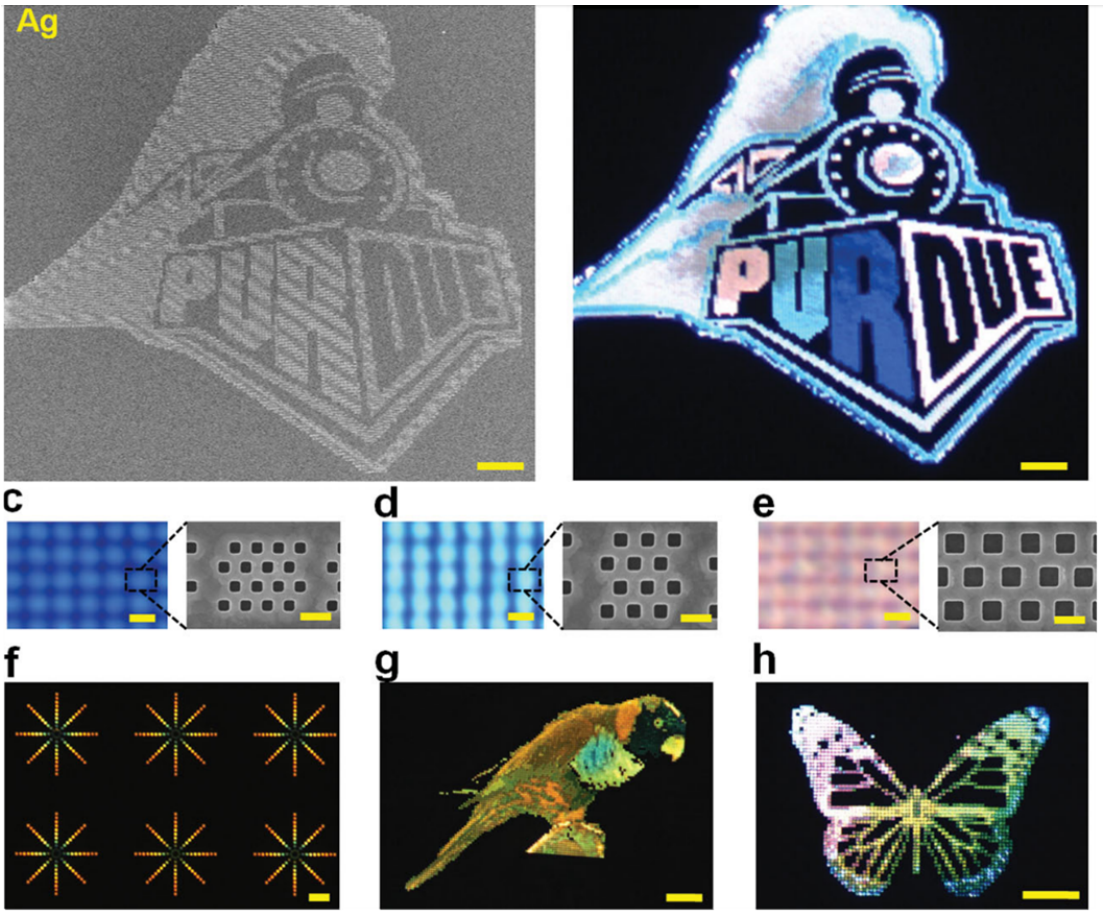


Figure 3.8: Various colour filtering patterns transferred to a Ag film using RNIL [17].

The RNIL applied in this research was carried out using an EVG 520 IS Hot Embosser. Silicon substrates were prepared with a 100 nm layer of target metal (Au, Ag or Al) via e-beam evaporation. Silicon master molds were fabricated using EBL and DRIE as described elsewhere in this chapter. Cold forging, as the name suggest does not require a thermal budget as the polycrystalline metal films are soft enough to readily imprint. In fact, it has been shown that at temperatures above 200°C local annealing occurs and reduces the film's imprint resolution [59]. The EVG 520 IS has a minimum temperature setting of 25°C, so this setting in lieu of no heating. The minimum force required for imprinting in Ag was determined to be 20 kN. Master slippage is an issue in the RNIL procedure as the MCN's facility is lacking a robust 4" wafer chuck, with only a graphite (maximum force 10 kN) chuck top plate available. For polymer imprint processes this is not an issue as the pattern will transfer only after heating, so initial slippage causes no damage. In the case of RNIL however, the metal is soft enough for the surface of the film to be scratched during a slippage event, as shown in Fig. 3.9. This slippage also lead to shear forces on the silicon master resulting damage to the nanofeatures. This novel fabrication process will be used and developments discussed in the coming chapters.

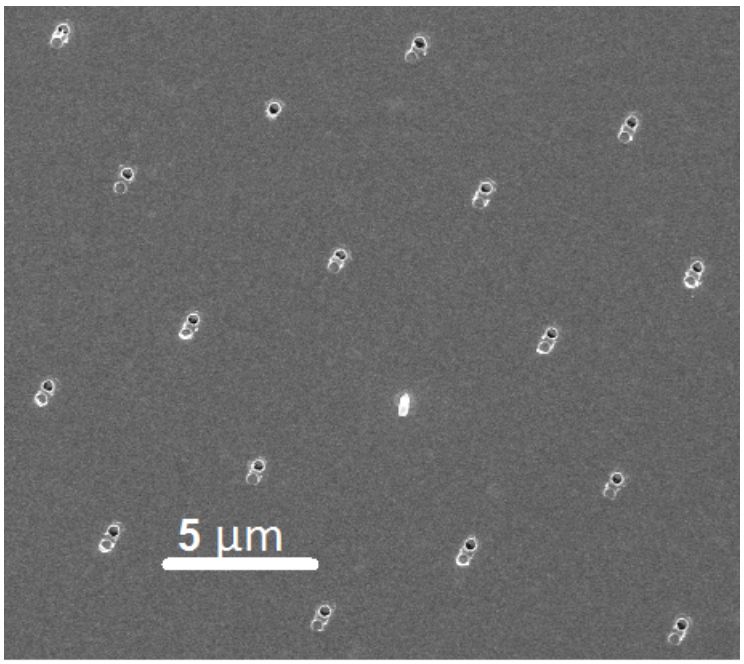


Figure 3.9: An RNIL imprint of circular nanoholes in 100 nm of Ag. Note the double imprint pattern due to master slippage and the piece of Si mater in the centre of the image.

3.5 Deep Reactive Ion Etching

Deep reactive ion etching (DRIE) allows for the fabrication of silicon based master templates for NIL and RNIL applications. An Oxford Instruments PLASMALAB100 ICP380 is first loaded with a blank silicon wafer and an oxygen plasma created to purge and prime the chamber. This is done several times until a strong plasma is maintained, which is indicated by less than 1 W refelcted RF power. A masked silicon wafer is then loaded into the chamber. The mask is a patterned layer of 20 nm thick chromium. The Cr pattern is defined with EBL using the aforementioned bilayer method and lift-off. The acetone dissolves the native chrome oxide layer, which results in dissolution of the thin chrome mask. To avoid this anisole, is used to dissolve the PMMA-MMA bilayer, as it does not affect the Cr structures. Once the Cr mask is loaded into the DRIE chamber and a vacuum of 5 mTorr is reached, a 30%-70% mix of SF_6 and C_4F_8 is pumped in cycles into the chamber. RF1 is 30W and RF2 is set to 1200W. Once a strong inductively coupled plasma (ICP) of these gases is established etching will occur. The silicon wafer is etched by SF_6 wherever

there is no Cr mask, whilst the C_4F_8 polymer gas acts as a passivation buffer to control the etching rate of the silicon and allow for high aspect ratio etching by passivating the sidewalls. The Cr mask is etch resistant, so the silicon below the mask will not be etched by the SF_6. The etch process lasts for 60 seconds and creates a 900 nm deep etch, the depth can be tailored by adjusting the etching time. After the DRIE process is completed the Cr is stripped with a 10% HNO_3 30% $(NH_4)_2Ce(NO_3)_6$ solution and the oxide layer removed with a 1:9 H_2SO_4 : H_2O bath for 20s. The master is then solvent cleaned and spun coated at 3000 rpm for 1 minute with the anti stick layer.

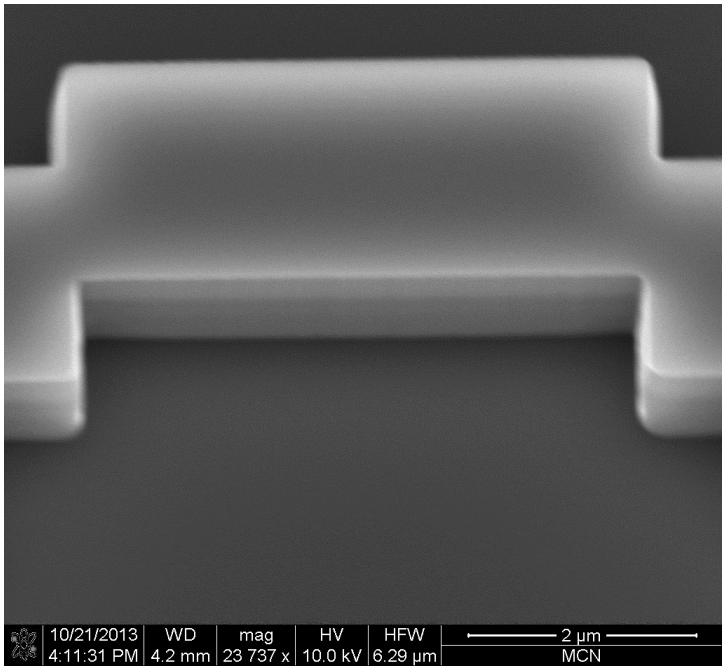


Figure 3.10: A DRIE etched Si wafer with vertical side walls. The etch depth in this case is 900 nm.

3.6 Numerical Methods

Numerical simulations of the interaction of electromagnetic waves with plasmonic structures aids in the design, characterisation and understanding, of the metamaterial devices. All simulations throughout the project are carried out on a customised work station with 18 2.00 GHz intel Xeon(R) E5-2650 cores and 256 GB of memory, running 64-bit Ubuntu 12.

3.7 The Finite Element Method in COMSOL Multiphysics

The finite element method (FEM) used here is implemented in COMSOL Multiphysics v4.3b and v4.4, to approximate solutions to Maxwells' Equations computationally. The FEM is used to convert partial differential equations (PDEs) to algebraic expressions, which can be solved via matrix inversion. This is achieved by discretisation the geometric domain of the boundary value problem into finite elements with a "mesh". Essentially, each mesh element approximates a small finite spatial length, ∂x. The smaller the mesh elements, the better the approximation but this is balanced by the increase in computational resources required. A rule of thumb employed here is to ensure no mesh element is larger than $\lambda/10$, where λ is the wavelength of the exciting field. A large mesh density is required where the field is changing rapidly with respect to space, such as metal dielectric boundaries or corners.

An example of the FEM discretization of a one dimensional second order PDE is as follows. Suppose we know $g(x)$ and wish to solve

$$f''(x) = g(x);\ 0 <= x <= 1, \tag{3.1}$$

with the boundary conditions given by

$$g(0) = 0 = g(1), \tag{3.2}$$

for $f(x)$. We can convert the problem into its work form by multiplying both sides of (3.1) by $h(x)$ then integrating both sides between 0 and 1, where $h(x)$ is at least a C^2 smooth function and $h(0) = 0 = h(1)$. This yields

$$\int_0^1 f''(x)h(x)dx = \int_0^1 g(x)h(x)dx. \tag{3.3}$$

Integrating by parts and applying the boundary condition $h(0) = 0 = h(1)$ to the left hand side of (3.3) gives

$$-\int_0^1 f'(x)h'(x)dx = \int_0^1 g(x)h(x)dx. \tag{3.4}$$

We now discretize $f(x)$ over the domain into n mesh nodes by expressing $f(x)$ as a weighted sum of polynomial basis functions, $p_i(x)$ given by

$$f(x) = \sum_{i=0}^{n} u_i p_i(x). \tag{3.5}$$

The accuracy of this approximation depends on the order of the polynomial basis functions; the higher order, the greater the accuracy and the higher the computational cost. The FEM requires that the basis polynomials have the property $p_i(x_j) = \delta_{ij}$ where x_j labels the mesh nodes.

We can recast (3.4) as

$$-\sum_{j=1}^{n} u_j \int_0^1 p_j'(x)p_i'(x)dx = \sum_{j=1}^{n} g_j \int_0^1 p_j(x)p_i(x)dx \tag{3.6}$$

where we decomposed $g(x)$ over the mesh nodes as in (3.5) and have used the result of Strang and Fix that all functions that satisfy the conditions on $h(x)$ can be represented by the basis functions $\{p_i\}$ [60].

Hence the initial boundary value problem has been reduced from a second order PDE to the algebraic problem of finding the constants $u_1, ..., u_n$. We can rewrite (3.6) as a matrix equation,

$$L\vec{u} = -M\vec{g} \tag{3.7}$$

where $\vec{u}$ and $\vec{g}$ are vectors containing the u_i and g_i, L and M are $n \times n$ matrices with elements given $L_{ij} = \int_0^1 p_j'(x)p_i'(x)dx$ and $M_{ij} = \int_0^1 p_j(x)p_i(x)dx$ respectively.

All that remains is to invert L and we have recovered an approximate solution for $f(x)$. The direct solver used to implement the FEM in this work is MUMPS [61].

3.8 RF module of COMSOL Multiphysics

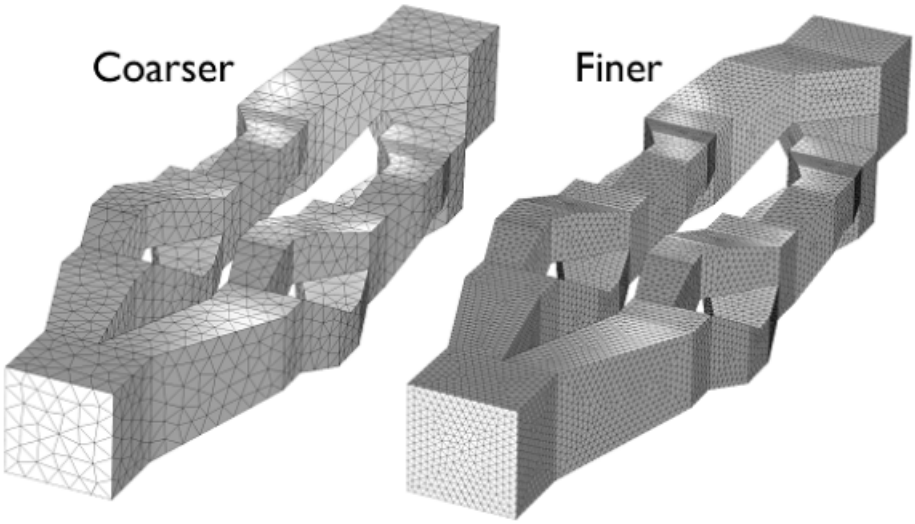


Figure 3.11: A comparison of different mesh densities generated by the COMSOL meshing algorithm [62].

The RF module of COMSOL Multiphysics is used for all the simulations used in this body of work. Optical constants for the materials used, such as Ag, Al, Ge and SU-8 are taken from the literature for bulk materials [45]. It is not well understood how these optical constants differ from bulk to thin film, nor on the technique used to deposit the films, but using properties of bulk metals provides a reasonable predictive tool. The RF module uses the FEM to solve the inhomogeneous Helmholtz Equation over the specified solution domain,

$$\nabla \times (\mu_r^{-1} \nabla \times \vec{E}) - k_0^2 \epsilon_r \vec{E} = 0, \tag{3.8}$$

where μ_r^{-1} is the relative permeability tensor, assumed here to be unity (non-magnetic), $\vec{E}$ is the electric field, k_0 is the free space wave number and ϵ_r is the relative permittivity tensor. Periodic boundary conditions are implemented

on the lateral boundaries to simulate the effect of an infinite array. A scattering boundary condition, with an incident field excitation on the entry plane of the geometry domain, and a scattering boundary condition with no wave excitation is used on the exit surface. Scattering boundary conditions are transparent to the specified wavelengths. Point dipole excitation can also be specified to simulate the classical coupling of quantum light sources to plasmonic structures, such as quantum dots, nitrogen vacancies in nanodiamonds, or erbium ions coupling to optical antennas [63].

3.9 Summary

This chapter covered the important elements involved in the fabrication of nanoscale optical elements, in particular EBL and FIB milling as enabling technologies for other, more scalable nanofabrication techniques, including NIL and RNIL. Both these imprinting techniques will be critical to the large scale implementation of nano-optical devices, especially plasmonic security features. Considerable background on the state of RNIL is also provided here so that the reader can compare the current state-of-the-art to the developments made in the research presented in the coming chapters. Finally an outline of the finite element method, used for design and optimisation, is presented, along with its implementation in COMSOL Multiphysics. Methods for the characterisation of these devices will be discussed in the next chapter.

Chapter 4

Optical Characterisation Techniques

This chapter contains details of all the relevant experiments undertaken to optically characterise the fabricated samples. The first section pertains to spectrometry and polarimetry of samples, including measuring Stokes' vectors and a method for determining a physically acceptable Mueller matrix. The following section details scanning fluorescent microscopy, lifetime measurements and far-field radiation pattern measurements for the characterisation of quantum emitter samples. Finally the techniques used in measuring the opto-electronic properties of polarisation sensitive MSM photodiodes are outlined. This chapter will be referenced throughout the remainder of the thesis.

4.1 Spectral Measurements

The spectral measurements throughout this work were performed in the School of Physics at the University of Melbourne. Three different light sources were used; a tungsten-halogen Ocean Optics HL-2000-FHSA lamp, a Fianium 450-SC supercontinuum white light source fibre laser and a 100 W Nikon V2A-LL halogen lamp. These light sources were utilized within two setups, an inverted microscope or in a bench-top setup.

4.1.1 Inverted Microscope

The inverted microscope, a Nikon Ti-U Eclipse equipped with a piezoelectric xy translation stage is coupled via a port to an Andor Shamrock 303i thermo-electrically cooled spectrograph. The Fianium fibre laser is free space coupled via a port at the back of the microscope for reflection measurements, whilst the Nikon halogen lamp can illuminate samples from above for transmission based measurements. The light from the Nikon lamp is collimated with a Nikon C-C Achromatic condenser to achieve near collimated illumination.

4.1.2 Bench-Top Optical Setup

An optical cage system offers flexibility for spectral and polarisation based measurements [64], both in reflection and transmission. Fig. 4.1 shows a schematic of the setup, where the sample is mounted on a xyz mechanical translation stage. Light from a multi-mode fiber-coupled tungsten-halogen bulb (Ocean Optics HL-2000-FHSA) is collimated with an Olympus Plan N 0.3 NA objective and focused onto samples using a 0.4 NA Olympus Plan N microscope objective. The state of polarisation of the exciting or detected field is controlled using a linear polariser (Thorlabs LPVIS050-MP) and a broad-spectrum quarter-wave plate (Thorlabs AQWP05M-600). The reflected field is redirected with a 50:50 non-polarising beamsplitter (Thorlabs BS016), focussed with a 50 mm focal length lens (Thorlabs LA1255-A) and fibre coupled to an Ocean Optics high quantum efficiency spectrometer (QE65000). A colour CCD and monitor is used to verify the location of collection area, relative to the sample arrays.

4.2 Polarimetry

Measurements of polarisation states of light in this work were carried out using the Stokes' vector formalism. To generate linearly polarised light a Thorlabs LPVIS050-MP linear polariser is used. Combining this with a Thorlabs AQWP05M-

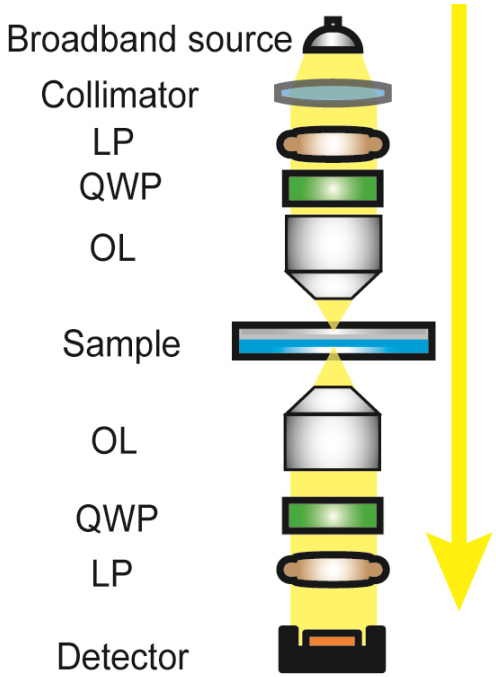


Figure 4.1: A schematic of the bench-top setup used for spectral and polarisation measurements.

600 quarter wave plate (QWP) with fast axis at $45°$ or $-45°$ to the transmission axis of the linear polariser will generate right or left circularly polarised (RCP or LCP) light, respectively. There are two methods of the polarisation action of our plasmonic devices; with Stokes' vectors or with Mueller matrices.

4.2.1 Stokes' Vectors

Stokes' vectors describe the polarisation state of an optical field. In this work Stokes' vectors, $\vec{S}$ are measured using Collet's technique (see [65]). The input polarisation state is held fixed and the output polarisation state measured in the following way; The intensity is recorded with the analyzer filtering $0°$, $45°$, $90°$ and RCP states. With this technique, the linear polariser and the QWP are fixed in the same mount with the fast axis at $45°$ to the transmission axis. This accounts for any attenuation differences that may occur by removing the QWP for linear polarisation state measurements. For linear polarisation measurements the linear polariser (LP) faces the sample and the QWP faces the detector, and as long as the detector is not polarisation sensitive (it is not in our case), the QWP only atten-

uates the beam. This ensures that when the LP-QWP combination is reversed to measure RCP, there is no difference in transmission introduced by adding or subtracting optical elements. The Stokes' vector components can then be calculated using the method outlined in [65].

One issue with this method is the fact that the tolerances in the manufacturing process of the linear polarisers (LPs) used is suboptimal, so that the markings indicating the transmission axes of the LPs are actually a combined $10°$ out from the true transmission axes, as shown in Fig. 4.2, where the transmission as a function of relative angle the polarisers was measured. Besides this error, Stokes' vector analysis is also not robust to alignment issues. It is likely that the measurement of the $x-$axis does not exactly coincide with the natural $x-$axis of the nanoscale device of interest. This alignment error can be accommodated for with Mueller matrix measurements.

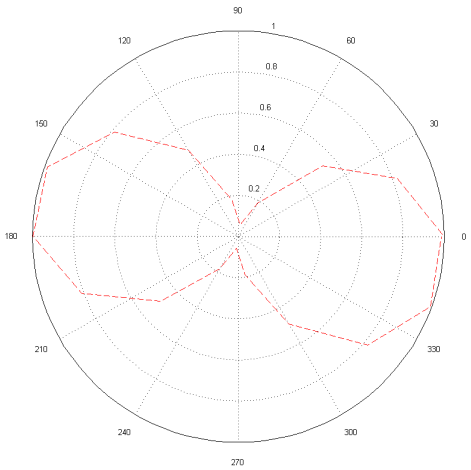


Figure 4.2: A polar plot of the intensity of light transmitted through two LPs as a function of relative angle as measured using markers provided by the manufacturer. There is a $10°$ offset from the expected curve.

4.2.2 Maximum Likelihood Measurement of Mueller Matrices

The maximum likelihood method for Mueller matrix measurement referred to in §5.2.1 is detailed below [66]. By obtaining a physical Mueller matrix it is possible to algebraically rotate the Mueller matrix of a plasmonic polarising element to

compensate for experimental misalignment, describe the response of the device for all input polarisation states and extract optical parameters such as retardation and diattenuation of the device, with confidence.

To ensure that the eigenvalues of the Hermitian coherency matrix H, related to the Mueller matrix M by

$$M_{\mu\nu} = Tr\{H[\sigma_\mu \otimes \sigma_\nu^*]\}, \tag{4.1}$$

are nonnegative, where σ_μ is the μ^{th} generator of the SU(2) symmetry group ($\mathbb{I}_{2\times2}$ and the 3 Pauli spin matrices) we must maximize $\mathcal{L}$. Using Wolfram Mathematica's FindMax function to maximize

$$\mathcal{L} = \sum_a \sum_b f_{ab} \ln \sum_{\mu=0}^{3} \sum_{\nu=0}^{3} H_{\mu\nu} Tr[\Pi_a \sigma_\mu \Pi_b \sigma_\nu^*], \tag{4.2}$$

where Π_a is the Jones matrix of polarisation state filter, a and f_{ab} is the measured intensity with the polariser in state b and analyzer set to state a, normalised to the measured intensity without the analyzer for input state b. In this work we use the standard 6 polarisation states, so that $a, b \in \{x, y, 45°, 135°, RCP, LCP\}$, thus there are 42 measurements in total (36 tomography measurements and 6 normalisation measurements). As the Mueller matrix has at most 16 independent values, this over-determination allows us to employ the maximum likelihood method. Once the values of the elements of H that maximizes $\mathcal{L}$ are found, the maximum likelihood Mueller matrix can be determined from 4.1. The positive semi-definite Hermitian restriction on H allows us to reduce the number of variables to fit to maximize $\mathcal{L}$ from 32 to 16, which leads to a drastic reduction in computational time required. The seeding of the Mathematica function FindMax must be performed with random variables, as it is possible for a local maximum, not a global maximum to be returned, leading to an unphysical result.

4.3 Fluorescence Scanning Confocal Microscopy, Time Correlated Single Photon Counting and Beaming Measurements

In order to characterise the effect of polarising plasmonic elements on the emission properties of adjacent quantum sources we need to map the spatial distribution of fluorescence as well as the excited state lifetime of the quantum emitters. The primary type of quantum emitters used in this work are quantum dots [67].

4.3.1 Fluorescence scanning confocal microscopy

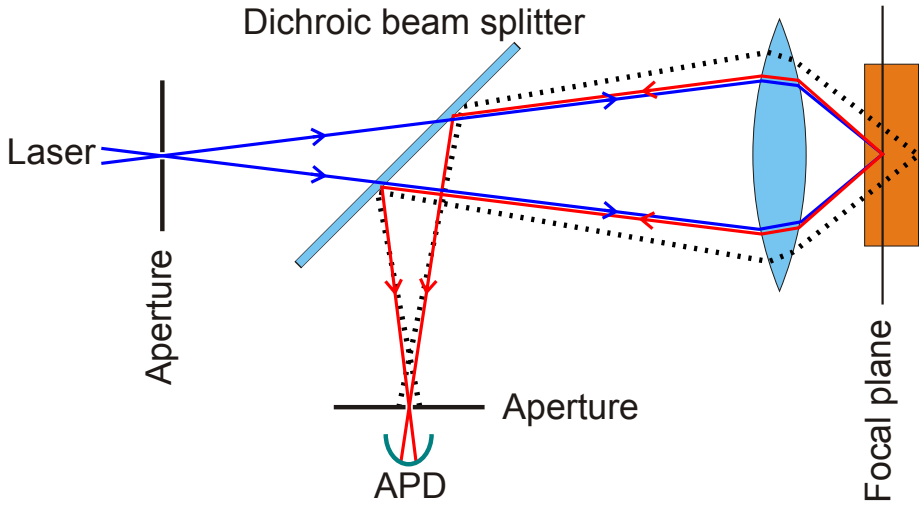


Figure 4.3: A schematic diagram of the scanning fluorescence confocal microscope used in this work. Short wavelength light is used to excite emitters in the focal plane. The emitted light is then focussed onto a pinhole aperture and then transmitted light intensity is measured by an avalanche photodiode (APD). Rays from beyond the focal plane are blocked by the aperture. The sample is scanned in the focal plane using a piezo-electric stage.

Typically in fluorescence microscopy the emission brightness is not sufficient for wide-field imaging. In practice this means optically probing our nano-structures requires a confocal scanning and binning technique. Here a Mad City Labs XY nanodrive stage is used to scan the sample with a stepsize down to 50 nm over areas up to 80 μm square. The excitation illumination is provided by a Fianium 450-SC supercontinuum source. The required wavelength is selected using a Fianium SuperChrome tunable filter. Light with a central wavelength of 465 nm

and linewidth of 10 nm from the SuperChrome is focussed onto a 50 μm pinhole to spatially filter the beam before it enters the 1.3 NA 100x Olympus oil immersion lens. This results in an illumination volume of around $(500\ \text{nm})^3$. The fluorescence is collected with the same objective and spectrally filtered using a dichroic beam splitter (Semrock Brightline 540 nm long pass) and then focussed onto another 50 μm pinhole aperture placed immediately in front of a high gain Perkin-Elmer SPCM-AQRH-14-FC avalanche photodiode (APD). The purpose of the second aperture ensures the detector images a similar volume to that being illuminated, essentially rays from outside this volume are focussed either before or after the plane of the pinhole and hence are blocked. The output of the APD is then binned as the the piezo-stage scans across the illumination spot. Figure 4.3 shows a schematic of the set-up. The microscope chassis employed is a Nikon Ti-80i Eclipse inverted microscope.

4.3.2 Time correlated single photon counting

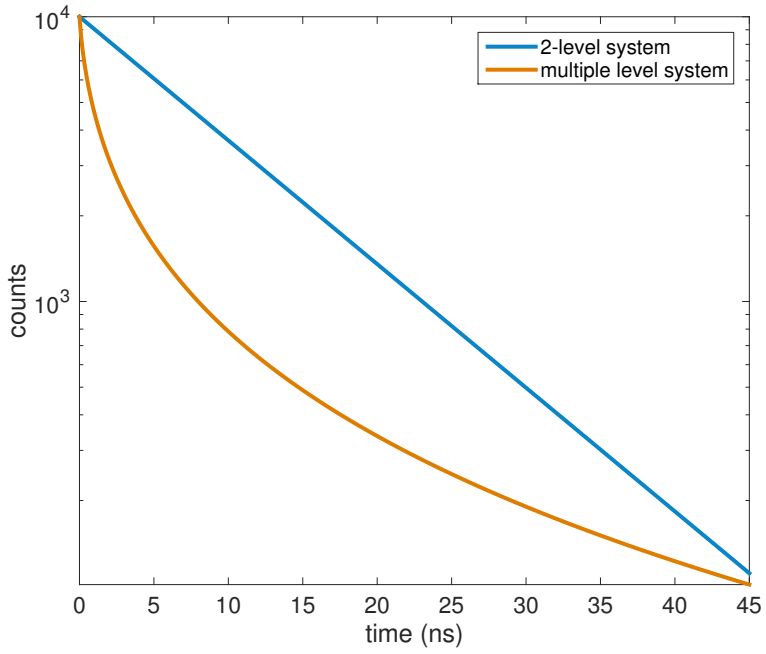


Figure 4.4: An example TCSPC result for a 2-level system (blue) and a system of multiple energy levels, either in one emitter or a collection of similar emitters (orange). Here the mean lifetime for both cases is 10 ns.

A reduction in excited state lifetime of a quantum emitter can point to weak coupling of the emitter's excited state to other decay channels provided by cavity or surface plasmon modes. This results in an increase in brightness via the Purcell effect (see §2.7). In order to characterise this radiative decay rate increase, we need to determine the average lifetime of the emitters in proximity to, as well as independent of, the cavity plasmon modes. To do this, time correlated single photon counting (TCSPC) is used. Using a pulsed laser source, with a repetition rate around 1 MHz, to pump the fluorescent source and by binning the arrival time of electrical pulses from the APD, using a PicoQuant TimeHarp 200 correlator card, it is possible to build a histogram of the distribution of decay times from a particular sample. In the simple case of a 2-level system the measured decay events will follow a single decreasing exponential distribution and the lifetime can be found by taking the mean. For quantum sources with a manifold of excited states or for groups of 2-level emitters it is necessary to model the distribution of lifetimes using other probability distribution functions, such as log-normal [68].

4.3.3 k-space Imaging of Emission Patterns

To determine how the quantum dot radiation pattern is modified by the presence of arrangements of nanoantennas one can either map the beam intensity directly by performing a confocal z-scan (that is bin the intensity as a function of spatial co-ordinates (x,y)), or, alternatively, map the k-vector (momentum) distribution of scattered or emitted radiation. The former method has the advantage of detailing the evolution of the beam whereas the latter is purely a far-field (Fraunhofer regime) measurement and in practice high spatial frequency information is lost due to the numerical aperture of the objectives used. Confocal mapping of a beam however can be very time consuming, as the final far-field radiation pattern can take up to 200 μm to emerge. This means, for a resolution of 1 μm the scan volume typically consists of one million data points per measurement. On the other hand, for a fixed wavelength, k-space imaging allows for rapid determina-

tion of the angular distribution of the scattered or emitted light and insight into its Fourier components [69].

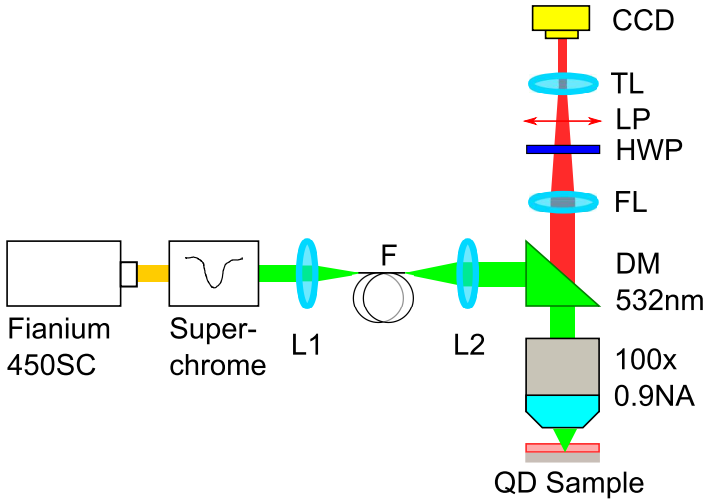


Figure 4.5: Schematic diagram of the Fourier microscope used for polarisation resolved k-space fluorescence imaging.

Figure 4.5 shows the Fourier microscope set-up used for polarisation resolved k-space measurements in this research project. Broadband light from a Fianium 450SC is spectrally filtered through the SuperChrome filter (532 nm central wavelength and 10 nm linewidth) and then focused (L1, 40x 0.6 NA Olympus Plan) onto the tip of a single mode fibre (F, Thorlabs SM450). The spatially filtered light is then recollimated (L2, Thorlabs F260FC-A) and sent to a 532 nm dichroic beam-splitter (DM, Semrock Brightline 540). Light is then focussed onto the sample with a Nikon 100x 0.9 NA CFI Plan NCG objective and the emission collected with the same objective. The pump beam is filtered by the dichroic mirror (DM) and k-space is accessed by placing a Fourier lens (FL, Thorlabs AC254-200-A-ML, f=200 mm) 200 mm from the back of the objective. A half waveplate (HWP, Thorlabs AHWP05M-600) and linear polariser (LP, Thorlabs VISA-050) allows for polarisation analysis and the HWP can be replaced by a quarter waveplate for circular polarisation measurements. A tube lens (TL, Thorlabs TTL200) is used in conjunction with a CCD USB camera (Point Grey, Grasshopper3 12.0 MP Mono) to collect the polarisation resolved k-space images.

4.3.4 Electronic Characterisation of Photodiodes

In order to measure the electronic performance of the polarisation sensitive MSM photodiodes a bench top system was assembled as shown in the schematic diagram in figure 4.6.

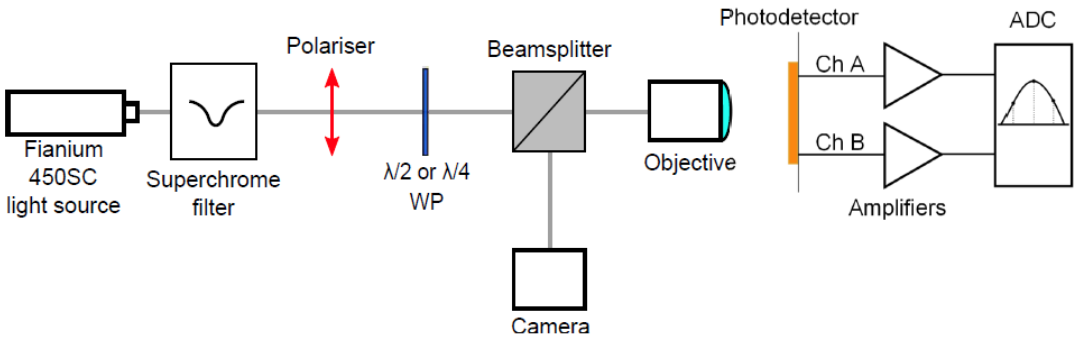


Figure 4.6: A schematic diagram of the experimental set-up used for the electrical and spectral characterisation of polarisation senstive MSM photodiodes.

A Fianium SC450 supercontinuum white light source was used to characterise the samples. The light source is coupled with a Fianium SuperChrome filter to adjust the central wavelength and bandwidth. A combination of polariser with half and quarter wave plates were used to produce and alter linear and circular polarisation states respectively. A half wave-plate and QWP were used in a Thorlabs PRM1Z8 rotation stage. A Nikon CFI Plan Fluor $\times$20 long working distance objective was used to uniformly illuminate the entire photodetector area. A polarisation insensitive 50:50 beam splitter (Thorlabs BS013) in conjugation with a CMOS USB camera (Thorlabs DCC1645C) was used to align the sample. After alignment the beam splitter was withdrawn from the system. Each MSM channel (Ch A and Ch B) is connected to custom built transimpedance amplifiers, with an amplification of 10^6 and the voltage signal is then digitised and recorded by a National Instruments USB-6343 DAQ analogue–digital converter (ADC). A Keithly 487 source meter is used for precise reverse biasing of the photodetectors.

4.4 Summary

This chapter presented details of all the relevant experiments conducted in the following chapters and equipment specifications are included to provide sufficient information for reproducibility. Spectrometry and polarimetry of samples, including measuring Stokes' vectors and a method for determining physically acceptable Mueller matrices were discussed. Scanning fluorescent microscopy, lifetime measurements and far-field radiation pattern measurements for the characterisation of quantum emitter samples were also presented. Finally the techniques used in measuring the opto-electronic properties of polarisation sensitive MSM photodiodes are briefly outlined. This chapter will be referenced throughout the remainder of the thesis.

Chapter 5

Circular Polarisation States and Plasmonics

5.1 Introduction

The research presented in this chapter focuses on generating, filtering, and measuring circularly polarised beams of visible light using engineered nanometric plasmonic surfaces. Design rules for plasmonic waveplates are established and a plasmonic quarter waveplate, capable of converting between circular and linear polarisation states, is demonstrated. An electrostatic dipole approximation is employed to describe the response of pairs of resonant nanoapertures to circularly polarised light. Using this model, a chiral aperture based metasurface is investigated and the differential transmission of circularly polarised light is maximised. Finally, the differential polarisation response of these nanoantennas is then used in a novel photodetector design to determine the degrees of linear and circular polarisation of an optical beam. The three nanophotonic devices demonstrated here could be deployed in telecommunication systems or advanced polarimeters.

5.2 A Plasmonic Quarter Wave Plate

There is considerable interest at present in the development of nano scale optical devices with potential applications as compact elements in imaging, data storage and as display components. In particular, there is a growing awareness of the potential of plasmonic devices to control and transform the polarisation states of transmitted or reflected light [70–81]. There have been previous investigations into a range of devices that have exploited the phase differences between orthogonal detuned dipoles [71, 73–75, 77, 81]. These have consisted of arrays of nanoparticles [71, 73, 77] or arrays of apertures [74, 75, 81]. In 2012, Roberts and Lin proposed the use of an array of asymmetric cross-shaped apertures exhibiting localized plasmonic aperture resonances as a means to produce an ultra-compact quarter-wave plate (QWP) [75]. This proposal was supported by simulations. Polarization devices based on localized surface plasmons (LSPs) are of interest due to their greater robustness to the angle of incidence compared to surface plasmon polaritons (SPPs) and potentially greater transmission than SPP based structures [21, 75]. Here we experimentally demonstrate a device based on the principles outlined in reference [75] and investigate its polarization and transmission properties.

5.2.1 Analytic model and numerical calculations

A schematic of the device under consideration is shown in Fig. 5.1(a). An infinite square array (period, P) of cross-shaped apertures of arm lengths, L, and widths, W are located in a silver film of thickness, T. The intensity transmission, calculated using the Finite Element Method (FEM), implemented in COMSOL Multiphysics 4.3a is shown in Fig. 5.1(b). The transmission, normalized to that in the absence of metal, is shown as a function of wavelength for a device with a square array of symmetric apertures with a fixed arm width of 40 nm and variable arm length in a Ag film of thickness 40 nm is shown in Fig. 5.1(b). The period of

the array is 300 nm and the refractive index of the substrate is taken to be 1.52. Optical constants of bulk Ag were taken from Johnson and Christie [45]. A clear resonance is seen in Fig. 5.2(a), where transmission of 700 nm light through the array as a function of antenna length is shown. This resonance is associated with the excitation of surface charges on the inner walls of the aperture leading it to behave as an electric dipole [82]. If a design wavelength of λ is selected and a Lorentzian dipole behaviour assumed, the amplitude transmission, t_λ, is given by:

$$t_\lambda(L) = -\frac{a}{i(L - L_{0\lambda}) + \frac{\Delta_\lambda}{2}} \tag{5.1}$$

where $L_{0\lambda}$ is the length at resonance and $\Delta\lambda$ the loss term (fullwidth at half maximum) at λ and a is a parameter depending on the amplitude transmission on resonance. This gives a power transmission,

$$T_\lambda(L) = \frac{|a|^2}{(L - L_{0\lambda})^2 + \frac{\Delta_\lambda^2}{4}} \tag{5.2}$$

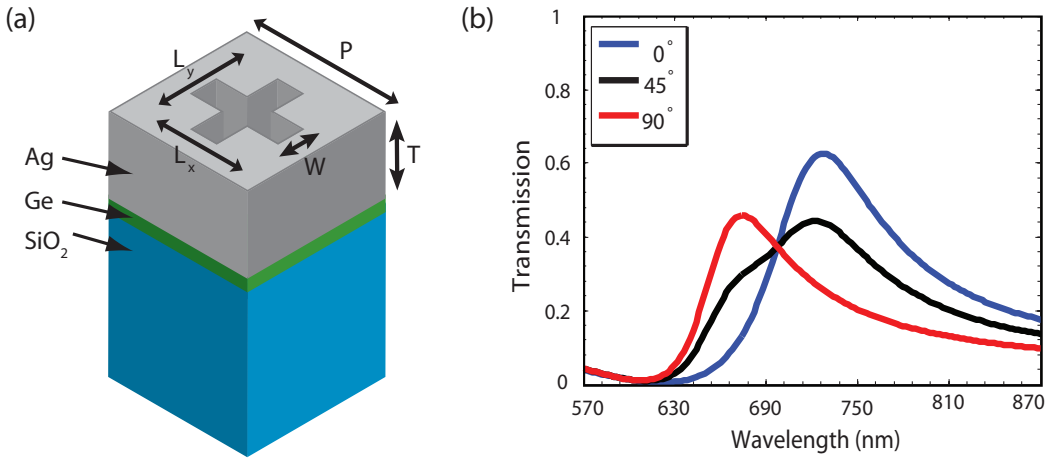


Figure 5.1: Schematic diagram of the unit cell of a plasmonic quarter-wave plate, (a). The geometric parameters are film thickness, $T = 40$ nm, slot width, $W = 40$ nm, unit cell periodicity $P = 300$ nm and L_x, L_y, the slot lengths, are varied. A 2 nm Ge adhesion layer is also shown in green. (b) Transmission spectra for an array of 120 nm by 140 nm cross apertures, with a period of 300 nm in a 40 nm Ag film calculated using the FEM for three polarization angles; 0° (blue line) 45° (black) and 90° (red). At a wavelength of 700 nm the intensity transmission is independent of the angle of linear polarization; this is the operating wavelength of the QWP.

and the phase of the transmitted field is

$$\Phi_\lambda = -\arctan\frac{2(L - L_{0\lambda})}{\Delta_\lambda}. \tag{5.3}$$

If the lengths of the cross arms in the x and y directions are equally detuned by δ, so that $L = L_{0\lambda} \pm \delta$, then the transmission should be independent of the state of linear polarization and there is a retardation, Γ_λ, between light polarized in the x and y directions, given by

$$\Gamma_\lambda = \Phi_y - \Phi_x = 2\arctan\frac{2\delta}{\Delta_\lambda}, \tag{5.4}$$

where the x-direction is positively detuned and the y-direction is negatively detuned. Hence, if we desire a specific retardation, we require a detuning given by:

$$\delta = \frac{\Delta_\lambda}{2}\tan\frac{\Gamma_\lambda}{2}. \tag{5.5}$$

In the case of a quarter-wave plate, the retardation due to each arm is $\pm\frac{\pi}{4}$ and the appropriate detuning is:

$$\delta = \frac{\Delta_\lambda}{2}. \tag{5.6}$$

If we select a design wavelength of 700 nm, the Lorentzian profiles have a resonant length, $L_{0\lambda}$ of 117 nm and width, Δ_λ, of 28 nm. This suggests that a detuning, δ, of $\pm$14 nm will produce a quarter-wave plate, operational at 700 nm.

5.2.2 Fabrication

An aperture array was fabricated in 40 nm thick layers of Ag deposited using an Intlvac Nanochrome II electron beam deposition system onto a glass microscope slide on a 2 nm adhesion layer of Ge. The aperture array was defined using Focused Ion Beam (FIB) milling with a FEI Helios NanoLab 600 Dual Beam system

using 30 keV Ga ions. An array with a periodicity of 300 nm and total dimension 160 μm$\times$160 μm was produced. Typical writing time is of the order of 110 minutes. The beam current used was 28 pA with a 3.5 nm step size and the dwell time was set to 3.8 ms. A single serpentine scan of the beam was employed over the target area. A scanning electron microscope (SEM) image of the device is shown in Fig. 5.2(b). From the SEM, it is apparent that the modelled square profile cross-apertures are significantly rounded and the fabricated crosses have vertical arm length (132.5 ± 7) nm and horizontal arm length (145 ± 6) nm.

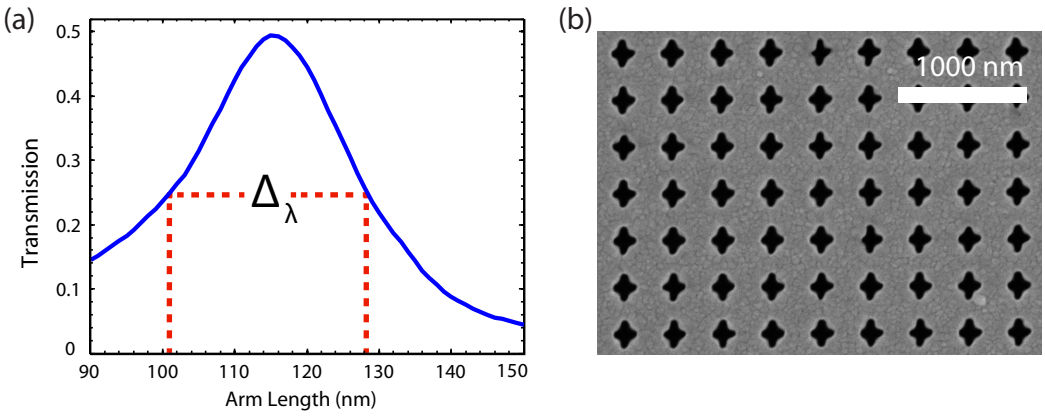


Figure 5.2: (a) Computed transmission, $T_\lambda(L)$, of 700 nm light through a rectangular aperture in a 40 nm Ag film on a SiO_2 substrate as a function of aperture length, L. The full-width-half-maximum, Δ_λ, is 28 nm and is indicated by the dashed lines. (b) An SEM image of the fabricated plasmonic QWP. The cross apertures were milled using a focused ion beam. Each element is 300 nm from its neighbour

5.2.3 Device characterization

The device was characterized in the bench-top polarimetry system shown in Fig. 5.3(a). Light from a multi-mode fibre/coupled tungsten-halogen bulb was collimated and focused onto samples using a 0.4 NA Olympus Plan N microscope objective. The state of polarization of the input field was controlled using a linear polariser and a broad-spectrum quarter-wave plate. The light transmitted through the device was analysed with an identical linear polariser and a quarter wave plate. Fig. 5.3(c) shows the measured transmitted intensity spectra. The polarization independent point is at a wavelength of 702 nm, in excellent agreement with the design wavelength of 700 nm. The model, however, underestimates

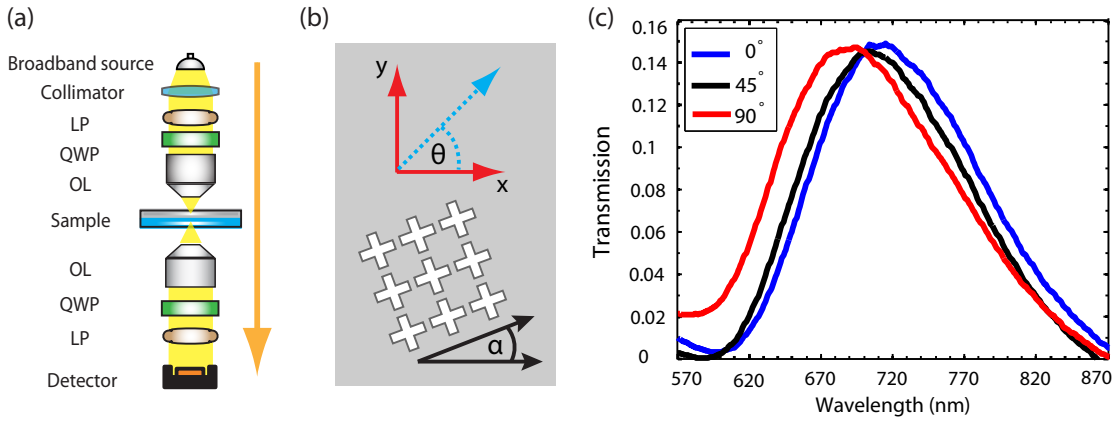


Figure 5.3: (a) A schematic diagram of the bench top polarimetry set up. The incident beam passes through a collimator, a linear polariser (LP) and an achromatic quarter wave-plate (QWP) and is then focused onto the array with an objective lens (OL). The analyser consists of the same optical elements, in reverse order. (b) The principal axis of the array forms an angle, α, with the x-axis. The angle of polarization, θ is measured from the x-axis. (c) The measured intensity of linearly polarized light transmitted through the plasmonic QWP for 0° (blue line) 45° (black line) and 90° (red line) angle of polarization. At a wavelength of 702 nm the transmission is polarization independent.

fabrication errors and the loss assumed when using the optical properties of bulk Ag [45]. This led to a reduction in the relative amplitude of the transmission of light polarized at 0°, which can be seen by comparing Figs. 5.1(b) and 5.3(c). Full polarization tomography (FPT) was then performed on the fabricated array. The maximum likelihood estimation method was used to calculate a Mueller matrix for the plasmonic QWP [66]. A set of 42 polarization measurements were performed, to measure the intensity of light, polarized at 0°, 45°, 90°, 135° with respect to the x-axis, left-and right-hand circular polarization states, transmitted in those same polarization states (36 measurements for all combinations of the 6 initial states and the 6 final states as well as 6 normalization measurements performed without the analyser). The measured Mueller matrix is shown in (5.7) and resembles the Mueller matrix of a classical depolarizing QWP [83],

$$M = \begin{bmatrix} 0.90 & 0.068 & 0.078 & -0.018 \\ 0.068 & 0.78 & 0.14 & 0.24 \\ 0.076 & 0.085 & 0.077 & -0.72 \\ 0.00 & -0.26 & 0.69 & -0.037 \end{bmatrix}. \tag{5.7}$$

Unlike the standard linear reconstruction algorithms typically used for FPT [84], the Hermitian matrix associated with M, found using the maximum likelihood estimation method is guaranteed to be positive semi-definite and is, thus, physical [17, 20]. In order to demonstrate the veracity of our Mueller matrix we use it to compute the resulting Stokes vector when the plasmonic array is illuminated with linearly polarised light at -45° to the x-axis.

$$M\vec{S}_{45^\circ} = \begin{bmatrix} 0.90 & 0.068 & 0.078 & -0.018 \\ 0.068 & 0.78 & 0.14 & 0.24 \\ 0.076 & 0.085 & 0.077 & -0.72 \\ 0.00 & -0.26 & 0.69 & -0.037 \end{bmatrix} \begin{bmatrix} 1 \\ 0 \\ -1 \\ 0 \end{bmatrix} = \begin{bmatrix} 0.82 \\ -0.067 \\ -0.0012 \\ -0.69 \end{bmatrix}, \tag{5.8}$$

which after normalization becomes

$$\vec{S}_{out} = \begin{bmatrix} 1 \\ -0.08 \\ 0.00 \\ -0.84 \end{bmatrix}. \tag{5.9}$$

The large value for S_3 indicates that the array is an approximation to a plasmonic quarter-wave plate, transforming linearly polarised light into near-circularly polarised light. It is possible to extract several optical properties of the sample from the Mueller matrix in (5.7). For instance, the phase retardance can be calculated, in this case it is 87.1°, which is very close to the desired phase retardance, $\Gamma_\lambda = 90^\circ$ for a QWP [83, 84]. The diattenuation, D, the differential transmission of orthogonal polarization states (which has a value between 0 and 1), can also be derived from the Mueller matrix. For this structure D = 0.084, which indicates a negligible dependence on polarization angle for the transmitted intensities at the operating wavelength [84].

Importantly, the principal axis of this plasmonic quarter-wave plate can also be extracted. The principal axis, in fact, lies 9.8° clockwise from the x-axis. It is expected that the principal axis of the plasmonic quarter-wave plate is coincident with the long arm of the crosses in the array. Hence, the horizontal arms of the crosses in the array are not parallel to the horizontal measurement axis as intended, but, in fact, form an angle of 9.8° with the horizontal measurement axis. The Mueller matrix, however, is robust to issues such as this. Rotating the sample by α is equivalent to performing a unitary basis transformation on M. The Mueller matrix for the rotated sample, $M'(\alpha)$ is given by [85],

$$M'(\alpha) = \begin{bmatrix} 1 & 0 & 0 & 0 \\ 0 & \cos\alpha & -\sin\alpha & 0 \\ 0 & \sin\alpha & \cos\alpha & 0 \\ 0 & 0 & 0 & 1 \end{bmatrix} M \begin{bmatrix} 1 & 0 & 0 & 0 \\ 0 & \cos\alpha & \sin\alpha & 0 \\ 0 & -\sin\alpha & \cos\alpha & 0 \\ 0 & 0 & 0 & 1 \end{bmatrix}. \tag{5.10}$$

The Stokes vector of a transmitted beam that was linearly polarized at -45° to the principal axis of the fabricated plasmonic quarter-wave plate can then be calculated,

$$M'(9.8^\circ)\vec{S}_{45^\circ} = \begin{bmatrix} 0.90 & 0.09 & 0.05 & -0.02 \\ 0.09 & 0.82 & -0.12 & -0.01 \\ 0.05 & -0.16 & 0.09 & -0.76 \\ 0.00 & 0.00 & 0.73 & -0.04 \end{bmatrix} \begin{bmatrix} 1 \\ 0 \\ -1 \\ 0 \end{bmatrix} = \begin{bmatrix} 0.85 \\ 0.13 \\ -0.04 \\ -0.73 \end{bmatrix}, \tag{5.11}$$

which upon normalization gives the output Stokes vector,

$$\vec{S'}_{out} = \begin{bmatrix} 1 \\ 0.16 \\ -0.04 \\ -0.86 \end{bmatrix}. \tag{5.12}$$

The degree of polarization is 0.88 and the degree of circular polarization of the transmitted beam is 0.86, ideally this would be 1, however due to imperfections in the fabrication process this was not realized.

5.3 A Nanoaperture based Chiral Metasurface

Generating circularly polarised beams with nanometric devices forms one half of a compact polarimetry system, which can be used for communication or sample analysis. The other half requires forming a polarisation analyser, by preferentially filtering out a particular circular polarisation state. This could be achieved by cascading a plasmonic QWP with an array of rectangular slot apertures, but the transmitted power in this case would be very low. In addition to creating a circular polarisation filter, arrays of nanoscale apertures in thin metallic films, when compared to their nanoparticle counterparts, are of particular interest for sensing and telecommunication applications because of the relatively high transmission contrast and background field reduction achievable with these devices. Furthermore, the reduced mode LSP volume inside the resonant aperture could lead to a reduction in the amount of analyte required for remote sensing applications [86]. The devices presented here are sensitive to visible wavelengths, but could be scaled to operate at longer wavelengths if required. These structures in question are fabricated using focused ion beam (FIB) milling, and their transmission sensitivity to the helicity of circularly polarized light is characterized. The finite element method (FEM) is used to provide further insight into the properties of these surfaces.

5.3.1 Design Considerations

As discussed in a previous section, §2.4.1 the far-field interference of circularly polarized light scattered by two plasmon dipole modes depends on the angle between the resonant dipolar LSP modes and the phase of these modes [32]. Figure

5.4 shows a schematic of the 2D planar chiral geometry considered. It consists of two slot apertures oriented at some angle with respect to each other and spatially offset. At a resonance of a mode of interest, surface charges appear on opposite sides of the narrow axis of the slot, leading to the existence of an electric dipole.

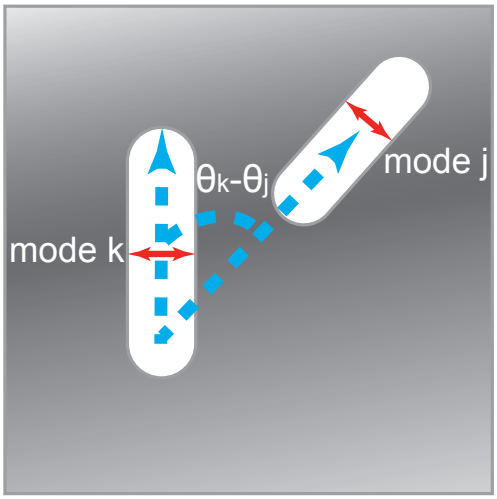


Figure 5.4: A plasmonic 2D planar chiral unit cell consisting of two offset slot apertures in a metallic film. The red arrows represent the electric dipole directions of LSP modes k and j. The separation angle, $(\theta_k - \theta_j)$, is shown in blue.

At resonance, a net dipole moment $\vec{\mathbf{p}}$, is induced within each aperture [87]. The power radiated by a dipole per unit solid angle is once again given by,

$$\frac{dP}{d\Omega} = \frac{\omega^4}{32c^3\epsilon_0\pi^2}(\hat{\mathbf{n}} \times \vec{\mathbf{p}}) \cdot (\hat{\mathbf{n}} \times \vec{\mathbf{p}}^*), \tag{5.13}$$

where $\hat{\mathbf{n}}$ is the unit vector in the direction of observation, $\vec{\mathbf{p}}$ is the complex dipole moment that may be shifted in phase relative to the incident light, c is the speed of light in vacuum, ω is the frequency of the incident field, and ϵ_0 is the permittivity of free space [32]. Exciting plasmon modes with normally incident circularly polarized light, eqn. A.8 gives the radiation pattern as proportional once again to

$$\sin(\phi_k - \phi_j)\sin[2(\theta_k - \theta_j)] \tag{5.14}$$

where ϕ_k and θ_k are the relative phase and angle of mode k [32]. To ensure the

resonance of mode k, does not depend on mode j, the apertures are positioned relative to one another to minimize the dipole-dipole coupling, ξ, between the LSP modes on each antenna [88]. It is well known that dipole-dipole coupling is proportional to

$$\xi \propto 3(\vec{p}_1 \cdot \vec{d})(\vec{p}_2 \cdot \vec{d}) - \vec{p}_1 \cdot \vec{p}_2 \tag{5.15}$$

where $\vec{\mathbf{p}}$ is the dipole moment of each LSP and d the displacement vector between the centre of each nanorod. Setting ξ to 0 and solving for d will give the co-ordinates of each nanorod for which there is no mode hybridisation. For a separation angle of $45°$, we find that a polar angle of $16.18°$ gives the nullcline in LSP hybridisation, which we wish to place our second nanoantenna along. Furthermore, it has been shown that in the case of particle arrays the asymmetric response of the chiral planar system is maximal when the difference in the resonant frequencies, $\Delta\omega$, of the LSP modes is

$$\Delta\omega = \frac{\gamma}{\sqrt{3}}, \tag{5.16}$$

where γ is the full-width at half maximum of the frequency response of each dipole mode [32].

The handedness-dependent term in (5.14), that is the term involving the $\mp$ sign, is zero when $\phi_k - \phi_j = 0$ or π, or when $\theta_k - \theta_j = 0$ or $\frac{\pi}{2}$, which means the interference effect that leads to a differential transmission of LCP and RCP light is not present for these cases. This situation would arise for a structure with parallel or orthogonal LSP modes, degenerate LSP modes (zero phase difference between the two modes) or highly non-degenerate modes (π phase difference). On the other hand, the observed difference in transmission of LCP and RCP light is maximal for a structure where the two LSP modes have a $\frac{\pi}{2}$ phase difference and have an opening angle of $45°$. To satisfy the phase difference condition, two slightly detuned apertures per unit cell are required. This can be achieved by introducing

a difference in aperture length, δ, of around 10 nm [89].

Although the above results were originally for LSP resonances in metal nanoparticles, the underlying principles are based on the properties of resonant LSP dipoles. In this regard we would expect similar conclusions to apply to LSP resonances in an array of nanoapertures in an ultra-thin metal film, where Bookers extension to Babinets principle may hold [90]. Differences due to the finite conductivity of the metal and the thickness of the metal film, however, would be anticipated.

5.3.2 Device Fabrication and Characterization

The study involved investigating the magnitude of the difference in the measured far-field intensity of LCP and RCP light transmitted through a 2D planar chiral array for four different separation angles, $30°$, $45°$, $60°$ and $90°$. Focused Ion Beam (FIB) milling was used to pattern arrays of pairs of apertures in a 50 nm thick silver film evaporated onto a fused silica substrate using an Intlvac Nanochrome II electron beam deposition system. A 2 nm layer of germanium was used to aid adhesion and reduce the Ag grain size in the film. Four separate arrays were milled using a Helios NanoLab 600 DualBeam FIB-SEM with a focused beam of 30 keV Ga ions with a beam current of 9.1 pA. The unit cell of each array consisted of a pair of rounded rectangular apertures at the various opening angles. The average width of the fabricated slots was 36 ± 3 nm whilst the average vertical slot length was 115 ± 7 nm and the angled slot 111 ± 6 nm. The dimensions of the holes in each of the four arrays were held constant so that the relative phase difference between the two LSP modes was constant. The arrays consist of 100 by 100 unit cells, each with a period of 300 nm. Figure 5.5 shows four scanning electron micrographs (SEMs) of the arrays.

The arrays were characterized using a Nikon Ti-U Eclipse inverted microscope. White light from a halogen source was passed through a Nikon C-C Achromatic condenser to achieve close to collimated, normally incident light. The incident

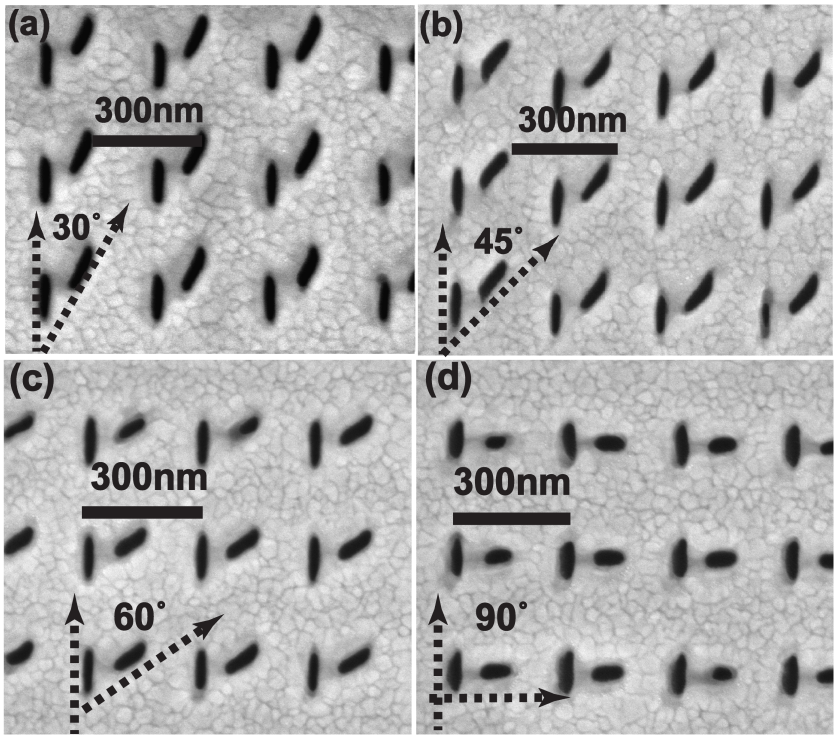


Figure 5.5: SEM images of the FIB fabricated chiral aperture arrays in a 50 nm Ag film. The separation angles are (a) $30°$, (b) $45°$, (c) $60°$ and (d) $90°$.

beam polarization was then varied from LCP to RCP using a linear polariser and a quarter wave plate. The transmission spectra of the left-and right-handed polarization states for each array was acquired with the Andor Shamrock 303i cooled spectrograph. The far-field transmission spectra and surface charge density were calculated using the Finite Element Method, as implemented in COMSOL Multiphysics 4.3b. Geometric parameters were obtained from experimental SEM images and the optical constants for bulk Ag film were taken from literature [45].

5.3.3 Experimental Results

Figure 5.6(a) shows the measured and calculated difference in transmission spectra (normalized to the input beam intensity) for the arrays with $45°$ and $90°$ separation angles, while figure 5.6(b) shows the measured, predicted and simulated polarization contrasts for all 4 separation angles. For the array with an opening angle of $45°$, LCP constructively interferes upon transmission, whereas RCP interferes destructively, leading to a 10% difference in transmission. The maximum

transmission difference occurs at a wavelength of 640 nm. The measured transmission of LCP and RCP light through an array with orthogonal LSP modes is very similar and hence the difference for the array with 90° separation angle is small. The fact that the experimentally determined transmission is weaker and the resonance broader than that calculated is attributed to variations in the geometry of the nanoaperture pairs across the array of apertures due to FIB fabrication errors and inaccuracies in the optical constants used in the simulations. The circular polarization contrast, $\frac{(I_L - I_R)}{(I_L + I_R)}$, where $I_{L(R)}$is the measured transmitted intensity of LCP (RCP) light, is plotted in figure 5.6(b) along with the calculated and predicted contrasts. The theoretical model is in good agreement with our results, both simulated and measured. The results depicted in figure 5.6 suggest a silver chiral metasurface on silica, with an opening angle of 45° can clearly discriminate between circular polarization states of incident light.

FEM Simulation Results

The inset of figure 5.6(a) shows the calculated difference in transmission for LCP and RCP through an array of pairs of nanoapertures and the complementary nanorod array for a 50 nm Ag film on a silica substrate. The rod array has a peak transmission difference red-shifted by 5 nm when compared to that of the aperture array. The transmission difference of the nanorod array is the opposite sign top the aperture array. The line shapes and amplitudes of both metasurfaces, however, are nearly identical. This indicates that the approximate application of Bookers extension to Babinets principle in this case is sound. The origin of the interference effect is revealed by calculating the surface charge density around the nanoholes for LCP and RCP incident fields. Figure 5.7 shows that, at a wavelength of 640 nm, in all cases both apertures support LSP modes, as required for interference to occur. For orthogonal LSP modes (bottom two rows), the distribution of charges around the apertures for a left handed field is the same as for a right handed field that has been horizontally reflected about the center of the unit

cell. This is not surprising as the unit cell in the orthogonal case exhibits mirror symmetry along this axis.

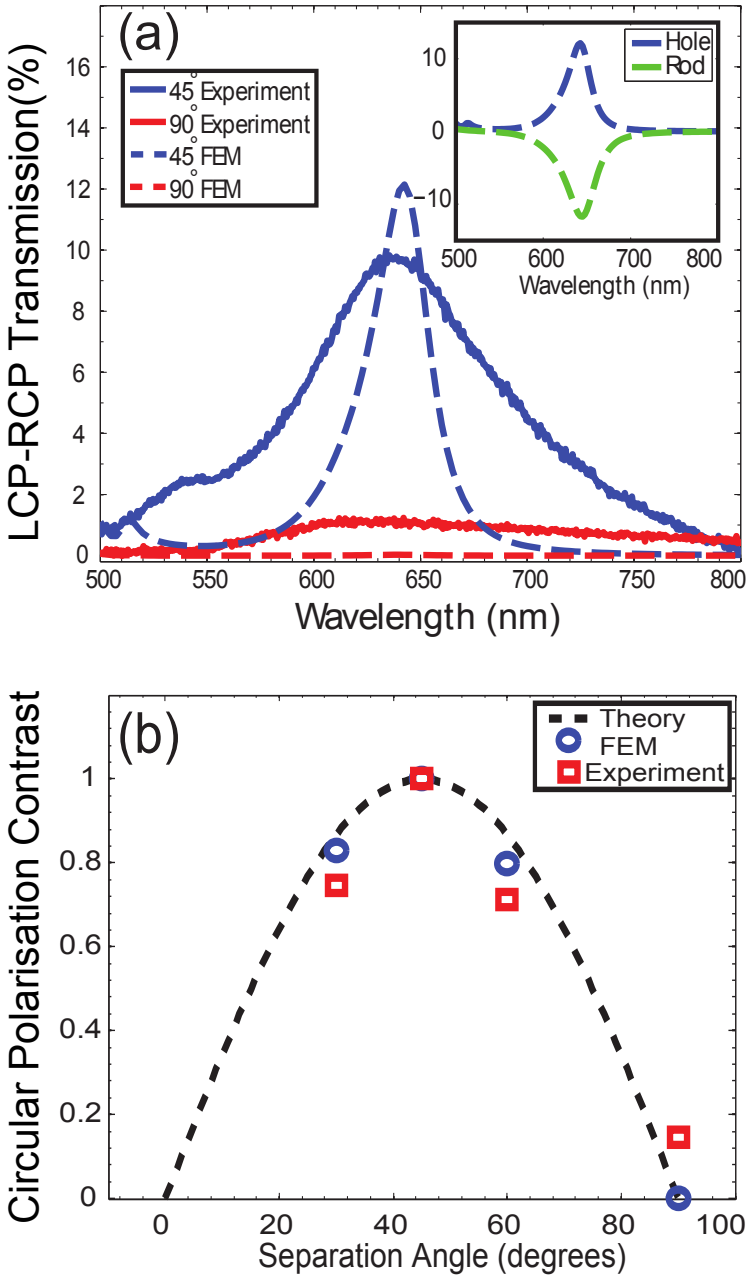


Figure 5.6: (a) The normalized difference in transmission for LCP and RCP through an array of apertures with separation angle 45° (blue line) and 90° (red line). The solid lines represent experimental results and the dashed lines are from simulation. The inset shows the calculated differential transmission through arrays of nanoholes (blue dashed) and nanorods (green dashed) of the same dimensions, with a 45° separation angle. (b) Circular polarization transmission contrast as a function of separation angle. The dotted line is $\sin 2\theta$, the red squares are the measured contrasts and the blue circles are the contrasts calculated using the FEM.

Hence, we see no difference in the transmission spectra between LCP and RCP

illumination. However, for the case where one mode is oriented at 45° to the other (top two rows of Figure 5.7), it is clear that there is no such mirror plane that will allow us to negate the effect of a parity switch of the exciting electric field. This is due to the chiral nature of these apertures breaking the mirror symmetry of the unit cell and leads to a difference in transmission of left and right circularly polarized fields, as observed in figure 5.6(a) and (b). An understanding of the difference in surface charge distributions is important for integration of this metasurface filter with a photodetector substrate to create a circular polarization sensitive detector.

FEM calculations show up to an 18% difference in transmission of LCP and RCP light is achievable. This agrees with the difference found for the complementary nanoparticle structure [32]. For this difference to be realized, however, each aperture must be precisely fabricated with the optimal dimensions to give a $\frac{\pi}{2}$ phase difference [89], allowing for maximal constructive and destructive interference.

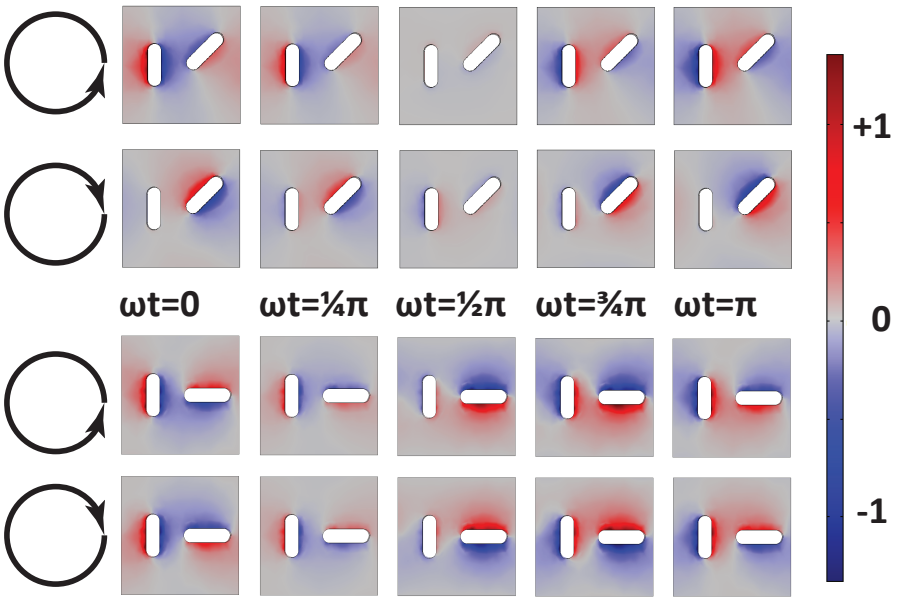


Figure 5.7: Normalized surface charge distributions (SCD) calculated using the finite element method to solve Maxwells equations. The blue regions indicate areas of a negative surface charge and the red regions indicate positive surface charge density. The top two rows are the SCD for a separation angle of 45° and the bottom two are for a 90° separation angle. The black arrows indicate the handedness of the incident field, with clockwise rotation corresponding to a RCP field. Each column is the SCD at different points of a half cycle, where ω is the frequency of the field and t is time.

5.4 Plasmonic Nanoantenna Coupled Photodiodes for Polarisation State Detection

Having developed plasmonic devices for generating and filtering circularly polarised light, attention turns to creating a compact and robust polarisation detection device. Typically the determination of polarisation states of optical beams involves first filtering polarisation states with optical elements and then detecting the intensities of each filtered beam with opto-electronic components such as CCDs or photodiodes. The resulting systems are usually bulky as well as expensive and it is sometimes difficult to maintain good alignment, especially in portable devices. To that end, the aim is to incorporate, using the plasmonic nanoantenna designs discussed in the previous section, the polarisation filtering *and* electronic detection in a single planar device. The following work was carried out in collaboration with Mr Evgeniy Panchenko.

5.4.1 Photodiode Design

In general, to convert optical information into an electronic signal, photons must be absorbed and converted into an electron-hole pair and these charges then need to be separated before they recombine. The charge separation is typically accomplished using a space charge region in a doped semiconductor. Here a region with a potential barrier or bandgap is biased such that when a photon excites a charge carrier above the barrier or into the conduction band, the charges are swept into an external circuit and the photocurrent measured. A simple method for creating a potential barrier in a semiconductor is to apply metal contacts directly to the substrate. The difference in work function between the metal and semiconductor will result in a depletion or accumulation (depending on whether the semiconductor is *p*- or *n*-type and on the applied bias potential) layer forming a region of space charge and a small Schottky barrier will be formed, this type of photodetector is known as a Schottky diode [91]. The appeal of such a device for

photodetection is the simplicity of fabrication as compared to the more sensitive, more complex, PIN photodiode. By combining two metal contacts on a semiconductor substrate a metal-semiconductor-metal (MSM) photodiode is created, which functions as two counterfacing Schottky diodes. Because of this, current will not flow through an MSM photodiode unless it is illuminated. This device is also relatively simple to fabricate and has been demonstrated to operate at very high bandwidths up to 140 GHz [92]. To create an MSM photodiode sensitive to visible light, $n-$type silicon (with a sheet resistivity of 10 Ω·cm) was chosen as the semiconductor substrate and aluminium used to form the Schottky barriers and nanoantennas. Aluminium is a natural choice as it easily forms a Schottky barrier with $n-$type silicon, has a high plasma frequency, which helps to counteract the large red shift associated with a Si substrate ($n_{Si} \approx 3.8$ for visible wavelengths), a protective native passivation layer as well as being fully CMOS compatible and cost effective. The biggest drawback to using Al for nanoantennas is the high optical losses and the interband transition in the metal which occurs around 780 nm. This has been shown to lead to broad, low Q factor, higher operating bandwidth resonances at optical frequencies [93].

5.4.2 Nanoantenna Enabled Differential MSM Photodiode

To determine the degree of linear or circular polarisation of a beam (assuming there are no exotic polarisation components, such as vortex beams) one must measure intensities in both orthogonal polarisation states, that is LCP and RCP or x- and y- polarised states. To do so "*on-chip*" a two channel MSM photodiode was created consisting of three Al leads, where the central lead is the common ground and each of the other leads will carry the photocurrent associated with a polarisation eigenstate. The difference between the photocurrent in each channel is then proportional to the degree of circular or linear polarisation incident on the photodiode. In order to make a particular MSM channel sensitive to a polarisation eigenstate the region between fingers was filled with nanorods for linear

polarisation or the previously discussed chiral nanoantennas for the detection of circular polarisation states. Also fabricated was a polarisation insensitive square nanoantenna design as a control for the experiment. Figure 5.9 shows SEM images of the three photodiode designs, with the antenna dimensions shown in the inset. A spiral shape was chosen over the standard rectangular interdigitation as it matches the typical optical beam shape better, does not have a linear polarisation dependence (unlike rectangular gratings) and the applied bias acts to shield carriers generated in one channel from drifting into the other channel.

5.4.3 Response of Chiral Nanoantennas to Linearly Polarised Light

To ensure a differential photocurrent is recorded only in response to a particular polarisation state it is important to understand the optical response of sets of nanoantennas to other polarisation states. For example, clearly a rectangular nanorod will have the same absorption cross-section for left- and right-circularly polarised light, regardless of the nanorod orientation. This means the measured photocurrent difference between linearly polarised detection channels when illuminated with circularly polarised light is zero. Conversely, it is not so obvious what the linear polarisation response of pairs of nanorods will be. Equation (A.7) is applied to the chiral structures discussed above to determine their response to linearly polarised light.

For linearly polarised light, polarised at angle α, the electric field $\mathbf{E}_0$, is given by $\mathbf{E}_0 = [\hat{x}\cos\alpha + \hat{y}\sin\alpha]E_0 e^{ikz}$. Inserting this into (A.7) and taking the dot product with $\mathbf{p}_k = p_k^{xy}(\hat{x}\cos\theta_k + \hat{y}\sin\theta_k)$ gives radiated power per solid angle

$$\frac{dP}{d\Omega} = \frac{ck^4}{32\pi^2\epsilon_0}\sum_k\sum_j |f_k||f_j|e^{i(\phi_k-\phi j)}(p_k^{xy}p_j^{xy})^2 \times \\ [\cos\alpha\cos\theta_k + \sin\alpha\sin\theta_k][\cos\alpha\cos\theta_j + \sin\alpha\sin\theta_j](\cos(\theta_k-\theta_j) + N_{kj}). \tag{5.17}$$

Applying a compound angle formula to the trigonometric terms yields a general formula for the far-field radiation pattern when linearly polarised light is scattered

by the LSP modes of a 2D planar plasmonic metamaterial (see §A for the full derivation). Explicitly, this key result is:

$$\frac{dP}{d\Omega} = \frac{ck^4}{32\pi^2\epsilon_0}\sum_k\sum_{j\leq k}|f_k||f_j|(p_k^{xy}p_j^{xy})^2\cos(\phi_k-\phi_j)(\cos(\theta_k-\theta_j)+N_{kj})\cos(\alpha-\theta_k)\cos(\alpha-\theta_j), \tag{5.18}$$

where α is the angle of the plane of polarisation in the xy-plane, θ_k is the angle of the k^{th} LSP mode in the xy-plane and N_{kj} is once again the off normal incidence term.

For a simple two LSP mode system, $(k, j \in \{1, 2\})$ excited by normally incident linearly polarised light, (5.18) reduces to

$$\begin{aligned}\frac{dP}{d\Omega} = \frac{ck^4}{32\pi^2\epsilon_0}[&|f_1|^2(p_1^{xy})^4\cos^2(\alpha-\theta_1)\\ &+|f_1||f_2|(p_1^{xy})^2(p_2^{xy})^2\cos(\phi_1-\phi_2)\cos(\theta_1-\theta_2)\cos(\alpha-\theta_1)\cos(\alpha-\theta_2)\\ &+|f_2|^2(p_2^{xy})^4\cos^2(\alpha-\theta_2)].\end{aligned} \tag{5.19}$$

It is interesting to note that only the middle term depends on the relative phase and relative separation angle of the plasmon modes. Figure 5.8 shows the calculated scattering from chiral nanoantennas when illuminated at normal incidence with linearly polarised light at the central frequency (so that excitation amplitudes, $|f|$ and dipole moments, p are equal) for nanoantennas separated by $45°$ as a function of phase difference and polarisation angle. From fig 5.8 we see that for all phase differences (that is, for all LSP resonance detunings) there exists a dependence on linear polarisation angle. It is also clear that the maximum differential response occurs for degenerate LSP modes.

Special Case I: Excitation of Two Degenerate LSP Modes

If the fundamental LSP modes on each nanoantenna are degenerate then $f_k(\omega) = |f_k(\omega)|e^{i\phi_k(\omega)} = f_j(\omega) = |f_j(\omega)|e^{i\phi_j(\omega)}$. This can be achieved with a unit cell consisting of two nanoslots or nanorods of the same length and width in a

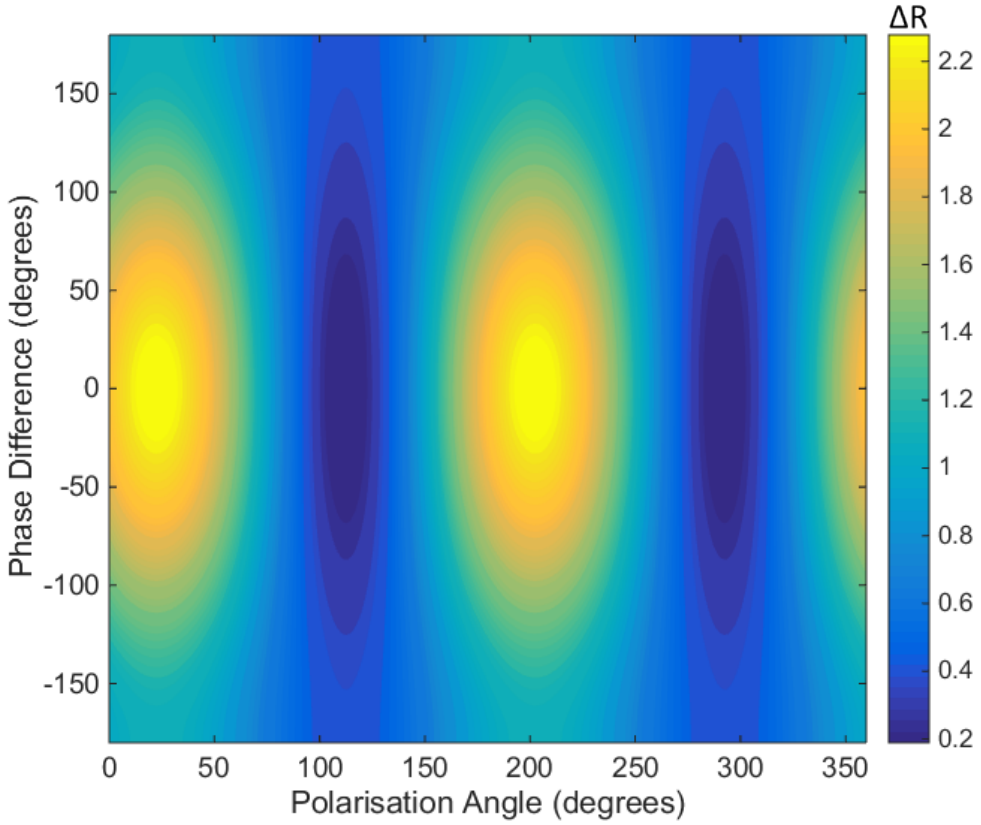


Figure 5.8: Difference, ΔR, between the scattering of linear polarised light from enantiomers of chiral nanoantennas with a 45° opening angle at normal incidence as a function of polarisation angle and LSP phase difference.

thin film. For this case (5.19) simplifies to

$$\frac{dP(\alpha)}{d\Omega} = \frac{ck^4}{32\pi^2\epsilon_0}|f(\omega)|^2(p^{xy})^4 \times \\ [\cos^2(\alpha-\theta_1) + \cos(\theta_1-\theta_2)\cos(\alpha-\theta_1)\cos(\alpha-\theta_2) + \cos^2(\alpha-\theta_2)]. \tag{5.20}$$

Setting the derivative with respect to polarisation angle, α, to zero and solving for α_{max} (the polarisation angle at which the scattering is maximum) gives

$$\alpha_{max}(\theta_1,\theta_2) = \frac{1}{2}\arctan\{\frac{\sin 2\theta_1 + \sin 2\theta_2 + \cos(\theta_2-\theta_1)\sin(\theta_2+\theta_1)}{\cos 2\theta_1 + \cos 2\theta_2 + \cos(\theta_2-\theta_1)\cos(\theta_2+\theta_1)}\}. \tag{5.21}$$

Equation (5.21) can be easily used to make predictions that can be compared with numerical full-field solutions to Maxwell's Equations as another test of the validity of (A.7). Without loss of generality, one of the LSP modes can be set parallel to

the x-axis, that is $\theta_1 = 0$. Then after some algebra, (5.21) simplifies to

$$\begin{aligned} \alpha_{max}(0, \theta_2) &= \frac{1}{2} \arctan(\tan(\theta_2)) \\ &= \frac{\theta_2}{2}. \end{aligned} \tag{5.22}$$

This result is strikingly intuitive, it is easy to imagine that the maximum overall LSP mode excitation would occur for a polarisation angle along a bisector of the two degenerate LSP modes.

Special Case II: Excitation of Two LSP Modes with $90°$ Phase Difference

For the chiral nanoantennas investigated in this chapter, we maximised the chiral response by ensuring a phase difference of $90°$ between the fundamental LSP modes on each nanoantenna. In this case, $\phi_1 - \phi_2 = 90°$ and eqn. (5.19) becomes proportional to

$$\cos^2(\alpha - \theta_1) + \cos^2(\alpha - \theta_2). \tag{5.23}$$

Hence, for chiral nanoantennas with the maximal differential response to circularly polarised light, there is also a differential response to linearly polarised light. In fact, the only separation angle that yields a linear polarisation angle independent response is $90°$, which we have seen has no differential response for circular polarisation handedness either. This also means the differential photocurrent of the photodiode with nanorods at $45°$ will depend on $\sin(2\alpha)$. This result is important as it limits the utility of our photodiode design to situations where it is already known whether the polarisation signal is circular or linear polarisation, such as in telecommunication systems. This restriction can be lifted by integrating chiral nanoantenna pairs with a randomised orientation so that the linear polarisation response is averaged out of the measured photocurrent. In this case this polarisation sensitive photodiode design can be applied in polarimetry measurements. If, however, the two LSP modes are neither degenerate nor $90°$ out of phase, say

due to slight fabrication defects, then the expected differential response will lie somewhere between these two special cases.

5.4.4 Fabrication of the Spiral Photodiode

An $n-$type Si wafer was spin coated with 240 nm PMMA 950k electron beam resist and then exposed with 100 kV EBPG5000+ electron beam lithography system (see §3.1 for more details). The patterns were generated using the freely available gdsCAD and gdspy Python packages, with a custom script to place the nanoantennas on spiral paths with a nearest neighbour distance of 280 nm. The exposure was then developed in 1:3 MIBK:IPA solution for 1 minute. The native oxide layer on the silicon substrate was stripped using 4% hydrofluoric (HF) acid for 1 minute and then immediately loaded into an IntlVac NanoChrome II e-beam evaporator. An aluminium layer with a thickness of 85 nm was deposited at 0.07 nm/s. After evaporation a lift-off step in heated acetone was performed. A wet dicing saw (Disco DAD321) was used to separate the photodetectors for packaging in a ceramic PLCC20 package and then electronic bonds from the sample to the package were made using a Kulicke and Soffa ball bonder.

5.4.5 Electro-Optical Properties of the Spiral Photodiode

The Fianium SC450 supercontinuum white light source was used in the characterisation of the samples. It was coupled with the SuperChrome tunable filter to select the wavelengths used during the photoresponse measurements. A combination of polariser with half and quarter wave plates was used to produce and alter linear and circular polarisation states respectively. A Nikon CFI Plan Fluor 20x extremely long working distance objective (0.4 NA) was used to illuminate the entirety of each spiral photodiode. A polarisation insensitive 50:50 beam splitter was used to align the beam. The experimental set-up is shown in figure 4.6. A pair of custom transimpedance amplifiers were designed and fabricated by Mr. Evgeniy Panchenko to equally amplify the signal from each channel of the dif-

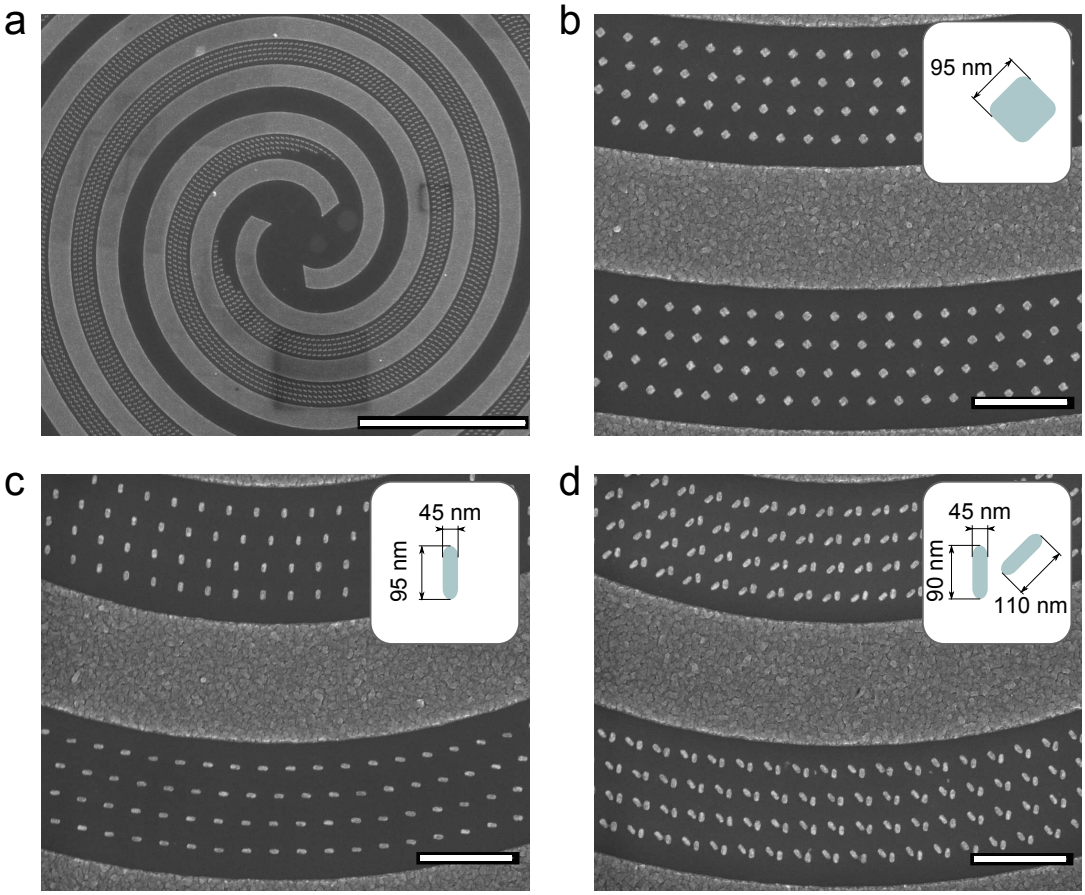


Figure 5.9: Scanning electron microscope image of the spiral photodetector (a). Nanoantennas are absent between two signal leads. The active regions with square (b), rectangular (c) and chiral (d) nanoantennas respectively. The scale bar for image (a) is 10 μm and 1 μm for images (b),(c),(d).

ferential photodetector. The amplification coefficient was fixed on both channels at 10^6. A Keithley 487 source meter was used for precision biasing of the MSM fingers. The voltage signal from each of the amplifiers was then collected by a National Instruments USB-6343 DAQ and recorded as a function of waveplate angle. The Keithley 487 source meter was also used to collect the I-V characteristics of each photodetector [94].

Figure 5.10 shows the device current as a function of applied bias voltage when the device is covered (black line) and exposed to the room lights (red line), which results in an order of magnitude increase in current. Typically the I-V characteristics of an MSM photodiode should be symmetric, however due to a defective bond, when positively biased there is less sensitivity than when under a negative bias. The inset of fig. 5.10 shows the photocurrent response of the

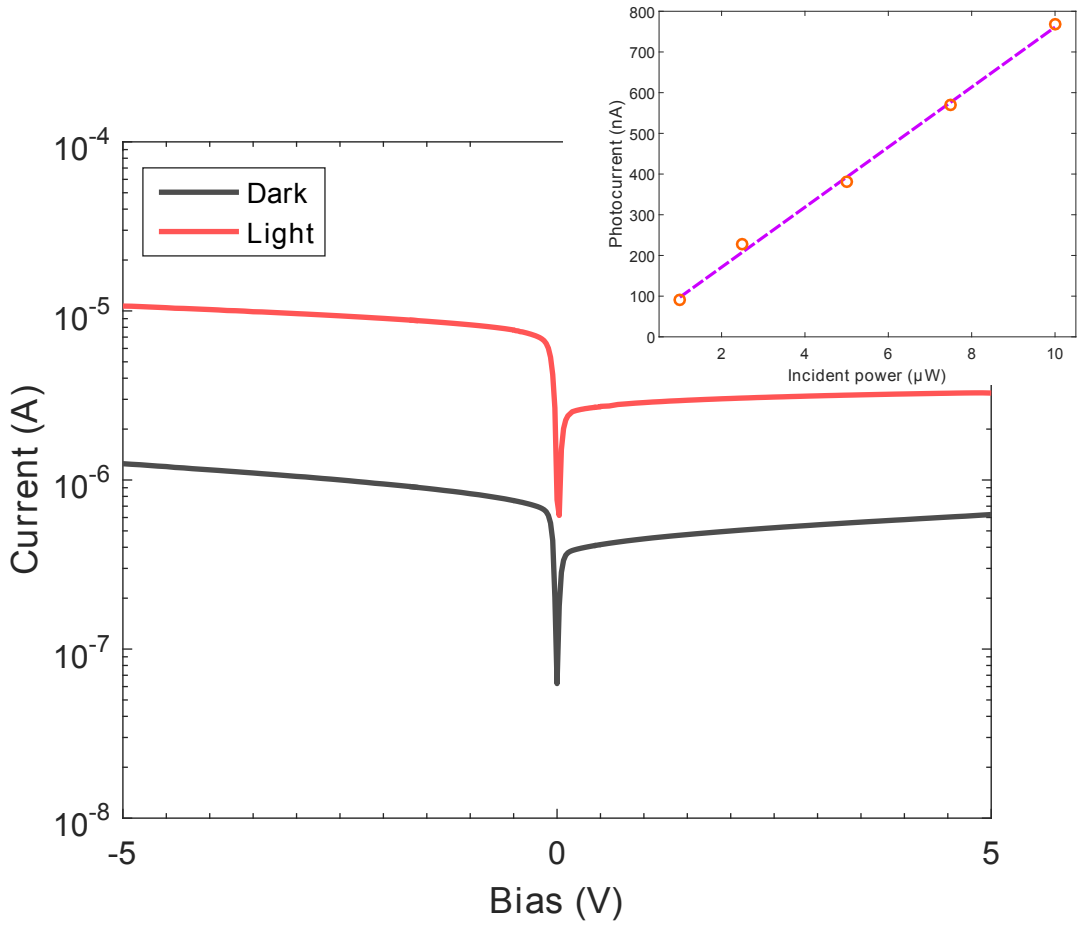


Figure 5.10: The current-voltage characteristics and power dependence (inset) of our MSM photodiode. The black I-V curve shows the dark current characteristics of the device, while the red curve shows the device performance with the room lights on, an order of magnitude increase in photocurrent.The inset shows the measured photocurrent for increasing 635 nm laser power.

device for -3V bias when illuminated with a 635 nm laser diode as a function of optical power. Here we see good device linearity and can deduce a responsivity at 635 nm of 80 mA/W, which is approximately an order of magnitude lower than state of the art MSM photodiodes [91].

5.4.6 Polarisation Sensitive Photodiode Performance

To determine the polarisation response of the photodetector we pass linearly polarised light at 45° to the principal axis of the photodiode is passed through a half waveplate (HWP) for the linear detector and through a quarter waveplate (QWP) for the circular detector. The photocurrent in each channel of the detectors is

measured as the waveplate rotates. This measurement is also performed on the control sample, with the square nanoantennas. Linearly polarised light passing through a half waveplate has its polarisation angle rotated 2θ where θ is the angle between the initial polarisation direction and the fast axis of the waveplate. This is represented by the orange line in fig. 5.11, where $S_{1,2,3}$ are the three Stokes parameters of the beam. For a linearly polarised beam passing through a quarter waveplate the situation is not so simple. To calculate the final polarisation state Jones calculus can be used. The Jones matrix, J for a QWP with fast axis oriented at θ relative to the horizontal axis can be calculated by

$$J = R(-\theta)J_{QWP}R(\theta) = e^{i\pi/4}\begin{bmatrix} \cos\theta^2 + i\sin\theta^2 & (1-i)\sin\theta\cos\theta \\ (1-i)\sin\theta\cos\theta & \sin\theta^2 + i\cos\theta^2 \end{bmatrix}, \qquad (5.24)$$

where $R(\theta)$ is the usual 2D rotation matrix and $J_{QWP} = e^{i\pi/4}\begin{bmatrix} 1 & 0 \\ 0 & i \end{bmatrix}$ [95]. We can then calculate the transmitted electric field, $\vec{E} = J\vec{J}$ (where $\vec{J} = \frac{1}{\sqrt{2}}\begin{bmatrix} 1 & 1 \end{bmatrix}^T$ is the Jones vector describing a linearly polarised beam at 45°) and from that determine the Stokes parameters (see §4.2.1 for further details). From the blue curve in fig. 5.11 we can see that as a QWP is rotated, the Stokes vector traces a 'figure 8' on the surface of the Poincaré sphere, passing from linearly polarised to RHCP back through *the same* linear polarisation state and then to LHCP. Importantly, if we project the Stokes vector path onto the S_1-S_2 plane (that is, the linearly polarised component) we see that this component oscillates between two points. These two points represent a linear component of $\pm 22.5°$, which as we have just seen in section 5.4.3 corresponds to the maximum scattering of linearly polarised light from each enantiomer of chiral nanoantenna. This will be important in understanding the differential signal measured from the chiral photodiode.

Figures 5.12(a-c) show the photocurrent measured for each polarisation sen-

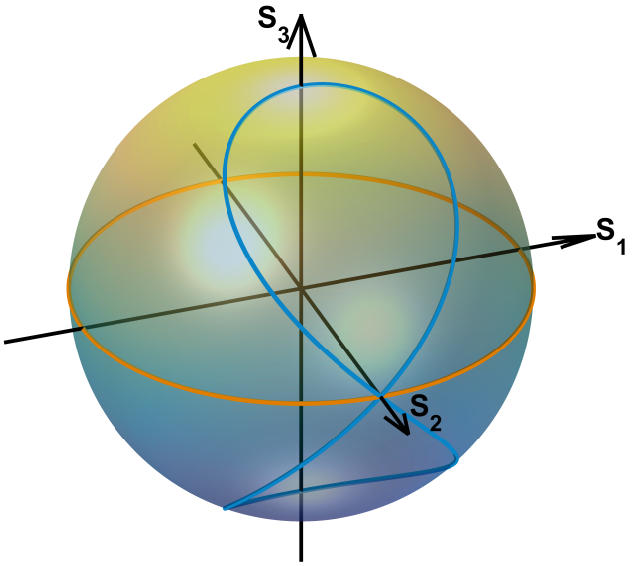


Figure 5.11: The incident polarisation state for a rotating waveplate (the blue line is for a QWP and the orange line is for a HWP) mapped onto the Poincaré Sphere. The curves depict the change in Stokes' vector for a 180° rotation of the waveplate.

sitive channel as a function of polarisation angle or QWP angle (c), with the respective nanoantenna design inset. Clearly there are random power fluctuations from the light source as well as an oscillatory signal due to the difference in transmission through the waveplates as they rotate due to Fresnel reflections. When taking the difference between each channel (figs. 5.12(d-f)) the noise is eliminated. This is the biggest advantage of differential signalling in data transfer, it is very robust to many types of noise. The linear photodetector follows Malus law as expected (fig. 5.12(d)), and allows for the determination of the degree of linear polarisation of a beam. The control sample (fig. 5.12(d)) shows no polarisation dependence as expected, whilst the chiral detector behaves as previously discussed, with maxima and minima in differential photocurrent corresponding to QWP angles of $\pm 22.5°$. Figures 5.12(g-j) show the differential photocurrent at important polarisations, (g) shows the photocurrent for polarisation along and across the nanorods in one channel and clearly show a change in polarity, whereas the square nanorods (i) show no significant change. Despite the chiral detector (j) response being dominated by a linear component, if the polarisation state is just switched between RHC and LHC a definite change in sign of the signal is present.

When used in conjunction with the linear detector (and another linear detector rotated 45°) it is possible to use the information provided by the chiral detector to recover the degree of circular polarisation of a beam.

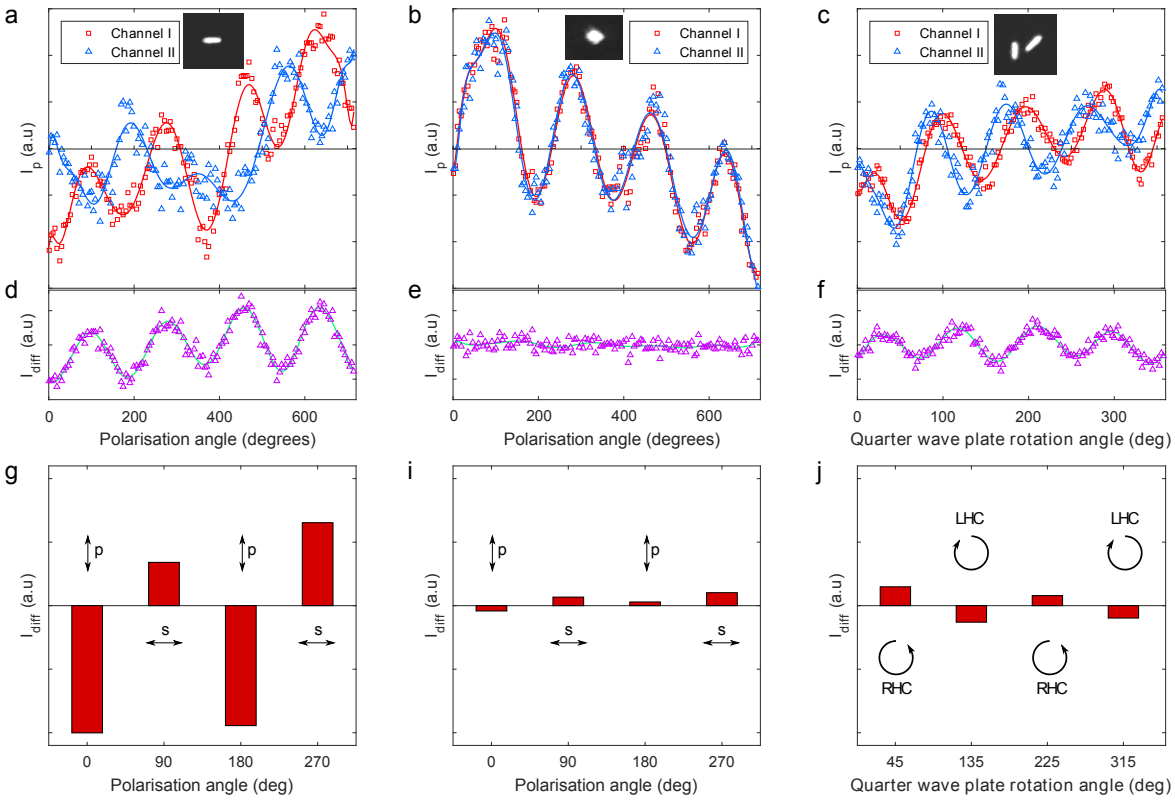


Figure 5.12: Normalised detected photocurrent for each channel of photodetectors with rectangular (a), square (b) and chiral (c) sets of nanoantennas (inset). As can be seen, the differential photocurrent of each photodetector (d),(e),(f) is not affected by power fluctuations in the raw signals. (g),(i) and (j) show the amplitude of the differential signal at each orthogonal state of polarisation, from which the degree of polarisation of the incident beam can be determined.

By examining the amplitude of the differential photocurrent for a range of wavelengths it is possible to determine the responsivity of our detector. To do so we perform the same polarisation rotation measurement for wavelengths from 500 nm to 800 nm in 25 nm steps with a linewidth of 10 nm. A power meter (Thorlabs PM100D with S150C) was used to ensure the optical power incident on the diode is equal for all wavelengths at 5 μW, varying the power using a variable ND filter (Thorlabs NDC-25-2) when required. Once again, a bias of -3V was

applied to the MSM diode. For each wavelength the difference between the maximum and minimum signal over the course of a full revolution of the waveplate is recorded. Figure 5.13 shows the differential responsivity of the linear photodetector, which is peaked at 650 nm, by design. The responsivity of the device is a combination of the absorption of photons in Si as a function of wavelength, the depth at which absorption occurs (as the MSM photodiode is a surface device, the electrons and holes could recombine if they are generated far enough below the surface that the applied bias has little effect) and of course the optical response of the nanoantennas. It seems the reflection spectra of the nanoantennas has the strongest effect here as Al antennas of this size on silicon have been shown to resonate at 700 nm [93]. To increase the dependence on the optical response of the nanoantenna a stronger resonance is needed. This could be achieved by employing a lower loss metal such as silver, isolating the antennas from the Si with an oxide layer so that longer antennas could be used or by simply increasing the packing density of the nanoantennas.

5.5 Summary

Three plasmonic nanoantenna based devices were investigated, with the aim of developing ultra-compact polarising elements, particularly for the generation of, filtering and detection of circularly polarised states. These devices could then be deployed in a plasmonic polarimeter.

A simple Lorentzian model was developed to design an ultra-thin plasmonic quarter-wave plate operational at optical wavelengths. One such design was fabricated in a 40 nm thin Ag film using focused ion beam lithography and full polarization tomography measurements were performed on this device. This device could be used in telecommunications technologies, new imaging systems and for bio-sensing applications.

Two dimensional planar chiral metasurfaces were investigated near resonance.

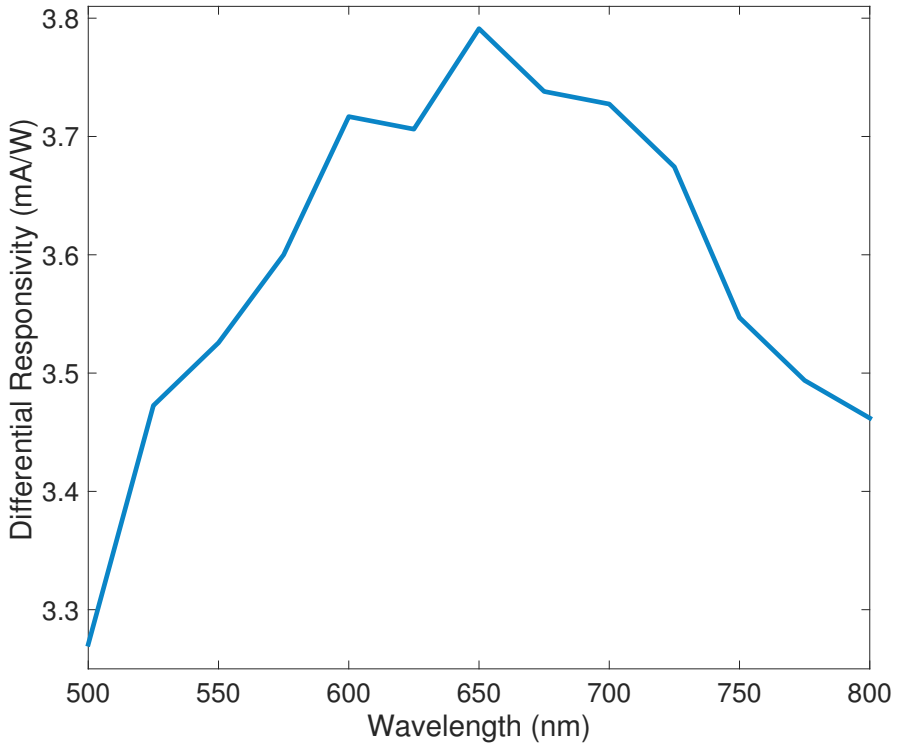


Figure 5.13: The amplitude of the difference in responsivity between each channel of the linear polarisation photodetector for x-polarised light as a function of wavelength. A -3V bias voltage was used and the optical power was kept fixed at 5 μW for each 10 nm linewidth range of wavelengths.

FEM calculations and experimental results show that chiral nanoholes exhibit a difference in transmission of circularly polarized light depending on the handedness of the incident field. Furthermore this effect is dependent on the relative angle of the LSP dipole modes of the metasurface. The device demonstrated here exhibited a 10% polarization contrast, which, according to FEM calculations could be increased to 18% with more precise FIB milling and use of single crystalline Ag films.

The differential MSM photodiode design presented here can be used to determine the polarisation state of an incident beam. The noise cancellation due to the differential nature of the device is useful for polarisation multiplexed telecommunications. The low Q-factor of the nanoantennas, which restricts the device sensitivity could be improved by using multiple lithography steps to place the nanoantennas on a lower refractive index dielectric or to allow the use of lower Ohmic loss materials such as silver [96].

Chapter 6

Scalable Fabrication of Nanocavities

6.1 Introduction

A pressing[1] issue in nanotechnology and especially nanophotonics is taking ideas from the laboratory and implementing them on the production line. As covered in the introductory chapters of this work, typical nanofabrication techniques such as electron beam lithography or focussed ion beam milling are costly, slow and therefore unsuited to industrial scale implementation. Here we investigate the application of a novel scalable nanofabrication technique to create optically driven resonant plasmonic nanocavities. The fabrication technique pursued is resistless nanoimprint lithography (RNIL, see §3.4.2), which requires no heating or cooling steps, reducing fabrication times, but still relies upon EBL to create the initial imprint master [17, 42]. Another potential upside is that one master can be cast and reused to imprint cavities of varying depths just by altering the applied pressure during imprinting [17]. Here we create single isolated nanocavities with RNIL and probe the parameter-space including the relationship between metal imprinted, applied pressure and resulting depth. The optical characteristics, including reflection, absorption and resonant wavelength, of the resulting cavities are then measured. From arrays of single cavities we then create nanocavity based metasurfaces, where the period is of the order of a wavelength or less,

[1] no pun intended

and demonstrate several applications of such arrays including, as a polarizing frequency selective surface or optical band-stop filter, as a colour pixel for printing [12] and as a simple refractive index sensor [97]. A general analysis and comparison of nanoapertures, nanocavities and perfect absorbers can be found in §2.5.

6.2 Creating Nanocavtites with RNIL: Effects of Applied Pressure and Material Choice

In this section the fabrication of nanocavities in silver, gold and aluminium films using RNIL is explored. A 100 mm [100] crystal orientation degenerately doped Si wafer is patterned using EBL and ICP-RIE. The etch mask used is 100 nm of HSQ and an etch chemistry of 30/5 sccm Cl_2/Ar is used to etch 160 nm deep nanofeatures. An anti-stick layer is applied to the Si master to aide master release after imprinting. An EVG 520S wafer bonder is used to perform the nanoimprint steps. A cycle time of 60s and various pressures are used. The thin metal films are prepared via electron beam evaporation. Figures 6.1 and 6.2 depicts the basic steps of this fabrication technique.

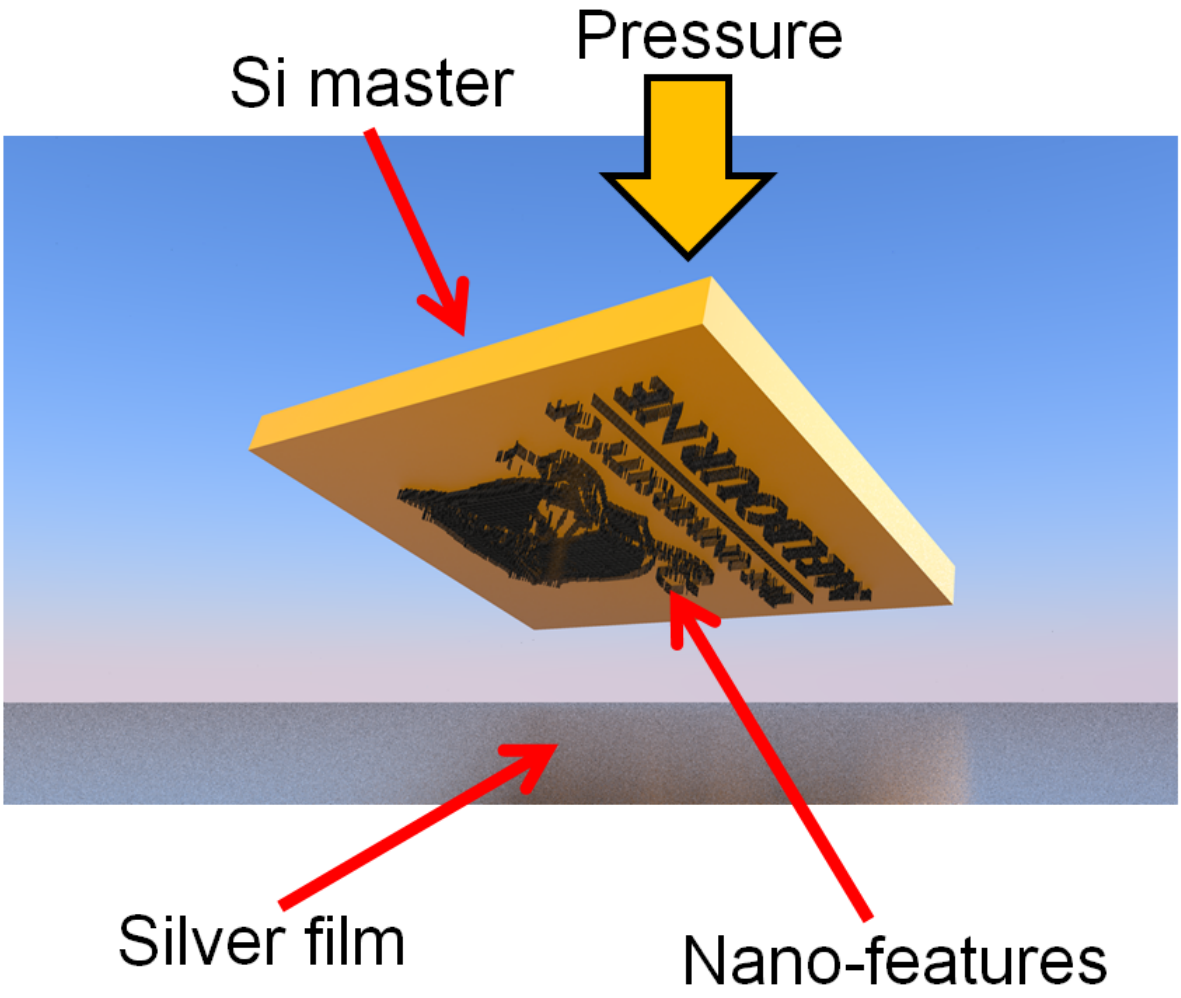


Figure 6.1: The RNIL process used here consists of lithogrpahic patterning of a Si master, then pressing the nanofeatures of the master into a metal film using a hydraulic press.

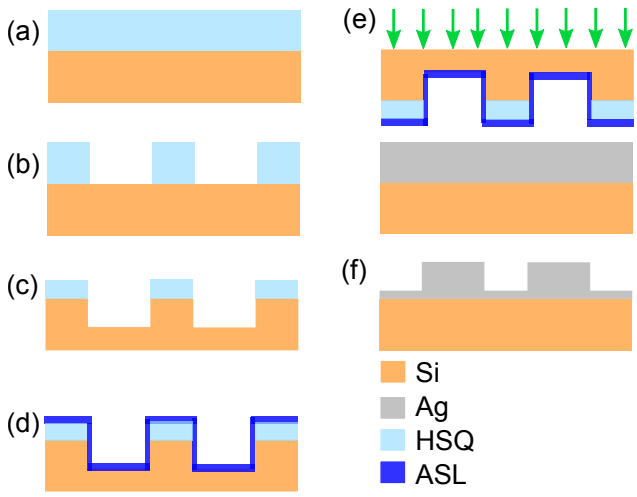


Figure 6.2: A depiction of the resistless nanoimprinting process. A 40 nm layer of HSQ is spun onto a silicon wafer (a), which is patterned using EBL (b) and etched using RIE (c), an anti-stick layer is applied to the master(d), then pressure is applied to force the master into into a silver film (e). The inverse pattern is now imprinted into the silver film (f).

The outcome of one imprint cycle (using the EVG 520S) tends to result in one of two outcomes: Either high fidelity reproduction of the master template in the metal film; albeit with some 'cast-off' or 'slag' around the edge of the cavities (as shown in fig.6.3); or with some degree, typically less than a micron, of multidirectional slippage, as shown in fig. 6.4. The increase in hydraulic force on the 520S during imprinting is performed in discrete steps, not in a continuous fashion, and this leads to the slip pattern showing multiple steps. The master will slip in one direction each time the force is increased, with the direction of slippage random for each step in pressure. The outcome of the imprint cycle is predicated on several factors including the amount of debris on the master and target film, the precise calibration of the 520S, any flexing of either the master or the substrate, the metallic crystal grain size of the evaporated films, as well as the presence of air pockets trapped between master and target. In the usual thermal or UV NIL process into polymer resists, slippage is not usually an issue as the resist is forced to conform around the mold features and tends to fill any gaps caused by slippage. In the case of imprinting directly into soft metal films the history of the contact between master and film is effectively recorded into the film. It should be noted that the single crystal Si wafers used here are 300-500 micron thick and will flex

under the forces applied during RNIL. The result of this is it is possible to have high fidelity imprints and slippage during the one imprint cycle for different parts of the wafer.

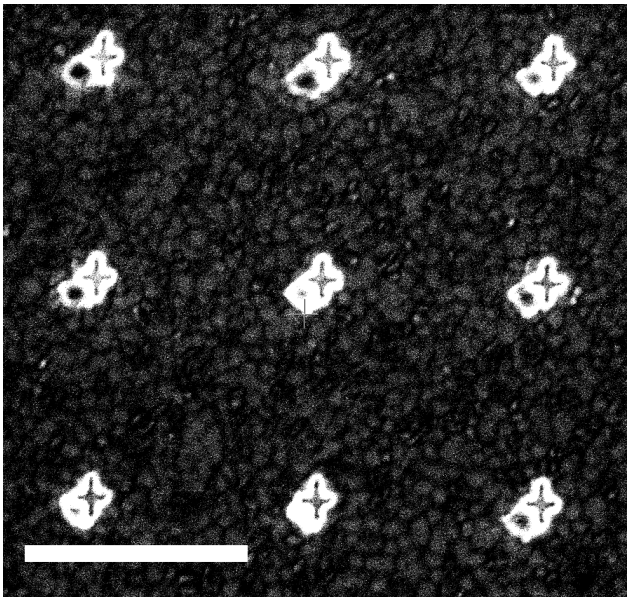


Figure 6.3: RNIL can be used to create complex shaped cavities: imprinted symmetric cross cavities in a 200 nm Au film. The scale bar is 1 μm and each cross arm is 120 nm by 40 nm. Excess metal from each cavity can be seen at the bottom left of each cross.

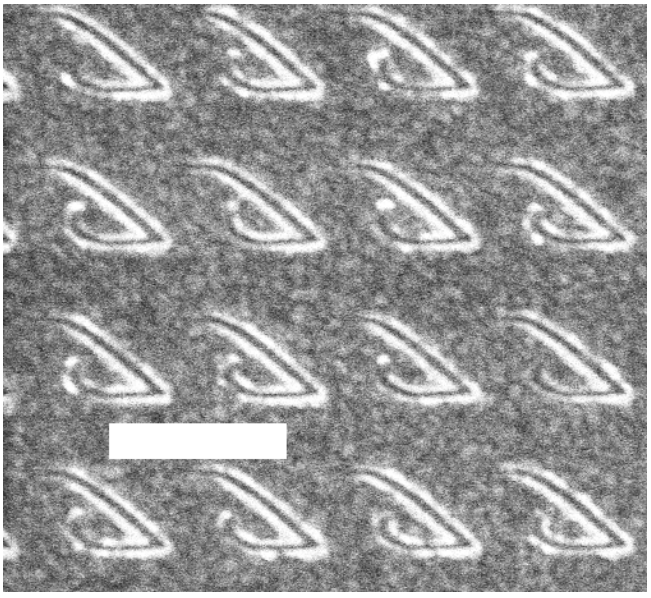


Figure 6.4: An example of slippage during the imprint process into a silver film. The master consisted of 50 nm x 50 nm (cross-section) squares, yet the resulting imprint is as shown. The scale bar is 300 nm.

Aside from imprint failures due to slippage, the other common mode of failure encountered was due to the material properties of the target film. Here the RNIL

properties of the important 'plasmonic metals': gold, silver, and aluminium are tested. Imprinting into thin Au and Ag films with a Si master posed no problems, in terms of required force, for the 520S, the typical force required was around 20 kN, half the 40 kN limit of the tool. Examples of imprinted Ag and Au films can be found throughout this chapter and the next (see for example fig. 6.3). Imprinting nanofeatures into Al films however, proved fruitless. It appears that a few nanometers of native oxide (Al_2O_3 is rated 9 on the Mohs hardness scale) is robust enough to distribute the applied force over a much greater area, even up to the embosser's 40 kN maximum output. Figure 6.5 shows an embossing attempt into a 200 nm Al film on a Si substrate using a 150 nm deep Si master, with a vacuum pressure of 5 mbar and imprint force of 40 kN, corresponding to an imprint pressure of 4.5 MPa. The inset shows a close up of one of the attempted nanocavities. Here it is clear the applied force is spread over an area larger than just the physical contact area between film and master. The depth of this feature is only 12 nm according to FIB-SEM measurements. The native oxide layer requires a greater force to penetrate than the tool is capable of, however once overcome, the imprinting of Al films should be as straightforward as that of Au and Ag films.

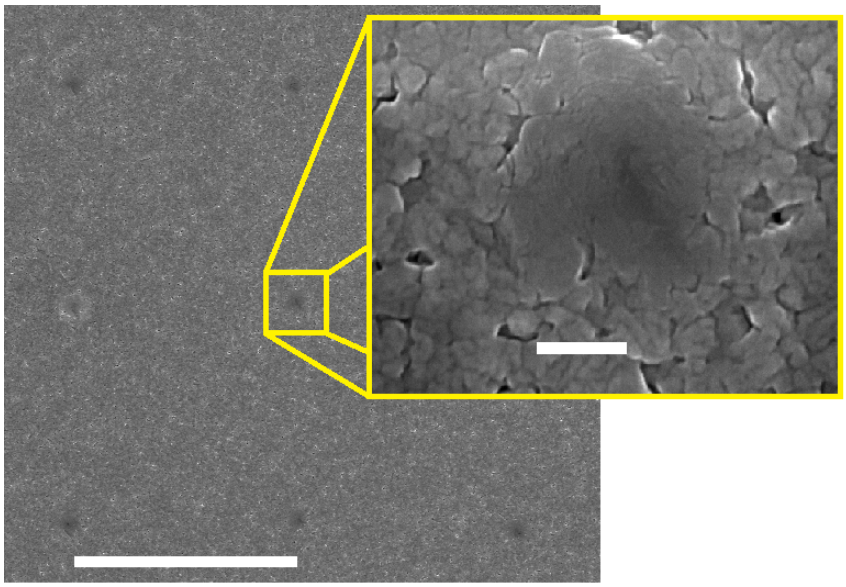


Figure 6.5: A failed attempt at imprinting nanocavities into Al. It appears the presence of the native oxide layer diffuses the applied force across a large area. The measured feature depth is only 12 nm. Large scale bar is 5 μm and 100 nm inset.

6.2.1 Imprint Pressure Determines Cavity Depth

In order to create complex nano-optical devices with resistless nanoimprint lithography it is important to build up a model of the imprinting process. To guide and calibrate our model we first assess the role of applied pressure during RNIL of single cavities in silver and gold films, two of the most important metals for plasmonic applications. A Si master, depicted in fig. 6.6, with nanorods 150 nm, 50 nm and 157 nm in length, width and height respectively, was created using the usual EBL and RIE process as described in §3.5. Each nanorod is separated by 5 μm from its nearest neighbours so that each resulting cavity can be individually addressed optically and array effects need not be considered when calculating the resonant wavelength. The etching process results in a slight sloping of the nanofeature sidewalls and the angle was measured to be 15° from vertical. The master was solvent cleaned of debris in an ultrasonic bath then the antistick layer was applied via spin coating and the excess ASL removed with liberal application of Novec 7100. Three metallic thin films were prepared via e-beam evaporation onto Si substrates; a 200 nm Ag film, a 200 nm Au film and a 90 nm Au film. The purpose of the 90 nm film was to investigate the case where the master's features are taller than the target film thickness. The master and metal substrates were then diced into 1 cm $\times$ 1 cm square pieces using a DISCO DAD321 wet dicing saw. This was done to reduce long range flexing of the master during imprinting and to save on cost, should the master break during the imprint process.

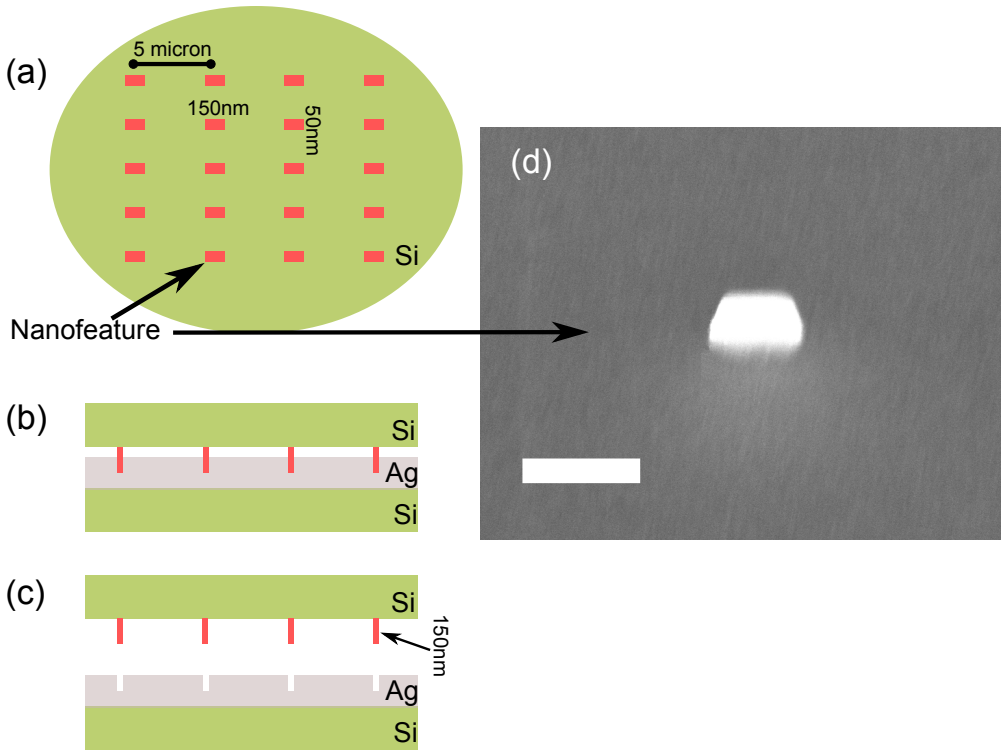


Figure 6.6: (a) The layout of the master used to create single nanocavities, each nanofeature is 5 μm apart and has cross-sectional dimensions of 150 nm by 50 nm. The features cover an entire 4" wafer. (b) and (C) The master is stamped into a thin metal film, either gold or silver and nanocavities created. The nanofeatures are 150 nm high and the cavity depth depends on the applied pressure. (d) A SEM image of one of the nanofeatures, taken at a tilt angle of $45°$, the scale bar is 200 nm and the measured height is 157 nm.

On the nanoscopic scale, the process of imprinting nanofeatures into metal films is closely related to the material hardness test known as nanoindentation [98]. Here a hard tip is pressed into the material under investigation and the resulting indent dimensions can give important mechanical properties of the material. Typically the resulting indent will be compared to a particular deformation model in order to determine properties such as the Young's modulus of plastic deformation, Y_p [99]. For ultrathin polycrystalline films typically sophisticated simulations involving a large number of dynamic points representing the position and velocity of rigid crystal grains which comprise the metal film are used. The process involves estimating the probability of crystal grains slipping past each other for a given stress, that depends on the microscopic properties of the film such as grain size and the forces between grains and even the shape and orientation of the grains. From these Monte-Carlo simulations and the measured indent

dimensions it is possible to determine the material parameters [100]. A simple working model of plastic deformation can be derived by relating the engineering strain $\varepsilon_E = \frac{\sigma_E}{Y_p}$ (where $\sigma_E = \frac{F}{A}$, F is the applied force and A is the original cross sectional contact area of the master and substrate) and the true strain, $\varepsilon_T = \frac{d}{h}$ (where d is the imprint depth and h is the original film thickness) [101],

$$\varepsilon_T = \ln(1 + \varepsilon_E). \tag{6.1}$$

Making the relevant substitutions and rearranging (6.1) yields

$$d = h \ln(1 + \frac{F}{Y_p A}), \tag{6.2}$$

where Y_p, which depends on the microscopic details of the film, can be used as a fit parameter to find the relationship between pressure and depth for each gold or silver film.

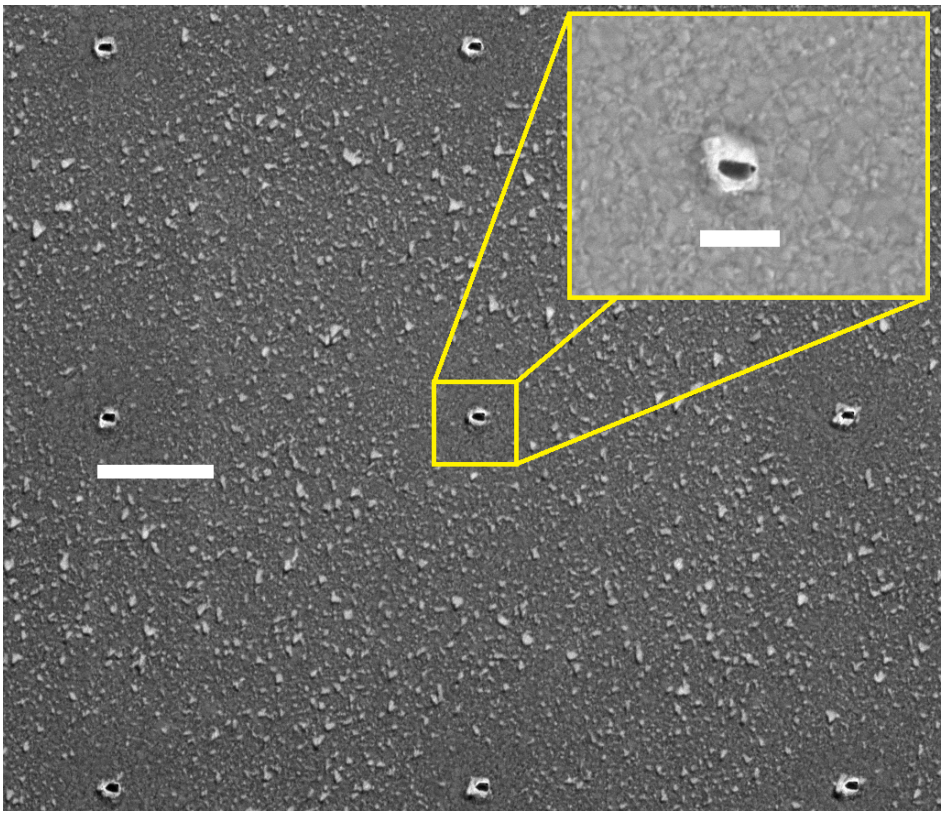


Figure 6.7: A nanoimprinted 200 nm gold film, here the cavities are 120 nm deep. The scale bar is 1 μm. A close up of a single nanocavity, scale bar 200 nm (inset).

Figure 6.7 shows an example of the single nanocavities studied in this section. The cavity entrance cross sectional shape is not quite rectangular due to the shape base of the nanofeatures of the master. The deformity is introduced during the RIE etching step. This deformation however, will not adversely affect the experiment as it is repeated for each cavity. The SEM image also indicates that there was no slippage between master and target substrate during imprinting and the nanofeatures were normal to the film surface as the metal cast-off around each cavity is distributed symmetrically.

Figure 6.8 shows the measured depth of imprinted single nanocavities as ascertained by FIB milling of 200 nm thick silver films. The silver dashed line represents the maximum possible imprint depth (157 nm, the height of the nanofeatures), the blue triangles are the depth measurements of the cavities prepared with particular imprint pressure and the blue dashed line is a line of best fit based upon equation 6.2. The film thickness, h is 200 nm, the contact area is $A = 150 \times 50 \times (\frac{10^4}{5})^2 = 3\ \mu\text{m}^2$ and the Young's modulus of plastic deformation, Y_p for this particular film is 2.24 MPa. The maximum depth of nanocavities in this silver film appears to be limited to around 125 nm, leaving 75 nm of silver at the bottom of the cavity, much more than the skin depth of silver at optical frequencies.

Figure 6.9 shows the same depth measurements for the two different sets of gold film samples. Figure 6.9(a) shows the experimental results for a 200 nm gold film, which appears to be more easily deformed than the silver films of the same initial thickness and has $Y_p = 1.63$ MPa. Again the imprint depth seems limited to around 120 nm on this embossing tool, but in contrast to the silver films the range of cavity depths achievable is reduced, due to the lower Young's modulus of plastic deformation. To increase the imprintable cavity depths a thinner film of gold (90 nm) was prepared on a silicon substrate. By reducing the initial thick-

ness, h, to below the height of the master's nanofeatures, the final cavity imprint depth, d, is also reduced.

Figure 6.9(b) shows the results of imprinting into an ultra thin film. First it should be noted that this type of imprinting lead to greater damage and higher losses of the silicon masters as well as target substrates, however the gold nanocavities in this case exhibited an only slightly increased value for Y_p of 1.77 MPa. The maximum depth achieved during imprinting was limited to around 55 nm, which still leaves 35 nm of gold at the bottom of the cavity, still greater than the skin depth at optical frequencies. Interestingly, these results show that by selecting the initial thickness of the target film it is possible to increase the range of cavity depths attainable. It also shows that as the cavity depth approaches the initial film thickness this simple model breaks down and we would need to account for the presence of the supporting substrate and its effects on the local Young's modulus of plastic deformation.

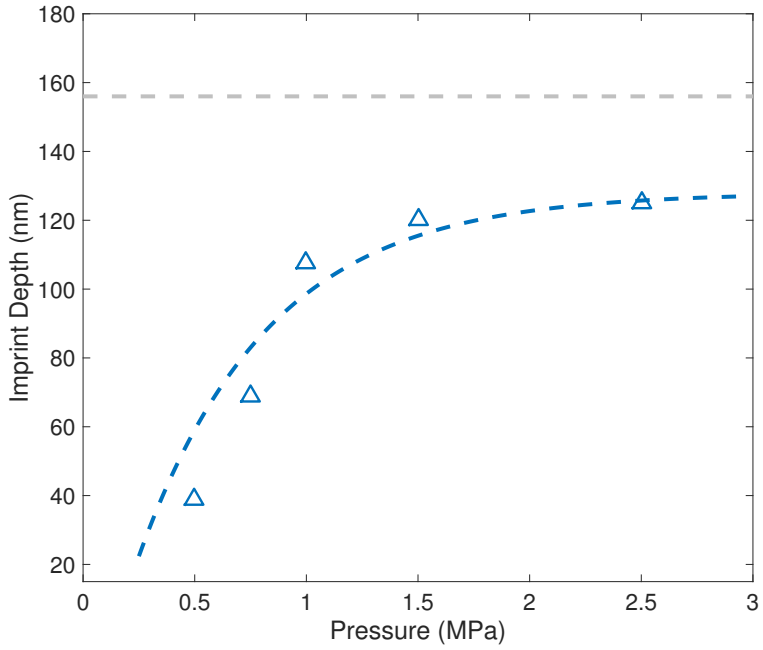
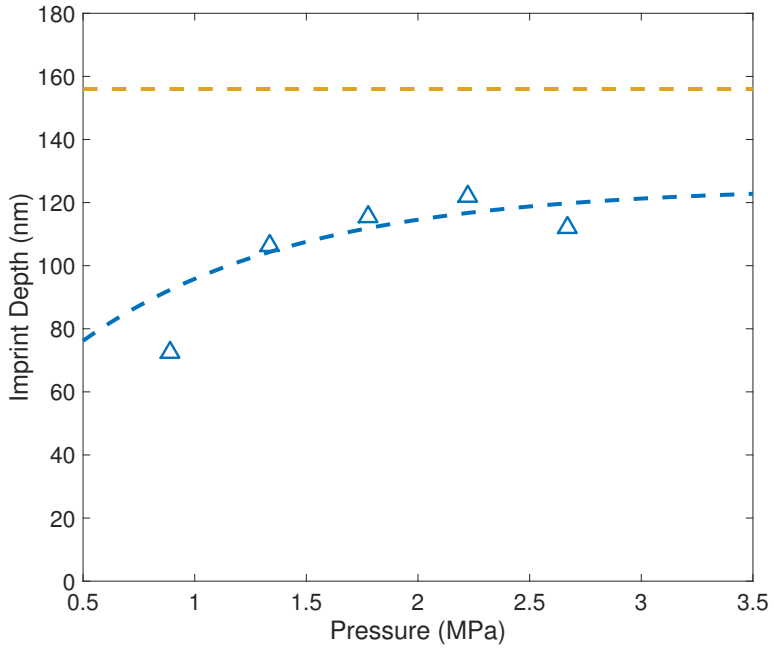
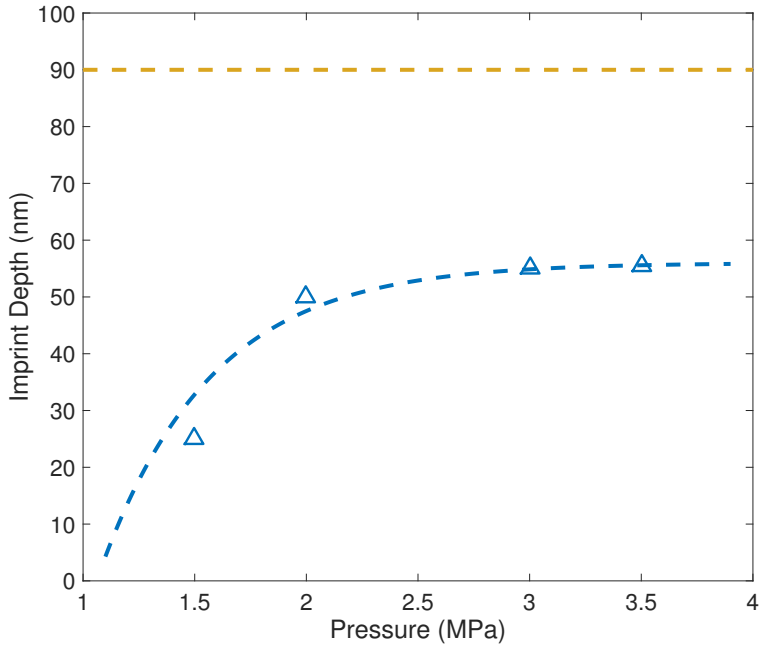


Figure 6.8: Imprint depth for 5 different applied pressures (triangles) for a 200 nm Ag film on a Si substrate. The silver dashed line is the maximum possible depth (157 nm, the height of the master). The blue dashed line is $d(P, 200; Ag)$, a logarithmic line of best fit.



(a)



(b)

Figure 6.9: Imprint depth for 5 different applied pressures (triangles) for a 200 nm (a) and a 90 nm (b) Au film on a Si substrate. The gold dashed lines are the maximum possible depth ((a) 157 nm, the height of the master and (b) 90 nm, the thickness of the film). The blue dashed lines are (a) $d(P, 200; Au)$ and (b) $d(P, 90; Au)$, logarithmic lines of best fit.

6.3 The Optical Properties of Scalable Plasmonic Nanocavities

To determine the range of the optical response of single nanocavities in gold and silver films fabricated using RNIL, absorption spectrocopy was performed using a CytoVita Hyperspectral microscope. A 100x 1.3 NA oil immersion Nikon lens was used with 1.44 refractive index matching oil covering the sample. The oil not only allows for a large numerical aperture, to capture all the possible scattered and diffracted light, but also red-shifts the cavity resonance towards the middle of the visible spectrum. This is desirable as the light source has a far greater intensity here than at shorter wavelengths and the detector is more sensitive at these wavelengths, which makes capturing single cavity spectra easier. The oil also simulates the effects of a thin transparent encapsulation layer which is commonly used to passivate devices or the effect of a biological cell. In order to reduce the noise and reduce the effect of slight cavity-to-cavity differences the absorption spectra are taken to be the average of 10 spectra from 10 individual cavities, each imprint pressure and for each film type (200 nm Ag, 200 nm Au and 90 nm Au).

The absorption[2] spectra for single silver nanocavities for a variety of imprint pressures is shown in figure 6.10. Here the resonance can be seen to increase in both amplitude and wavelength as increasing pressure is used for embossing. Figure 6.11 shows the experimental results for the 90 nm gold film (a) and the 200 nm gold film (b). The same general trend is observed in both cases where increased imprint leads to red-shifted resonances. The gold cavities absorb up to 40% of the incident light, whereas the silver cavities only reach 25% absorbance.

[2] strictly speaking, 1-R

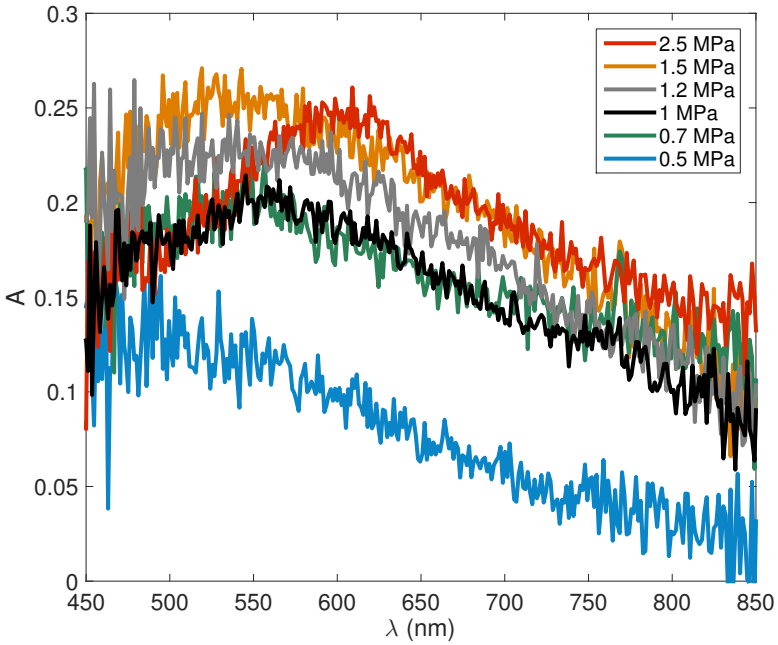
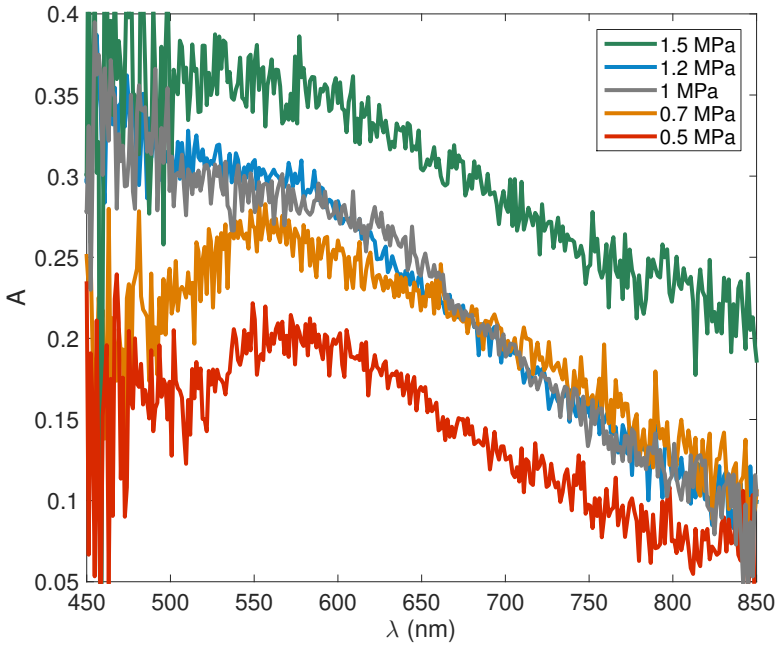


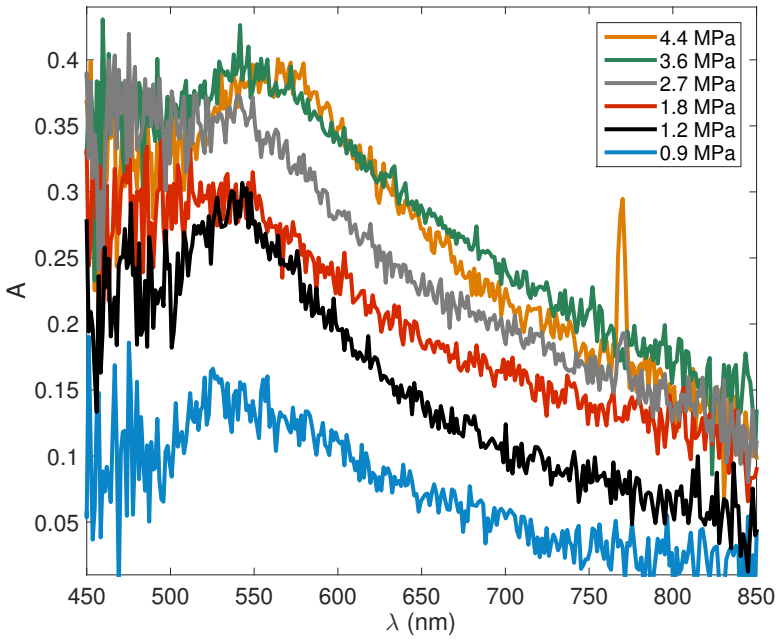
Figure 6.10: Single nanocavity absorption spectra for varied applied imprint pressure in a 200 nm thin Ag film on a Si substrate.

6.3.1 Cavity Depth Determines Resonant Wavelength

Equation (6.2) can be combined with the Fabry-Perot (FP) resonance condition (2.11) and the MIM waveguide dispersion relation(2.8) to find a relationship between the applied imprint pressure and the resulting resonant wavelength of the cavities. The utility of this as a scalable technique for the fabrication of plasmonic metasurfaces should not be overlooked. It allows for post master fabrication tuning of the metasurface response as required, just by adjusting the applied imprint pressure or the initial film thickness. Figure 6.12 shows a summary of the effect of the imprint pressure used during RNIL on the optical response of single nanocavities. The peak wavelength and absorbance for various imprint pressures is shown for a 200 nm silver film, as well as 90 nm and 200 nm thick gold films. Evidently the absorption peak red-shifts with increasing imprint pressure, in accordance with the increasing cavity depth. The silver film sample showed the greatest optical range from 480 nm to 610 nm, a large section of the visible spectrum. The colours in this case however, were underwhelming as the absorption



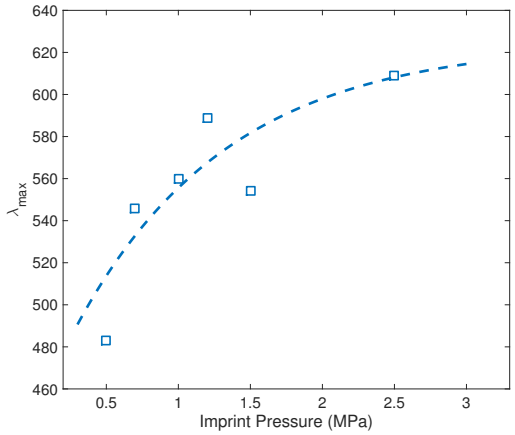
(a) 90 nm Au film



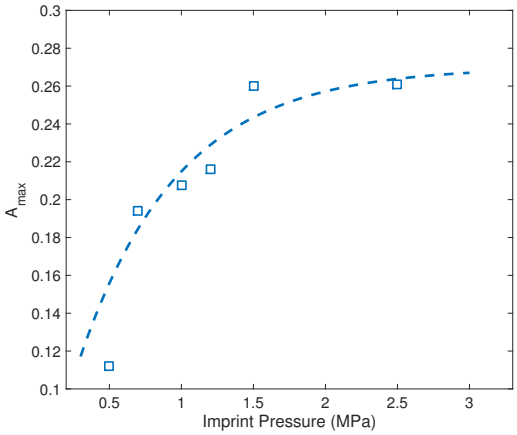
(b) 180 nm Au film

Figure 6.11: Single nanocavity absorption spectra for varied applied imprint pressure in a 90 nm Au film (a)and a 180 nm thin Au film (b) on Si substrates.

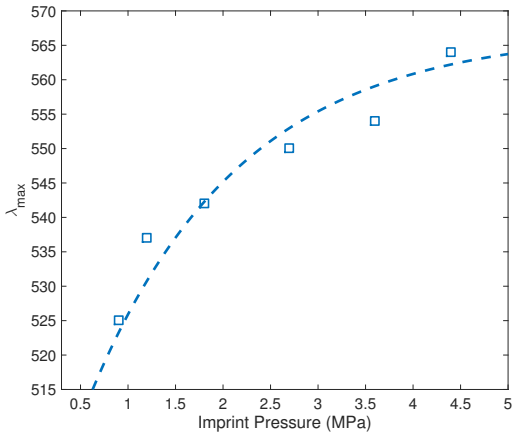
ranges from only 0.12 to 0.26. This suggests the spectral overlap between the MIM waveguide mode and the FP mode is suboptimal. Either deeper imprinting or higher refractive index oil could improve the spectral overlap. The gold films showed a limited spectral range from 520 nm to 580 nm, due in part to the lower variance in depth with pressure found for the gold samples. The gold samples did however exhibit a large maximum value of absorption, ranging from 0.15 to 0.4, which can be attributed to the increased losses in gold around these frequencies due to the interband transition in the metal. The results summarized in figure 6.12 show that RNIL has potential for the scalable creation of optical nanocavities in thin metal films, with the added bonus of modifying the optical properties of the fabricated devices with no expensive refabrication steps, but simply by adjusting the film thickness and the pressure used. The model used here gives a useful 'ball-park' estimation of the cavity resonant wavelength during the master design phase, for industrial applications, a calibration run of various pressures would be required for each unique master before committing to a large imprinting project.



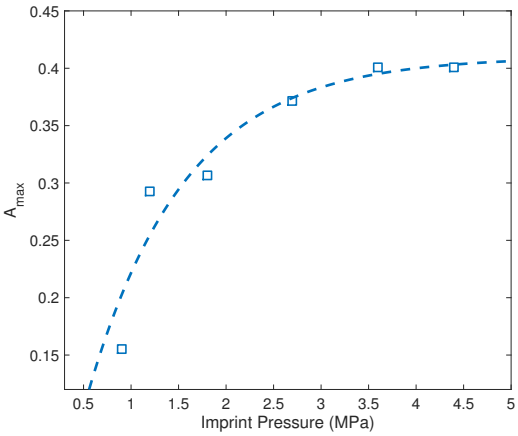
(a) 200 nm Ag film.



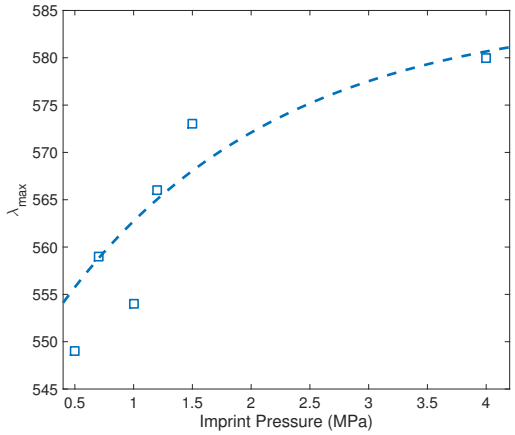
(b) 200 nm Ag film.



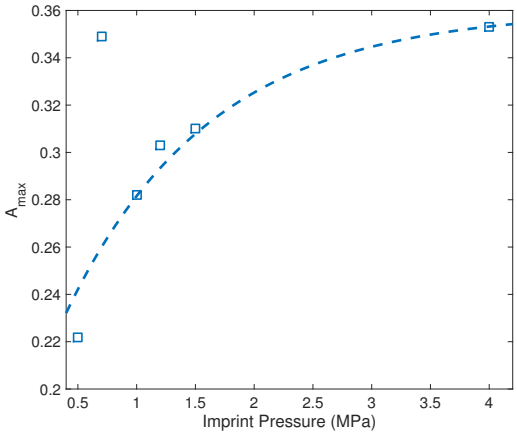
(c) 90 nm Au film.



(d) 90 nm Au film.



(e) 200 nm Au film.



(f) 200 nm Au film.

Figure 6.12: Peak absorption wavelengths of nanocavities as a function of the applied imprint pressure (a)(c)(e). Maximum absorption of nanocavities as a function of the applied imprint pressure (b)(d)(f). The dashed lines are logarithmic lines of best fit to guide the eye.

6.4 Nanocavity Arrays as Optical Elements

An understanding of the relevant physics at play was gained in the previous section by studying the optical response of single nanocavities produced via RNIL. By considering only single cavity diffractive effects, Bloch wave (SPP) and cavity-cavity coupling effects were suppressed as well as simplifying the mechanical model developed for the imprint process [102]. To increase the visibility of an RNIL based feature dense arrays of nanocavities should be used, where the spacing of cavities is on the order of or less than a wavelength. In this case the array can be considered a metasurface and provide a strong optical response as well as form high resolution printed images.

The aim of the following section is to demonstrate coverage of large areas with nanocavities is feasible and requires no extra imprinting time using RNIL, as well as to demonstrate a strong polarisation response, which can form the basis for metasurface based optical elements such as a polarising bandstop filter. In addition colourful, high resolution images are imprinted directly into gold and silver films and these arrays are shown to act as local refractive index sensing substrates.

6.4.1 Large Area Arrays

The production of a silicon master covered with square centimetres of nanofeatures is a very time consuming task, the initial step requires 10s of hours of electron beam lithography which makes it prohibitively expensive to produce very large area prototype masters. However it is important to demonstrate the large scale capabilities of RNIL and to probe the effect of long range flexing of the master during imprinting. To that end a 70 mm x 70 mm area of a [100] Si wafer was patterned with 200 nm x 50 nm nanorods with a 5 μm pitch. HSQ was once again used as an RIE etch mask and the features were etched to 150 nm in height. The master was then solvent cleaned and treated with an anti-sticking layer. The total

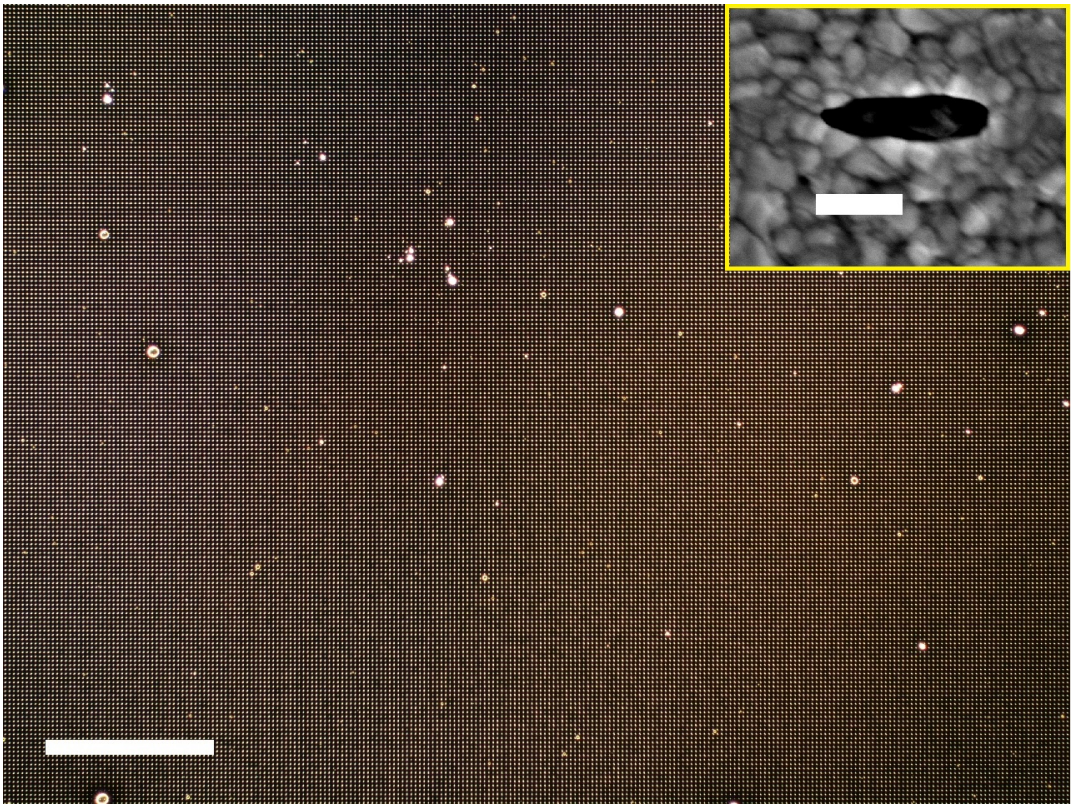


Figure 6.13: A large area array of nanocavities (see inset) imprinted into a silver film. The scale bar is 200 μm and 100 nm in the inset. The total area imprinted was 4900 mm^2.

lithography time was 13 hours. To reduce the destructive effects of master slippage and long range flexing of the master (see figure 6.4) a 5 mm thick Ti plate was used to help provide rigidity and two graphite pads were used to absorb the initial jerk force applied by the EVG 520S Hot Embosser. Figure 6.13 shows a low magnification (20x) dark field microscope image of a 200 nm Ag film embossed at 3.2 MPa of pressure. As can been seen the imprint covers a large area with very good uniformity and as the SEM inset shows, good fidelity of pattern replication. The total imprinted area was 4900 mm^2, which is much larger than the typical security feature or components found in the typical optics laboratory.

6.4.2 Scalable Polarising Frequency Selective Metasurfaces

The nanocavities fabricated to demonstrate the very large area imprint capabilities of RNIL in the previous subsection are highly anisotropic, which leads to a strong preference for a particular linear polarisation state at the cavity resonance wave-

length. As previously discussed polarisation control is highly desirable for optical components in general and in particular for creating pixles for lithographs [12]. A Python script was developed to turn bitmap images into GDSii files which can then be used with electron beam lithography and RNIL to produce iconographic meta-surface polarising arrays operating in the visible spectrum. Figure 6.14 shows a silicon master comprised of 200 nm x 50 nm nanorods, etched to a depth of 150 nm, arranged in the shape of The University of Melbourne's crest, with a 300 nm array spacing. The regions with fine detail, such as Victory's wings and the text, consist of only a few nanorods. The master was embossed at room temperature, with a pressure of 3.5 MPa, under a 5 mbar vacuum, into a 200 nm silver film on a silicon substrate.

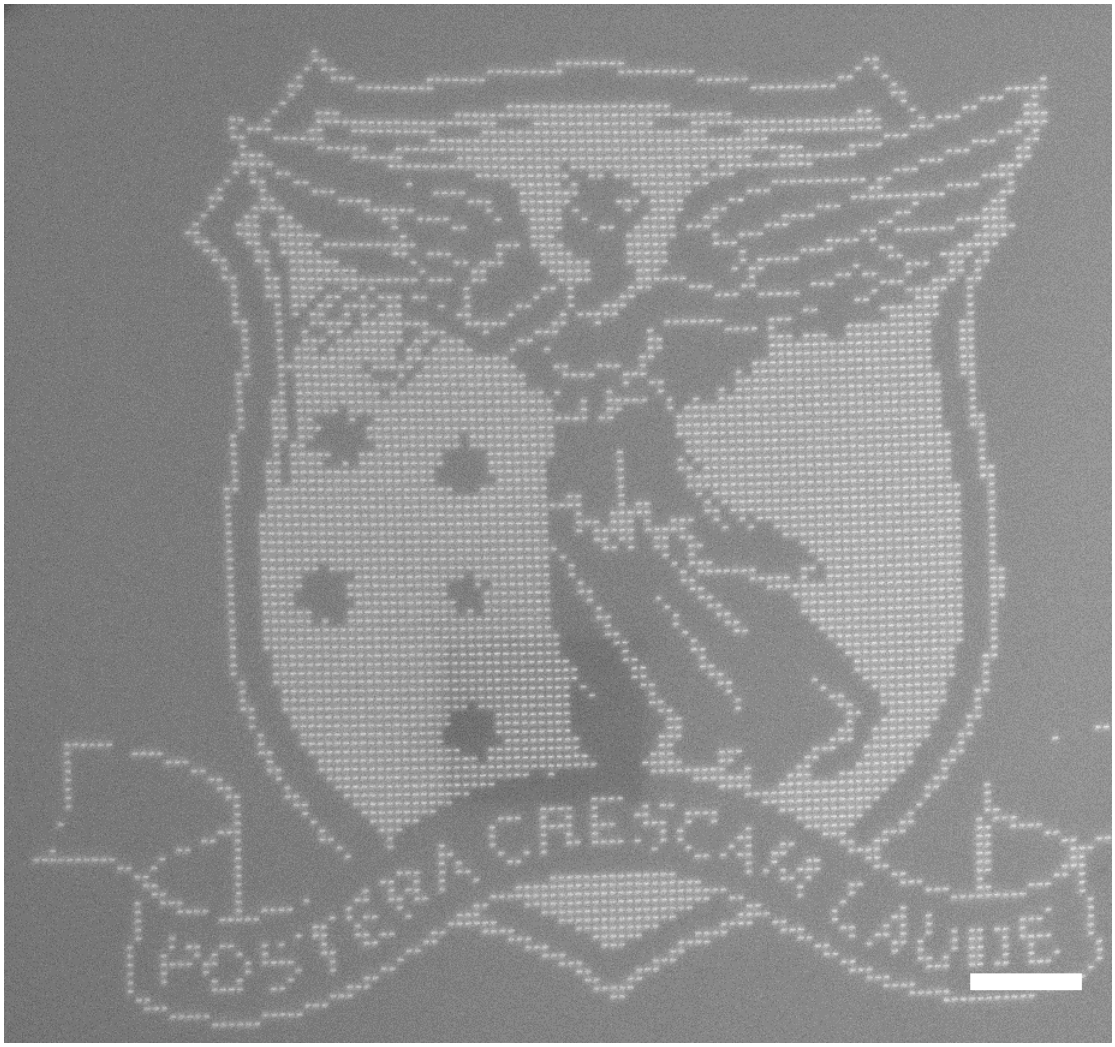


Figure 6.14: An SEM image of a HSQ/Si master template, consisting of a structured array of 200 nm by 50 nm nanorods. The white scale bar is 5 μm. The image has been reversed.

Figure 6.15 shows the imprinted pattern in the silver film, here the cavities are faithfully reproduced across the patterned area, including the fine details. Figure 6.16 shows an atomic force microscope (AFM) trace across the short axis of the nanocavities, it can be seen that the cavities are slightly wider than the master, at around 70 nm are in fact, 300 nm apart and around 50 nm deep. The excessive metal cast off can also be seen at the opening of each cavity. The reduction in imprint depth comes from the higher density of nanofeatures, as this template design is far from the single cavity limit. In this case the Young's modulus of plastic deformation is estimated (as there is only one data point) to be 3.15 MPa, 40% higher than the comparable single cavity case.



Figure 6.15: An SEM image of the imprint in a silver film produced using the master shown in Fig. 6.14. Note the fine details are made up of only a few nanocavities. The white scale bar is 5 μm

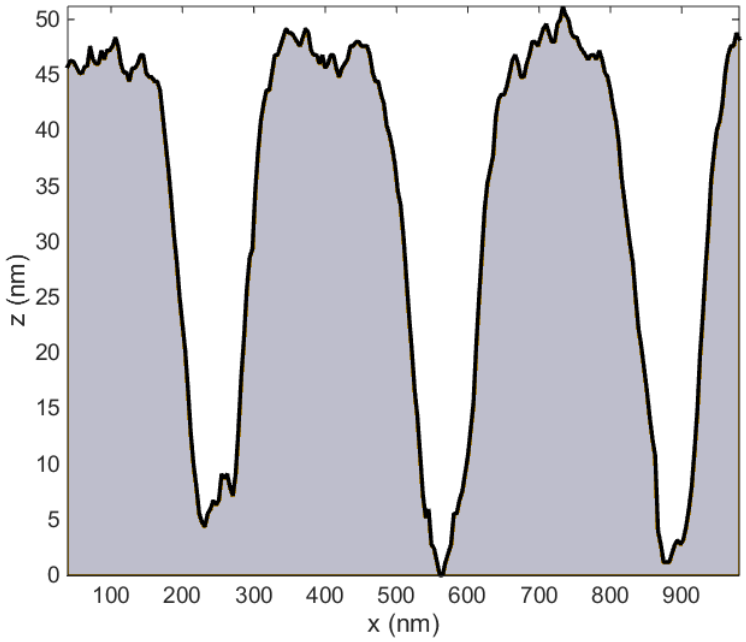


Figure 6.16: AFM trace of the nanoimprinted cavity array in a 200 nm Ag film. The imprint depth is 45 nm, including the pile up of excess metal at the cavity opening.

Polarisation Response of the Metasurface

Absorptive polarisation devices are typically characterised by their polarisation extinction ratio (PER), which is the ratio of the reflection of one linear polarisation state to the other, in this case the square of the electric field component perpendicular to the long axis of each cavity to the component parallel (ratio of reflection of TM to TE excitation) [43]. The PER of the University crest array was measured using a Fianium 450SC light source, 100x 1.3 NA Nikon oil immersion objective, 1.48 refractive index matching oil, an Andor Solis 303i cooled spectrograph and Thorlabs LP050-VISA linear polariser. The results are shown in figure 6.17. It can be seen that the extinction ratio at resonance is better than one decade between polarisation states at a wavelength of 660 nm. It can also be seen that the full width at half maximum (FWHM) is 80 nm, with no substantial polarisation effect outside of the region 550 nm to 730 nm.

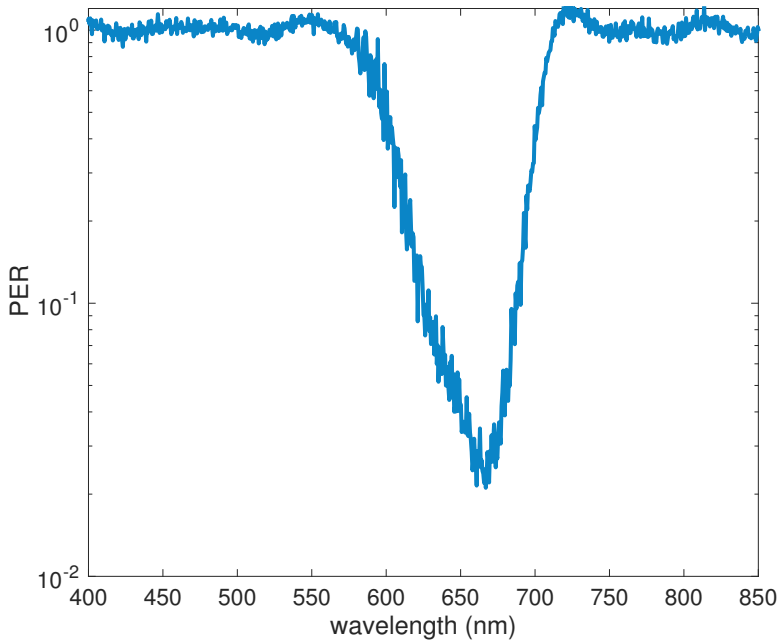


Figure 6.17: Polarisation extinction ratio (PER) of the nanoimprinted metasurface shown in Fig. 6.18(a) at normal incidence.



(a) **(b)**

Figure 6.18: Darkfield microscope images of the University Crest metasurface imprinted into a thin silver film (a) and the MCN logo metasurface imprinted into a thin silver film (b). The nanocavities comprising the metasurfaces are the same dimensions.

Dark Field Scattering Images

When the nanocavities are excited and viewed under bright field conditions they act as absorptive spectral (and polarisation) filters. When illuminated and observed with a dark field microscope the nanocavities selectively scatter light at the cavity resonance wavelength, this is a direct result of the Optical Theorem [1].

Figure 6.18 shows two dark field images of the University crest (a) in a silver film coated with PMMA ($n = 1.5$) and the Melbourne Centre for Nanofabrication (b) in silver without a superstrate encapsulation layer. It is clear from 6.18 that there is a strong colour response exhibited by these dense nanocavity arrays, in addition to the strong polarisation response. This response can be tuned to fabricate vibrant security features with both covert and overt properties, even after the fabrication of a master shim just by adjusting the pressure used during the imprinting step.

6.4.3 Refractive Index Sensing Substrates

Besides tuning the spectral response through the application of pressure during the embossing step, it is possible to alter the absorption proprieties of a nanocavity based metasurface by applying a superstrate of a particular refractive index. This is due to the fact that both MIM waveguide gap plasmons and Fabry-Perot cavities are sensitive to the refractive index of the surrounding media, such as passivation layers [44]. Refractive index sensing is also important in bioscience as many components of cells are transparent [103–105]. A scalable, low cost, refractive index sensitive, microscope slide would be a very useful addition to the bioscience arsenal. Figure 6.19 shows a refractive index sensitive metasurface fabricated via RNIL of a 200 nm gold film. The dark field image shows two distinct regions, a green-yellow region where nanocavities scatter light in air and a red region, where the nanocavities are covered with a small drop of water ($n = 1.33$). The water droplet simulates a live cell. Since we know the nanocavity spacing in this case is 2.5 μm we can use that to measure the size of the cell just by counting the red dots in a dark field microscope image, a task which is easily digitized [106]. Potentially this could be used to test how different treatments affect the growth rate of certain cells [107].

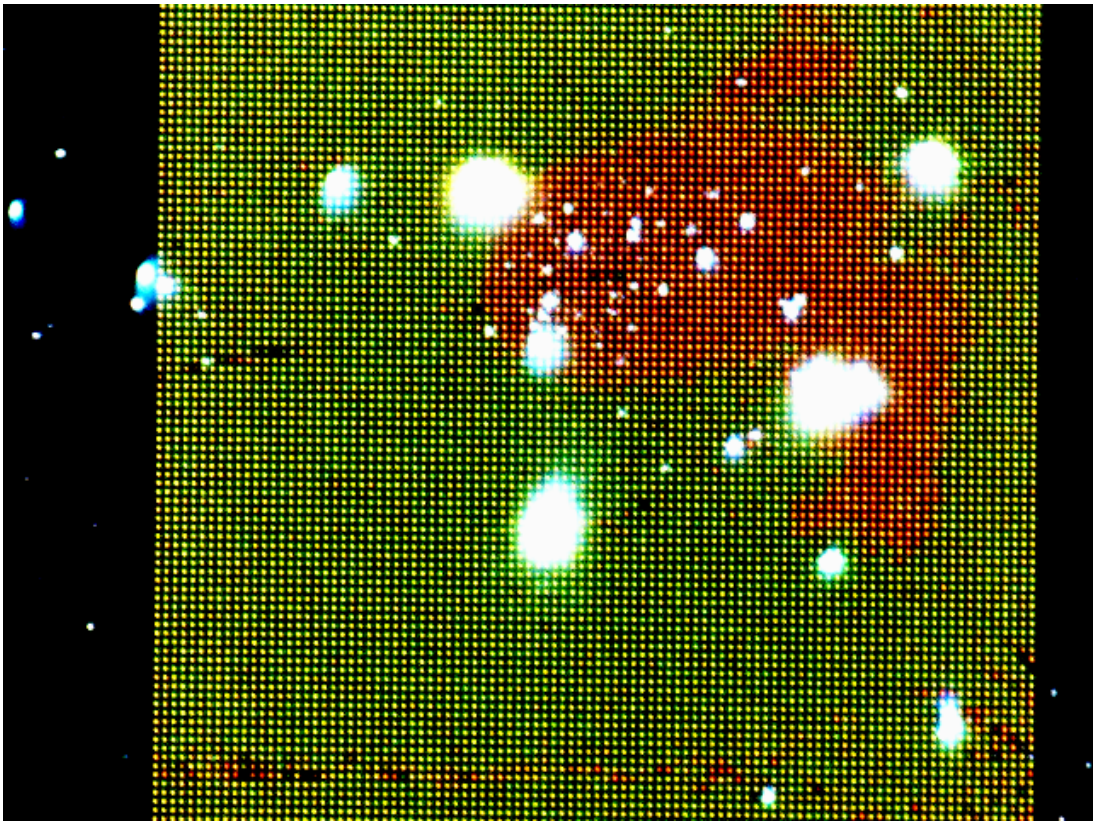
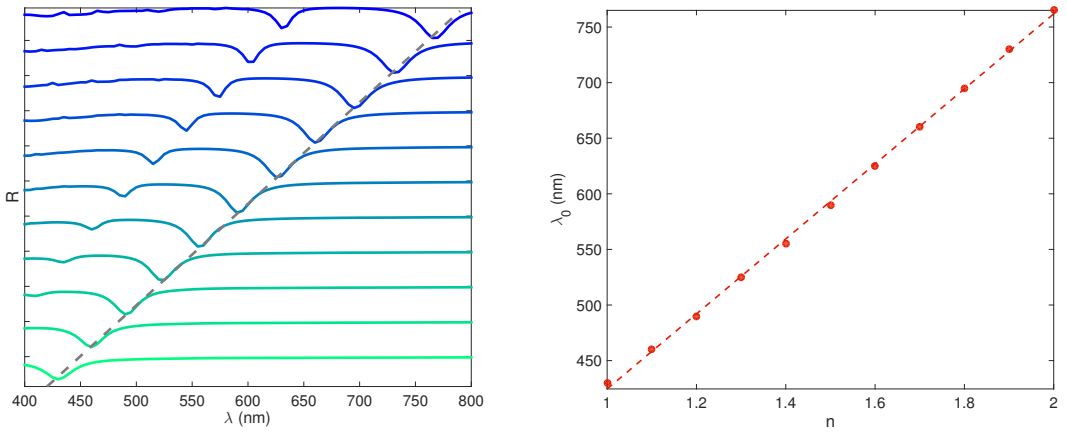


Figure 6.19: Imprinted refractive index sensor array in a gold film. The red region indicates the presence of water in the nanocavities. The bright white regions are silicon debris left over from the master failing during imprint.

Sensitivity and Range of a Nanocavity Based Refractive Index Sensor

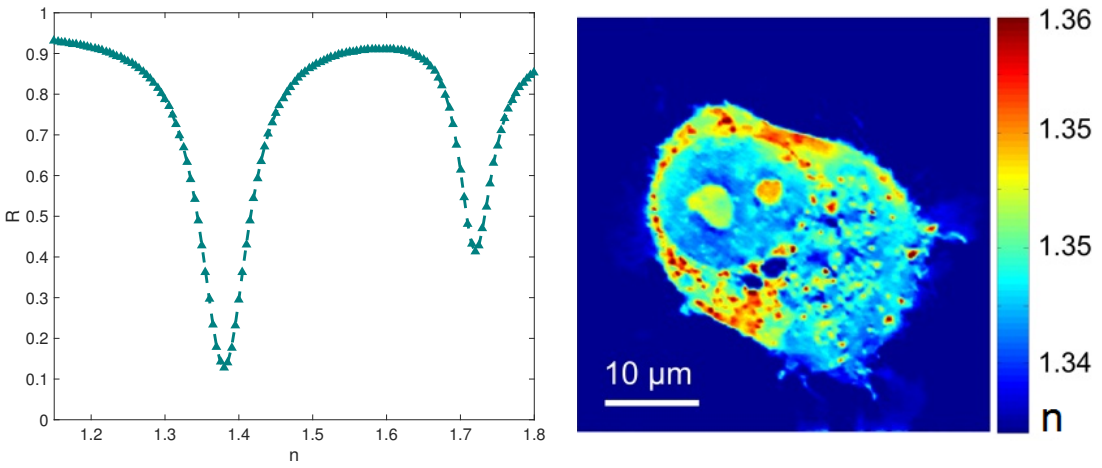
Finite element method calculations of reflection spectra from an array of silver nanocavities 100 nm x 50 nm x 50 nm (LxWxH), with an array period of 300 nm, are shown in figure 6.20(a). Here the cavity dimensions were held fixed and the surrounding superstrate refractive index was varied from $n = 1$ to $n = 2$. As expected, the resonant wavelength of the cavity mode depends linearly on the refractive index of its environment. By plotting the resonant wavelength (figure 6.20(b)) as a function of refractive index we find the sensitivity of such a device to be 337 nm per refractive index unit and the cavity resonance red-shifts linearly with increasing refractive index.



(a) **(b)**

Figure 6.20: (a) FEM calculated reflection spectra for nanocavity arrays for superstrates with n=1 to n=2 (from bottom to top, in steps of $\Delta n = 0.1$). (b) Resonant wavelength, λ_0 as a function of refractive index.

Tracking the resonant wavelength of nanocavities to determine local refractive indices requires a broadband light source and a spectrometer. Another potential technique, that requires only a fixed wavelength laser and a camera, is to convert the reflected intensity into a refractive index. Calibration could be performed simply by taking the reflectance from an unpatterned part of the silver substrate and then the measured intensity value in the camera image would represent a refractive index value. Figure 6.21(a) shows the calculated reflection from the nanocavity array at $\lambda = 532$ nm as a function of refractive index. Due to the spectral symmetry of the cavity resonances the effective range this technique would work is limited to refractive indices on only one side of the resonance, to avoid the problem of multivalued index values from one intensity value. The index value this region is centred is set by the cavity dimensions and the wavelength of the laser in use. For example, in figure 6.21(a), the device would operate with refractive indices from $n = 1.2$ to $n = 1.4$ with a peak sensitivity (which depends on the gradient of this curve) at $n = 1.35$, which is the typical range for many important features of cells, which are mostly water ($n = 1.33$) and components that have a refractive index between $n = 1.34$ and $n = 1.39$ (see figure 6.21(b)) [3]. Here the reflected intensity falls from 0.93 to 0.15, easily detectable with a modest camera.



(a) (b)

Figure 6.21: (a) Reflection from a nanocavity array as a function of superstrate refractive index. (b) An example refractive index tomograph of a CA9-22 cell taken from [108].

6.5 Summary

Resistless nanoimprint lithography can address a significant problem currently faced by nanophotonics, namely most nanophotonic devices are not fabricated using industrially scalable techniques. This is a major barrier that will need to be overcome before there is large-scale uptake of nanophotonic devices. To better understand the capabilities and limitations of RNIL, single cavity masters were fabricated and embossed into silver, aluminium and gold films. The aluminium embossing unfortunately failed, potentially due to the hardness of the native oxide layer. Nevertheless, cavities of varying depths and shapes were imprinted in silver and gold. After imprinting, the Si master can be re-used approximately 8 times before the nanofeatures are degraded by wear. This issue can be overcome by substituting the Si master for one composed of Ni, which has been shown to imprint high fidelity patterns even after 8000 imprint cycles [109]. It was also shown that by adjusting the applied imprint pressure it is possible to tune the nanocavity's resonant properties. Silver nanocavities offered lower absorption but a greater pressure tuning range, due to a higher Young's modulus of plastic deformation. Several applications of nanocavity metasurfaces were proposed including a spec-

tral notch filter, absorptive polarisation filter, high resolution colour printing and refractive index sensing substrates for bioscience applications. The scalability of the technique was demonstrated by imprinting a 7 cm by 7 cm array of nanocavities. With RNIL it is possible to create one large area master template and create metasurfaces with a range of optical responses just by varying the pressure used in the imprinting step or by judicious choice of superstrate refractive index.

Chapter 7

Plasmonic Cavities for Quantum Source Control

7.1 Introduction

In chapter 5 plasmonic nanoantennas were combined with a semiconducting substrate to create a compact polarisation sensitive detector. In that case the plasmonic component acted only to filter the polarisation state of the incident light before absorption in the semiconductor. It is possible however to couple plasmons with semiconductor excitons to actively alter the quantum properties of an emitter, such as a quantum dot or a fluorescent molecule or alter the spectral absorption of a low cost semiconductor such as TiO_2. In this chapter the use of plasmonic metal-insulator-metal (MIM) nanocavities coupled to thin films of semiconductor or semiconductor nanocrystal doped films are investigated. Particular attention is paid to the alteration of quantum properties due to the plasmon-exciton interaction such as the radiative decay rate enhancement of the emitters, the polarisation state of the emission, or the absorption and electric detection of sub-bandgap energy photons[1]. Potential applications are also discussed.

[1] This particular discussion can be found in Appendix C

The first section describes an application of resistless nanoimprint lithography (RNIL) for the creation of a plasmonic metasurface and demonstrates its application to the enhancement and control of radiation by quantum dots. The metasurface consists of an array of cold-forged rectangular nanocavities in a thin silver film. High quantum efficiency graded alloy CdSe/CdS/ZnS quantum dots were spread over the metasurface and the effects of the plasmon-exciton interactions characterised. There is a four-fold increase in the radiative decay rate of the QDs and emission brightness, compared to QDs on glass, along with a degree of linear polarisation of 0.73 in the emitted field. Such a surface could potentially be integrated with current QD display or organic solar cell designs.

The second section explores the integration of semiconductor quantum dots (QDs) into the dielectric layer of a metasurface Fabry-Perot (actually, more correctly, a Gires-Tournois) etalon. One side of the cavity is formed using an array of silver nanoantennas, the other is an optically thick silver mirror. This configuration, where one surface of an etalon is replaced with a metasurface, is renamed as a "metalon", for the sake of brevity. The nanoantennas provide extra radiative decay pathways for the exciton and so lead to a reduction in the exciton lifetimes. The incorporation of QDs in thin PMMA films is optimized, as the etalon response depends strongly on the dielectric film thickness, which in turn depends on the spin coating properties of the PMMA. This film thickness is tuned to provide significant spectral overlap between the cavity absorption and the QD emission. This course of investigation is to understand the effect of polymer layer thickeness on the operation of a plasmon-exciton device such as an enhanced QD-LED.

In the final section of this chapter a reimagining of the canonical plasmonic bullseye structure inspired by Huygens' Principle for the enhancement and focussing of light emitted from a QD film is investigated. FEM calculations are used to optimise the device parameters such as beam divergence, brightness and polarisation. The device is fabricated using EBL and spin coating QD doped PMMA

and then characterised by polarisation resolved confocal fluorescence scans and far-field imaging techniques. Such a device could find use in a photonic communication system, where information could be multiplexed across polarisation states and frequencies.

7.2 Quantum Dot–Metasurfaces

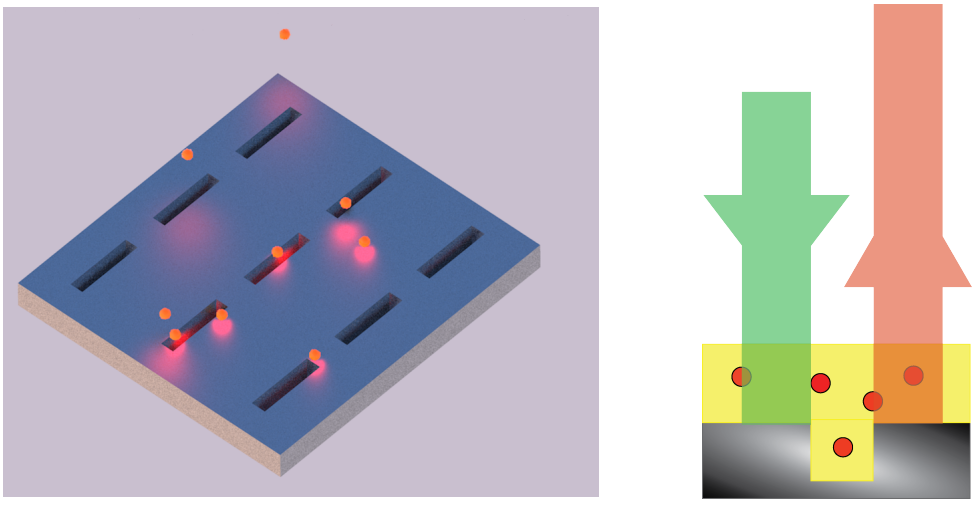
Quantum emitters coupled to a plasmonic metasurface exhibit several useful properties including the alteration of excited state lifetimes and emitted polarisation state. It is surprisingly straightforward to integrate a metasurface into today's QD-LED architecture, where the metallic back-contact can be structured with cold forging to cost effectively increase the QD pixel brightness and polarize the emission from each pixel. This would allow for 3D display technology and further reduce the cost and energy consumption of QD displays. The same cold forging techniques can also be readily extended to increase the efficiency of QD-based or organic solar cells, although the metasurface response should be polarization independent in this case.

The weak coupling of excited quantum states to cavity modes can lead to emission enhancement via the Purcell effect [51], which then results in devices with a higher external quantum efficiency (EQE) and lower power consumption. Photonic and plasmonic interactions have previously been investigated to produce enhanced and polarised emission from quantum sources [55, 110–113]. Plasmonic designs have the advantage of being highly compact and readily integrable with current QD display designs.

Precisely fabricated plasmonic devices have been used to demonstrate enhancement of the directivity, polarisation and intensity of QD emission [114, 115]. These approaches, however, rely on slow and costly fabrication techniques such

as electron beam lithography or focused ion beam milling. Here an application of a cost-effective, high throughput, scalable nanofabrication technique, known as resistless nanoimprint lithography (RNIL) or cold forging is demonstrated [59]. A thorough investigation of the RNIL process and the optical nanocavities created is presented in chapter 6. Using this technique it is possible to demonstrate both radiative decay rate enhancement and control of emission polarisation due to the interaction of quantum dot excitons with the plasmonic modes of an array of nanocavities.

Previously, the spectral response of plasmonic cavities created with RNIL in §6.2.1 and other methods [43,59,116] showed surprisingly sharp and short wavelength resonances, compared to apertures of similar dimensions [89]. The modes supported by these nanocavities have a node of the electric field near the metallic end of the cavity and an antinode at the open end. This fact permits strong blue resonances in the nanocavities, something that is critical to colour displays, this is difficult to achieve with nanoapertures and is a major issue for current organic LED (OLED) based displays. Figure 7.1 is an illustration of the QD-nanocavity metasurface.



(a) (b)

Figure 7.1: (a) An array of nanocavities in a thin silver film, covered with CdSe/CdS/ZnS QDs. (b) The QDs can be excitied with green light then emit red light, which drives a cavity plasmon mode.

7.2.1 Fabrication and Experimental Methods

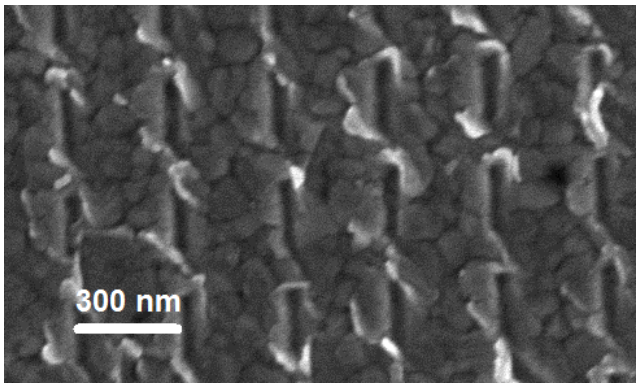


Figure 7.2: A scanning electron micrograph of the resistless nanoimprinted cavity array in a silver film. The cavities are highly asymmetric, measuring 200 nm long by 40 nm wide.

The resulting nanocavities are shown in the scanning electron micrograph in Fig. 7.2. The rectangular nanocavities are 40 nm wide and 200 nm long, with an array period of 300 nm. Atomic force microscopy reveals the cavity depth to be approximately 40 nm $\pm$ 3 nm. Excess metal from the nanocavities is squeezed out to the side, where the cast off can be seen as the bright areas around the cavities in Fig. 7.2.

The spectral emission properties of semiconductor nanocrystals or quantum dots, such as emission wavelength and linewidth, as well as intensity, can be tailored during the growth process. Due to their small size, high brightness and relative stability, quantum dots are an attractive solution for some of the challenges of modern photonics, such as solar energy harvesting [117], telecommunication and energy efficient illumination [118]. QDs are also readily integrable with plasmonic structures, which allows for further control over their emission properties, such as beam steering [119], polarisation or radiative decay rate enhancement [67].

The quantum dots used here consisted of a 4.5 nm diameter CdSe core with a 6 nm thick graded alloy $Cd_xZn_{1-x}S$ shell [120]. The final QD diameters were

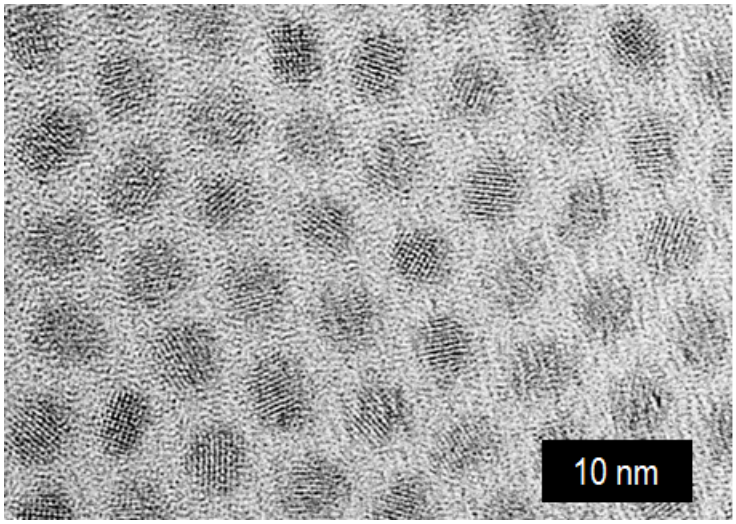


Figure 7.3: A HRTEM image of the monodisperse graded alloy shell QDs.

normally distributed about 10 nm $\pm$ 2 nm. Due to the small variation in QD size, the absorption and decay properties of each QD in this sample were similar. The growth process is detailed elsewhere [120]. At the time of growth these QDs exhibited an 80% quantum efficiency, and a mean lifetime of 17 ns in a 15 μM concentrated solution, with hexane as the solvent. Figure 7.3 shows a high resolution transmission electron microscopy (HRTEM) image of the QDs used in this experiment. The sample shows low dispersion in QD size, which leads to narrow emission bands for the QD/SU8 mixture. This also helps reduce the spread in decay rates of our QDs.

To incorporate the quantum dots with the nanoimprinted metasurface, the QDs were mixed into SU8 2000.5 to provide environmental stability. The final QD concentration in the SU8 film was 1.4 μM. The SU8/QD mixture was then drop-cast onto the patterned silver film and sealed with a glass cover slip. The SU8 was then cured under UV light. The SU8 layer thickness of 12 μm was determined using confocal microscopy.

Fluorescence scans were performed using a Nikon Ti-80i inverted microscope fitted with a 100x 1.3 NA oil immersion lens, a Perkin Elmer SPCM-AQRH-14-FC avalanche photo diode (APD) and a Mad City Labs NanoDrive xy piezo stage.

Fluorescence spectra and the nanocavity reflectance spectrum were measured using an Andor Solis cooled spectrograph CCD array. Fluorescent lifetime measurements were carried out using the time correlated single photon counting (TCSPC) technique using a synchronised Picoquant TimeHarp 200 and the APD. Information about the quantum dot radiative lifetime and decay rate distribution was retrieved by fitting an exponential decay weighted by a log normal distribution to the TCSPC data [68]. The light source used for these measurements was an NKT SuperK supercontinuum photonic crystal fiber laser, with a 10 MHz repetition rate. The broadband light was filtered with a high optical density 531 nm $\pm$ 11 nm bandpass filter (531/22 Brightline) and a 531 nm longpass dichroic beamsplitter (532 nm Brightline Laser Dichroic Beamsplitter), resulting in a spatially coherent pumping spectrum of 532 nm to 540 nm. The reflected light from the sample was then collected from the dichroic beamsplitter through a 532 nm long pass filter (532 nm RazorEdge LWP) and focused onto the APD. The range of wavelengths detectable with this set up is 541 nm to 1100 nm.

7.2.2 Results and discussion

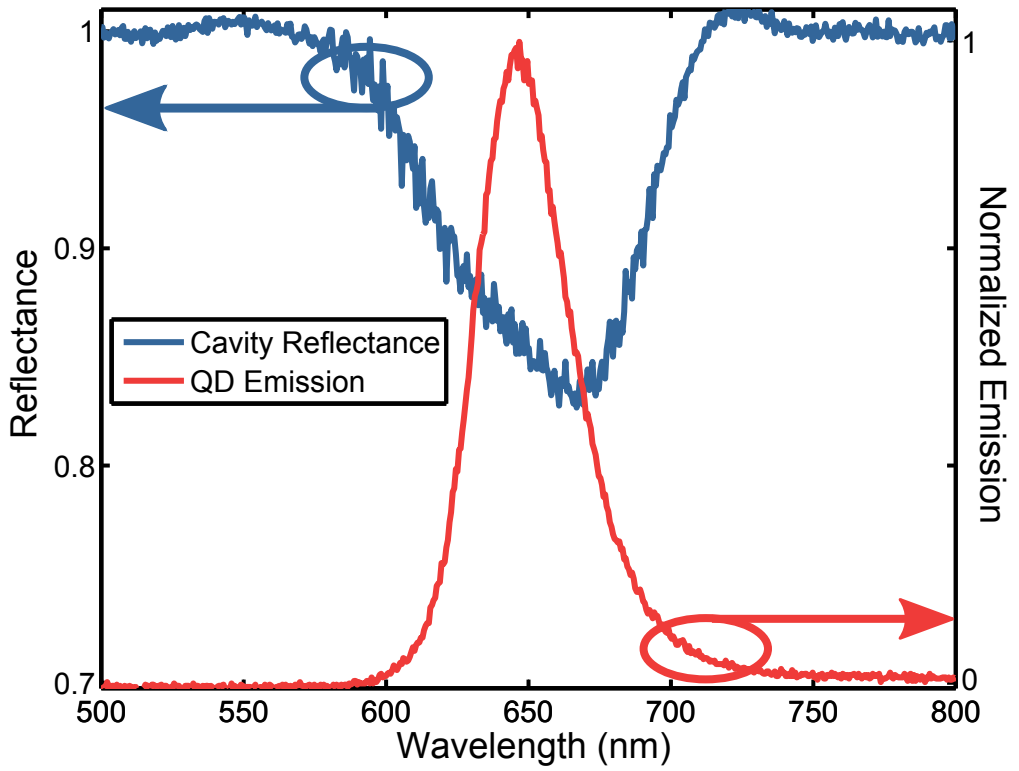


Figure 7.4: The measured reflectance of the SU8 encapsulated silver nanocavity array (blue) and the normalized emission from the $Cd_xZn_{1-x}S$ quantum dots in SU8, measured on a glass microscope slide (red).

The measured cavity reflectance spectrum, shown in Fig. 7.4, has a dip in reflection at a wavelength of 670 nm, with a full-width-at-half-maximum of 70 nm, as determined by fitting a Lorentzian to the spectrum. This can be attributed to the excitation of the fundamental cavity mode, which is broadened due to irregularities in the fabricated cavity dimensions and higher material losses. Fig. 7.4 also shows the measured fluorescence spectrum of the $Cd_xZn_{1-x}S$ QDs. The pump laser excites the quantum dot excitons and these decay with a peak emission wavelength of 645 nm. The QD emission band overlaps with the fundamental resonant mode of the nanocavities, which permits weak coupling between the QD excited state and the plasmonic cavity mode. The bright regions in the scanning fluorescence image shown in Fig. 7.5 are from quantum dots located in close proximity to the plasmonic nanocavities, where the interaction between plasmons and excitions is strongest. The fine details (text, outline, and wings) in Fig. 7.5

are dimmer than central parts as they are only one or two nanocavities wide so the overall intensity sampled by the microscope objective is lower in these regions. The plasmon-exciton coupling leads to a two-fold increase in the intensity of the collected light, compared to the background fluorescence of the QDs on the Ag film and a 95% increase in the external quantum efficiency of the device. This is a manifestation of the Purcell effect, where the introduction of extra radiative decay pathways (that is, an increase in the local density of optical states), via coupling of the QD excitons to plasmon cavity modes, has greatly increased the excited state decay rate, so more photons per unit time are collected when the QDs interact with the plasmonic nanocavities. This enhancement effect is in addition to of any Purcell enhancement produced by proximity of the QDs to the unpatterned Ag film and the SU8 encapsulation layer.

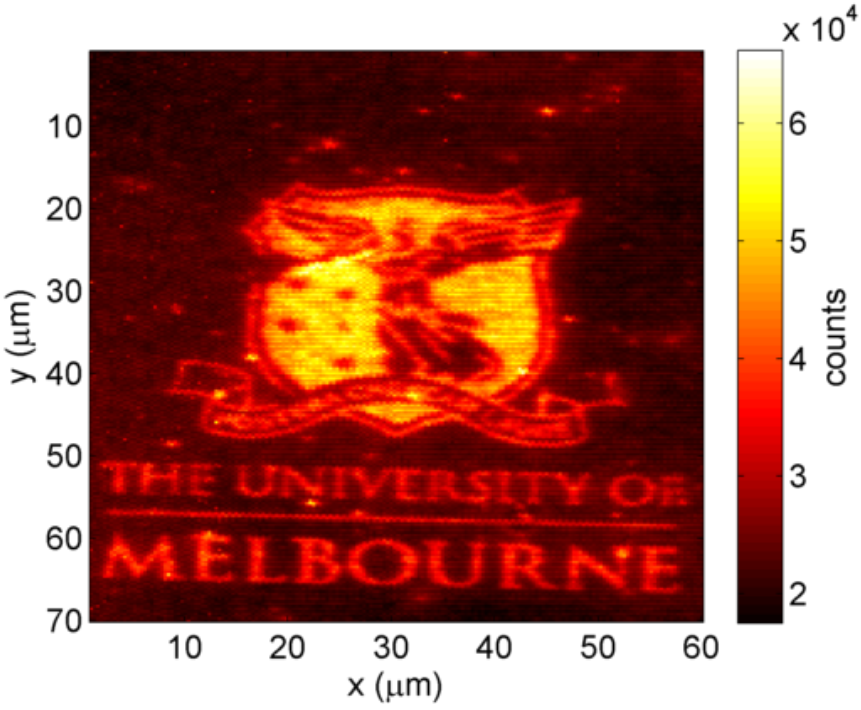


Figure 7.5: A fluorescence microscope scan of the quantum dots interacting with the nanoimprinted cavities. The emission from QDs near the cavities have around 3.5 times the intensity than for QDs near the bare Ag film. This is evidence of coupling between the plasmonic cavity modes and the quantum dot excitons.

Figure 7.6 shows the collected counts from the QD/SU8 sample on a silver film. A 532 nm CW laser was used to pump the QDs through a 0.90 NA 100x Olympus Objective. The objective is mounted on a XYZ piezo stage with a 200 μm

scan range in all three directions. The emission was collected through the same lens, passed through a 532 nm dichroic filter into a single-moded optical fiber connected to an avalanche photodiode. The 60 μm core of the optical fiber acts as a pinhole aperture to give the system confocal optical sectioning. By collecting emission at various heights above the silver film and above the nanocavity array, the effect of spectator QDs can be observed. The collected emission from 6 μm above the metallic surface is still 10% of the maximum value. This affects the lifetime data and the degree of polarization measurements. By focusing on the silver film and then retracting the objective until QD fluorescence is no longer observed, it is possible to measure the thickness of the SU8 layer. Figure 7.7 shows the silver surface, with many bright QD aggregates and the same region with the objective 12 μm further away from the sample, where only a few aggregates are visible. Further than 12 μm QD aggregates are no longer visible in the scanned image, thus the thickness is 12 μm.

Figure 7.8 shows the measured spectra for quantum dots near and far from the nanocavity array for the same pump power and collection times. From these spectra it is possible to estimate the increase in external quantum efficiency of the device due to the coupling between cavity plasmons and QD excitons. To do so, one must integrate the counts with respect to wavelength for each spectrum and take the ratio, which yields 1.95, or an increase in EQE of 95%.

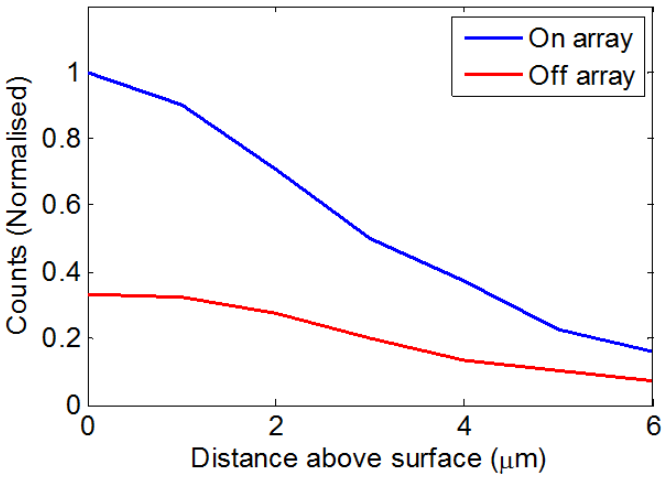


Figure 7.6: A comparison of the collected fluorescence from the QDs above the cavity array (blue) and above the unpatterend film (red).

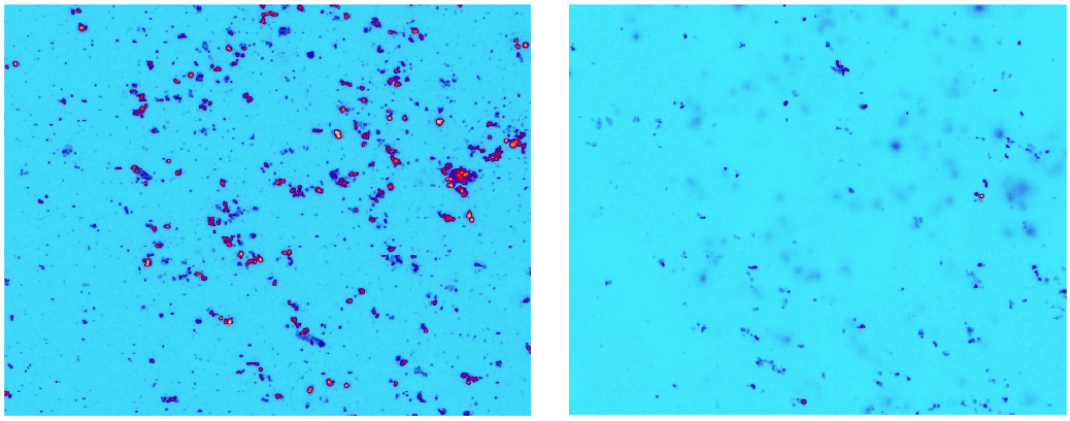


Figure 7.7: Confocal scans of the QD/SU8 mixture on the unpatterned silver film, (a) at the silver surface and (b) 12 μm from the silver surface.

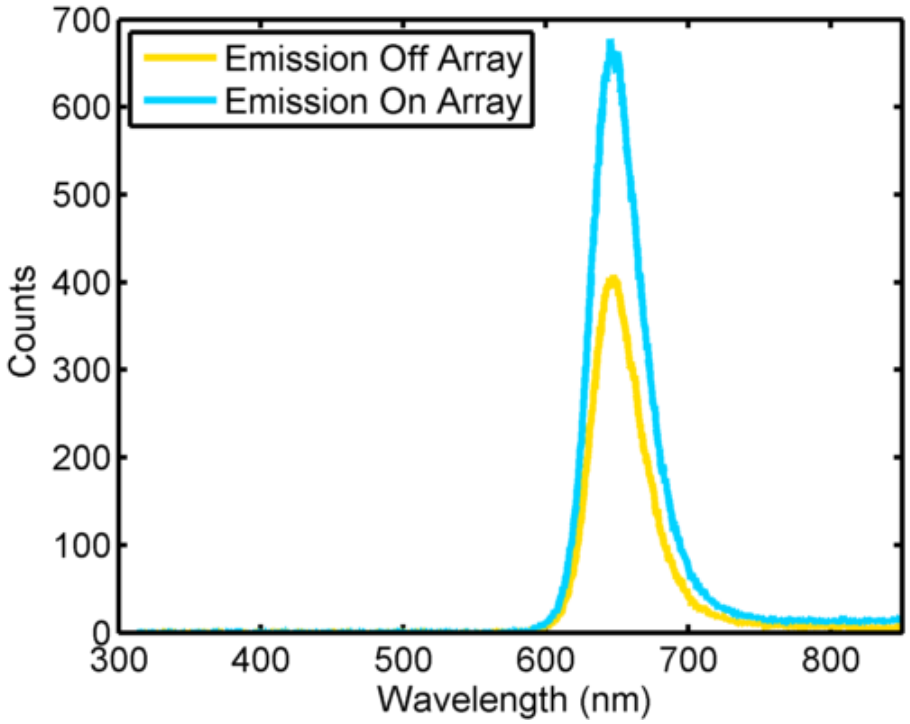


Figure 7.8: Spectra from QDs on the cavities (blue) and on the unpatterned silver (yellow). The presence of the cavities increases the EQE by 95%.

Scanning the sample and collecting spectra with an analyser at either $0°$ or $90°$ to the long axis of the nanocavities, reveals the emitted light near the imprinted cavities has a preferential polarisation direction perpendicular to the long axis of the cavities, whereas light from QDs away from the cavities is unpolarised. This is consistent with the excitation of the cavity mode that has this polarisation. By comparing the recorded intensities for both polarisation states, the degree of linear polarisation (DOLP) can be calculated. The spatial variation of the DOLP is shown in Fig. 7.9, with a maximum value of 0.73 from the cavity array. The measured value is reduced due to the presence of 'spectator' QDs throughout the 12 μm thick SU8 film, as identified using confocal microscopy. Quantum dots more than 5 μm above the cavities do not appear to behave differently to QDs the same height above the unpatterned film. The degree of linear polarisation could be increased by using a much thinner (~ 30 nm) film of QDs, as would be found in a commercial QD display.

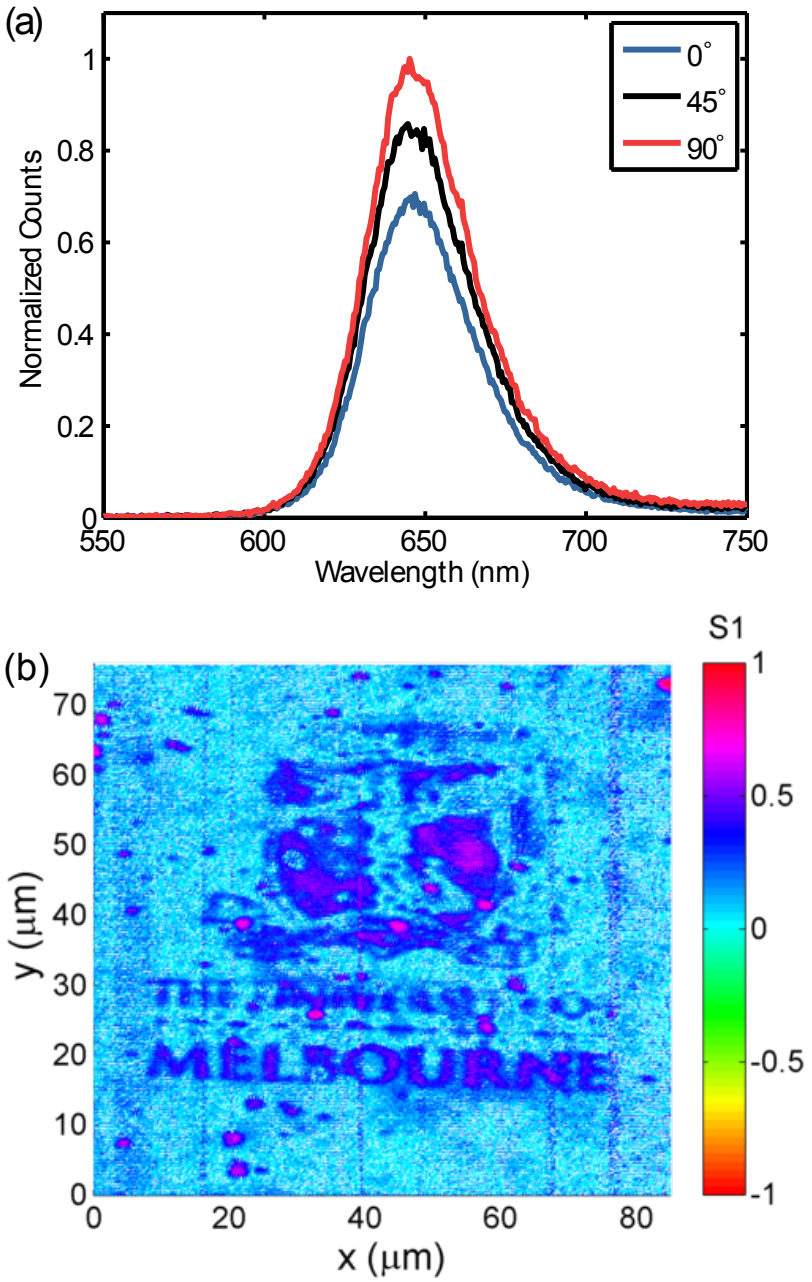


Figure 7.9: Normalised emission spectra (a) for the cavity coupled quantum dots with an analyser at 0° (blue), 45° (black) and 90° (red) to the long axis of the nanocavities. (b) the spatial distribution of the degree of linear polarisation, or S1, of the QD emission. The value of S1 for light collected above the cavities is up to 0.73, whilst over the Ag film it is 0.

The time correlated single photon counting histograms shown in Fig. 7.10(a) have been normalised so that the maximum count is one. This allows for easy comparison of QD lifetimes for the 3 environments; in SU8 on glass, in SU8 on the unpatterned silver film and in SU8 on the nanoimprinted metasurface. Each histogram can be thought of as a probability density function, $f(t)$, representing

the probability of detecting a photon at some time, t, after the excitation pulse. For a single emitter, with a single excited state, $f(t)$ will be an exponential decay; $f(t) = e^{-\Gamma t}$, where the decay rate, $\Gamma = 1/\tau$ and τ is the excited state lifetime. To fit the decay characteristics for more realistic cases with an ensemble of different emitters, each with multiple excited states, a stretched exponential is a popular choice for $f(t) = e^{-(\Gamma t)^{\beta}}$. [120] Here, following the lead of van Driel *et al.* [68], the lifetime distribution is modelled using

$$f(t) = \int_0^{\infty} e^{-\Gamma t}\, \sigma(\Gamma)\, \mathrm{d}\Gamma, \tag{7.1}$$

where $\sigma(\Gamma)$ represents the distribution of total decay rates of, in this case, multiple quantum dots. The decay rate distribution function, $\sigma(\Gamma)$, is modelled as a lognormal distribution so that

$$\sigma(\Gamma) = \frac{1}{\Gamma_m w \sqrt{\pi} e^{\frac{-w^2}{4}}} e^{-(\frac{\ln\Gamma - \ln\Gamma_m}{w})^2}, \tag{7.2}$$

where Γ_m is the most frequent total decay rate and w is related to $\Delta\Gamma$, the width of the distribution, by $\Delta\Gamma = 2\Gamma_m \sinh(w)$ [67]. The advantage of using this analysis of the decay behavior of the QD excitons compared to the stretched exponential approach is that Γ_m and $\Delta\Gamma$ can easily be physically interpreted, whereas β does not have a straightforward physical interpretation [68].

To fit $f(t)$ using equations (7.1) and (7.2), to the TCSPC data shown in Fig. 7.10(a), a cost function approach was employed to find the values of Γ_m and w that minimise the difference between the measured data and $f(t)$ over the 35 ns measurement window. Once Γ_m and w have been estimated, one can generate the total decay rate distribution functions, $\sigma(\Gamma)$, find $f(t)$ and then calculate the expected lifetime using,

$$\tau = \int_0^{\infty} t\, f(t)\, \mathrm{d}t. \tag{7.3}$$

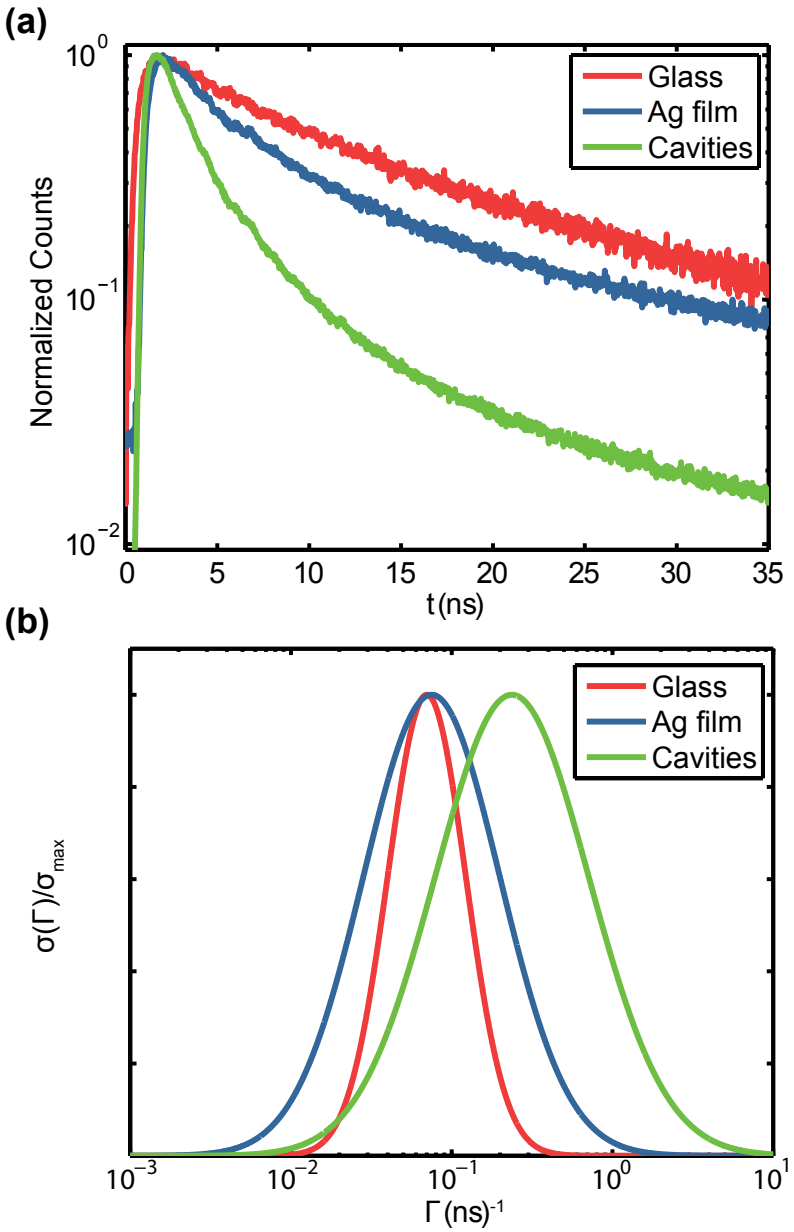


Figure 7.10: (a) Normalised TCSPC histograms for quantum dots in SU8 from the same batch on glass (red) with $\tau = 17.4$ ns, on the bare silver film (blue) $\tau = 14.4$ ns and on the nanoimprinted cavity array (green) $\tau = 3.9$ ns. It is clear that plasmon-exciton interactions lead to a greatly reduced radiative lifetime. (b) The calculated total decay rate distributions $\sigma(\Gamma)$, normalized to their peak values, σ_{max}, for quantum dots in SU8 on glass (red), on an unpatterned silver film (blue) and on nanoimprinted cavities (green). The mean decay rate increases from $\Gamma_m = 0.07$ per ns for QDs on glass to $\Gamma_m = 0.237$ per ns for the cavity coupled QDs, an increase of three and a half times. The spread of the decay rate distribution also increases from $\Delta\Gamma = 0.14$ per ns for QDs on glass to $\Delta\Gamma = 0.56$ per ns for cavity coupled QDs.

The total decay rate distributions calculated from the TCSPC data using equations (7.1) and (7.2) are shown in Fig. 7.10(b), normalized to their peak values, σ_{max}. For the case of the graded alloy quantum dots suspended in cured SU8 on a glass substrate, the mean lifetime, τ was found to be 17.4 ± 1.2 ns with a most

frequent total decay rate, Γ_m of 0.07 per ns. For QDs on the unpatterned silver film, an average lifetime of 14.4 ± 0.89 ns and a Γ_m of 0.138 per ns was calculated. For QDs interacting with the nanoimprinted metasurface, the lifetime was reduced to 3.9 ± 0.31 ns and the most frequent exciton decay rate increased to 0.237 per ns. By comparing the lifetime values for quantum dots in SU8 on glass, τ_0, and near the nanocavities, τ_c, one can estimate the Purcell enhancement factor, $F_p = \frac{\Gamma_c}{\Gamma_0} = \frac{\tau_0}{\tau_c}$, of this scalable metasurface to be $F_p = 4.46$. This enhancement factor agrees with the measured increase in QD brightness near the plasmonic nanocavities in Fig. 7.5.

The Purcell factor associated with the nanoimprinted metasurface can be increased by fine tuning of the cavity dimensions to increase the spectral overlap of the exciton and cavity frequencies. Further improvement can be achieved by reducing the plasmon damping in the cavity by reducing the crystal grain sizes of the Ag film and more precise control of QD position by use of another lithographic step. That being said, the Purcell factor and associated polarisation of emission demonstrated here, with this cost effective technique, compares favourably with previously reported enhancements using direct write approaches [121]. Other potential extensions includes designing and fabricating a metasurface that will impose a particular circular polarisation on the QD emission, which is superior for use in 3D display technologies compared to linearly polarised light. This can be achieved by tailoring multipolar plasmon modes, [122] or with a chiral metasurface [123].

7.3 A Quantum Dot Doped Gires-Tournois Metalon

Recently attention has turned to creating plasmonic devices with near unity absorption at specific wavelengths [124, 125]. Similar radio frequency and microwave devices are well known as the Salisbury screen [46]. The physics behind the operation of such devices is the same interference effect found in Fabry-Perot

cavities and etalons, but in this case one of the 'mirrors' is formed using a metasurface [46, 125]. The general structure involves an array of nanorods separated from a conductive ground plane by a thin dielectric layer. This dielectric layer can also be doped with emitters such as quantum dots or organic dyes. This structure is similar to that found in plasmon enhanced QD-LEDS or OLEDs, where the mirror plays the role of a back electrical contact. The thickness of the dielectric layer would then control the brightness of the emission as well as its quantum properties. The nanorod dimensions can also be tuned to give the largest spectral overlap between the emitters and the metalon. Optimising the QD-doped polymer film thickness for maximum Purcell enhancement will be an important, straightforward design consideration for cavity–plasmon–exciton devices. In particular for plasmon-enhanced organic solar cell designs or high brightness QD-LEDs. Figure 7.11 depicts a QD doped metalon, with 40 nm high nanoantennas of varying lengths on a glass substrate, separated from a 200 nm Ag mirror by a QD doped PMMA (henceforth QD-PMMA) layer, of varying thickness, applied via spin coating. The device's optical properties (reflection, absorption) are determined by the QD-PMMA layer thickness and the nanoantenna length. The device is pumped with blue light and the red emission is collected. The change in quantum properties (mean excited state lifetime, quantum efficiency) is determined by the spectral overlap between the cavity mode and the QD emission as well as the cavity quality factor, Q [126].

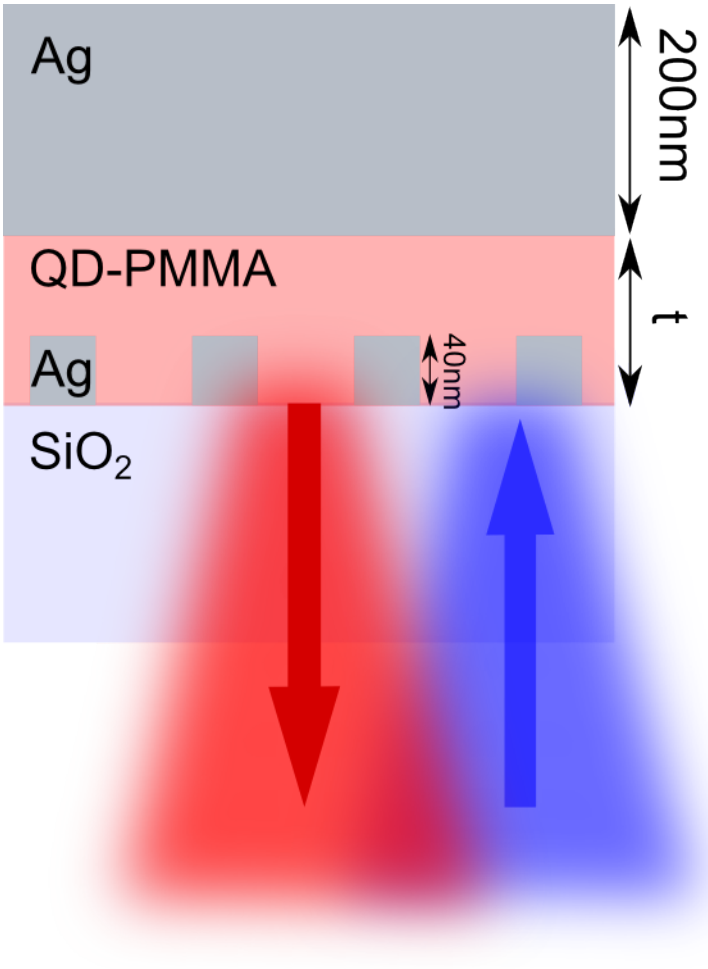
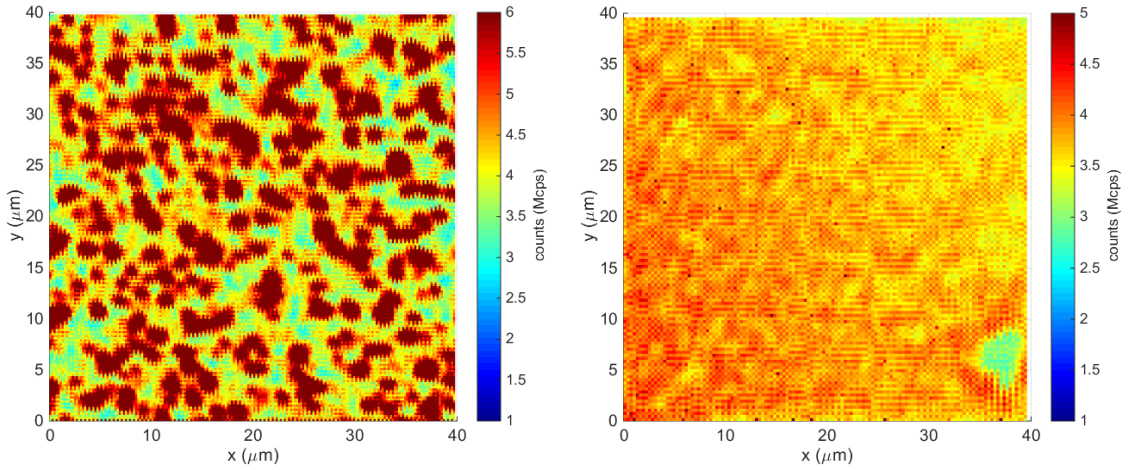


Figure 7.11: An array of silver nanoantennas on a glass substrate is covered with QD doped PMMA of varying thickness, t, then a 200 nm silver mirror is evaporated on top to form a QD doped metalon. The device can be pumped with blue light and emits red light.

7.3.1 Fabrication of the Device and Integration of QDs

Silver nanoantenna dimensions were optimized using FEM calculations and the optimal dimensions were found to be 65 nm x 65 nm x 40 nm, the small size being due to the strong plasmon sensitivity to the refractive index of the QD-PMMA. Silver was selected due to its low ohmic losses and very high reflectivity. A range of nanoantennas with lengths from 55 nm to 75 nm were fabricated on a 75 mm SiO_2 wafer using EBL. The reason for producing devices with a range of nanoantenna size was to ensure uncertainties stemming from the optical properties used in the FEM calculations and possible systematic fabrication defects could be accounted for in the experiment. A 35 nm Cr charge dissipation layer was evaporated on

to a 160 nm thick layer of PMMA 950k A2 prior to EBL. Electron beam evaporation was used to deposit the silver then lift-off in warm acetone was performed to remove the excess metal. The QD-PMMA layers were then applied by spin coating. The QD-PMMA layer thickness was controlled by varying the concentration of PMMA polymer in the solvent from 0.75% to 3%. This method was used as simply varying the spin coating speed would not give a large enough range of final film thickness, t, to be of interest (for $n = 1.53$ and a wavelength of 650 nm the subradiant and superradiant modes of the etalon occur when t is an integer multiple of 110 nm) and SU8, as used in the previous section is not suitable for such thin films. The same quantum dots as used in the previous section were used, with a final concentration of 100 nM. Dilution of the QD-PMMA was performed with anisole, as it has been shown to produce the smoothest PMMA films. The QDs however, are poorly soluble in anisole, which leads to the conglomeration of large QD groups within the ultrathin film. By using a solvent in which the QDs have a greater solublity in, chlorobenzene, it is possible to overcome this issue. Figure 7.12 shows confocal fluorescence microscope (CFM) scans of identical QD-PMMA films prepared using (a) anisole and (b) chlorobenzene. The QD clumping can clearly be seen in the anisole case, and is greatly reduced in the chlorobenzene case. To obtain a truly uniform film, with no QD conglomeration, it is possible to terminate the ligands on the QDs with MMA, making them perfectly soluble in anisole, but this is not straightforward. Eight QD-PMMA on metasurface samples were prepared, of which only half were viable samples, due to several factors including glass substrate failure, failure to produce silver nanoantennas (due to EBL focussing issues) and contamination. The final dielectric layer thicknesses, as measured by optical profilometry, are shown in figure 7.13. Finally a 200 nm thick silver mirror was deposited onto of the samples via electron beam evaporation.



(a) CFM scan of QDs in PMMA-A.

(b) CFM scan of QDs in PMMA-C.

Figure 7.12: CFM images of QD-PMMA with (a) anisole and (b) chlorobenzene as the solvent.

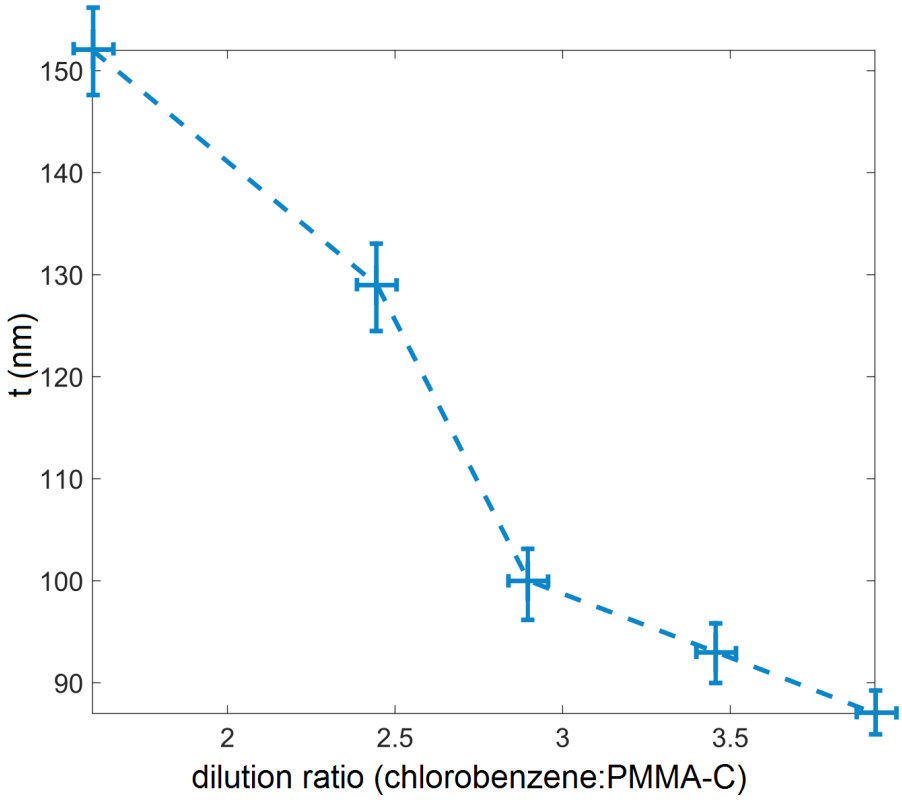


Figure 7.13: Measured film thickness of the spin coated QD-PMMA polymer as a function of dilution ratio. 3% PMMA in chlorobenzene (PMMA-3C) was diluted with chlorobenzene.

7.3.2 Device Characterisation and Results

Metalon Absorption

The four viable metalon samples were optically characterised using the spectroscopy system described in §4.1.1. Reflection spectra, R, from the metalon arrays were collected using the supercontinuum light source and a 100x Nikon 0.9 NA objective and then normalised to reflection from a silver mirror. Assuming no light is transmitted through the 200 nm Ag back mirror, and the light scattered outside the collection cone of the 0.9 NA objective is negligible, then the metalon absorption is $A = 1 - R$. Figure 7.14 shows the absorption spectra for four QD-PMMA dielectric layer thicknesses, t, overlaid with the measured QD emission spectrum. In order to understand the absorption spectra, the metalon's optical path length must be adjusted to account for the height of the nanoantennas (40 nm), the change in refractive index of the PMMA layer due to QD doping, as well as the field penetration into silver at optical frequencies (or alternatively the reflected phase from the back mirror) [127]. Metalons with $t = 87$ nm and $t = 129$ nm have resonances closer to that of the QD emission peak ($\lambda = 650$ nm), whilst $h = 152$ nm and $h = 100$ nm have higher quality factors, Q, both of which are important for Purcell enhancement. Unfortunately, due to unavoidable issues with the evaporation of smooth metal films on PMMA substrates [128], where large surface roughness leads to reduced reflectivity, perfect (unity) absorption is not achieved in these metalons, as has been demonstrated elsewhere [48].

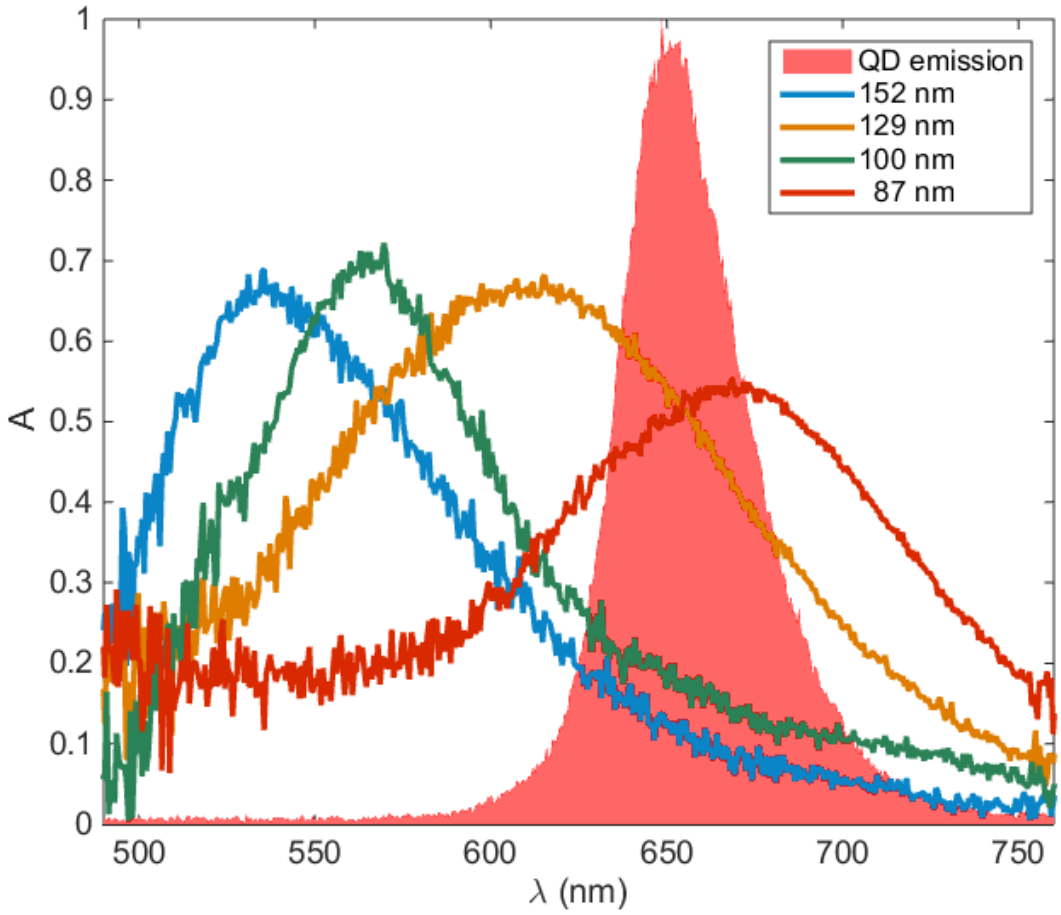
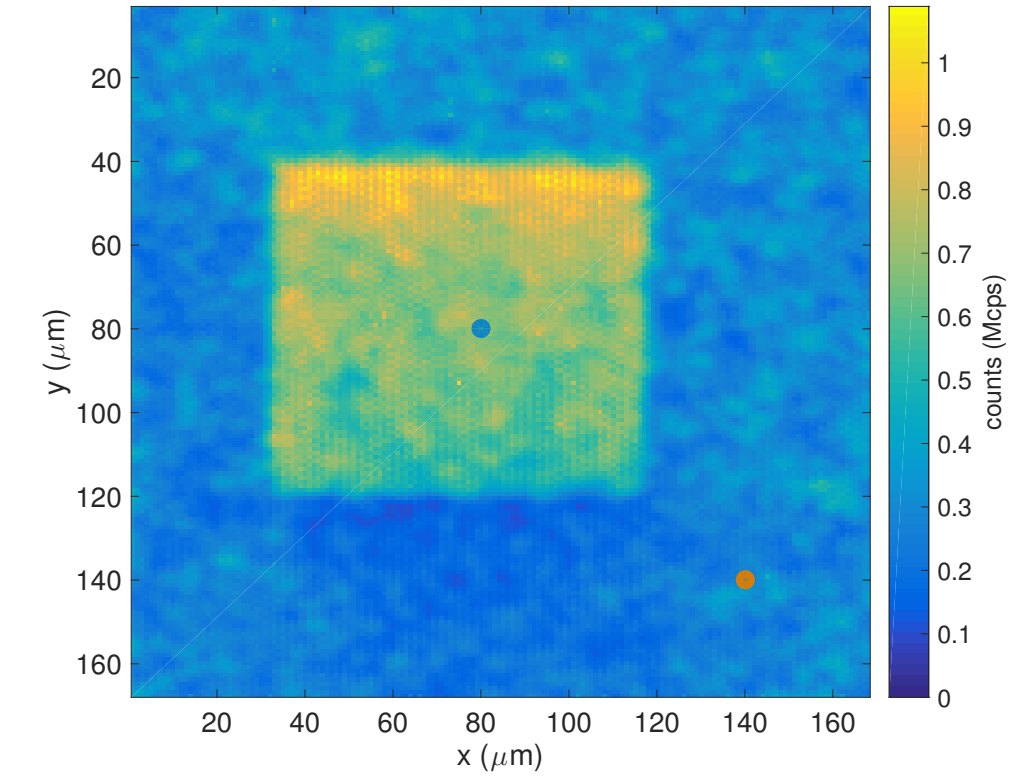


Figure 7.14: Absorption spectra for 5 different QD-PMMA film thicknesses, the emission spectrum of the QD-PMMA is superimposed under the absoprtion spectra.

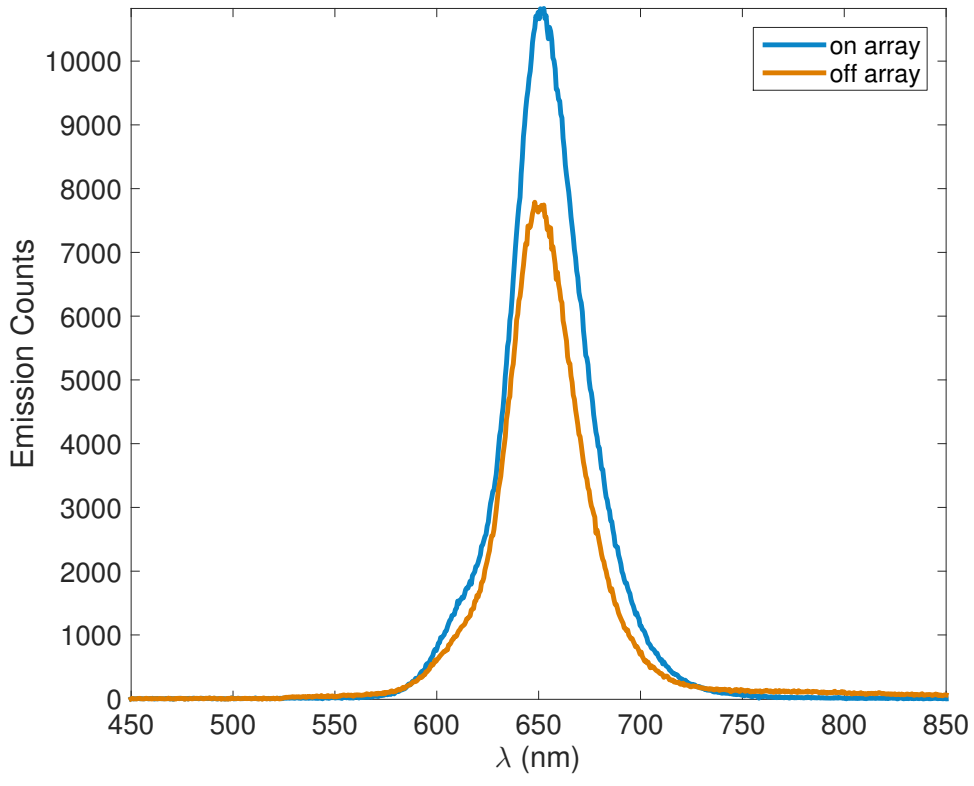
Quantum Properties of doped Metalons

Scanning confocal fluorescence microscopy (CFM, see section 4.3.1 for detailed discussion) was performed on the metalon samples. Figure 7.15 shows a CFM image of the 150 nm QD-PMMA layer metalon and the emission spectra from on the array and off the array, indicated by the blue and yellow circles. The scans were conducted using the supercontinuum laser set to a 5 MHz repetition rate and spectrally filtered using a Fianium SuperChrome-VIS set to a centre wavelength of 480 nm and a linewidth of 10 nm. The excitation beam is filtered using a dichroic beamsplitter as in the previous section. For this metalon, one sees a near two fold increase in brightness of ≈ 1.6x, as well as an increase in emission linewidth from 50 nm to 70 nm. There is no evidence of Rabi splitting (which is seen in quantum

systems coupled to high Q cavities, such as dyes in a laser cavity), this is due to the fact that the plasmon damping rate, through optical and heating losses from the cavity, is much greater than the strength of the coupling between the excitons and the cavity modes, that is, these metalons operate in the weak coupling regime. As such the Purcell enhancement should be the dominant quantum effect and should manifest itself as a reduction in excited state lifetime.



(a)



(b)

Figure 7.15: A CFM scan of the 150 nm thick metalon (a) and the emission spectrum on (blue) and off (orange) the metasurface array (b). The location of the measurements is indicated in (a) by the coloured circles.

To determine the radiative decay rates, Γ, TCSPC measurements were conducted on each metalon sample and for the QD-PMMA is silver and on glass substrates. The results are shown in figure 7.16. There is a reduction in mean lifetime from 17 ns for QD-PMMA on glass to 0.83 ns for the 129 nm metalon. There is a two-fold decrease in lifetime between QD-PMMA on a silver film and in the 152 nm metalon, consistent with the emission spectra in figure 7.15. The same fitting procedure as in the previous section was used to estimate the mean radiative decay rate from the TCSPC data. From the estimated mean radiative decay rate the Purcell factor, $F_p = \frac{\Gamma}{\Gamma_0}$ is calculated, and is shown on the right hand axis of figure 7.17 (blue line).

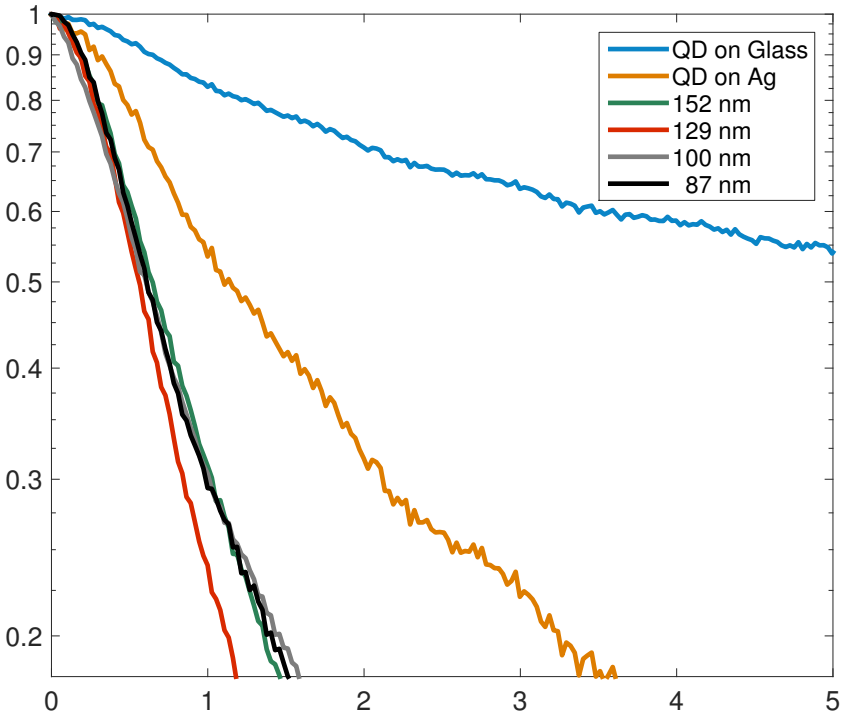


Figure 7.16: Fluoresence lifetime measurements for QD-PMMA on glass, silver mirror and in the metalon. The y-axis is logarithmic.

The Purcell factor is a direct result of Fermi's Golden Rule and as such depends on the product of the spectral overlap, S, between the QD emission and the metalon resonance, and the Q-factor of that resonance (see §2.7). The left hand axis of figure 7.17 (red line), shows the product $Q \times S$ as calculated from the absorption and emission spectra in figure 7.14. As can be seen, the product $Q \times S$,

which is proportional to F_p, determined from spectral measurements follows the F_p as determined from TCSPC data as a function of thickness. The error bars for F_p measured via TCSPC (blue line) are derived from the standard deviation, w, used when fitting the decay rate distribution to the lifetime data using 7.2. The error bars for $Q \times S$ are estimated using the sum of the mean square error (MSE) for each of the Lorentzian fits as a measure of uncertainty for the Q-factor and spectral overlap S. The metalon with $t = 129$ nm has the highest Purcell enhancement factor, a modest 28, whereas $t = 100$ nm gives the lowest with $F_p = 19$. This is congruent with the absorption spectra where $t = 129$ nm metalon has the largest spectral overlap with the QD emission and $t = 100$ nm metalon has the least. The outlier to this analysis is the thinnest metalon, $t = 87$ nm, which has a large $Q \times S$ value but a low Purcell enhancement. This is perhaps in part due to close proximity of the quantum emitters to the metal surfaces of the antennas or mirror (at most only 23 nm) allowing for a large increase in non-radiative transfer processes. In short, enough of the emitters are close enough to the metal to be quenched by non-radiative energy transfer.

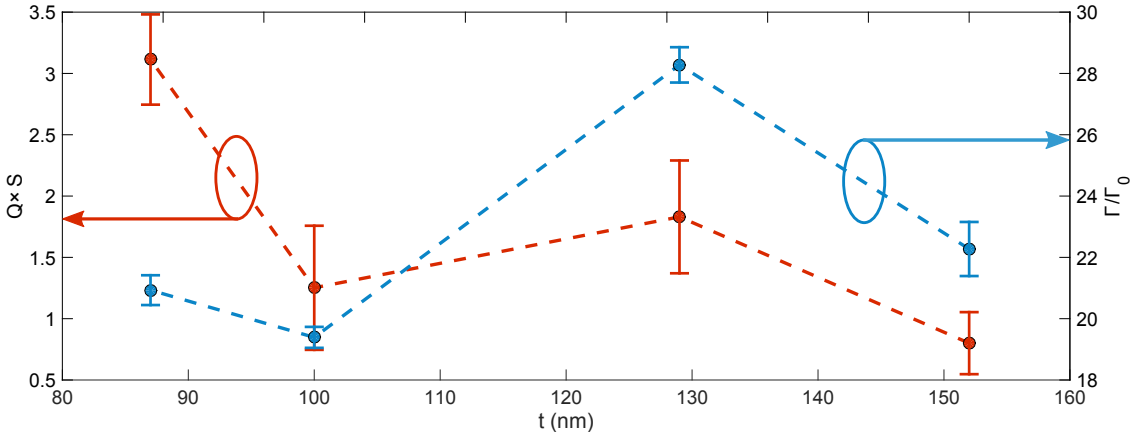


Figure 7.17: A comparison of each cavities Q-factor $\times$ the spectral overlap between QD emission and cavity absorption (red line) and the Purcell factor increase in radiative decay rate determined from fluoresence lifetime measurements of the QDs as a function of QD-PMMA layer thickness, t.

7.4 Polarised Bullseye Slot Nanoantennas for QD emission shaping and Polarisation

One of the most widely-reported forms of beam-shaping elements found in plasmonics is transmission through a metallic bullseye lens (or antenna) [129], which is related to the Fresnel zone plate lenses found in lighthouses and synchrotrons around the World [130]. Recently bullseye lenses have been used to collimate or focus light emission from fluorescent sources such as QDs [131], and dyes [132]. However to date there have been no reports of controlling the emission polarisation state of the resulting beam using a plasmonic bullseye lens. Here a modified slot based bullseye structure is investigated, where the usual corrugations of the bullseye lens have been replaced with rings of nanocavities. As radiation from subwavelength nanocavities behave much like a point dipole, replacing the corrugations does not substantially alter the beam shaping properties. By making this alteration there is now an extra degree of freedom, that is, the cavity orientation, which can be exploited to control the overall polarisation of the emanating beam. As described in the first section of this chapter, silver nanocavities coupled to quantum dot doped films will enhance the emission brightness and polarise the emission. By arranging these cavities into carefully spaced rings it is possible to generate an enhanced brightness, collimated and polarised beam from quantum emitters. To create a linear polarised beam all the nanocavities should be oriented in the same direction [133].

7.4.1 FEM Beam Optimisation

The cavity-QD coupling should be optimised to ensure strong polarisation of the emission and increased brightness, but since the same metal and dielectric is being used and the same QDs as found in §7.2, the same lateral cavity dimensions (40 nm x 200 nm) can be used. The depth of the cavity also controls the amount of the Purcell enhancement, with maximum enhancement reached when the cavity

depth is $\frac{\lambda}{4n}$, which for $\lambda = 650$ nm and the effective mode index, for the fundamental mode, is $n = 1.5$ (see §2.5.1 for the calculation of nanocavity dispersion diagrams) in the cavity is 200 nm.

The shape of the interference pattern from the slot bullseye antenna (sBE) depends on the sum of the complex field components from each nanocavity [69]. The simplest case to consider is where all the QD coupled cavities emit photons in phase, which ensures that the resulting far field radiation pattern depends only on the lateral positions of the nanocavities. In reality the phase of emission is completely random, which lowers the efficiency of the device, but does not change the shape of the beam if a statistically meaningful number of emission events are recorded (that is, a long enough exposure time during the measurement).

Ebbesen *et al.* suggests that in this case there are two parameters that will allow for the optimisation of the ring radii; the period between each ring, p and the distance from the centre of the bullseye to the first ring, a [134]. Each cavity in the simulation contains one electric point dipole at the local field maximum (the centre of the cavity mouth), oriented randomly in the surface plane, randomised using MATLAB LiveLink to generate a uniformly distributed random number between 0 and 2π, for the polarisation angle. The frequency of each dipole corresponds to a free space wavelength of 650 nm. The current amplitude of each dipole is fixed at 1 W. The substrate is silver, with material properties taken from [45], the superstrate is 100 nm thick layer of PMMA (with refractive index set to $n = 1.5$) and the remaining domain is air. A hemispherical far field domain boundary is placed 3 μm from the silver/PMMA interface and is centred on the centre of the bullseye structure. A 2D parametric sweep over p and a was performed (see figure 7.19). By calculating and plotting the far-field radiation pattern for each value of p and a, it is possible to determine the optimal set of values via inspection. The FEM calculations suggest values of $p = 380$ nm and $a = 525$ nm will result in a collimated beam of emitted light for emission at $\lambda = 650$ nm.

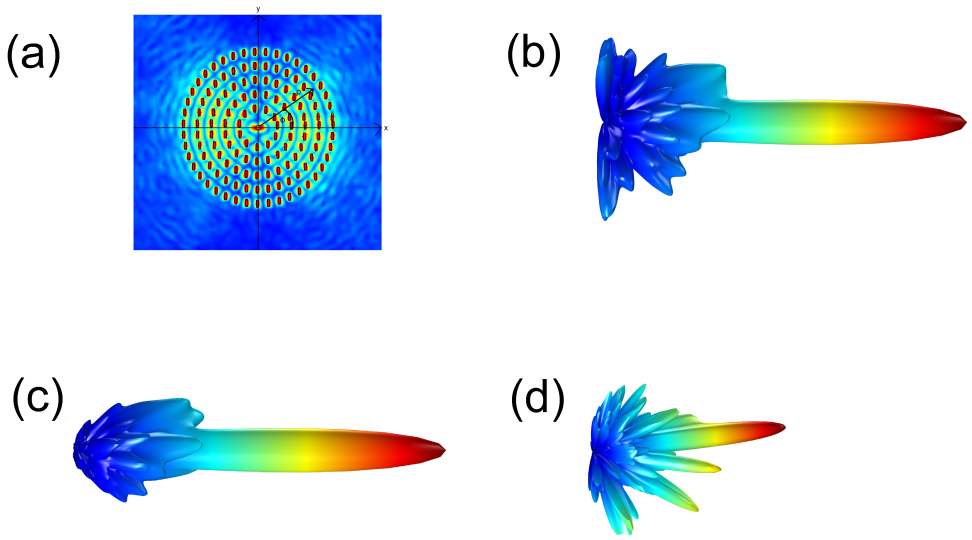


Figure 7.18: FEM calculation results for the optimised sBE structure: (a) electric field amplitude at the silver/QD-PMMA interface, (b) the total far-field radiation pattern and x- and y-polarised components, (c) and (d) respectively, all with the same scale.

Figure 7.18 shows the FEM calculation results for the optimal values, $p = 380$ nm and $a = 525$ nm. The magnitude of the electric field at the metal-dielectric interface is shown in figure 7.18(a). As expected, the electric field intensity, excluding in the nanocavities themselves, follows Malus' Law, where the field intensity depends on $\cos^2\phi$, where ϕ is the azimuthal position co-ordinate of the nanocavity. So nearer the x-axis there is much stronger electric field than those that lie along y. The far-field radiation patterns shown in figures 7.18(b-d), all plotted with the same fixed scale. Clearly, even with the randomized cavity emission, in the far-field, for these particular parameters, there is a strong collimating behaviour arising from the rings of nanocavities. Furthermore, when the far-field pattern is resolved in to $|E_x|$ (c) and $|E_y|$ components (d), it is clear that the majority of the photons in the central (collimated) beam are x-polarised and the small y-polarised component would be insignificant to the overall beam polarisation after some propagation distance. The final result being a collimated, linearly polarised beam from a quantum emitter doped polymer coupled to the slot bullseye structure. This approach does not consider the effect the high refractive index quantum dots have on the effective refractive index of the QD-PMMA,

which could alter both the cavity resonance and the beam shape. Furthermore the contribution to the radiation pattern from spectator QDs in the polymer film are assumed to be negligible compared to the nanocavity emission, which is true only if the cavities provide significant emission enhancement. This calculation also assumes there is maximal coupling between a single emitter in each cavity and the cavity modes and that each emitter will radiate with the same uniform intensity.

7.4.2 Fabrication

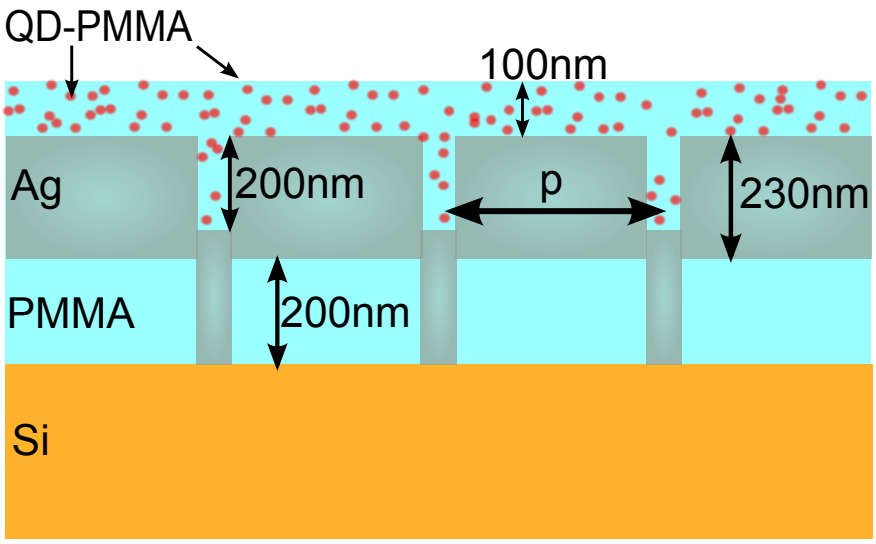


Figure 7.19: A schematic cross section of the slot bullseye structure covered in a layer of QD-PMMA. p is the radial spacing of the nanocavities. The first ring of nanocavities is offset from the centre of the bullseye by a, so occurs at $p + a$.

To fabricate the bullseye slot antennas, a custom Python 2.7 script was used to create the required layout files for EBL. A 200 nm PMMA-A4 film on a silicon substrate was prepared using a 3500 rpm spin coating speed and optical profilometry to confirm the film thickness and uniformity. The pattern was exposed using a 500 pA beam current with a 2 nm beam step size. Following exposure and development, a 230 nm silver film was deposited via e-beam evaporation. Care was taken to ensure the substrate was perfectly normal to the evaporation direction. The silver overfills the PMMA cavities by 30 nm, and due to the strongly directional

deposition 200 nm deep nanocavities are left in the silver film. A cross-sectional device schematic is shown in figure 7.19.

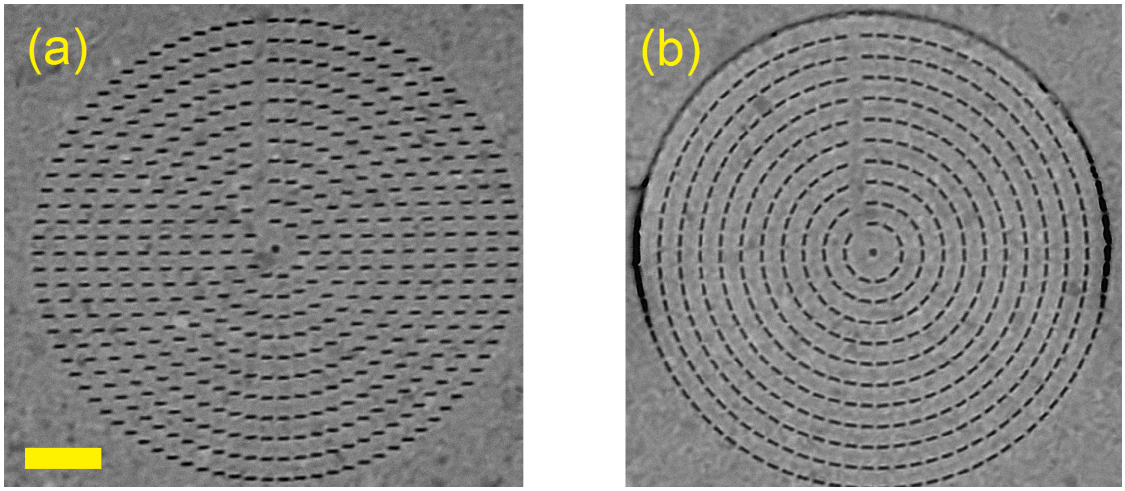


Figure 7.20: SEM images of the linear (a) and azimuthal (b) sBE structures. The scale bar is 1.2 μm.

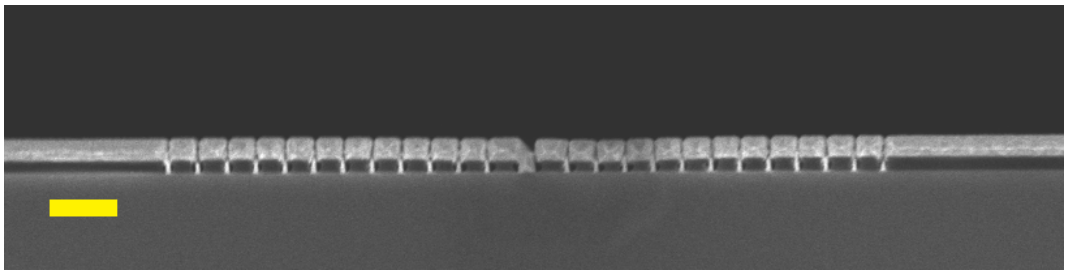


Figure 7.21: SEM cross sectional image of the azimuthal sBE structures, taken through the centre of the device. The scale bar is 1 μm.

The wafer was then cleaved into 10 mm x 10 mm squares. A 100 nm layer of QD-PMMA (the solvent used is chlorobenzene and the QD concentration is 90 nM) is then spun onto the silver film and allowed to air dry, as the post-baking of samples was found to cause the silver film to bubble and crack, due to the underlying PMMA layer out-gassing anisole vapour. Figure 7.20 shows SEM images of the structures prior to coating with the QD-PMMA. It can be seen from a cross-section of the azimuthal sBE device, shown in figure 7.21, that the large aspect ratio of the fabricated structure does not detrimentally affect the cavity geometries.

7.4.3 Polarisation Resolved Scanning Confocal Imaging of the Bullseye

Polarisation resolved scanning confocal fluorescence microscopy (CFM) was performed on the linear and azimuthal sBE structures to measure the local effect of the rings of nanocavities on the QD fluorescence. Figure 7.22 shows the resulting intensity, I, scans when the analyser is in the x- and y-polarisation orientations, normalised to the background fluorescence, as well as the first Stokes' parameter, S_1 for both sBE structures. For the linear sBE sample there is almost no signal above the fluorescence background for the x-polarised scan, however the y-polarised scan shows a uniform circular region with twice the intensity of the fluorescence background. From these two scans it is possible to calculate the spatial distribution of the degree of linear polarisation using $S_1 = \frac{I_x - I_y}{I_x + I_y}$. The emission from the region of the linear sBE has an S_1 value of -0.85, indicating a nearly totally linearly y-polarised emission pattern. In fact this value possibly underestimates the true polarisation state of light from this region as the x-polarised scan likely still has a contribution from 'spectator' QDs similar in intensity to the background fluorescence. That is, the nanocavities do not completely polarise the emission from all the quantum dots inside the bounds of the bullseye, but only those close enough to the cavities be strongly influenced by the plasmon presence. To increase the degree of polarisation a thinner QD-PMMA film could be used, or a lower QD concentration. The azimuthal sBE, which resembles the canonical BE structure, is symmetric under spatial co-ordinate exchange ($x \Leftrightarrow y$) and as such so is the near-field intensity pattern. Thus, the spatial distribution of the S_1 value is *anti*-symmetric under reflection about $x = y$. This is the distribution one would expect of a radially-polarised beam [135].

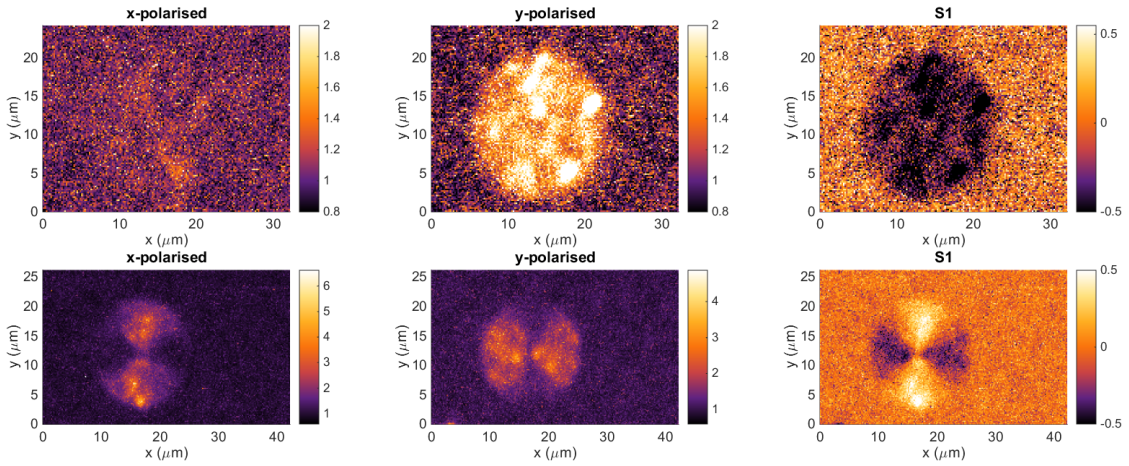


Figure 7.22: CFM scans of the emission from linear (top row) and azimuthal (bottom row) sBE structures. The x- and y-polarised scans are the first two columns respectively and the final columnn shows the spatial distribution S_1 parameter for both devices.

As expected the nanocavites also provide extra radiative decay paths to the QD exciton and thus a Purcell enhancement. TCSPC data is shown in figure 7.23, where the mean lifetime on the sBE is 1.92 ± 0.12 ns, down from 4.18 ± 0.22 ns for the QDs on bare silver, which accounts for the 2-fold brightness enhancement found in the CFM scans.

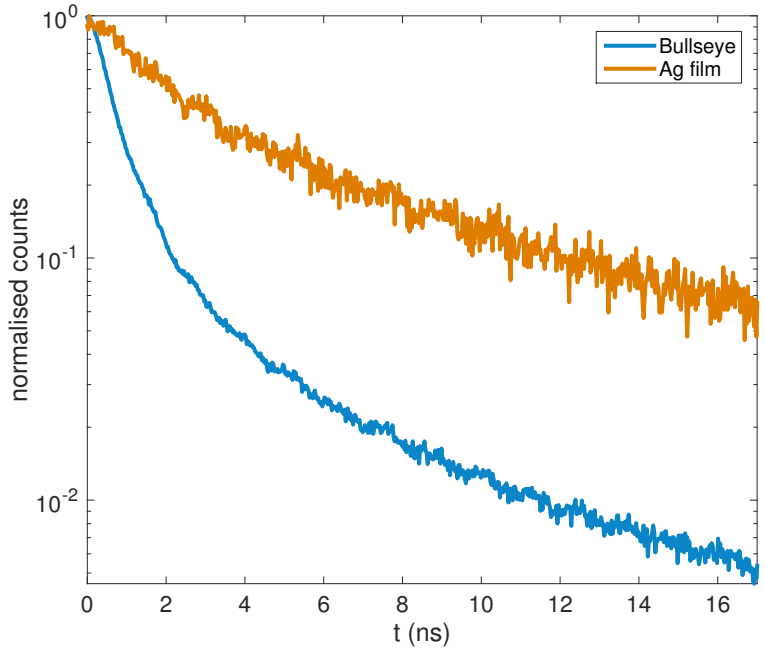


Figure 7.23: TCSPC data from QDs near the linear sBE structure (blue) and on the unpatterned silver film (orange).

7.4.4 Polarisation Resolved Far-Field Intensity Patterns

Polarisation resolved Fourier plane (or k-space) imaging was performed on both sBE structures, see §4.3.3 for detailed experimental methods and Appendix B for calibration and normalisation methods used. By imaging the back focal plane of the objective it is possible to determine the in-plane wavevector, (k_x, k_y), distribution of the emitted light [69]. For a fixed wavelength and a constant superstrate refractive index, the k-space image gives information on the angular distribution of the radiation. Figures 7.24, 7.25 and 7.26 show the relevant polarisation resolved far-field images for the linear sBE. For the emission from QD-PMMA on an unpatterned region of silver film, the k-space distribution is typical of that of an emitter near a mirror (see ref. [136] for example), where there is a wide distribution of emission angles.

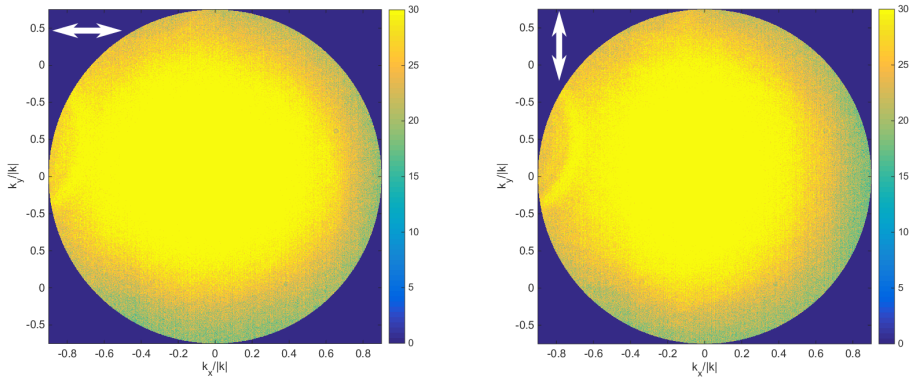


Figure 7.24: Polarisation resolved k-space emission intensites for QD-PMMA on unpaterned silver (control sample).

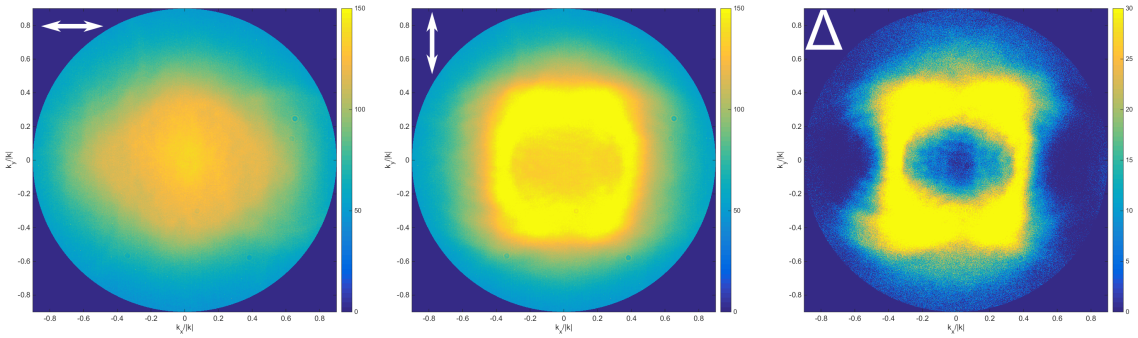


Figure 7.25: Polarisation resolved k-space intensites for the linearly polarised sBE structure, the arrows indicate analyzer direction and Δ denotes the difference between the k-space distributions.

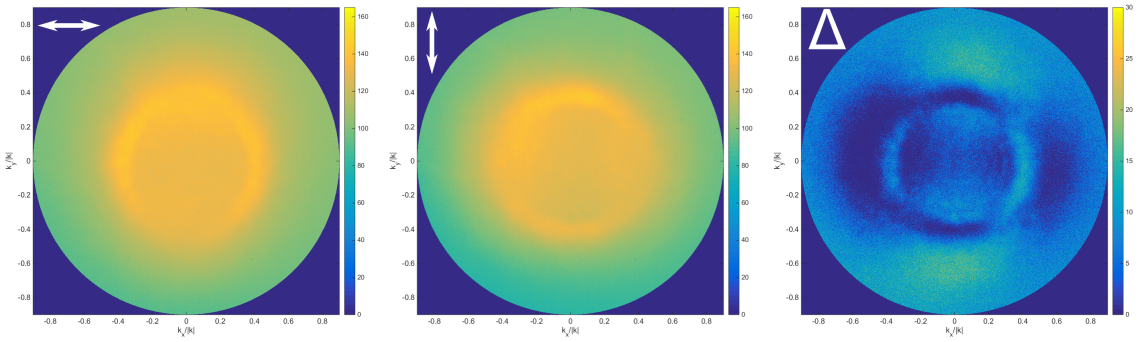


Figure 7.26: Polarisation resolved k-space intensites for the azimuthally polarised sBE structure,the arrows indicate analyzer direction and Δ denotes the difference between the k-space distributions.

For the y-polarised linear sBE measurements, shown in figure 7.25, it can be seen that there is a bright ring for low (k_x, k_y) values, with a mean radius of $\sqrt{k_x^2 + k_y^2}/k_0 = 0.36$. This bright ring does not appear in the x-polarised case. By subtracting the x-polarised image from the y-polarised, the difference becomes clear. This points to a y-polarised conical beam, with a beam divergence angle of $21°$, from the linear sBE structure. For a collimated beam, this value should be approaching $0°$. The FWHM of the emission cone can be estimated by fitting a Lorentzian to one of the two peaks in a linecut taken at $k_y = 0$. This yields a normalised momentum spread, $\Delta k_x = 0.042$, corresponding to an angular spread of $5.3°$. This value suggests that the sBE design does indeed collect and shape the emission as a bullseye antenna should, but that the ring spacing p needs to be adjusted in order to properly collimate the beam. The k-space distribution of emission from the azimuthal sBE structure, shown in figure 7.26, also shows significant beaming, with a similar beam divergence pattern, with a mean radius of 0.39 or $23°$. The FWHM of the momenta distribution for this sample is $\Delta k_x = 0.031$, but due to higher mean k_x, the angular spread is $2.5°$, half that of the linear sBE. The polarised images show there is no overall linear polarisation (integrating over the entire k-space), but there are two sets of lobes with orthogonal linearly polarised light within the emission cone. Such lobes are typical of a cylindrical vector beam of radially-polarised light [135], however once again the sBE ring spacing would need to be adjusted to collimate this emission. A

radially-polarised beam of light from a nanodevice could be very useful for exciting co-axial waveguide modes, nanofibre or nanowire optical modes or even long-lived dark-plasmon modes [137].

Discrepancy Between Simulation and Experimental Results

FEM calculations were used to find the geometric parameters, p and a, which optimised the collimating action of the sBE lens. The values found via simulation did not yield a collimated beam, but resulted, experimentally, in a polarised emission cone. This result is typical of a bullseye antenna with suboptimal ring spacing, either too large or too small. Alternatively, there is an accumulated phase difference of the fields radiated from each slot, which depends on the ring spacing, as well as the dielectric's refractive index, which alters the final superposition of the fields. Figure 7.27 shows two simulations of the linear sBE structure with $p = 380$ nm and $a = 525$ nm, the dimensions of the sBE fabricated. The superstrate refractive index is varied from 1.45 to 1.6 in steps of 0.01 RIU. The results shown suggest the difference in FEM simulation and the experimental results shown above can be accounted for with just a 0.04 RIU change in superstrate refractive index. This small change leads to an accumulation of phase, resulting in an emitted cone rather than a beam. This change in refractive index could be due to excess solvent in the QD-PMMA (refractive index of chlorobenzene is 1.53) or the presence of the QDs themselves ($n_{QD} = 2.5$).

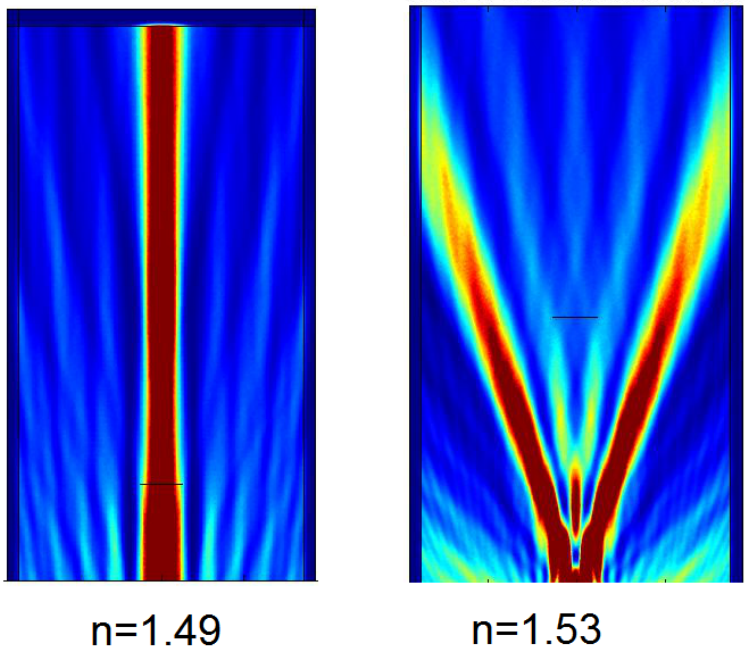


Figure 7.27: FEM calculations of the radiated electric field for the linear sBE with superstrate index $n = 1.49$ (left) and $n = 1.53$ (right). A small discrepency in material properties leads to a large change in the radiation pattern.

7.5 Summary

This chapter covered the integration of plasmonic cavity metasurfaces with QD excitons for the enhanced generation of light and how these devices could be incorporated into current QD-LED based devices. In the first section an application of a robust and scalable nanofabrication technique for creating plasmonic nanocavity arrays in metallic films was demonstrated. Applying a mono-disperse solution of CdSe/CdS/ZnS graded alloy quantum dots suspended in cured SU8 to a nanoimprinted metasurface resulted in nearly a 4-fold enhancement in radiative decay rate and brightness, as well as a high degree of linear polarisation of the emission close to 0.73. This technique will prove useful in the development of polarised QD displays found in consumer electronics, QD based light harvesting and photodetection as well as being extended for use in telecommunication and photonic computing applications. In the second section a QD doped metalon (metasurface etalon) was investigated, including the incorporation of quantum

dots into very thin polymer films. It was found that chlorobenzene outperformed anisole as a solvent in this case as the QDs had greater dispersion and produced films with much more uniform QD distributions. The metalon produced a reduction in lifetime of 22 times when compared to the same quantum dots on glass and half the lifetime of QDs in the surrounding glass/QD-PMMA/Ag mirror structure. The final section covered the development of a bullseye antenna comprised of nanocavities and covered with QD-PMMA. By orienting the cavities in the same direction it is possible to polarise the emitted beam as well as enhancing and collecting the emission into a thin cone of light. The degree of linear polarisation of the beam was found to be -0.85 and the emission was enhanced 8 times compared to the same QDs on glass with a beam FWHM of 5°, at an emission angle of 21°.

Chapter 8

Conclusions and Future Work

8.1 Thesis Goals

The overaching goal of this body of work was to develop novel plasmonic polarising features using cutting edge nanophotonics. The following specific goals guided the research herein:

- Development of compact metasurfaces that alter the polarisation state of an incident beam.
- Design and prototyping of a novel metasurface based photodetector to determine the polarisation state of a beam.
- Investigate scalable nanofabrication techniques and device designs, in particular those amenable to a high-throughput printing press environment.
- Produce scalable plasmonic metasurfaces which alter the absorption and emission of photons from quantum sources.

8.2 Outcomes of Work

To achieve the goals outlined above a variety of plasmonic devices, both active and passive, were investigated.

Polarisation Manipulation and Detection

For the alteration of polarisation states an asymmetric cross aperture device was fabricated and design rules laid out. The final metasurface converted linear polarisation to circular, with $S_3 = 0.86$ being the final degree of circular polarisation. Furthermore a chiral aperture metasurface was developed using Bookers' extension to Babinet's Principle. It was found that by optimising the interference between the plasmonic modes of the apertures that a 40 nm patterned silver film could provide 10% difference in transmission of orthogonal circular polarised states. The chiral metasurface was adjusted for use in an aluminium and silicon based polarisation sensitive photodetector. Such a device could potentially be a compact solution to reduce the cost and maintenance of bulk polarisation optics used in polarimetry measurements.

Scalable Fabrication of Nanocavity Metasurfaces

Resistless nanoimprint lithography can address a roadblock currently faced by nanophotonics, namely most devices are not fabricated using industrially scalable techniques. This is a barrier that will need to be overcome before there is large scale uptake of nanophotonics. To better understand the capabilities and limitations of RNIL single cavity masters were fabricated and embossed into silver, aluminium and gold films. Cavities with varying depths and shapes were imprinted in silver and gold. It was shown that by adjusting the applied imprint pressure it is possible to tune the resonant properties of the nanocavities. Silver nanocavities offered lower absorption than gold nanocavities but a greater pressure tuning range, due to a higher Youngs' modulus of plastic deformation. Several applications of nanocavity metasurfaces were demonstrated including a spectral notch filter, absorptive polarisation filter, high resolution colour printing and refractive index sensing substrates for bioscience applications. The scalability of the technique was demonstrated by imprinting a 7 cm by 7 cm array of

nanocavities. Hence, with RNIL, it is possible to create a single large area master template and create metasurfaces with a range of optical responses just by varying the pressure used in the imprinting step or by judicious choice of superstrate refractive index.

Plasmonic Metasurfaces for the Alteration of Emission from Quantum Sources

In chapter 7 the coupling of plasmonic metasurfaces to excitions, such as those supported by quantum dots or wide-band-gap semiconductors, was explored. The primary outcome of the research was distinct changes in the emission rates of quantum dots when placed near plasmonic nanocavity arrays. Metal-insulator-metal nanocavities, created using nanoimprint lithography, provided 4 times the emission brightness associated with a four-fold mean excited state lifetime reduction. The emission from QDs near these rectangular cavities was strongly linearly polarised.

A second type of optical cavity, based on the Fabry-Perot etalon, was also investigated. An array of nanorods, coated with QD doped polymer 130 nm thick and sealed with a silver back-mirror, produced a Purcell enhancement factor of 28.

Finally, a slot based bullseye antenna was developed, which, in addition to the collection and focussing of emission previously demonstrated elsewhere [131], also provides a mechanism for controlling the overall polarisation of the emission beam. Furthermore, through the optimisation of cavity dimensions it was possible to increase the QD emission brightness by a factor of two.

8.3 Key Contributions to Knowledge Stemming from the Work

- Outlined design rules for dipole based wave plates (see §5.2.1 and Ref. [89]).
- Calculated and optimised (2.5x improvement) the response of chiral pairs of slot nanoantennas (see §5.3.3 and Ref. [123]).

- Developed a CMOS-compatible nanometric polarisation photodetector, the first of its kind capable of Stokes polarimetry (see §5.4.5 and Ref. [94]).
- Demonstrated the range of visible wavelength resonances achievable with direct nanoimprinting of single cavities in metal films, using a single imprint master (see chapter 6).
- Demonstrated Purcell enhancement and polarisation for QD-LED geometry analogue via scalable nanopatterning of back contact (see §7.2 and Ref. [133]).
- Added a degree of freedom to the canonical bullseye antenna which allows for the arbitrary polarisation and focussing of quantum dot emission (see §7.4).

8.4 Future Work

Possible further work building on the outcomes of this thesis has been separated into two sections. Firstly, the further expansion of the polarisation photodetector to full Stokes' vector polarimetry is presented. Secondly, possible expansion on the scalable fabrication of nanophotonic devices is discussed.

8.4.1 Extended Spiral Photodiode for Full Stokes' Polarimetry

Although the nanoantenna-enabled polarisation sensitive MSM photodiodes discussed in §5.4.5 were capable of determining the degree of linear or circular polarisation of an incident light beam, the current design is not yet capable of measuring the Stokes' vector of a beam. For applications such as Mueller matrix imaging of biological samples or birefringence imaging of stresses in transparent materials, a single photodiode design, comprising linear, $\pm 45^{\circ}$ and circular polarisation detection channels is needed. Figure 8.1 shows a GDSII file for a potential design. Each pair of channels, from left to right, forms a subset photodiode de-

signed to measure one Stokes' parameter. The relative difference in photocurrent from each pair of channels can then be used to determine values for S_1, S_2 and S_3. By careful calibration of the device prior to use in an experiment, S_0 can be determined from the weighted sum of the photocurrents from each channel. The operating wavelength range would be fixed as it is dependent on antenna dimensions and substrate absorption, but as seen in §5.4.5, the combination of Al antennas and Si substrate produces a low Q, broadband response. Such a device would operate best at the red end of the visible spectrum between 620-720 nm. On the other hand, by spatially separating the nanoantennas from the high refractive index Si, with a thermal oxide layer for example, it would be possible to significantly blue-shift and narrow the operating range. Another benefit of isolating the antennas from the substrate is that non-CMOS compatible materials could be used, such as Ag or Au, which would allow for further optimisation of the device, depending on the application. In particular this configuration should allow for implementation of chiral nanoantennas with a circular polarisation dependent relative transmission difference of up to 18%, as calculated in §5.3.3. The electrical properties of the photodiode could also be improved by gettering the substrate to remove impurities [138], electronic isolation of the contact pads from the substrate to reduce leakage currents, an increase in the ratio of active detection area to metal lead area as shown in figure 8.1 or by using a metal with a larger Schottky barrier, such as Ti, for the leads, to reduce currents driven by thermal diffusion.

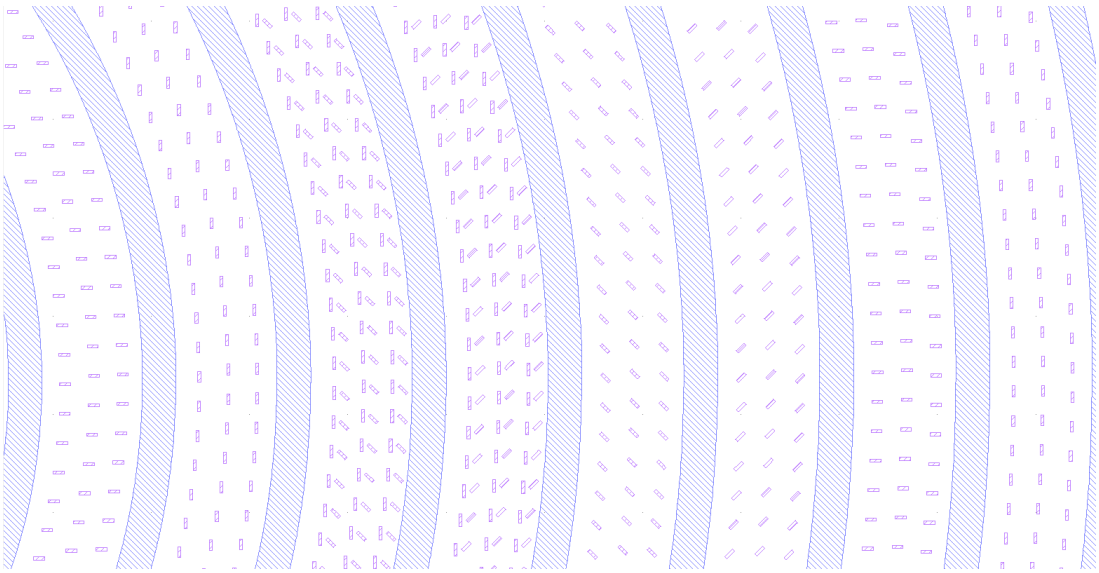


Figure 8.1: GDSII layout file of 6 intertwined MSM photodiodes capable of full Stoke's Vector readout. Each pair of channels is designed to detect one of the polarisation eigenstates.

8.4.2 Nanoimprint Version of QD-Slot-Bullseye

The nanoslot based bullseye (sBE) structures presented in §7.4 were created using common EBL techniques, which allows for very precise control of the cavity dimensions, in particular the cavity depth. The cost of devices fabricated with EBL however, is prohibitively expensive for large scale production. To reduce the cost of these polarising, collimating devices, one could apply the RNIL techniques outlined in §3.4.2. Figure 8.2 shows a rendered image of a Ni master which could be used to produce the linear polarised sBE for QD-PMMA emission at 650 nm. The master would be created using EBL, e-beam evaporation and Ni electroplating. The largest difficulty in creating sBEs with RNIL will be reducing the master–substrate slippage and precisely controlling the final depth of the nanocavities. As the sBE relies on the Purcell effect to polarise and enhance the QD emission, and the enhancement needs to be large enough so that the far-field radiation pattern is dominated by light from the nanocavities and not the surrounding QD-PMMA film (so that a collimated beam is formed), the cavity dimensions are critical. The sensitivity of sBEs to fabrication defects is therefore higher than for the other QD-plasmon devices demonstrated in this thesis. Controlling these factors will be the

largest obstacle to the large scale implementation of sBEs.

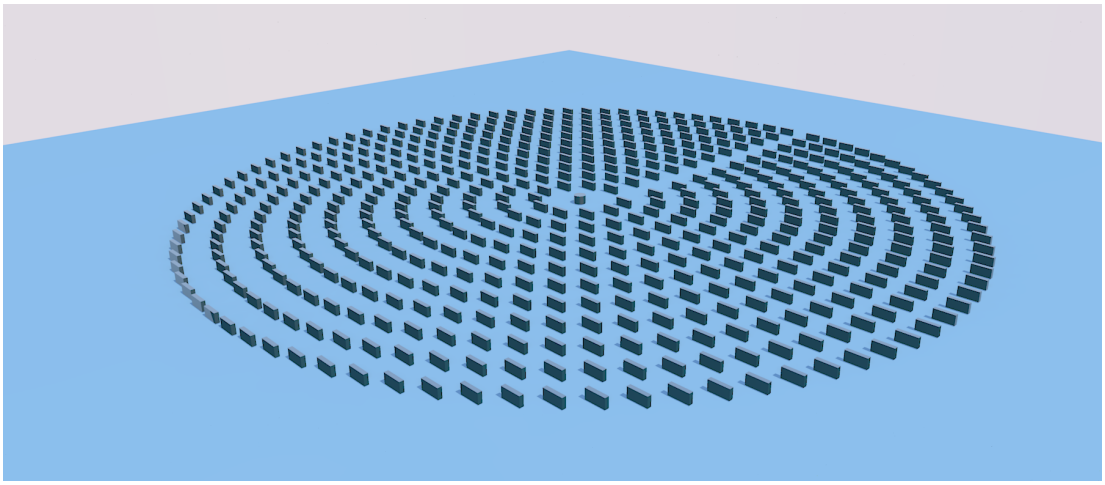


Figure 8.2: Artist's impression of a RNIL master for imprinting a linear slot bullseye.

8.5 Summary

This thesis has presented a variety of plasmonic devices, both active and passive, for the generation, filtering and detection of polarised optical states. Plasmonic quarter-wave plates and chiral aperture metasurfaces were developed to generate and filter circular polarisation states respectively. Chiral nanoantennas were also deployed in a MSM photodiode to determine the polarisation state of an incident optical beam. Resistless nanoimprint lithography was investigated as a means to prepare scalable polarising metasurfaces. One such metasurface was then used to polarise and enhance the emission from a quantum dot doped polymer film. Finally, an arrangement of nanocavities into a bullseye antenna was used to polarise, enhance and focus the emission of light from a QD-doped PMMA film.

Appendices

Appendix A

Far-field Scattering and Localised Surface Plasmon Resonances

To determine the far-field response of a 2D planar plasmonic structure, we need to understand the interaction between the incident EM waves and the electrons at the surface of the structure. Here we follow the work of Davis *et al.* [32], by making the electrostatic approximation, and so decoupling the magnetic flux density from the electric field in Maxwell's Equations, we can model the field scattered from a collection of nano-antennas as a sum over excitation modes. The excited modes are the localised surface plasmons (LSPs) on the surface of metallic nano-features, excited by the incident light field. The electrostatic approximation applies to this case because the particle size is much smaller than wavelength of the incident field. To mathematically describe the far-field scattering we start with the power radiated per solid angle for a dipole emitter:

$$\frac{dP}{d\Omega} = \frac{ck^4}{32\pi^2\epsilon_0}(\hat{n} \times \mathbf{p}) \cdot (\hat{n} \times \mathbf{p}^*), \tag{A.1}$$

where c is the speed of light *in vacuo*, k is the wavenumber, ϵ_0 is the permitivitty of free space, $\mathbf{p}$ is the complex dipole moment, $\mathbf{p}^*$ is its conjugate and $\hat{n}$ is a unit vector in the scattered direction.

If we have an array of particles, we have

$$\frac{dP_{total}}{d\Omega} = \sum_r \frac{dP_r}{d\Omega}, \tag{A.2}$$

where r numbers each of the elements in the array. We shall suppress this henceforth, but we shall be aware that the sum over r in fact applies to all of the following results. We then make the eigenmode decomposition,

$$\mathbf{p} = \sum_k a_k \mathbf{p}_k, \tag{A.3}$$

of the dipole moment. Here k runs over all of the LSP modes and a_k is the excitation amplitude, given in [31] as

$$a_k(\omega) = f_k(\omega)\mathbf{p}_k \cdot \mathbf{E}_0 \tag{A.4}$$

$f_k(\omega)$ is a complex variable ($f_k = |f_k|e^{i\phi_k}$). It is related to the *polarizability* of the nanoparticle in question [32]. This factor can be found by applying a simple Drude model.

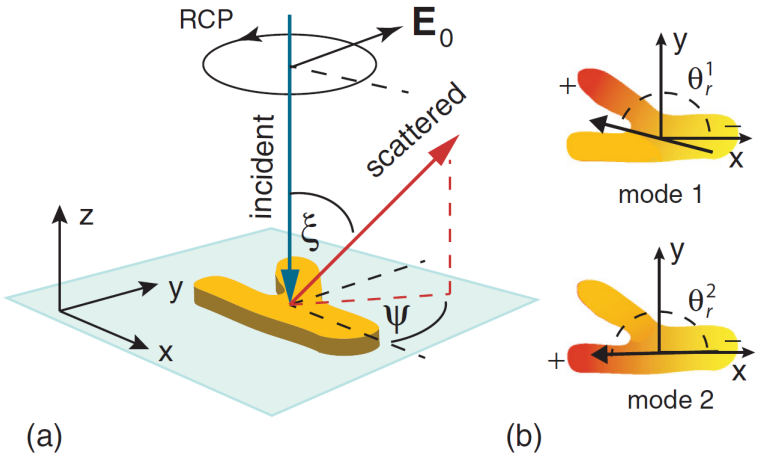


Figure A.1: Example of LSP modes of a chiral nanoparticle [32]

Next we employ the vector identity $(\hat{n} \times \mathbf{p}) \cdot (\hat{n} \times \mathbf{p}^*) = \mathbf{p} \cdot \mathbf{p}^* - (\hat{n} \cdot \mathbf{p})(\hat{n} \cdot \mathbf{p}^*)$ and resolve $\hat{n}$ into xy-plane and z components: $\hat{n} = \cos\xi\hat{z} + \sin\xi(\cos\psi\hat{x} + \sin\psi\hat{y})$, where ξ and ψ are depicted in Fig. A.1. We can do the same thing with $\mathbf{p}_k$ in (A.3),

$\mathbf{p}_k = p_k^z\hat{z} + p_k^{xy}(\cos\theta_k\hat{x} + \sin\theta_k\hat{y})$ where p_k^{xy} is the projection of the k^{th} LSP mode onto the xy-plane and θ_k is the angle between the excited mode and the x-axis. Hence, $\mathbf{p}_k \cdot \hat{n} = \cos\xi p_k^z + \sin\xi\cos(\theta_k - \psi)p_k^{xy}$, where we have used a compound angle formula to simplify the $\cos\psi\cos\theta_k + \sin\psi\sin\theta_k$ term. Inserting this into (A.1), along with our LSP eigenmode decomposition we get

$$\frac{dP}{d\Omega} = \frac{ck^4}{32\pi^2\epsilon_0}\sum_k\sum_j a_k a_j^* p_k^{xy} p_j^{xy}(\cos(\theta_k - \theta_j) + N_{kj}), \tag{A.5}$$

where N_{kj} is the scattering term due to light off normal incidence and is given by

$$\begin{aligned} p_k^{xy}p_j^{xy}N_{kj} = {} & p_k^z p_j^z \sin^2\xi - p_k^{xy}p_j^{xy}\sin^2\xi\cos(\theta_k - \psi)\cos(\theta_j - \psi) \\ & - \frac{1}{2}\sin 2\xi[p_k^{xy}p_j^z\cos(\theta_k - \psi) + p_j^{xy}p_k^z\cos(\theta_j - \psi)]. \end{aligned} \tag{A.6}$$

Clearly it can be seen that $N_{kj} = N_{jk}$ and when $\xi = 0$, that is for normally incident light, $N_{kj} = 0$. Then we combine (A.4) and (A.5) to get

$$\frac{dP}{d\Omega} = \frac{ck^4}{32\pi^2\epsilon_0}\sum_k\sum_j |f_k||f_j|e^{i(\phi_k - \phi j)}(\mathbf{p}_k \cdot \mathbf{E}_0)(\mathbf{p}_j \cdot \mathbf{E}_0^*)p_k^{xy}p_j^{xy}(\cos(\theta_k - \theta_j) + N_{kj}). \tag{A.7}$$

Now to investigate the interference effect in the far-field of light scattered by two co-planar LSP modes, we set the incident electric field to be circularly polarised: $\mathbf{E}_0 = E_0(\hat{x} \pm i\hat{y})$, where +(-) is for a LHCP(RHCP) field. Following the lead of Davis and Eftekhari [32], we insert $\mathbf{p}_k \cdot \mathbf{E}_0 = p_k^{xy}E_0 e^{\pm i\theta_k}$ into (A.7), which results in

$$\frac{dP}{d\Omega} = \frac{ck^4E_0^2}{32\pi^2\epsilon_0}\sum_k\sum_j |f_k||f_j|e^{i((\phi_k - \phi_j)\pm(\theta_k - \theta_j))}(p_k^{xy}p_j^{xy})^2(\cos(\theta_k - \theta_j) + N_{kj}). \tag{A.8}$$

We then note that if we expand the exponential using Euler's identity, we get

$$\begin{aligned} \frac{dP}{d\Omega} = {} & \frac{ck^4E_0^2}{32\pi^2\epsilon_0}\sum_k\sum_j |f_k||f_j|(p_k^{xy}p_j^{xy})^2[\cos(\theta_k - \theta_j) + N_{kj}][\cos(\phi_k - \phi_j)\cos(\theta_k - \theta_j) \\ & \mp\sin(\phi_k - \phi_j)\sin(\theta_k - \theta_j) \pm i\cos(\phi_k - \phi_j)\sin(\theta_k - \theta_j) + i\cos(\theta_k - \theta_j)\sin(\phi_k - \phi_j)], \end{aligned} \tag{A.9}$$

the imaginary parts are odd functions, and the real part is even (recall $N_{kj} =$

N_{jk}, under dummy index interchange ($k \leftrightarrow j$). We can then use this fact and the identity $\sum_k \sum_j a_k b_j = \frac{1}{2}(\sum_k \sum_j a_k b_j + \sum_j \sum_k a_j b_k)$ to rid ourselves of the imaginary terms in (A.9).

Doing this finally yields the result reported in [32]:

$$\frac{dP}{d\Omega} = \frac{ck^4 E_0^2}{32\pi^2 \epsilon_0} \sum_k \sum_{j \leq k} |f_k||f_j|(p_k^{xy} p_j^{xy})^2 [\cos(\theta_k - \theta_j) + N_{kj}][\cos(\phi_k - \phi_j)\cos(\theta_k - \theta_j) \mp \sin(\phi_k - \phi_j)\sin(\theta_k - \theta_j)]. \tag{A.10}$$

Appendix B

Calibration of Polarisation Resolved Far-Field Emission Pattern Images

In order to calibrate the polarisation resolved far-fiedl imaging a 400 μm square 2000 nm period, 50:50 duty cycle diffraction grating was fabricated adjacent the sBE structures. When illuminated with $lambda = 600$ nm laser light the diffraction pattern, see figure B.1, observed on the CCD camera had three distinct orders. For a grating period of 2000 nm and refractive index of $n = 1.5$, the third diffracted order is at the angle corresponding to a Numerical Aperture of 0.9, exactly the NA of the microscope objective in use. Knowing the pixel number in the image of the $m = \pm 3$ orders allows us to calibrate the far-field imaging system. Further more, the lower orders can be used to check the calibration as they should occur at NA=0.3 and NA=0.6 in the image. The zeroth order reflection gives us the centre coordinate of our far-field image. For a fixed wavelength, the co-ordinates in the NA calibrated far-field image will give the momentum distribution of the emitted photons.

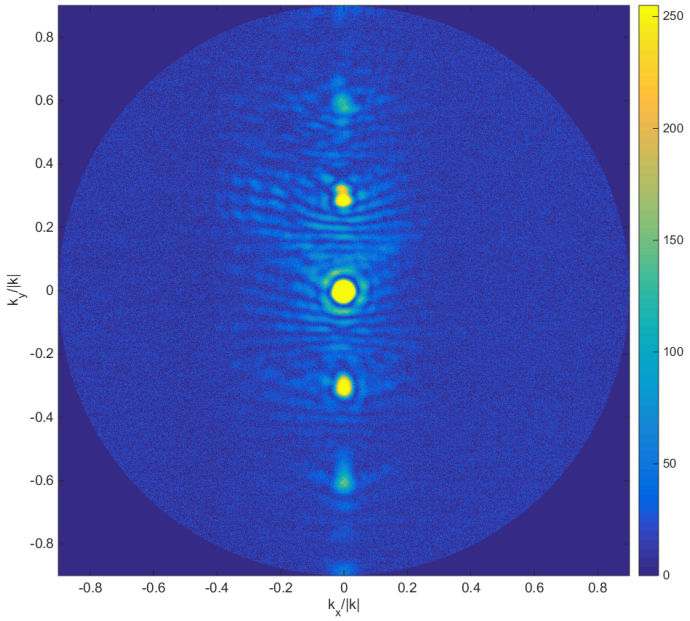


Figure B.1: Diffraction pattern from a 2000 nm period grating as measured by the far-field imaging set-up.

Appendix C

Random Plasmonic Metalon for Hot Carrier Generation

C.1 Introduction

This appendix covers the controlled evaporation of very thin ($\leq$ 10 nm) metal films to make random metasurfaces for the generation of hot charge carriers. The experimental work covered here was carried out by Dr Daniel Gomez and Dr Charlene Ng of the CSIRO. It is included in this thesis as it contains work on the simulation of large, dense arrays of random nanoparticles, which could form the basis of a low cost metallic printing material or as a solar driven security feature. The following work was published in *ACS Nano* [47].

In addition to altering the emission properties of QDs in §7, plasmon-exciton coupling is also investigated in the context of a transparent photodetector. The detector is comprised of a thin, transparent film of TiO_2 (a wide band-gap semiconductor) sandwich between a back contact mirror and a random gold metasurface. When sub-band-gap photons excite a plasmon there is a small probability the plasmon will decay into a hot electron which is then injected into the semiconductors conduction band. Here a detailed finite element analysis is developed in

order to help understand the complex physical interaction taking place. This device could form a highly novel covet security feature as it would appear to merely be a coloured region, but when connected to an ammeter and illuminated a small current would flow. The fabrication steps required to manufacture this device are thermal evaporation and annealing, no lithographic step is required. Potentially this feature could be produced on a large scale and at low cost.

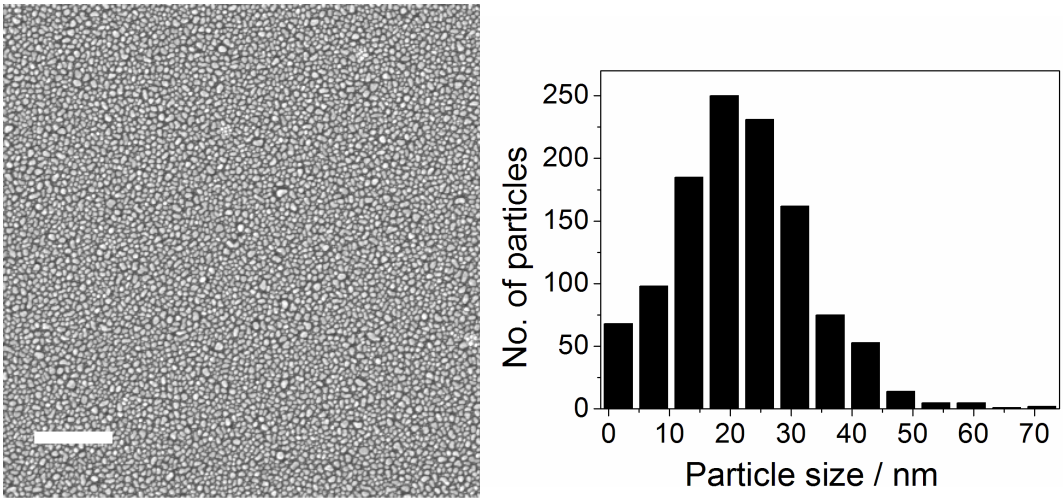
The cost of devices formed with this e-beam evaporation technique is low as there is no lithographic step required and the evaporative step is scalable. The random metasurface is used as one side of a randomized Fabry-Perot cavity, greatly increasing the spectral range of the device's absorbance. FEM modelling is used to understand where in the structure the absorption occurs and how it can be optimized for use in solar driven photocatalysis.

C.2 A Broadband Gires-Tournois Metalon Based Hot Electron Photodetector

In addition to the enhancement of quantum emission, a metasurface based etalon can also be used to mediate hot electron transfer into a semiconducting substrate's conduction band, even at photon energies below that of the bandgap [139]. That is, a measurable photocurrent can be generated when illuminating the device with light that does not have enough energy to directly create a hole-electron pair in the semiconductor. Such systems are interesting in their own right as well as applications in solar power or photocatalytic hydrogen production [47] and could find use as a novel active security feature [140]. A large increase in absorption cross-section provided by nanoantennas, however thus far, the incident photon conversion efficiency (IPCE) of such devices are less than 1% and thought to have a theoretical maximum efficiency of less than 10%, as the hot electron injection

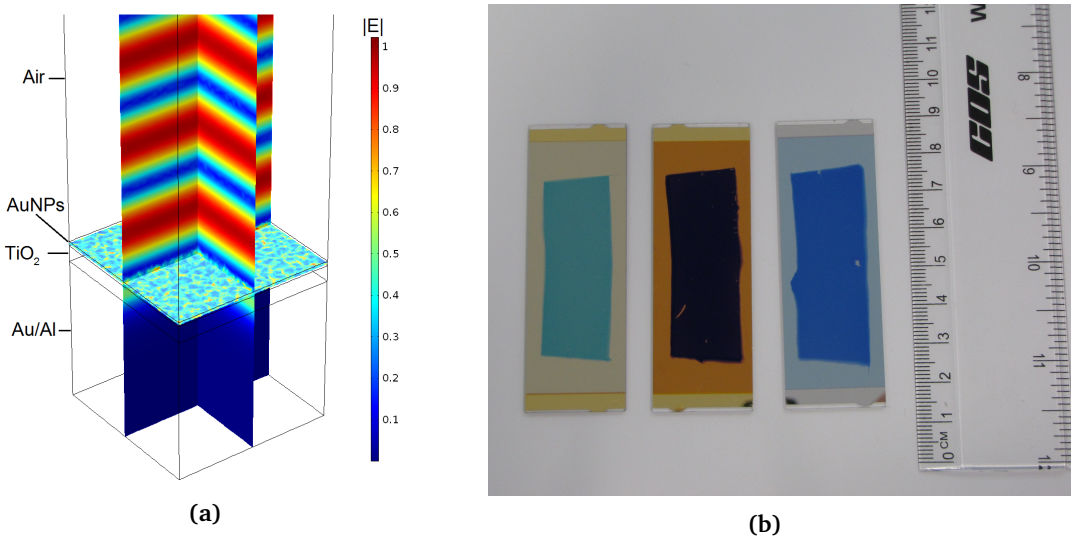
mechanism is a low probability event [141]. As such devices cannot yet (and may never) compete on efficiency with well established Si photovoltaic designs they must be fabricated with more energy and cost efficient techniques.

Here TiO_2 is the chosen semiconductor as it is a cheap, abundant, wide bandgap transparent semiconducting oxide. It typically has a refractive index around 2.4 and, unlike silicon, provides good adhesion to the noble metals commonly used in plasmonics. 250 nm Al or Au layers are evaporated onto glass substrates and act as mirrors *and* back contacts. 50 nm of TiO_2 is then deposited in an oxygen rich atmosphere to ensure stoichiometric titania is deposited. Finally a 7 nm layer of gold or aluminium is deposited. Due to the surface energy of such a thin film on the TiO_2 film, nanoislands (held together by surface tension) of gold are formed. Figure C.1 shows an SEM image of the gold nanoparticle (AuNP) metasurface created with thin film evaporation as well as the distribution of particle size. The mean particle size is 22.4 nm. For such small AuNP's it is well known from Mie theory that the absorption cross-section is much larger than the scattering cross-section [23]. The large spread of nanoparticle sizes leads to a strongly absorbing broadband optical response. Figure C.2(a) shows the structure of the metalon as implemented in COMSOL Multiphysics, with electric field norm at $\lambda = 650$ nm. Figure C.2(b) shows a photograph of three metalon samples (Au mirror 50 nm TiO_2 AlNP, Au mirror 50 nm TiO_2 AuNPs and Al mirror 50 nm TiO_2 AuNPs). Immediately it is obvious that the AuNP–Au mirror system provides very high broadband absorption as the metalon appears very black. Henceforth the investigation focusses on this system. The scalable nature of this simple fabrication technique is also clearly demonstrated by the large area uniformly covered by the nanoparticles.



(a) (b)

Figure C.1: (a) SEM of the random gold metasurface (scale bar is 1 μm) and (b) Measured size distribution of the Au nanoparticles.



(a) (b)

Figure C.2: (a)Metalon geometry used in FEM calculations, overlaid with calculated electric field at $\lambda = 650$ nm and (b) photograph of the large area metalons (from left to right) AlNPs on 50 nm TiO_2 on Au mirror, AuNPs on 50 nm TiO_2 on Au mirror and AuNPs on 50 nm TiO_2 on Al mirror.

C.2.1 Finite element method (FEM) calculations of Fields and Absorption in Random Metalons

To generate a measurable photocurrent the majority of the absorption and thus generation of hot electrons should occur in the AuNP layer. To determine the distribution of absorption FEM calculations are used. The FEM calculations were carried out using COMSOL Multiphysics 5.0, using the model geometry shown in

figure C.2(a). The model consists of a 500 nm x 500 nm x 2000 nm unit cell, with periodic boundary conditions on the sides and scattering boundary conditions for the top and bottom boundaries. The nanoparticle (AuNP) layer was 14 nm thick, the TiO_2 layer was allowed to have variable thickness and the reflecting mirror had a fixed thickness of 150 nm. The refractive index of Au taken from literature [45]. The AuNP layer thickness was determined by calculating the surface coverage of nanoparticles (47%) from the SEM image shown in the main text and applying volume conservation. A 7 nm solid gold film has the same volume as a 14 nm film with 47% surface coverage, so take 14 nm as the average height of the nanoparticles. The optical constants of the TiO_2 film were taken from ellipsometry data. Illumination was modelled with a plane wave launched from the top boundary of the simulation geometry.

Figure C.3 shows the scheme used to calculate the total absorption in the metal/semiconductor/metal structures and the absorption of light by the AuNP film and the reflecting layer. The first step is to convert the measured SEM image to a monochrome bitmap. A function f is then created whose value at a particular coordinate (x, y) in the image is 1 if there is gold at that location and 0 otherwise:

$$f(x,y) = \begin{cases} 0 & \text{pixel(x,y) = black,} \\ 1 & \text{pixel(x,y) = white.} \end{cases} \tag{C.1}$$

With f, it is possible to define a spatially dependent relative permittivity:

$$\epsilon(x,y,\lambda) = \epsilon_0 + f(x,y)(\epsilon_{Au}(\lambda) - \epsilon_0). \tag{C.2}$$

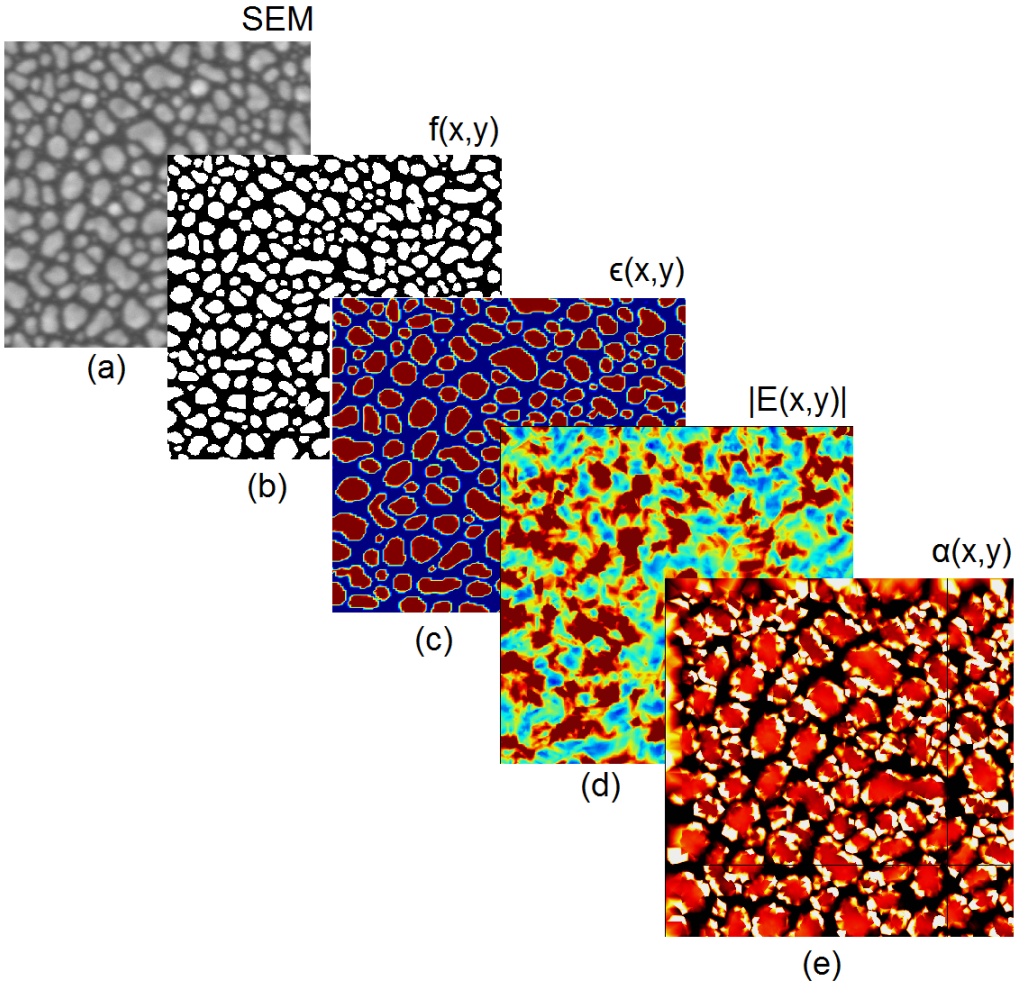


Figure C.3: A scheme for calculating absorption from SEM image. Convert the SEM (a) into a monochrome bitmap (b), then use this to define a material with $\epsilon(x, y)$, a spatially dependant relative permittivity, (c). This material can then be used in FEM calculations to determine the electric field (d) and thus the electromagnetic absorption, α, in the layer (e).

C.2.2 Broadband Absorption

Figure C.4 shows the optical properties of the fabricated metalon. Multiple reflections in the semiconductor layer lead to a suppression of reflected light and a large increase in absorption [125], as shown in the inset to figure C.4(A). The diffuse and specular reflectance (R) and transmittance (T) spectra from the metalon were measured by Dr. Ng using a UV-VIS spectrophotometer (Perkin-Elmer Lambda 1050) with an integrating sphere and small spot kit. With these two measurements, the absorbance was calculated as $A = 1 - R - T$. Figure C.4(B) shows the absorption spectra for the metalon, 50 nm TiO_2 on a gold mirror, AuNPs on

TiO_2 without a mirror and bare TiO_2. The bare TiO_2 shows no absorbance, as the band-gap corresponds to a UV wavelength of 370 nm, The samples with just a mirror or just an AuNP layer show a broad absorption peak of around 20%, whereas the metalon has absorbance around 80% over a spectral range of 500 nm, much wider and higher than the metalons presented in the previous section. Figure C.4(C) shows the calculated electric field intensity distribution in the metalon at $\lambda = 650$ nm. A field node can be seen at the AuNP, where there is also strong field confinement due to the LSPs excited on the AuNPs. The effect of this is shown in figure C.4(D), where the absorption in each metallic layer is calculated. We see for shorter wavelengths the total system absorption tends towards the absorption in the mirror, this is because at these shorter wavelengths the field node is forced closer to mirror and the interband transition in gold (at $\lambda = 500$ nm) inhibits the plasmonic response of the AuNPs. For wavelengths above 500 nm the majority of the absorption occurs in the nanoparticle layer, which is critical for the electrical aspects of the device to work.

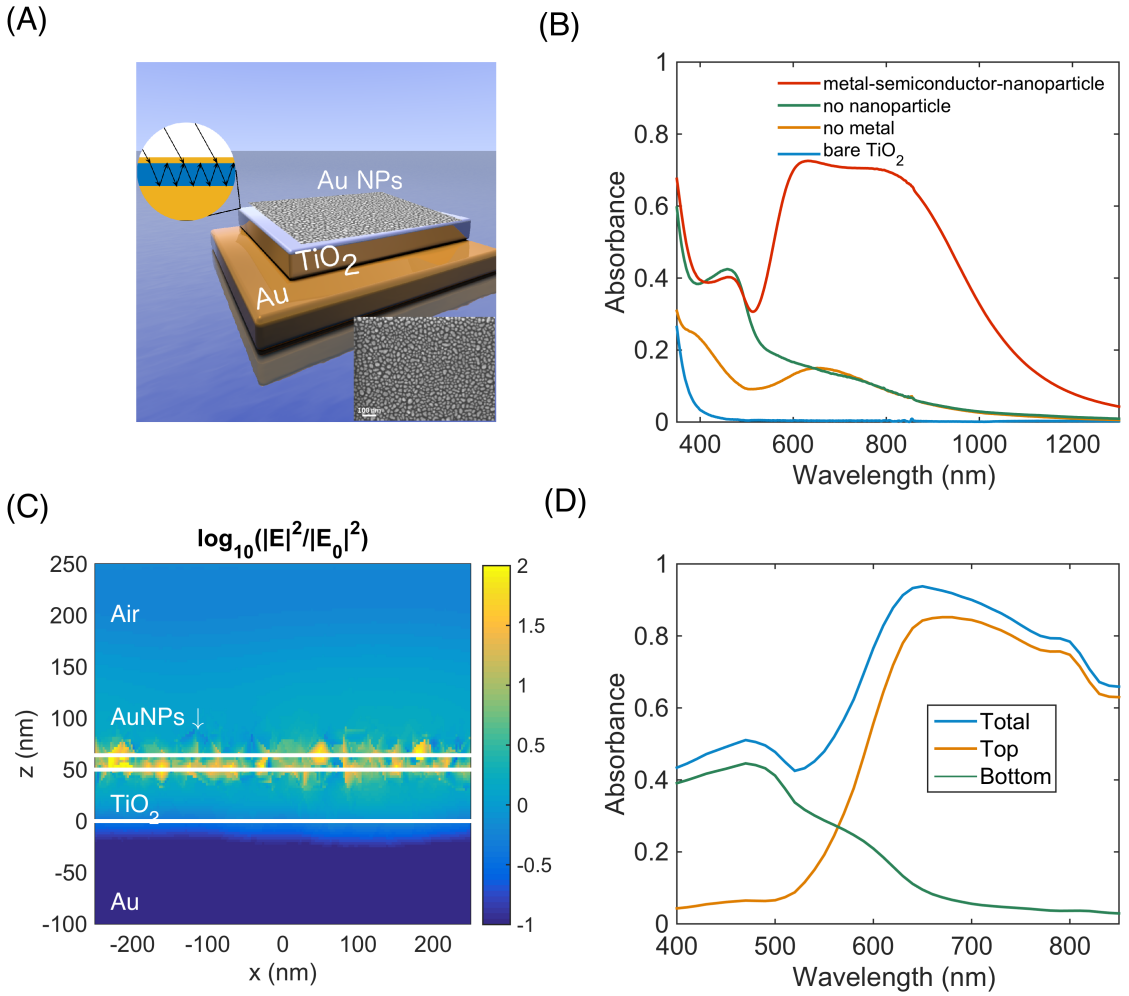


Figure C.4: Architecture and working principle of plasmonic broadband absorber structure. (A) Schematic of the broadband absorber structure with TiO_2 positioned in between the Au mirror and Au nanoparticles. Inset: multiple internal reflection and interference interpretation of unit absorption [125]. Also shown is an SEM of the Au nanoparticle monolayer. (B) Absorbance spectra of the metalon, metalon without Au NPs, metalon without mirror and bare TiO_2 on glass. (C) Spatial distribution of the Electric field of the metal–semiconductor–nanoparticle structures at 650 nm. The values are shown on a logarithmic scale of the absolute magnitude square of the electric field relative to the incident field. (D) Plot of the absorption of incident light *vs.* wavelength for the top and bottom metal layers.

C.2.3 Sub-Bandgap Hot Electron Injection Photocurrent

In order to measure the photocurrent and IPCE of the broadband metalon device the designed structure and platinum wire was employed as the working electrode and counter electrode respectively in a 2 electrode system, as shown in figure C.5(A). The exposed surface area of the working electrode was 1 cm in diameter. The electrolyte solution used was 0.5 M Na_2SO_4 (anhydrous, Sigma-Aldrich, $\geq$99%) with 20 v/v % amount of methanol (Sigma-Aldrich, $\geq$99.9%) or

ethanol (Sigma-Aldrich, $\geq$99.9%) as the sacrificial reagent. The 0.5 M Na_2SO_4 was employed to reduce the resistance in the electrolyte solution. Prior to the photocurrent measurements, the solutions were purged with N_2 gas to remove electron scavenging O_2. The working potential was set at +0.5 V versus the Pt wire and the devices were illuminated with light from a 300 W Xenon lamp (Newport Model no. 669092) using a $\geq$ 495 nm cut-off filter (Thorlabs FGL-495). The applied voltage and photocurrent I were recorded with a potentiostat (AutoLab PGSTAT204). To measure the IPCE values, light from the Xenon lamp was coupled to a monochromator with a bandwidth of 5 nm at full width at half maximum (FWHM). The light intensity P of the monochromatic light at each wavelength was measured using a Thorlabs optical power and energy meter (Model. PM100D). The incident photon to electron efficiency (IPCE) was calculated by the following formula:

$$\text{IPCE} = 100 \times \frac{I(A/cm^2)}{P(W/cm^2)} \times \frac{1240}{\lambda(nm)}. \tag{C.3}$$

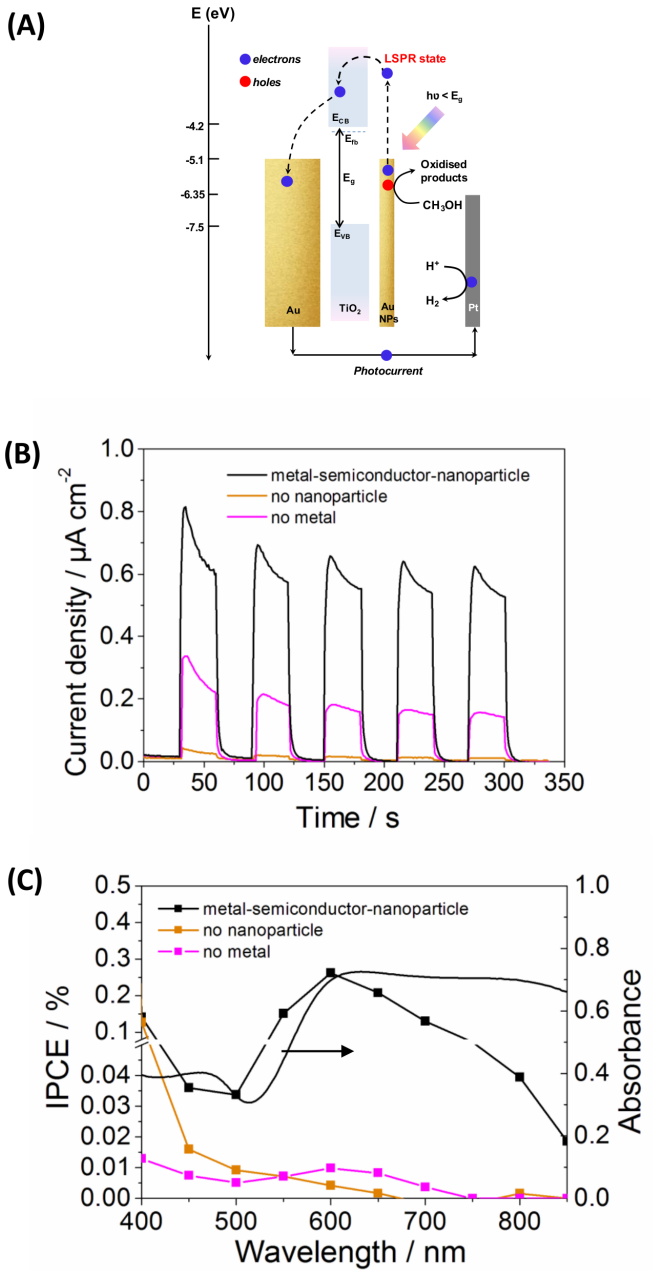


Figure C.5: Photoelectrochemical and absorption performance of the plasmonic broadband absorber structure. (A) Illustration of the working principle: Upon visible light illumination and plasmon non–radiative relaxation, hot electrons in the Au nanoparticles can be injected into TiO_2 and be transported subsequently to the Pt counter electrode and measured as photocurrents. E_{CB}, E_{VB} and E_g refer to conduction band, valence band and band gap energy of TiO_2 respectively. (B) Photocurrent generation under both visible light illumination ($\lambda \geq 495$ nm) and in the dark in a 2 electrode system vs Pt wire; applied voltage of 0.5 V and 0.5 M Na_2SO_4 + 20 v/v% methanol electrolyte solution. (C) IPCE values for the metalon (black), TiO_2 on a gold mirror (orange) and on glass (pink). Also shown is the absorption spectrum of the metal–semiconductor–nanoparticle structure (solid black).

Figure C.5(B) shows the measured current density as a function of time with the illumination cycled on and off. During an on cycle there is a slow decrease

in current density due to accumulation of oxygen around the AuNPs effectively slowing the scavenging of holes from the AuNPs, which slows the production of hot electrons. Nevertheless the metalon exhibits 4 times the photocurrent than the AuNP layer on TiO_2 without the back reflecting mirror and 56 times the current detected for the sample without the metasurface.

Figure C.5(C) shows the calculated ICPE for the samples. The metalon exhbits a peak efficiency of 0.3% at $\lambda = 600$ nm, paltry compared to the 20% achieved with mono-Si solar cells. However this comparison is unfair as solar cells operate above the band-gap, a much more efficient process. The IPCE closely follows the spectral absorption of the metalon for $\lambda \leq 700$nm. At longer wavelengths the photon energy, E_p, is not enough to inject hot electrons from the gold Fermi level, E_F, across the Schottky barrier, E_{SB}, that is $E_p + E_F < E_{SB}$, so the efficiency tails off as E_p approaches $E_{SB} - E_f$. The IPCE for the other two samples is negligible as the total absorption is low.

C.2.4 Summary

This appendix introduced a random metalon for the generation of hot electrons from sub-band-gap photons. By evaporation of very thin gold films onto TiO_2 substrates with a gold back contact it was possible to absorb 80% of incident light over a 500 nm spectral range and convert 0.3% of photons into a measurable photocurrent.

Bibliography

[1] J. D. Jackson, *Classical electrodynamics*. Wiley, 1999.

[2] Y. Shirasaki, G. J. Supran, M. G. Bawendi, and V. Bulović, "Emergence of colloidal quantum-dot light-emitting technologies," *Nature Photonics*, vol. 7, no. 1, pp. 13–23, 2013.

[3] J. Beuthan, O. Minet, J. Helfmann, M. Herrig, and G. Müller, "The spatial variation of the refractive index in biological cells," *Physics in medicine and biology*, vol. 41, no. 3, p. 369, 1996.

[4] S. B. Mehta, M. Shribak, and R. Oldenbourg, "Polarized light imaging of birefringence and diattenuation at high resolution and high sensitivity," *Journal of Optics*, vol. 15, no. 9, p. 094007, 2013.

[5] R. Hegedüs, S. Åkesson, R. Wehner, and G. Horváth, "Could vikings have navigated under foggy and cloudy conditions by skylight polarization? on the atmospheric optical prerequisites of polarimetric viking navigation under foggy and cloudy skies," in *Proceedings of the Royal Society of London A: Mathematical, Physical and Engineering Sciences*, vol. 463, no. 2080. The Royal Society, 2007, pp. 1081–1095.

[6] L. Li, T. Li, X. Tang, S. Wang, Q. Wang, and S. Zhu, "Plasmonic route to reconfigurable polarization optics," *arXiv preprint arXiv:1405.1311*, 2014.

[7] J. Wang, J.-Y. Yang, I. M. Fazal, N. Ahmed, Y. Yan, H. Huang, Y. Ren, Y. Yue, S. Dolinar, M. Tur *et al.*, "Terabit free-space data transmission employing

orbital angular momentum multiplexing," *Nature photonics*, vol. 6, no. 7, pp. 488–496, 2012.

[8] K. Katoh, K. Hammar, P. J. Smith, and R. Oldenbourg, "Birefringence imaging directly reveals architectural dynamics of filamentous actin in living growth cones," *Molecular biology of the cell*, vol. 10, no. 1, pp. 197–210, 1999.

[9] S. Chen, W. Liu, Z. Li, H. Cheng, and J. Tian, "Polarization state manipulation of electromagnetic waves with metamaterials and its applications in nanophotonics," in *Metamaterials-Devices and Applications*. InTech, 2017.

[10] S. Linic, P. Christopher, and D. B. Ingram, "Plasmonic-metal nanostructures for efficient conversion of solar to chemical energy," *Nature materials*, vol. 10, no. 12, pp. 911–921, 2011.

[11] A. F. Koenderink, A. Alù, and A. Polman, "Nanophotonics: Shrinking light-based technology," *Science*, vol. 348, no. 6234, pp. 516–521, 2015.

[12] T. D. James, P. Mulvaney, and A. Roberts, "The plasmonic pixel: large area, wide gamut color reproduction using aluminum nanostructures," *Nano Letters*.

[13] Z. Liu, H. Lee, Y. Xiong, C. Sun, and X. Zhang, "Far-field optical hyperlens magnifying sub-diffraction-limited objects," *Science*, vol. 315, no. 5819, pp. 1686–1686, 2007.

[14] X. Zhou and L. Zhou, "Analysis of subwavelength bandpass plasmonic filters based on single and coupled slot nanocavities," *Applied optics*, vol. 52, no. 3, pp. 480–488, 2013.

[15] M. Alam, J. S. Aitchison, and M. Mojahedi, "Compact and silicon-on-insulator-compatible hybrid plasmonic te-pass polarizer," *Optics Letters*, vol. 37, no. 1, pp. 55–57, 2012.

[16] M. Imboden and D. Bishop, "Top-down nanomanufacturing," *Physics Today*, vol. 67, no. 12, pp. 45–50, 2014.

[17] L. Varghese, L. Fan, Y. Xuan, C. Tansarawiput, S. Kim, and M. Qi, "Resistless nanoimprinting in metal for plasmonic nanostructures." *Small*, 2013. [Online]. Available: http://dx.doi.org/10.1002/smll.201300168

[18] R. W. Wood, "Xlii. on a remarkable case of uneven distribution of light in a diffraction grating spectrum," *The London, Edinburgh, and Dublin Philosophical Magazine and Journal of Science*, vol. 4, no. 21, pp. 396–402, 1902.

[19] L. Novotny and B. Hecht, *Principles of Nano-Optics*. Cambridge Univ Pr, 2006.

[20] H. Ghaemi, T. Thio, D. e. a. Grupp, T. W. Ebbesen, and H. Lezec, "Surface plasmons enhance optical transmission through subwavelength holes," *Physical Review B*, vol. 58, no. 11, p. 6779, 1998.

[21] L. Lin, L. Hande, and A. Roberts, "Resonant nanometric cross-shaped apertures: Single apertures versus periodic arrays," *Applied Physics Letters*, vol. 95, no. 20, pp. 201 116–201 116, 2009.

[22] J. Cadusch, T. James, T. Davis, and A. Roberts, "A metamaterial antenna approach to near infra-red polarisation state control," *Conference on Optoelectronic and Microelectronic Materials and Devices (COMMAD) 2012*, pp. 63 – 64, 2012.

[23] S. A. Maier, *Plasmonics: fundamentals and applications*. Springer, 2007.

[24] G. Mie, "Beiträge zur optik trüber medien, speziell kolloidaler metallösungen," *Annalen der physik*, vol. 330, no. 3, pp. 377–445, 1908.

[25] I. Aitchison and A. Hey, *Gauge theories in particle physics*. Taylor & Francis, 2004, vol. 2.

[26] A. Garcia-Etxarri and J. Dionne, "A framework for surface enhanced circular dichroism spectroscopy mediated by non-chiral nanoantennas," *Arxiv preprint arXiv:1209.0288*, 2012.

[27] W. McBride, "Thalidomide and congenital abnormalities," *Lancet*, vol. 2, no. 1.358, 1961.

[28] R. D'Amato, M. Loughnan, E. Flynn, and J. Folkman, "Thalidomide is an inhibitor of angiogenesis," *Proceedings of the National Academy of Sciences*, vol. 91, no. 9, p. 4082, 1994.

[29] B. Barlogie, R. Desikan, P. Eddlemon, T. Spencer, J. Zeldis, N. Munshi, A. Badros, M. Zangari, E. Anaissie, J. Epstein *et al.*, "Extended survival in advanced and refractory multiple myeloma after single-agent thalidomide: identification of prognostic factors in a phase 2 study of 169 patients," *Blood*, vol. 98, no. 2, pp. 492–494, 2001.

[30] S. Zumdahl, *Chemical principles*. Brooks/Cole Pub Co, 2007.

[31] K. C. Vernon, A. M. Funston, C. Novo, D. E. Gómez, P. Mulvaney, and T. J. Davis, "Influence of particle- substrate interaction on localized plasmon resonances," *Nano Letters*, vol. 10, no. 6, pp. 2080–2086, 2010.

[32] F. Eftekhari and T. Davis, "Strong chiral optical response from planar arrays of subwavelength metallic structures supporting surface plasmon resonances," *Physical Review B*, vol. 86, no. 7, p. 075428, 2012.

[33] V. Valev, N. Smisdom, A. Silhanek, B. De Clercq, W. Gillijns, M. Ameloot, V. Moshchalkov, and T. Verbiest, "Plasmonic ratchet wheels: switching circular dichroism by arranging chiral nanostructures," *Nano Letters*, vol. 9, no. 11, pp. 3945–3948, 2009.

[34] P. Alitalo and S. Tretyakov, "Electromagnetic cloaking with metamaterials," *Materials today*, vol. 12, no. 3, pp. 22–29, 2009.

[35] S. Zhang, Y.-S. Park, J. Li, X. Lu, W. Zhang, and X. Zhang, "Negative refractive index in chiral metamaterials," *Physical review letters*, vol. 102, no. 2, p. 023901, 2009.

[36] J. Pendry, "A chiral route to negative refraction," *Science*, vol. 306, no. 5700, pp. 1353–1355, 2004.

[37] Z. Fan and A. O. Govorov, "Plasmonic circular dichroism of chiral metal nanoparticle assemblies," *Nano Letters*, vol. 10, no. 7, pp. 2580–2587, 2010.

[38] A. Kuzyk, R. Schreiber, Z. Fan, G. Pardatscher, E.-M. Roller, A. Högele, F. C. Simmel, A. O. Govorov, and T. Liedl, "Dna-based self-assembly of chiral plasmonic nanostructures with tailored optical response," *Nature*, vol. 483, no. 7389, pp. 311–314, 2012.

[39] G. Snatzke, "Circular dichroism and optical rotatory dispersionprinciples and application to the investigation of the stereochemistry of natural products," *Angewandte Chemie International Edition in English*, vol. 7, no. 1, pp. 14–25, 1968.

[40] J. B. Khurgin, G. Sun, and R. Soref, "Practical limits of absorption enhancement near metal nanoparticles," *Applied Physics Letters*, vol. 94, no. 7, p. 071103, 2009.

[41] J. A. Fan, C. Wu, K. Bao, J. Bao, R. Bardhan, N. J. Halas, V. N. Manoharan, P. Nordlander, G. Shvets, and F. Capasso, "Self-assembled plasmonic nanoparticle clusters," *Science*, vol. 328, no. 5982, pp. 1135–1138, 2010.

[42] S. Y. Chou, P. R. Krauss, and P. J. Renstrom, "Nanoimprint lithography," *Journal of Vacuum Science & Technology B*, vol. 14, no. 6, pp. 4129–4133, 1996.

[43] S. Kim, Y. Xuan, V. P. Drachev, L. T. Varghese, L. Fan, M. Qi, and K. J. Webb, "Nanoimprinted plasmonic nanocavity arrays," *Optics Express*, vol. 21, no. 13, pp. 15 081–15 089, 2013.

[44] H. T. Miyazaki and Y. Kurokawa, "Squeezing visible light waves into a 3-nm-thick and 55-nm-long plasmon cavity," *Physical review letters*, vol. 96, no. 9, p. 097401, 2006.

[45] E. D. Palik, *Handbook of optical constants of solids*. Academic press, 1998, vol. 3.

[46] A. Kwadrin, C. I. Osorio, and A. F. Koenderink, "Backaction in metasurface etalons," *Physical Review B*, vol. 93, no. 10, p. 104301, 2016.

[47] C. Ng, J. J. Cadusch, S. Dligatch, A. Roberts, T. J. Davis, P. Mulvaney, and D. E. Gómez, "Hot carrier extraction with plasmonic broadband absorbers," *ACS nano*, vol. 10, no. 4, pp. 4704–4711, 2016.

[48] N. Liu, M. Mesch, T. Weiss, M. Hentschel, and H. Giessen, "Infrared perfect absorber and its application as plasmonic sensor," *Nano Letters*, vol. 10, no. 7, pp. 2342–2348, 2010.

[49] M. K. Hedayati, M. Javaherirahim, B. Mozooni, R. Abdelaziz, A. Tavassolizadeh, V. S. K. Chakravadhanula, V. Zaporojtchenko, T. Strunkus, F. Faupel, and M. Elbahri, "Design of a perfect black absorber at visible frequencies using plasmonic metamaterials," *Advanced Materials*, vol. 23, no. 45, pp. 5410–5414, 2011.

[50] F. G. De Abajo, "Colloquium: Light scattering by particle and hole arrays," *Reviews of Modern Physics*, vol. 79, no. 4, p. 1267, 2007.

[51] E. M. Purcell, "Spontaneous emission probabilities at radio frequencies," *Physical Review*, vol. 69, p. 681, 1946.

[52] C. Sauvan, J.-P. Hugonin, I. Maksymov, and P. Lalanne, "Theory of the spontaneous optical emission of nanosize photonic and plasmon resonators," *Physical Review Letters*, vol. 110, no. 23, p. 237401, 2013.

[53] M. Altissimo, "E-beam lithography for micro-/nanofabrication," *Biomicrofluidics*, vol. 4, no. 2, p. 026503, 2010.

[54] M. Köfferlein, "Klayouthigh performance layout viewer and editor," *Version 0.23*, vol. 11.

[55] T. James, Z. Teo, D. Gomez, T. Davis, and A. Roberts, "The plasmonic j-pole antenna," *Applied Physics Letters*, vol. 102, no. 3, p. 033106, 2013.

[56] A. Agosta, "Enhancement of erbium photoluminscence using plasmonic nanostructures," *MSc. thesis*, 2013.

[57] P. Wrobel, T. Stefaniuk, M. Trzcinski, A. A. Wronkowska, A. Wronkowski, and T. Szoplik, "Ge wetting layer increases ohmic plasmon losses in ag film due to segregation," *ACS applied materials & interfaces*, vol. 7, no. 17, pp. 8999–9005, 2015.

[58] A. Kinkhabwala, Z. Yu, S. Fan, Y. Avlasevich, K. Müllen, and W. Moerner, "Large single-molecule fluorescence enhancements produced by a bowtie nanoantenna," *Nature Photonics*, vol. 3, no. 11, pp. 654–657, 2009.

[59] L. T. Varghese, L. Fan, Y. Xuan, C. Tansarawiput, S. Kim, and M. Qi, "Resistless nanoimprinting in metal for plasmonic nanostructures," *Small*, vol. 9, no. 22, pp. 3778–3783, 2013.

[60] W. G. Strang and G. J. Fix, *Analysis of the finite element method*. Prentice-Hall, 1973.

[61] P. R. Amestoy, I. S. Duff, J.-Y. LExcellent, and J. Koster, "Mumps: a general purpose distributed memory sparse solver," in *Applied Parallel Computing. New Paradigms for HPC in Industry and Academia*. Springer, 2001, pp. 121–130.

[62] "http://www.comsol.com/blogs/meshing-and-optimization-in-engineering-magazines/."

[63] T. D. James, T. J. Davis, and A. Roberts, "Optical investigation of the j-pole and vee antenna families," *Optics Express*, vol. 22, no. 2, pp. 1336–1341, 2014.

[64] "Thor labs website," 2017. [Online]. Available: https://www.thorlabs.com/navigation.cfm?guide_id=2004

[65] E. Collett, "Measurement of the four stokes polarization parameters with a single circular polarizer," *Optics Communications*, vol. 52, 1984. [Online]. Available: http://dx.doi.org/10.1016/0030-4018(84)90286-4

[66] A. Aiello, G. Puentes, D. Voigt, and J. Woerdman, "Maximum-likelihood estimation of mueller matrices." *Optics Letters*, vol. 31, no. 6, pp. 817–819, 2006.

[67] D. Ratchford, K. Dziatkowski, T. Hartsfield, X. Li, Y. Gao, and Z. Tang, "Photoluminescence dynamics of ensemble and individual cdse/zns quantum dots with an alloyed core/shell interface," *Journal of Applied Physics*, vol. 109, no. 10, p. 103509, 2011.

[68] A. Van Driel, I. Nikolaev, P. Vergeer, P. Lodahl, D. Vanmaekelbergh, and W. Vos, "Statistical analysis of time-resolved emission from ensembles of semiconductor quantum dots: Interpretation of exponential decay models," *Physical Review B*, vol. 75, p. 035329, 2007.

[69] C. I. Osorio, A. Mohtashami, and A. F. Koenderink, "K-space polarimetry of bullseye plasmon antennas," *Scientific reports*, vol. 5, 2015.

[70] Y. Gorodetski, E. Lombard, A. Drezet, C. Genet, and T. W. Ebbesen, "A perfect plasmonic quarter-wave plate," *Applied Physics Letters*, vol. 101, 2012. [Online]. Available: http://dx.doi.org/10.1063/1.4766189

[71] M. A. Kats, P. Genevet, G. Aoust, N. Yu, R. Blanchard, F. Aieta, Z. Gaburro, and F. Capasso, "Giant birefringence in optical antenna arrays with widely tailorable optical anisotropy," *Proceedings of the National Academy of Sciences*, vol. 109, no. 31, pp. 12 364–12 368, 2012.

[72] N. Yu, P. Genevet, M. A. Kats, F. Aieta, J.-P. Tetienne, F. Capasso, and Z. Gaburro, "Light propagation with phase discontinuities: generalized laws of reflection and refraction," *Science*, vol. 334, no. 6054, pp. 333–337, 2011.

[73] A. Pors, M. G. Nielsen, G. D. Valle, M. Willatzen, O. Albrektsen, and S. I. Bozhevolnyi, "Plasmonic metamaterial wave retarders in reflection by orthogonally oriented detuned electrical dipoles," *Optics Letters*, vol. 36, no. 9, pp. 1626–1628, 2011.

[74] E. Khoo, E. Li, and K. Crozier, "Plasmonic wave plate based on subwavelength nanoslits." *Optics Letters*, vol. 36, no. 13, pp. 2498–2500, 2011.

[75] A. Roberts and L. Lin, "Plasmonic quarter-wave plate." *Optics Letters*, vol. 37, no. 11, pp. 1820–1822, 2012.

[76] A. Drezet, C. Genet, and T. W. Ebbesen, "Miniature plasmonic wave plates," *Physical review letters*, vol. 101, no. 4, p. 043902, 2008.

[77] J. Yang and J. Zhang, "Subwavelength quarter-waveplate composed of l-shaped metal nanoparticles," *Plasmonics*, vol. 6, no. 2, pp. 251–254, 2011.

[78] F. Wang, A. Chakrabarty, F. Minkowski, K. Sun, and Q.-H. Wei, "Polarization conversion with elliptical patch nanoantennas," *Applied Physics Letters*, vol. 101, no. 2, p. 023101, 2012.

[79] P. G. Thompson, C. G. Biris, E. J. Osley, O. Gaathon, R. M. Osgood, N. C. Panoiu, and P. A. Warburton, "Polarization-induced tunability of localized surface plasmon resonances in arrays of sub-wavelength cruciform apertures," *Optics express*, vol. 19, no. 25, pp. 25 035–25 047, 2011.

[80] R. Gordon, A. Brolo, A. McKinnon, A. Rajora, B. Leathem, and K. Kavanagh, "Strong polarization in the optical transmission through elliptical nanohole arrays," *Physical review letters*, vol. 92, no. 3, p. 037401, 2004.

[81] P. F. Chimento, N. V. Kuzmin, J. Bosman, P. F. Alkemade, G. W. t Hooft, and E. R. Eliel, "A subwavelength slit as a quarter-wave retarder," *Optics express*, vol. 19, no. 24, pp. 24 219–24 227, 2011.

[82] J.-H. Choe, J.-H. Kang, D.-S. Kim, and Q.-H. Park, "Slot antenna as a bound charge oscillator," *Optics express*, vol. 20, no. 6, pp. 6521–6526, 2012.

[83] M. Born and E. Wolf, *Principles of optics: electromagnetic theory of propagation, interference and diffraction of light*. CUP Archive, 1999.

[84] P. Chen, Y. Lo, T. Yu, J. Lin, and T. Yang, "Measurement of linear birefringence and diattenuation properties of optical samples using polarimeter and stokes parameters." *Optics express*, vol. 17, no. 18, pp. 15 860–15 884, 2009.

[85] C. Collet, J. Zallat, and Y. Takakura, "Clustering of mueller matrix images for skeletonized structure detection," *Optics express*, vol. 12, no. 7, pp. 1271–1280, 2004.

[86] Z. Li, A. W. Clark, and J. M. Cooper, "Annular nanoplasmonic void arrays as tunable surface enhanced raman spectroscopy substrates," *Applied Physics Letters*, vol. 105, no. 3, p. 033115, 2014.

[87] Z. Zhang, R. Peng, Z. Wang, F. Gao, X. Huang, W. Sun, Q. Wang, and M. Wang, "Plasmonic antenna array at optical frequency made by nanoapertures," *Applied Physics Letters*, vol. 93, no. 17, p. 171110, 2008.

[88] T. Davis, D. Gómez, and K. Vernon, "Simple model for the hybridization of surface plasmon resonances in metallic nanoparticles," *Nano Letters*, vol. 10, no. 7, pp. 2618–2625, 2010.

[89] J. J. Cadusch, T. D. James, and A. Roberts, "Experimental demonstration of a wave plate utilizing localized plasmonic resonances in nanoapertures," *Optics express*, vol. 21, no. 23, pp. 28 450–28 455, 2013.

[90] H. G. Booker, "Slot aerials and their relation to complementary wire aerials (babinet's principle)," *Electrical Engineers-Part IIIA: Radiolocation, Journal of the Institution of*, vol. 93, no. 4, pp. 620–626, 1946.

[91] B. Van Zeghbroeck, "Principles of semiconductor devices," *Colarado University*, 2004.

[92] S. Y. Chou and M. Y. Liu, "Nanoscale tera-hertz metal-semiconductor-metal photodetectors," *Quantum Electronics, IEEE Journal of*, vol. 28, no. 10, pp. 2358–2368, 1992.

[93] S. Earl, D. Gómez, T. James, T. Davis, and A. Roberts, "Material effects on v-nanoantenna performance," *Nanoscale*, vol. 7, no. 9, pp. 4179–4186, 2015.

[94] E. Panchenko, J. J. Cadusch, T. D. James, and A. Roberts, "Plasmonic metasurface-enabled differential photodetectors for broadband optical polarization characterization," *ACS Photonics*, vol. 3, no. 10, pp. 1833–1839, 2016.

[95] E. Hecht and A. Zajac, "Optics addison-wesley," *Reading, Mass*, pp. 301–305, 1974.

[96] J.-S. Huang, V. Callegari, P. Geisler, C. Brüning, J. Kern, J. C. Prangsma, X. Wu, T. Feichtner, J. Ziegler, P. Weinmann *et al.*, "Atomically flat single-crystalline gold nanostructures for plasmonic nanocircuitry," *Nature communications*, vol. 1, p. 150, 2010.

[97] G. Sharp, M. Yuce, and X. Hu, "Metamaterial fishnet structure formed from nanoimprint lithography," 2013.

[98] Y. Huang, F. Zhang, K. Hwang, W. Nix, G. Pharr, and G. Feng, "A model of size effects in nano-indentation," *Journal of the Mechanics and Physics of Solids*, vol. 54, no. 8, pp. 1668–1686, 2006.

[99] I. Plans, A. Carpio, and L. Bonilla, "Toy nanoindentation model and incipient plasticity," *Chaos, Solitons & Fractals*, vol. 42, no. 3, pp. 1623–1630, 2009.

[100] M. Lichinchi, C. Lenardi, J. Haupt, and R. Vitali, "Simulation of berkovich nanoindentation experiments on thin films using finite element method," *Thin solid films*, vol. 312, no. 1, pp. 240–248, 1998.

[101] N. E. Dowling, *Mechanical behavior of materials: engineering methods for deformation, fracture, and fatigue*. Prentice hall, 1993.

[102] A. Djalalian-Assl, J. J. Cadusch, Z. Q. Teo, T. J. Davis, and A. Roberts, "Surface plasmon wave plates," *Applied Physics Letters*, vol. 106, no. 4, p. 041104, 2015.

[103] W. Song, X. Zhang, A. Liu, C. Lim, P. Yap, and H. M. M. Hosseini, "Refractive index measurement of single living cells using on-chip fabry-pérot cavity," *Applied physics letters*, vol. 89, no. 20, p. 203901, 2006.

[104] Y. Shen, J. Zhou, T. Liu, Y. Tao, R. Jiang, M. Liu, G. Xiao, J. Zhu, Z.-K. Zhou, X. Wang *et al.*, "Plasmonic gold mushroom arrays with refractive index sensing figures of merit approaching the theoretical limit," *Nature Communications*, vol. 4, 2013.

[105] I. M. White and X. Fan, "On the performance quantification of resonant refractive index sensors," *Optics Express*, vol. 16, no. 2, pp. 1020–1028, 2008.

[106] J. A. Richards and J. Richards, *Remote sensing digital image analysis*. Springer, 1999, vol. 3.

[107] G. Nilsson, J. Belasco, S. Cohen, and A. Von Gabain, "Growth-rate dependent regulation of mrna stability in Escherichia Coli," 1984.

[108] J.-W. Su, W.-C. Hsu, C.-Y. Chou, C.-H. Chang, and K.-B. Sung, "Digital holographic microtomography for high-resolution refractive index mapping of live cells," *Journal of Biophotonics*, vol. 6, no. 5, pp. 416–424, 2013.

[109] Y. Zhou, M. Asbahi, G. Luo, T. Eriksson, S. Yamada, P. V. Krishnan, and B. Heidari, "High volume manufacturing of nanoimprint lithography produced devices: addressing the stamp supply challenge," in *SPIE Advanced Lithography*. International Society for Optics and Photonics, 2010, pp. 76 371X–76 371X.

[110] A. Akimov, A. Mukherjee, C. Yu, D. Chang, A. Zibrov, P. Hemmer, H. Park, and M. Lukin, "Generation of single optical plasmons in metallic nanowires coupled to quantum dots," *Nature*, vol. 450, no. 7168, pp. 402–406, 2007.

[111] D. Englund, D. Fattal, E. Waks, G. Solomon, B. Zhang, T. Nakaoka, Y. Arakawa, Y. Yamamoto, and J. Vučković, "Controlling the spontaneous emission rate of single quantum dots in a two-dimensional photonic crystal," *Physical review letters*, vol. 95, no. 1, p. 013904, 2005.

[112] K. Tanaka, E. Plum, J. Ou, T. Uchino, and N. Zheludev, "Multifold enhancement of quantum dot luminescence in plasmonic metamaterials," *Physical Review Letters*, vol. 105, no. 22, p. 227403, 2010.

[113] N. Ganesh, W. Zhang, P. C. Mathias, E. Chow, J. Soares, V. Malyarchuk, A. D. Smith, and B. T. Cunningham, "Enhanced fluorescence emission from quantum dots on a photonic crystal surface," *Nature Nanotechnology*, vol. 2, no. 8, pp. 515–520, 2007.

[114] L. Novotny and N. Van Hulst, "Antennas for light," *Nature Photonics*, vol. 5, no. 2, pp. 83–90, 2011.

[115] J.-H. Song, T. Atay, S. Shi, H. Urabe, and A. V. Nurmikko, "Large enhancement of fluorescence efficiency from cdse/zns quantum dots induced by resonant coupling to spatially controlled surface plasmons," *Nano Letters*, vol. 5, no. 8, pp. 1557–1561, 2005.

[116] J. Zhang, J. Ou, K. MacDonald, and N. Zheludev, "Optical response of plasmonic relief meta-surfaces," *Journal of Optics*, vol. 14, no. 11, p. 114002, 2012.

[117] A. Nozik, "Quantum dot solar cells," *Physica E: Low-dimensional Systems and Nanostructures*, vol. 14, no. 1, pp. 115–120, 2002.

[118] B. S. Mashford, T.-L. Nguyen, G. J. Wilson, and P. Mulvaney, "All-inorganic quantum-dot light-emitting devices formed via low-cost, wet-chemical processing," *Journal of Materials Chemistry*, vol. 20, no. 1, pp. 167–172, 2010.

[119] A. Djalalian-Assl, D. Gomez, A. Roberts, and T. Davis, "Frequency-dependent optical steering from subwavelength plasmonic structures," *Optics Letters*, vol. 37, no. 20, pp. 4206–4208, 2012.

[120] K. Boldt, N. Kirkwood, G. A. Beane, and P. Mulvaney, "Synthesis of highly luminescent and photo-stable, graded shell cdse/cd x zn1–x s nanoparticles by in situ alloying," *Chemistry of Materials*, vol. 25, no. 23, pp. 4731–4738, 2013.

[121] H. Mertens and A. Polman, "Plasmon-enhanced erbium luminescence," *Applied Physics Letters*, vol. 89, no. 21, p. 211107, 2006.

[122] S. S. Kruk, M. Decker, I. Staude, S. Schlecht, M. Greppmair, D. N. Neshev, and Y. S. Kivshar, "Spin-polarized photon emission by resonant multipolar nanoantennas," *ACS Photonics*, vol. 1, pp. 1218–1223, 2014.

[123] J. J. Cadusch, T. D. James, A. Djalalian-Assl, T. J. Davis, and A. Roberts, "A chiral plasmonic metasurface circular polarization filter," *Photonic Technology Letters*, vol. 26, pp. 2357–2360, 2014.

[124] Y. Chong, L. Ge, H. Cao, and A. D. Stone, "Coherent perfect absorbers: time-reversed lasers," *Physical review letters*, vol. 105, no. 5, p. 053901, 2010.

[125] H.-T. Chen, "Interference theory of metamaterial perfect absorbers," *Optics express*, vol. 20, no. 7, pp. 7165–7172, 2012.

[126] H. M. Doeleman, E. Verhagen, and A. F. Koenderink, "Antenna-cavity hybrids: matching polar opposites for purcell enhancements at any linewidth," *arXiv preprint arXiv:1605.04181*, 2016.

[127] T. Maniv and H. Metiu, "Electrodynamics at a metal surface. ii. fresnel formulas for the electromagnetic field at the interface for a jellium model within the random phase approximation," *The Journal of Chemical Physics*, vol. 76, no. 5, pp. 2697–2713, 1982.

[128] J.-H. Choi, S.-K. Sung, C.-H. Kim, Y.-H. Jung, J.-Y. Jung, J.-H. Jeong, and E.-S. Lee, "Bilayer hybrid nanoimprinting method for fabricating embedded silver nanostructure arrays with enhanced photoluminescence," *Journal of Nanophotonics*, vol. 8, no. 1, pp. 083 089–083 089, 2014.

[129] H. J. Lezec, A. Degiron, E. Devaux, R. Linke, L. Martin-Moreno, F. Garcia-Vidal, and T. Ebbesen, "Beaming light from a subwavelength aperture," *Science*, vol. 297, no. 5582, pp. 820–822, 2002.

[130] W. Chao, J. Kim, S. Rekawa, P. Fischer, and E. H. Anderson, "Demonstration of 12 nm resolution fresnel zone plate lens based soft x-ray microscopy," *Optics Express*, vol. 17, no. 20, pp. 17 669–17 677, 2009.

[131] N. Livneh, M. G. Harats, S. Yochelis, Y. Paltiel, and R. Rapaport, "Efficient collection of light from colloidal quantum dots with a hybrid metal–dielectric nanoantenna," *ACS Photonics*, vol. 2, no. 12, pp. 1669–1674, 2015.

[132] A. Mohtashami, C. I. Osorio, and A. F. Koenderink, "Angle-resolved polarimetry of antenna-mediated fluorescence," *Physical Review Applied*, vol. 4, no. 5, p. 054014, 2015.

[133] J. J. Cadusch, E. Panchenko, N. Kirkwood, T. D. James, B. C. Gibson, K. J. Webb, P. Mulvaney, and A. Roberts, "Emission enhancement and polarization of semiconductor quantum dots with nanoimprinted plasmonic cavities: towards scalable fabrication of plasmon-exciton displays," *Nanoscale*, vol. 7, no. 33, pp. 13 816–13 821, 2015.

[134] O. Mahboub, S. C. Palacios, C. Genet, F. Garcia-Vidal, S. G. Rodrigo, L. Martin-Moreno, and T. Ebbesen, "Optimization of bulls eye structures for transmission enhancement," *Optics express*, vol. 18, no. 11, pp. 11 292–11 299, 2010.

[135] R. Dorn, S. Quabis, and G. Leuchs, "Sharper focus for a radially polarized light beam," *Physical review letters*, vol. 91, no. 23, p. 233901, 2003.

[136] L. Novotny and B. Hecht, *Principles of nano-optics*. Cambridge university press, 2012.

[137] D. Gómez, Z. Teo, M. Altissimo, T. Davis, S. Earl, and A. Roberts, "The dark side of plasmonics," *Nano Letters*, vol. 13, no. 8, pp. 3722–3728, 2013.

[138] J. Kang and D. Schroder, "Gettering in silicon," *Journal of Applied Physics*, vol. 65, no. 8, pp. 2974–2985, 1989.

[139] S. Mukherjee, F. Libisch, N. Large, O. Neumann, L. V. Brown, J. Cheng, J. B. Lassiter, E. A. Carter, P. Nordlander, and N. J. Halas, "Hot electrons do the impossible: plasmon-induced dissociation of H2 on Au," *Nano Letters*, vol. 13, no. 1, pp. 240–247, 2012.

[140] A. Rhelimi, "Active security device including an electronic memory," Mar. 2 1999, US Patent 5,877,547.

[141] T. P. White and K. R. Catchpole, “Plasmon-enhanced internal photoemission for photovoltaics: theoretical efficiency limits,” *Applied Physics Letters*, vol. 101, no. 7, p. 073905, 2012.